ETH_zürich_

Empa
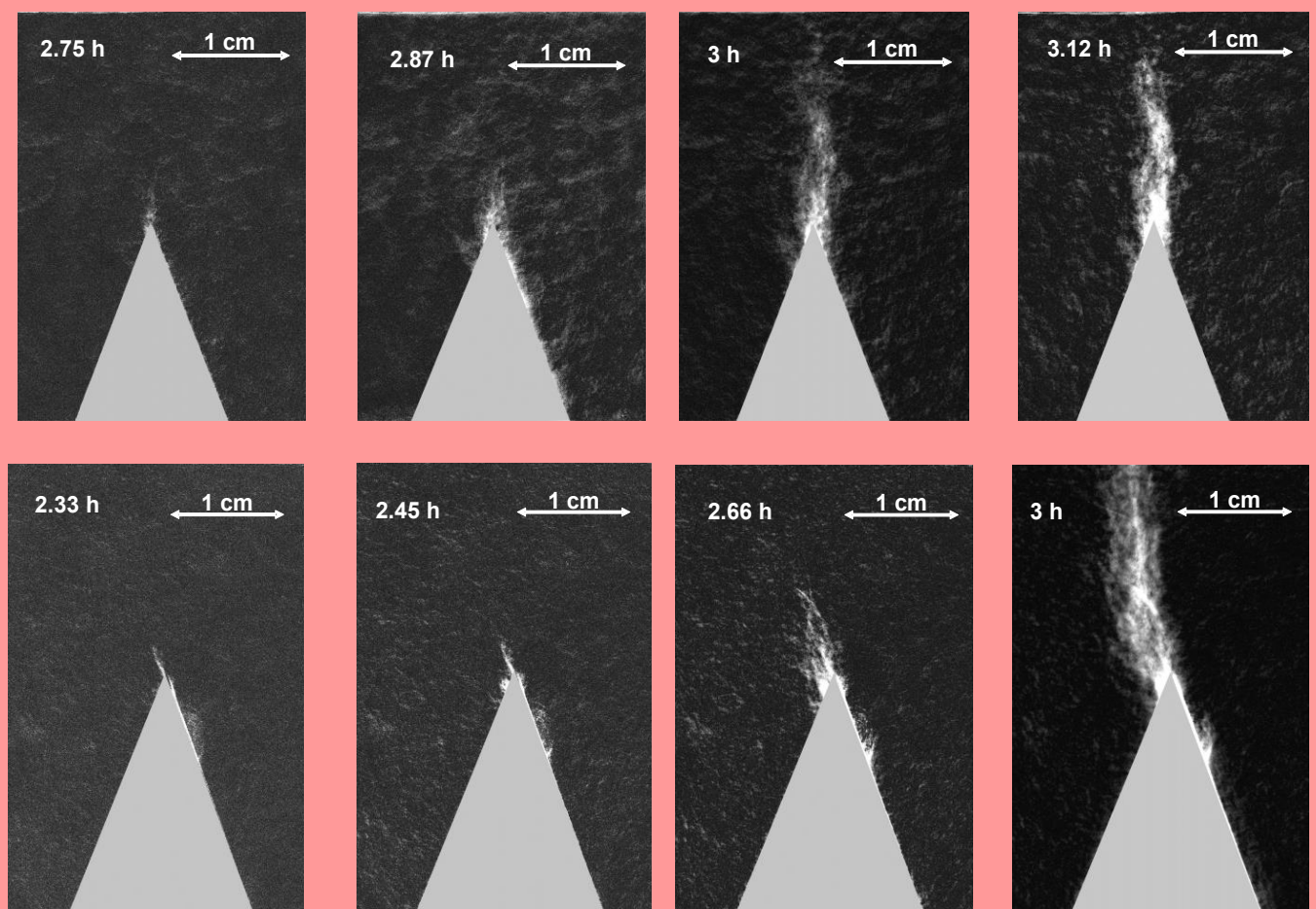Materials Science and Technology

PLASTIC SHRINKAGE CRACKING IN CONCRETE: FROM MECHANISMS TO MITIGATION STRATEGIES

DISS. ETH NO. 24939

Sadegh Ghourchian

ETH Zurich, D-BAUG, Institute for Building Materials (IfB)

Empa, Concrete and Construction Chemistry Laboratory

2018

DISS. ETH NO. 24939

PLASTIC SHRINKAGE CRACKING IN CONCRETE: FROM MECHANISMS TO MITIGATION STRATEGIES

A thesis submitted to attain the degree of

DOCTOR OF SCIENCES of ETH ZURICH

(Dr. sc. ETH Zurich)

presented by

SADEGH GHOURCHIAN

M.Sc. in Civil-Structural Engineering, University of Tehran

born on 22.08.1984

citizen of Iran

accepted on the recommendation of

Prof. Dr. Pietro Lura examiner
Dr. Mateusz Wyrzykowski co-examiner
Prof. Dr. Laura De Lorenzis co-examiner
Prof. Dr. Guillaume Habert co-examiner
Dr. Siavash Ghabezloo co-examiner

2018

To my parents

and

my sister

"Suffering is a gift. In it is hidden mercy."

-Jalal ad-Din Muhammad Rumi (Mowlana)

Preface

The problem of global warming is so serious and significant that recently worldwide nations signed the Paris Agreement to take necessary actions to limit the global warming below 2 °C compared to the pre-industrial levels. Many efforts have been made in the field of civil engineering to minimize the contribution of Portland cement production to the man-made CO_2 emissions, by developing green cements and furthermore, producing concretes with improved durability and mechanical performance. The latter is not possible, unless thorough knowledge about volume changes and cracking of concrete at early ages is gained. The aim of this study is to provide fundamental knowledge about the behavior of fresh cementitious materials, which are at high risk of cracking while still fresh (so-called *plastic shrinkage cracking*). Indeed, plastic shrinkage, according to some sources, may be the cause of roughly 80% of early-age cracking in concrete structures.

Here, I would like to acknowledge all people helped and supported me during my PhD project. I gratefully appreciate Prof. Dr. Pietro Lura who supervised me during this project, for his kind support and excellent creative comments and guidance, from the experiments to the analytical methods, which allowed me to succeed in my work. Furthermore, I need to thank Dr. Mateusz Wyrzykowski, my second supervisor, for the fruitful discussions we made, especially on the poromechanics model development, which allowed me to overcome the modeling complexities. Moreover, I would like to acknowledge ETH Zurich and Empa (Swiss Federal Laboratories for Materials Science and Technology), for providing an outstanding research environment for young scientists to flourish their talent. I appreciate the staff of the Concrete/Construction Chemistry laboratory of Empa, for their help in conducting the experimental work. Also I would thank the external reviewers for their efforts in reviewing the thesis.

Last but not least, I thank my parents, Mrs. Shamsi Mahdieh and Prof. Dr. Hedayatollah Ghourchian, and my sister Nikoo, for their love and support, which motivated me to prevail the difficulties during my PhD studies in Switzerland.

Sadegh Ghourchian
Dübendorf, December 2017

Abstract

Early-age cracking of cementitious materials jeopardizes their service life. A thorough understanding of the involved mechanisms is needed to mitigate cracking with effective and appropriate methods. One of the most common types of cracking is caused by plastic shrinkage, which can occur from time of casting and before the time of final set.

This PhD dissertation is dedicated to poromechanics modeling of plastic shrinkage and cracking in fresh cementitious materials. The model is based on a generalized consolidation equation derived in this project, which includes the chemical shrinkage together with moisture flow according to Darcy's law. This allows to predict deformations of concrete in the plastic phase due to self-weight consolidation and early-age drying using genuine experimental data as an input. Furthermore, plastic shrinkage cracking was studied by establishing a failure envelope, which requires the estimated pseudo-elastic limit as an input. Both models for moisture transfer and solid mechanics were implemented in COMSOL Multiphysics® software.

The study was started by characterization of material properties, i.e. coefficient of permeability and bulk modulus in the bleeding state derived from the simple bleeding test, and was expanded to the material properties for the drying state, which included the determination of the water retention characteristic curve (WRCC) for fresh cementitious materials.

Novel experimental methods were utilized for the model validation, including digital image correlation (DIC) system for measurements of three dimensional plastic shrinkage and Tempe cell and tensiometers for WRCC, together with the ASTM C1579-13 standard and X-ray radiography for crack quantification.

According to the developed models, the plastic shrinkage cracking mechanisms were explained extensively and different mitigation strategies were analyzed according to the thorough understanding gained in the project.

Sommario

La fessurazione precoce dei materiali cementizi compromette la loro durata. Per mitigare la fessurazione con metodi appropriati ed efficaci, è necessaria una conoscenza approfondita dei meccanismi coinvolti. Uno dei tipi più comuni di fessurazione è causato dal ritiro plastico, che può verificarsi dal momento del getto fino alla presa.

Questa tesi di dottorato è dedicata alla modellistica poromeccanica del ritiro plastico e della fessurazione in materiali cementizi freschi. Il modello si basa su un'equazione di consolidamento generalizzata derivata in questo progetto, che include il ritiro chimico insieme al flusso di umidità secondo la legge di Darcy. Ciò consente di prevedere deformazioni del calcestruzzo nella fase plastica a causa del consolidamento dovuto al peso proprio e a causa dell'essiccazione, utilizzando dati sperimentali originali come input. Inoltre, la fessurazione dovuta a ritiro plastico è stato studiata stabilendo un criterio di resistenza, che richiede la stima del limite pseudo-elastico come input. Entrambi i modelli per il trasporto dell'umidità e per la meccanica dei solidi sono stati implementati nel software COMSOL Multiphysics®.

Lo studio è cominciato dalla caratterizzazione delle proprietà del materiale, cioè il coefficiente di permeabilità e modulo di compressibilità nello stato di bleeding derivato dal test standard di bleeding, ed è stato esteso alle proprietà del materiale durante lo stato di essiccazione, includendo anche la determinazione della curva caratteristica di ritenzione idrica (WRCC) per materiali cementizi freschi.

Per la validazione del modello sono stati utilizzati nuovi metodi sperimentali, compreso il sistema di correlazione di immagini digitali (DIC) per misure di ritiro plastico in tre dimensioni e celle Tempe e tensiometri per la WRCC, insieme allo standard ASTM C1579-13 e radiografia a raggi X per la quantificazione delle cricche.

Nello spirito dei modelli sviluppati in questa tesi, i meccanismi di fessurazione plastica sono stati spiegati nel dettaglio e diverse strategie di mitigazione sono state analizzate in base alla comprensione approfondita acquisita nel progetto.

Table of contents

List of figures

List of tables

Nomenclature

b [m/s]: bleeding rate

B [Pa]: bulk modulus

B_0 [Pa]: initial bulk modulus

B_b [Pa]: bulk modulus in bleeding state

B_e [Pa]: bulk modulus in drying state

B_s [Pa]: bulk modulus of solid grains

c [Pa]: cohesion in Mohr-Coulomb model

C [Pa]: cohesion in Drucker-Prager model

C_B [kg/m^2]: bleeding capacity

C_d [m^2/s]: diffusivity coefficient

e [kg/m^2/h]: evaporation rate

e_c [kg/m^2/h]: critical evaporation rate

E [Pa]: elastic modulus

E_a [kJ/mol]: the apparent activation energy of concrete

F_B [m^2/kg]: Blaine fineness of the cement

F_S [-]: shape factor

F_{TE} [(m/m)^2]: electric tortuosity

F_{TH} [(m/m)^2]: hydraulic tortuosity

G [Pa]: shear modulus

$\vec{g}$ [m/s^2]: gravity acceleration vector

h [m]: height of sample

$\boldsymbol{I}$ [-]: unit tensor

I_1 [Pa]: first invariant of the effective stress tensor

J_2 [Pa^2]: second invariant of the effective deviatoric stress tensor

K [m^2/Pa·s]: mobility coefficient

k_{eff} [m/s]: effective coefficient of permeability

k_r [-]: relative permeability

L [m]: thickness

L_e [m]: actual distance of flow

m [-]: pore size distribution index

$\dot{m}_{hydr}$ [kg/m^3·s]: rate of water consumption during cement hydration

M_{cem} [kg/m^3]: the initial mass of cement in the mixture

$\vec{n}$ [m]: normal direction vector of the surface

n [m^3/m^3]: porosity

n_{cap} [m^3/m^3]: capillary porosity

n_e [m^3/m^3]: effective porosity

n_{tot} [m^3/m^3]: initial volumetric water content (mixing water)

p_a [Pa]: atmospheric pressure

p_{ae} [Pa]: air entry pressure

p_{ae-t0} [Pa]: initial air entry pressure

p_c [Pa]: capillary pressure

p_{over} [Pa]: applied air overpressure

p_{c-safe} [Pa]: safe capillary pressure

p_{pel-c} [Pa]: compressive pseudo-elastic limit

p_{pel-t} [Pa]: tensile pseudo-elastic limit

q [m/s]: pore fluid flux

$\dot{Q}$ [J/(s·g)]: isothermal heat flux

r [m]: equivalent pore radius (according to Young-Laplace equation)

R [J/mol K]: universal gas constant

R_c [Ω·m]: electrical resistivity of concrete

R_f [Ω·m]: electrical resistivity of pore fluid

R_p [Ω·m]: electrical resistivity of paste

S [m^2/m^3]: specific surface area of the wetted material
S_{ap} [m^2/m^3]: apparent specific surface area
S_h [m^2/m^3]: hydrodynamic surface area
S_w [-]: saturation degree
t [min]: time from mixing start
t_{cast} [min]: casting time from mixing start
t_{FSB} [h]: time of final set (Vicat) in the bleeding state
t_{FSD} [h]: time of final set (Vicat) in the drying state
t_{ISD} [h]: time of initial set (Vicat) in the drying state
t^* [min]: hydration characteristic time
T_c [K]: actual concrete temperature
T_{iso} [K]: reference isothermal temperature
V_{agg} [m^3]: aggregate volume
V_f [m^3]: fluid volume
V_p [m^3]: paste volume
V_t [m^3]: total concrete volume
W_v [m^3/m^3]: volumetric water content
z [m]: elevation from bottom of sample

α [-]: hydration degree

α_c [-]: a factor which accounts for the volumetric ratio of the stagnant water for concrete

α_p [-]: a factor which accounts for the volumetric ratio of the stagnant water for cement paste

α_s [-]: a factor which accounts for the volumetric ratio of the stagnant water

β [1/Pa]: compressibility of pore fluid

γ [Pa·m]: surface tension of pore fluid

$\varepsilon_{xx} = \varepsilon_{yy}$ [-]: horizontal strains

ε_{zz} [-]: vertical strain

ε_{vol} [-]: volumetric strain

θ [rad]: contact angle

κ [m^2]: intrinsic permeability

λ [degree]: angle of stress path

λ_b [1/Pa]: compressibility of the bulk

μ [Pa·s]: dynamic viscosity of the pore fluid

ν [-]: Poisson's ratio

ξ [-]: parameter defining the maximum effect of capillary pressure on fresh concrete stiffness

ξ_V [-]: parameter defining the maximum effect of capillary pressure on fresh concrete stiffness calibrated by the Vicat test

ρ_{cem} [kg/m^3]: cement density

ρ_f [kg/m^3]: density of the pore fluid

ρ_s [kg/m^3]: solid density

ρ_w [kg/m^3]: density of water

σ_{sw} [Pa]: self-weight stress

σ_{ex} [Pa]: external load (stress)

σ_{eff} [Pa]: effective stress

σ_r [Pa]: effective restraint stress

σ_{yc} [Pa]: uniaxial compressive strength

σ_{yt} [Pa]: uniaxial tensile strength

φ [degree]: angle of internal friction in Mohr-Coulomb model

ϕ [degree]: angle of internal friction in Drucker-Prager model

ψ_p [Pa]: pore fluid's pressure potential

ψ_m [Pa]: matric potential

ψ_T [Pa]: total pore fluid potential

ψ_z [Pa]: pore fluid gravitational potential

ω [1/Pa]: parameter controlling the rate of increase of fresh concrete stiffness with capillary pressure

ω_V [1/h]: parameter controlling the rate of increase of fresh concrete stiffness with capillary pressure, calibrated by the Vicat test

This page is intentionally left blank.

Chapter 1. Introduction

1.1. Background and research motivation

Mineral binders have been the most used construction materials since about 5000 B.C. [1], e.g. earthen materials, quicklime, gypsum plaster and cement. They are mixed with water and aggregates to form a porous solid substance. Among them, Portland cement is a modern binder, invented in the 19th century [2]. It is a hydraulic binder, based mainly on calcium silicates: tricalcium silicate (C_3S, referred to as *alite*) and dicalcium silicate (C_2S, referred to as *belite*). The minor phases include: tricalcium aluminate (C_3A) and tetra-calcium aluminoferrite (C_4AF) [3]. The utilized cement chemistry notations refer to: $C=CaO$, $S=SiO_2$, $A=Al_2O_3$, $F=Fe_2O_3$.

The silicates in Portland cement react with water, leading to the formation of the dominant binding phase, nanocristalline Calcium Silicate Hydrate (C-S-H) (see *Fig. 1. 1*). C-S-H is the phase that is mainly responsible of the mechanical properties of hydrated cementitious materials, binding chemically inert aggregates and producing structural elements with high strength and durability.
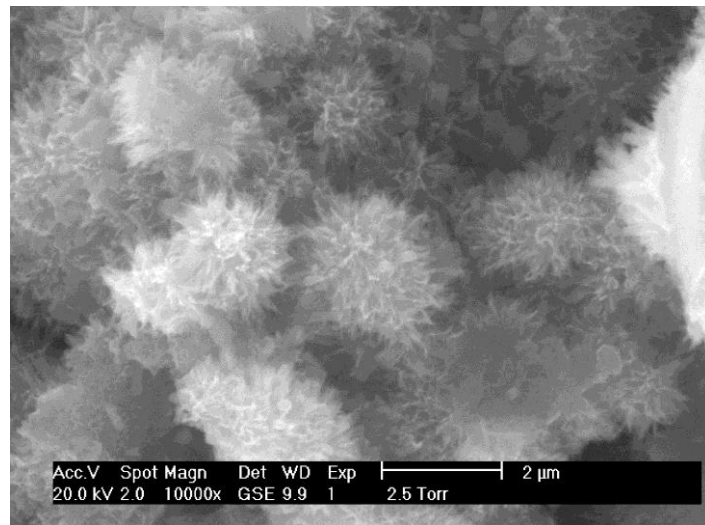
Fig. 1. 1. Calcium Silicate Hydrates. From [4]

Thanks to the strength and durability of the cement made materials, i.e. mortars and concretes, civil engineers were able to build a modern infrastructure, e.g. commercial and residential buildings, dams, high-rise towers, long-span bridges, railways and roads. However, limited resources (e.g. energy, raw materials in some countries) on the Earth for the production of the cement [5], and furthermore, CO_2-emissions as the by-product of cement production industry [5,6] (about 8 % of global emissions [7]), which contribute to global

warming with other modern industries [8], led civil engineering specialists to improve the performance of cementitious materials towards a more sustainable infrastructure.

At the moment, some main strategies (see *Fig. 1. 2*) to improve the sustainability of cementitious materials include:
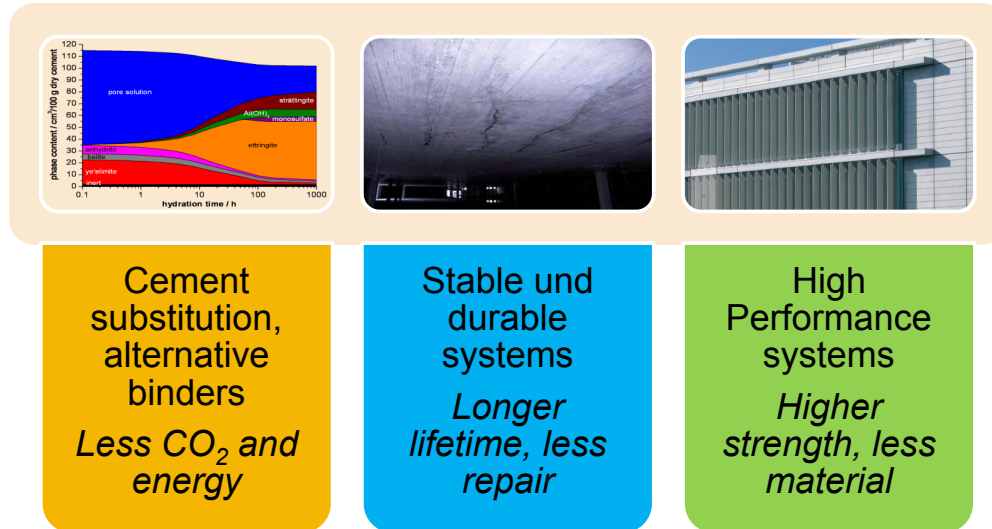
Fig. 1. 2. Main strategies to improve the sustainability of cementitious materials [3]

1- Developing green cements [9], by limiting the production of cement clinker and instead, adding of Supplementary Cementitious Materials (SCMs) and fine fillers, referred to as blended cements, or by substituting Portland cement clinker with new eco-friendly binders with lower CO_2 footprint (e.g., Alkali-activated materials, calcium sulfoaluminate cements, carbonation-based binders).

2- Improving the durability of cementitious materials, which would prolong their lifetime and ultimately decrease cement consumption. Measures to increase the durability include the mitigation of early-age cracking [10] to minimize the repair and rehabilitation of structures. This takes often the form of reducing the volume changes that induce cracking when restrained, e.g., shrinkage, thermal expansion and expansion due to Alkali Silica Reaction (ASR). The mentioned cracks increase concrete's permeability dramatically, facilitating the ingress of harmful substances, e.g. chloride and sulfate ions, jeopardizing the service life of reinforced concrete structures [11].

3- Using cementitious materials with higher mechanical properties, high-performance and ultra-high-performance concrete, to build slender, more efficient structures with an ultimate economy of raw materials [12].

This study focuses on the second approach outlined above and in *Fig. 1. 2*, and is dedicated to investigating the mechanisms of formation of cracks that appear sometime after concrete casting and before the final setting time, during the dormant hydration period until the beginning of the hydration acceleration period (see *Fig. 1. 3*).
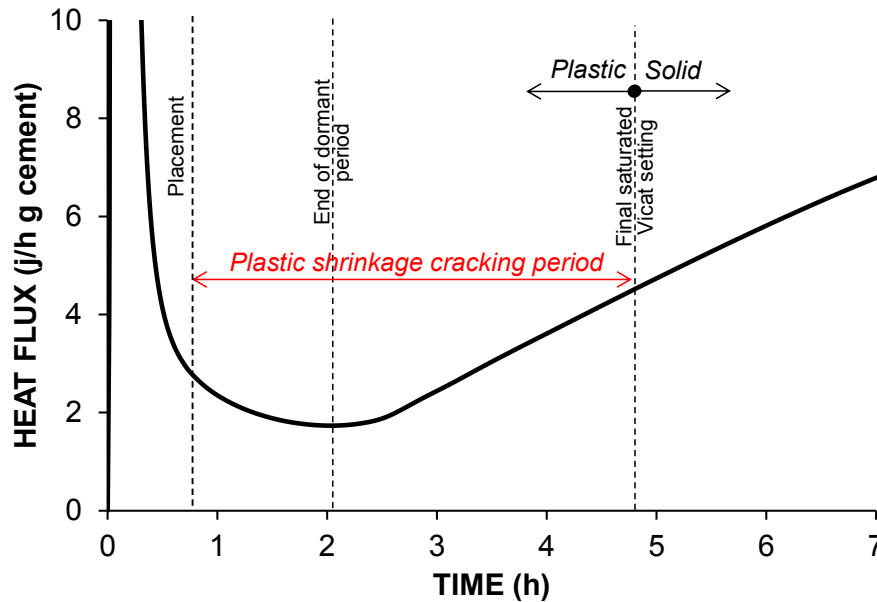
Fig. 1. 3. The short time period in which concrete may crack only due to plastic shrinkage. The figure shows actual results; for different types of cementitious materials, the heat flux in time may vary.

An ideal cementitious material needs to be plastic initially, maintaining enough workability for some time after production, allowing for the transportation and efficient casting/compaction, and then undergoing an accelerated evolution of the mechanical properties. Therefore, ground gypsum is added to the cement clinker powder, to control the fast hydration of tricalcium aluminate (C_3A-minor phase of the Portland cement clinker), that in the absence of gypsum would lead to flash-setting [13]. When gypsum is present, C_3A instead reacts to form a calcium sulfoaluminate containing large amounts of water in its crystal structure, called ettringite. This initial reaction, in which ettringite precipitates in the form of small rod-like crystals [13] (see *Fig. 1. 4*), is highly exothermic and lasts only for a few minutes. Then the dormant hydration period starts, when the hydration reactions proceed very slowly, allowing enough time for concrete transportation and placement. In this period, workability of the concrete decreases and the stiffness increases slowly. At the end of the dormant period, in the hydration acceleration period, the precipitation of C-S-H accelerates, leading to bridging of solid particles and percolation of the solids through the microstructure. After the fluid-solid transition (corresponding in concrete practice to setting), the stiffness and the strength of the concrete increase rapidly.
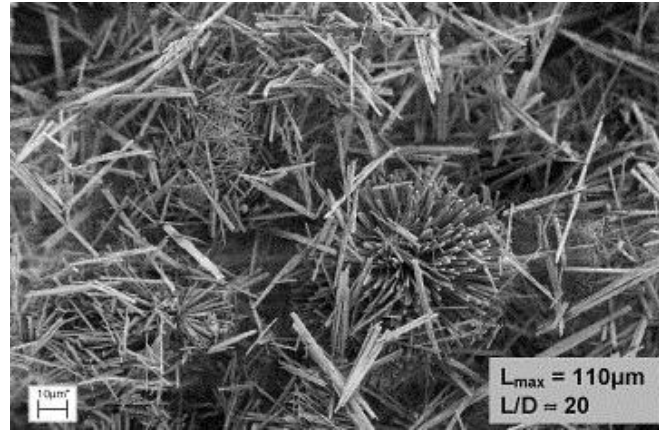
Fig. 1. 4. Rod-like crystals of ettringite [14]

During the dormant period (see *Fig. 1. 3*), concrete is plastic with an insignificant strength, which makes it highly susceptible to failure and cracking. Accordingly, it is mentioned that plastic shrinkage is the source of roughly 80% of the early-age cracking of reinforced concrete structures [15]. After placement, concrete can be considered as a suspension of solid particles in water (see *Fig. 1. 5*). Since this suspension does not have a solid structure to retain its own weight, the particles settle in the liquid and as a consequence self-weight hydrostatic pressure forms in the pores of fresh concrete. The gradient of total pore water potential leads to the upward movement of water and to the increment of effective stress on the solid particles, i.e. volumetric consolidation. In this thesis, this phenomenon is referred to as the *bleeding state*.
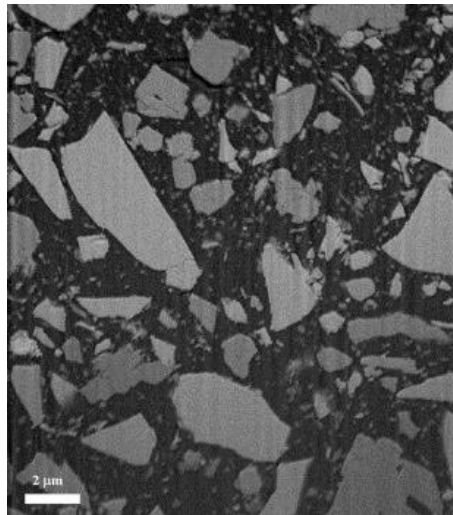
Fig. 1. 5. Suspension of cement particles in the pore fluid in a fresh paste in the bleeding state, obtained by Cryo-nanotomography [16]

Furthermore, when bleeding water evaporates completely, the water in the pores of the concrete starts to evaporate. The latter is close to when the bleeding rate becomes less than the evaporation rate. At this point, air-liquid menisci form in the surface pores of the concrete

(see *Fig. 1. 6*), leading to an increase in the capillary pressure and further volumetric consolidation in the *drying state*. In both of mentioned physical states, consolidation (the reduction of the pore water pressure of fresh plastic concrete and increment of the effective stress acting on the solid particles) leads to compressive volumetric strain, referred to as *plastic shrinkage*.
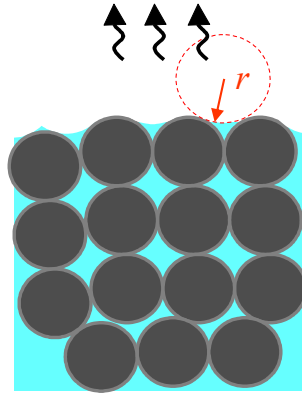
Fig. 1. 6. Menisci formation on the surface of concrete, in the drying state [17]

The evaporation rate of free water and the bleeding rate are two key quantities for studying plastic shrinkage. The former is related to the environmental conditions and the temperature of the concrete, while the latter is a material property depending on the permeability and the bulk modulus evolution, which are functions of cement hydration. For fresh concrete on the construction site, the environmental conditions and the evaporation rate change during the day (see *Fig. 1. 7*), which can also affect the material properties (due to the influence of the temperature on cement hydration). Therefore, the plastic shrinkage states can change according to the weather conditions during casting and before setting and the bleeding rate and bleeding capacity of the concrete.
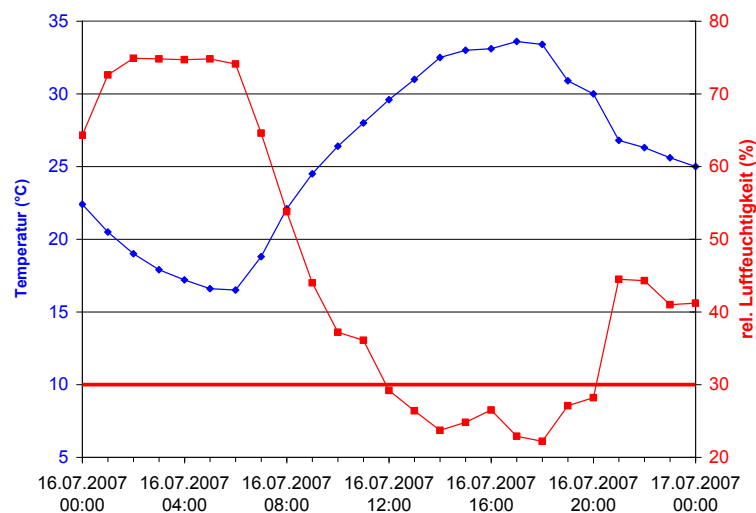
Fig. 1. 7. Variation of temperature (Temperatur) and relative humidity (rel. Luftfeuchtigkeit) during a summer day in Dübendorf, Switzerland [3]

Since structural concrete is always restrained (e.g., by the reinforcement, differential depth or knobs and dents on the substrate base, and the friction between the fresh concrete and substrate base), incompatibility of deformations occurs, which leads to the concentration of the eigenstress or restraint stress. When the stresses increase beyond the strength limit, concrete fails, which can appear in the form of localized or distributed cracking. Cracks can appear on the surface with cracks growing to a width larger than 1 mm and length of 50 to 1000 mm, which can be spaced in an irregular pattern from 50 to 700 mm apart [18] (see *Fig. 1. 8* and *Fig. 1. 9*). Cracking accelerates the ingress of harmful substances (e.g. chloride ions) into the hardened concrete, leading to the reduction of serviceability.
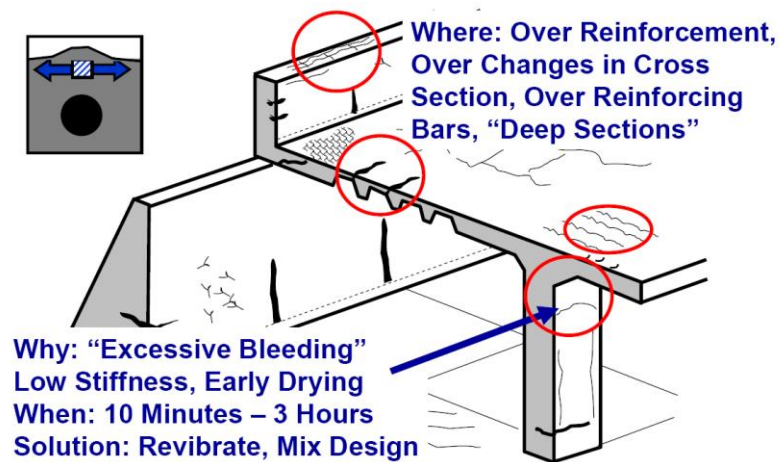
Fig. 1. 8. Plastic shrinkage cracking in the bleeding state [19]

Fig. 1. 9. Plastic shrinkage cracking in the drying state. Photo courtesy of Dr. Andreas Leemann, Empa

Mitigation methods for plastic shrinkage cracking include active and passive methods. *Active methods* work to prevent concrete from cracking occurring in the drying state cracking by fogging/wetting of concrete surfaces (see *Fig. 1. 10*). These approaches are labor intensive, expensive and not always practical, especially when there is no model to estimate the critical

cracking period [18] and the length of curing cannot be precisely determined. *Passive methods* are methods that purposefully change the material properties of the fresh concrete. For example, viscosity modifiers are useful in controlling the cracks in the bleeding state by reducing the coefficient of permeability and therefore decreasing bleeding and settlement [20]. Furthermore, in particular for the drying state, shrinkage reducing admixtures (SRA) can be utilized [17]. SRA reduce the surface tension of water, i.e. they reduce the air entry pressure and consequently the volumetric deformation that happens before the air-entry point. The mentioned admixtures are expensive and might reduce the mechanical properties [21]. Therefore, an optimized dosage needs to be utilized, according to the available material and environmental factors. Consequently, models are needed to couple all of the environmental and material properties together with the structural boundary conditions, to determine the state of the shrinkage and the possibly mitigation methods, and the optimized dosage of admixtures. Furthermore, once the fundamental mechanisms of plastic shrinkage cracking are understood, it would be possible to estimate the critical cracking period to apply external curing only for the shortest period of time that is strictly necessary. Additionally, a better understanding of the acting mechanisms may lead to inventing new mitigation methods or to combinations of the available mitigation methods to increase their efficiency.

Fig. 1. 10. Fog spraying to prevent plastic shrinkage cracking in the drying state [22]

To model the plastic shrinkage cracking, fresh concrete is considered as a porous material, possessing water filled capillary voids similar to saturated soils. A powerful approach utilized in soil mechanics to study the behavior of soils under the multiaxial stress is referred to as *poromechanics,* which employs the *effective stress principle* [23,24] as the dominant law for calculating the stresses acting on the solid particles. It was established first in 1925 by Karl von Terzaghi (*Fig. 1. 11*), an Austrian civil and geotechnical engineer and geologist, known

as the father of soil mechanics [25]. Terzaghi's work was a breakthrough in the studies related to the porous materials, e.g. soils, since calculation of the effective stress allowed civil engineers to use already available solid mechanics principles, e.g. Hooke's law, to design soil structures. He furthermore proposed the one-dimensional volumetric consolidation equation [26] by coupling the effective stress theory, Hooke's law, Darcy's law and the mass conservation equation of fluid and solids, referred to as the Terzaghi's theory of consolidation. This is still a robust and widely used method in simulating the saturated soils' behavior under external loading.

The core of this PhD thesis is based on Terzaghi's theory of consolidation, which is used for calculating the effective hydrostatic stress and shrinkage and furthermore for simulating the development of restraint stresses and cracking. It can be utilized as a fundamental and practical approach for cracking mitigation in early-age concrete. An innovation of this study is that Terzaghi's consolidation equation for soils was expanded to cementitious materials by adding a term that takes into account the chemical shrinkage. Furthermore, robust methods are proposed for determination of the properties of fresh concrete, to be utilized in the poromechanics model. Additionally, the obtained eigenstrain was used in a structural mechanics model, based on the Cauchy-Navier equilibrium equations to estimate the self-equilibrated stress (eigenstress) and failure. The structure of the dissertation is explained in the next section.

Fig. 1. 11. Karl von Terzaghi: founder of modern geotechnical engineering [27]

1.2. Dissertation structure

Except for Chapters 1 and 8, all other chapters are devoted to present novel results obtained during this PhD project. While each chapter is presented as a paper, all chapters are connected by a logical flow and each chapter is a prerequisite to the next chapter. The papers have been either already published (i.e. Chapters 2, 3 and 4) or they have been submitted for review to leading journals in this field.

- **Chapter 1 – Introduction**

The present Chapter, appearing as the first Chapter of the dissertation, is dedicated to the brief introduction of cement, concrete and plastic shrinkage cracking problem. The utilized basic theory for the explanation of involved mechanisms is presented, furthermore the structure of the dissertation is introduced.

- **Chapter 2 – Literature review**

This Chapter presents a brief literature review; from the traditional crack mitigation techniques based on active methods to the passive modern methods. Furthermore, the available experimental and analytical/numerical methods utilized for studying plastic shrinkage and cracking of concrete are discussed. Methods utilized in this thesis to eliminate mentioned drawbacks are explained. This Chapter was partially published in:

Ghourchian S, Wyrzykowski M, Lura P. A practical approach for reducing the risk of plastic shrinkage cracking of concrete. RILEM Technical Letters. 2017 Dec 19;2:40-4.
DOI: https://doi.org/10.21809/rilemtechlett.2017.45

- **Chapter 3 – The bleeding test: a simple method for obtaining the permeability and bulk modulus of fresh concrete**

The material properties play an important role in the poromechanical models, controlling the materials behavior. They can be mutually dependent, making their determination difficult and complicated, especially for plastic concrete. Therefore, the first step of this PhD project was to propose accurate and robust, independent methods for determination of the coefficient of permeability (referred to as permeability in this study) and bulk modulus of fresh concrete. Permeability is a moisture transfer property which relates the gradient of pore pressure to the flux in Darcy's law. The bulk modulus is a parameter which explains the volumetric stiffness of the material. Their determination was performed by simulating the bleeding test, which is a common and easily performed measurement. The bleeding rate was then correlated to the

permeability. Furthermore, once the permeability is obtained independently, the evolution of the bulk modulus was obtained considering an exponential evolution, by simulating the bleeding test performed on the samples with different heights. This is considered to be a breakthrough for this PhD thesis, since no reliable method was previously available to obtain the permeability of fresh concrete accurately and independently. Furthermore, state-of-the-art methods could not evaluate the bulk modulus of fresh concrete. This Chapter was published in Cement and Concrete Research:

Ghourchian S, Wyrzykowski M, Lura P. The bleeding test: a simple method for obtaining the permeability and bulk modulus of fresh concrete. Cement and Concrete Research. 2016 Nov 30;89:249-56.
DOI: https://doi.org/10.1016/j.cemconres.2016.08.016

- **Chapter 4 – Susceptibility of Portland cement and blended cement concretes to plastic shrinkage cracking**

Poromechanics models need experimental methods for their validation. The verification is performed mainly by comparing the evolution of the state variable, i.e. pore pressure, with the experimentally-measured data. Moreover, the validation can be performed by the result of the model, i.e. shrinkage, as the secondary variable. This chapter explains the novel method utilized in this PhD project for determination of three-dimensional shrinkage by employing a 3D Digital Image Correlation (DIC) System. Furthermore, the susceptibility of concretes made of different cements to plastic shrinkage cracking was studied. The discussion was made according to the material properties obtained according to the method proposed in the previous chapter/paper. Eventually, the crack sizes measured with the ASTM C1579 method were correlated to the deformations measured by DIC and to the material properties. It was found that the rate of the bulk modulus evolution brought about by cement hydration has a dominant effect on the size of the observed cracks. The rate of evolution of the mechanical properties was strongly correlated to the clinker content of the different blended cements that were used in the concrete mixtures. The latter was explained according to simulated hydration characteristic time and measured dormant hydration period. A practical consideration that can be derived from this study is that blended cements with lower clinker content are in general at higher risk of plastic shrinkage cracking and may need special measures to limit this issue. This study was published in Cement and Concrete Composites:

Ghourchian S, Wyrzykowski M, Baquerizo L, Lura P. Susceptibility of Portland cement and blended cement concretes to plastic shrinkage cracking. Cement and Concrete Composites. 2018 Jan 1;85:44-55.
DOI: https://doi.org/10.1016/j.cemconcomp.2017.10.002

- **Chapter 5 – A poromechanics model for plastic shrinkage of fresh cementitious materials**

In the drying state, air-liquid menisci form on the concrete surface and the capillary pressure that develops additionally consolidates the bulk. The capillary pressure is primarily related to the pore size. In research on granular and porous materials, e.g., soil physics, the relationship between the capillary pressure (related to the pore size) and the volumetric water content is given by the Water Retention Characteristic Curves (WRCC). Therefore, for modeling the plastic shrinkage in the drying state, the WRCC needs to be known in addition to the previously-obtained bulk modulus and permeability. In this chapter, a method is proposed for determining the WRCC of fresh cementitious materials. Furthermore, a generalized consolidation equation was derived for cementitious materials by considering the chemical shrinkage term that leads to self-desiccation. The bulk modulus and the permeability in the bleeding state, which are functions of degree of hydration of the cement, were determined by the method proposed in Chapter 3. The latter was extended to the drying state by including the effect of the capillary pressure on the stiffness. The experiments and the model verification were performed on a plain mortar and a mortar with silica fume substitution to check the model's robustness in showing the effect of the change in pore size. DIC shrinkage measurements and pore pressure measurements by tensiometers were utilized to validate the model. It is found that silica fume accelerates the solid percolation and pore pressure evolution by increasing the initial bulk modulus, which also leads to higher horizontal shrinkage. Moreover, a method was proposed to estimate the evolution of the pseudo-elastic limit, the limit of elastic-plastic material behavior under hydrostatic stress. This study was submitted for publication to Cement and Concrete Research:

Ghourchian S, Wyrzykowski M, Lura P. A poromechanics model for plastic shrinkage of fresh cementitious materials. submitted to Cement and Concrete Research, 2017 Nov.

- **Chapter 6 – On the mechanism of plastic shrinkage cracking in fresh cementitious materials**

Available methods for plastic shrinkage failure quantification rely on the measurement of the final crack size after propagation. On the other hand, in some cases cracks might not propagate to the surface, making the latter methods useless. A crack, even when it does not propagate to the surface, may facilitate the ingress of water and harmful ions into concrete structures. To address these concerns, a novel method was proposed for the detection of crack

initiation by X-ray radiography. The structural boundary conditions were according to the ASTM C1579 standard, with some modifications in the geometry of the molds to optimize it for mortars. After the validation of the model in the previous paper/chapter, it was used to simulate plastic shrinkage cracking for the mentioned structural boundary conditions. The simulated plastic shrinkage was used as input to a simultaneously running structural mechanics model according to the Cauchy-Navier equilibrium equations to obtain the restraint stresses. Moreover, Bresler-Pister and Rankine failure criteria were proposed according to the pseudo-elastic limit obtained in the previous chapter. The failure models were adapted according to the Drucker-Prager with cap model and Griffith's envelope. The failure mechanisms were discussed according to the simulated shrinkage and proposed failure models. Furthermore, a safe capillary pressure limit was proposed as a benchmark to prevent plastic shrinkage cracking in the drying state. It was found that capillary pressure stiffening is the predominant reason of plastic shrinkage cracking in the drying state. This Chapter was submitted for publication to Cement and Concrete Research:

__Ghourchian S__, Wyrzykowski M, Plamondon M, Lura P. On the mechanism of plastic shrinkage cracking in fresh cementitious materials. submitted to Cement and Concrete Research, 2018 Mar.

- **Chapter 7 – Performance of passive methods in plastic shrinkage cracking mitigation**

This Chapter investigates the performance of difference passive methods in controlling the plastic shrinkage cracking. Furthermore, the mechanism of action of the utilized methods is explained extensively according to the findings of previous Chapters. This Chapter was submitted for publication to Cement and Concrete Composites:

__Ghourchian S__, Wyrzykowski M, Baquerizo L, Lura P. Performance of passive methods in plastic shrinkage cracking mitigation. submitted to Cement and Concrete Composites, 2018 Jan.

- **Chapter 8 – Conclusions**

This chapter summarizes the main conclusions about mechanisms of plastic shrinkage cracking that have resulted from the numerical and experimental work. Further steps are proposed towards the expansion of the proposed model to be utilized for extending the service life of reinforced concrete structures.

This page is intentionally left blank.

Chapter 2. Literature review

Abstract

In this chapter, a conventional method for mitigation of plastic shrinkage of fresh concrete based on comparing bleeding and evaporation rates (the former based on the commonly observed values of bleeding rate and the latter estimated by means of the commonly-used ACI nomograph) is critically assessed. It is shown that even if the initial bleeding rates are sufficiently high (i.e. higher than the evaporation rates), cracking may still occur if all the bleed water is lost by evaporation between the times of initial and final set, leading to the rise of capillary pressure. An alternative and more conservative method should be thus based on the total (accumulated) amount of bleed water compared to the total amount of evaporated water. The former should take into account the concrete's properties and the geometry of the member, while the latter can be assumed based on the nomograph method.

Furthermore, methods of plastic shrinkage measurements are presented, including recent approaches that allow to perform accurate shrinkage measurements while minimizing the artifacts. In a further section, methods of quantification of plastic shrinkage cracking are reviewed. Finally, analytical/numerical methods utilized to study plastic shrinkage and plastic shrinkage cracking are presented. In all sections, the approaches utilized in this PhD dissertation for addressing and possibly eliminating the mentioned drawbacks are described as well.

2.1. A practical approach for reducing the risk of plastic shrinkage cracking of concrete[1]

2.1.1. Introduction

Fresh concrete after placing undergoes deformations that are due to settlement of solids in the mixture and further due to drying as water evaporates from the exposed surfaces. These deformations occur during the stage when concrete is still plastic and hence are referred to as *plastic shrinkage*. High magnitudes of plastic shrinkage together with low tensile strength at early age often lead to opening of large cracks that may seriously impair concrete service properties and its designed lifetime, see *Fig. 2. 1*.

---

[1] This section was published in: *Ghourchian S, Wyrzykowski M, Lura P. A practical approach for reducing the risk of plastic shrinkage cracking of concrete. RILEM Technical Letters. 2017 Dec 19;2:40-4. DOI: https://doi.org/10.21809/rilemtechlett.2017.45.*

Fig. 2. 1. Plastic shrinkage cracks appearing on the concrete surface few hours after placement. Photo courtesy of Dr. Andreas Leemann, Empa.

In the literature [28–34], plastic shrinkage cracking was primarily related to the evaporation of bleed water, leading to onset of capillary pressure and eventually cracking. In 1957, Lerch [28] stated that:

Plastic shrinkage cracks develop shortly after the sheen disappears from the surface of concrete and when this type of cracking starts, it can be observed to proceed very rapidly.

The "sheen" mentioned by Lerch was due to the presence of water that flows towards the upper surfaces of concrete right after placement and accumulates on them in a process called bleeding. Bleeding is due to self-weight consolidation of solids in the fresh concrete occurring due to the higher density of the solids compared to the density of the pore water [24,35]. The moment when the sheen at the concrete surface disappears indicates the complete evaporation of the bleed water. This happens a certain time after the evaporation rate has exceeded the bleeding rate, depending on the amount of bleed water that has accumulated on the surface and on the environmental conditions, see *Fig. 2. 2*. The fact that cracking is detected "soon after" the evaporation rate exceeds the bleeding rate was also reported by Menzel [36]. Therefore, many efforts have been made to estimate the moment at which this phenomenon occurs and to mitigate these fast-growing cracks by appropriate measures during construction [33,34]. Accordingly, ACI 305R-10 [34] proposed the well-known method based on ensuring that the evaporation rate is lower than the bleeding rate of concrete. The evaporation rate can be estimated with the nomograph shown in *Fig. 2. 3*. This nomograph was based on methods used in hydrology for predicting the rate of evaporation from lakes and reservoirs.
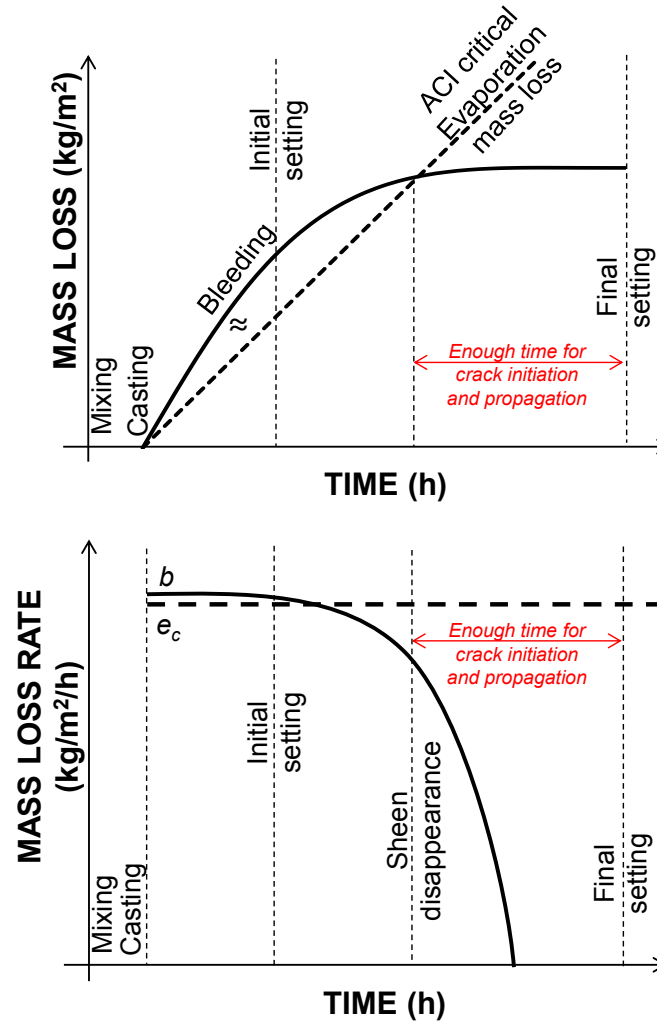
Fig. 2. 2. The time gap between the times of initial and final set, in which plastic shrinkage cracking can occur, after the sheen disappearance, in the drying state. b and e_c are the bleeding rate and the critical evaporation rate, respectively.

It is worthwhile to mention that the rate of evaporation of free water and bleed water from mortars during the constant evaporation rate period (CRP) are almost identical [17], while for concretes, due to their larger aggregate volume (corresponding to a lower volumetric water content) [37], the CRP evaporation rate is likely lower (see Chapter 4 and [38,39]). Therefore, the ACI nomograph is likely not able to provide accurate estimations of the rate of evaporation of concrete, at least not after the bleed water is removed completely from the surface of the concrete [34,38,40]. It is noticed that the CRP continues for some time after the disappearance of the bleed water from the concrete surface, as long as the concrete's intrinsic permeability is constant (see Chapters 4 and 5). On the other hand, some studies showed that the evaporation rate of concrete samples during the CRP agreed well (see Chapter 4 and [39]), or was even higher [41] than estimations based on the nomograph. The latter can be accidental, due to the fact that the wind speed utilized for obtaining the nomograph is based

on measurements at 0.5 m above the evaporating surface, and air temperature and relative humidity at a level approximately 1.2 to 1.6 m higher than the evaporation surface [34]. Therefore the ACI method should be only utilized when the appropriate wind speed data and test conditions are available [34].
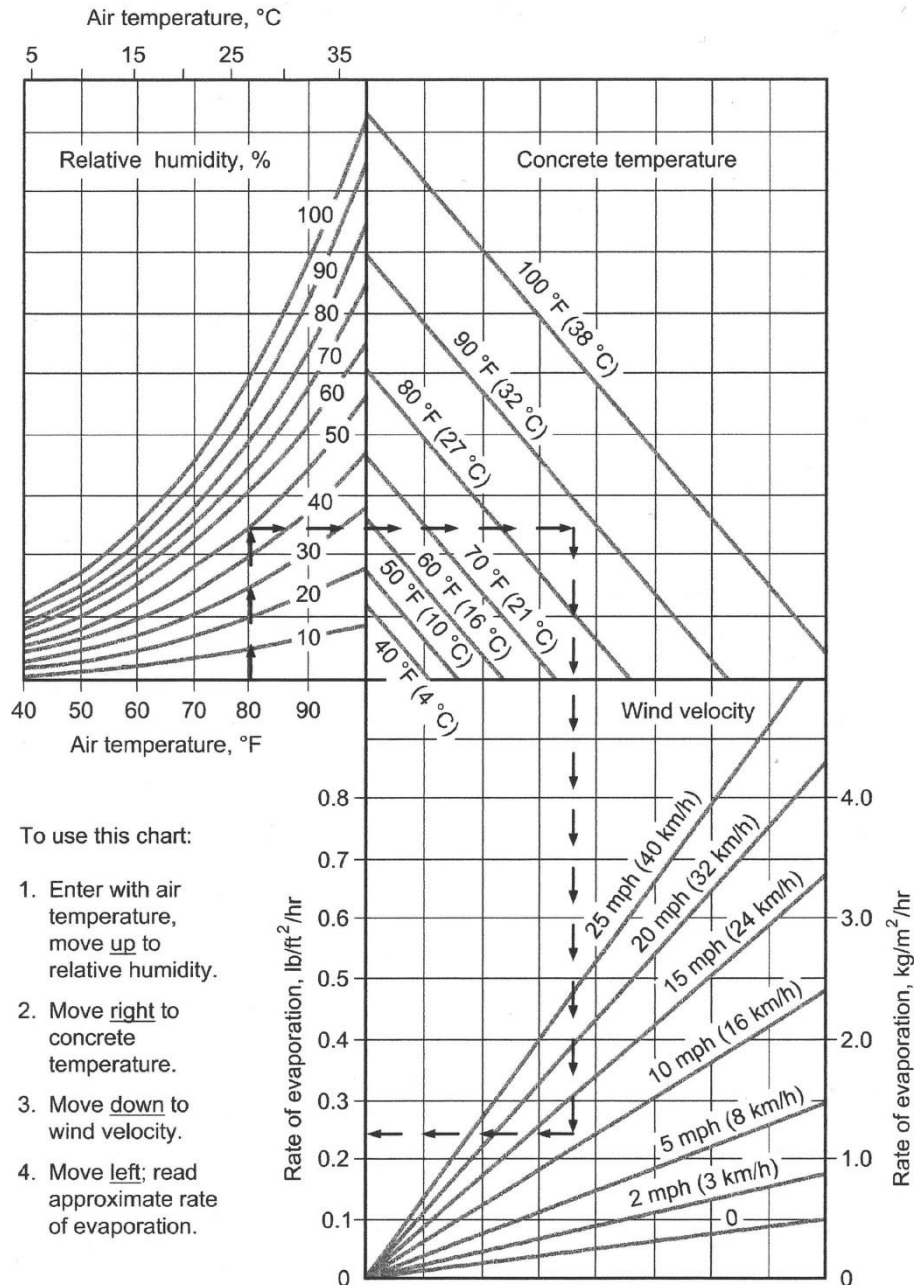
Fig. 2. 3. ACI nomograph for estimating the rate of evaporation of surface bleed water [34]

In addition, the actual temperature of the concrete at the time of casting needs to be utilized in the calculations and the changes of air temperature and relative humidity during casting and finishing of fresh concrete need to be taken into account [42]. Furthermore, the wind speed utilized in the calculations should not be based on transient gusts of wind [34].

While the ACI method specifies a method for the estimation of the evaporation rate of free water (i.e. the water sink at the surface), there is no recommended estimation method for the bleeding rate of concretes. While the water sink depends primarily on the environmental conditions, the bleed water source depends mainly on the concrete itself and the height of the element (see Chapter 3 and [36,43]). Instead, the ACI method recommends only a value for the critical rate of evaporation: concrete placement is supposed to be safe when the evaporation rate is estimated to be below this value, or otherwise appropriate curing measures should to be implemented. According to the ACI method [34], commonly quoted values for normal concretes and silica fume containing concretes are 1 $kg/m^2/h$ and 0.25 $kg/m^2/h$, respectively. Moreover, for the state of New York and the city of Cincinnati, 0.75 and 0.5 $kg/m^2/h$, were recommended, respectively [34]. Similarly, Canadian Codes and Australian references recommended 0.75 and 0.5 $kg/m^2/h$, respectively [33]. These recommended critical evaporation rates originate from the fact that they are lower than the bleeding rates measured on concretes in a number of studies, e.g. [33,35,43]. Considering that Powers [35] observed bleeding rates in the range 1.1-4.1 $kg/m^2/h$ (see also [33]), the limit of 1 $kg/m^2/h$ appears to be conservative. However, the simplified approach with the assumed lower bound of bleeding rate described above can be criticized for the following reasons:

I.   As also mentioned in the ACI method [34], concrete's bleeding properties can vary according to the permeability, the bulk modulus evolution and the height of the element, see also Chapter 3 and [36]. Therefore, the idea of specifying a maximum critical evaporation rate (or, inversely, a minimum concrete's bleeding rate) without explicitly considering these factors can lead to improper estimation of the cracking risk [39].

The bleeding rate (and as will be discussed later, the bleeding capacity) may be seriously reduced when using finer cements, fine fillers (e.g. silica fume), stabilizers, lower w/c, higher temperature, see also [32,34,43–45]. Most of these factors were already recognized by Menzel [36].

II. Even if the (initial) bleeding rate is higher than the evaporation rate according to the ACI recommendation, around the time of initial set the bleeding rate will invariably decrease, see *Fig. 2. 2*. Consequently, the bleed water accumulated on the surface will be lost. If the removal of accumulated bleed water occurs before the time of final set, the corresponding onset of capillary pressure will lead to cracking. Since cracking proceeds rapidly, as mentioned already by Lerch [28], few minutes would be enough

for crack propagation and severe damage. The results shown in [41,46,47] are in line with the latter concept. The issue of the increased risk of cracking in the short time after bleeding stops ("critical period") was already raised by Menzel [36]. As long as the short time windows between the decrease of bleeding rate and the time of final set, together with the relatively high bleeding rates observed in many concretes, in the past usually assured that there was enough accumulated bleed water to avoid the rise of capillary pressures, the rate approach cannot be considered conservative, in particular for the concretes used nowadays. In addition to the lower bleeding rates (and thus lower bleeding capacity) mentioned in point 1, this is particularly because of the prolonged time window between the times of initial and final set caused by the application of plasticizers, or replacement of cement with inert fillers or with slow-reacting supplementary cementitious materials (see Chapter 4).

III.   Plastic shrinkage cracking is not limited to the cracks caused by the evaporation of pore water and capillary pressure. Even if we assume ideal external curing, which keeps the concrete surface saturated and postpones the evaporation of pore water until after the time of final set, a residual risk of cracking due to plastic settlement cracking (self-weight consolidation) remains due to the bleeding process itself [15,48–50].

It should be noted that the problem of cracking that may occur after evaporation of all bleed water (independently of the initial bleeding rate) in the critical period after bleeding stops was in fact recognized already by Menzel [36], see also [43]. Nevertheless, most likely due to complexity of the modeling approach to address this problem, a simple approach with fixed minimum bound of bleeding rate was adopted instead by ACI [34].

To address the complex problem of plastic shrinkage cracking, the strategy of modeling fresh concrete following a poromechanics framework has been used in this PhD project. In fact, the proposed model is able to couple the material properties and the geometry of a concrete element with the environmental factors, to finally estimate the cracking risk. In this project, the development of a poromechanics model has been accompanied by the design and interpretation of experiments targeted at assessing the material properties needed as input for the model. In addition, extensive experimental validation of the model was performed, taking different boundary conditions into account. Accordingly, based on these extensive studies, a simple mitigation method is presented in the next section, which is based on estimating the total capacity of bleed water and assuring that it remains higher than the total amount of the evaporated water until the time of final set. The total bleeding capacity can be estimated

based on consolidation equation [24] that can be nowadays easily implemented in a numerical form, see Chapter 3.

2.1.2. Improvement of the ACI nomograph approach based on the fresh concrete properties

As mentioned in the previous section, the ACI method does not take into account the material properties. Therefore, here a simple method is presented which would allow to mitigate plastic shrinkage following the ACI approach but in a more effective way. As shown in *Fig. 2. 4*, one can write eq. (2-1) to obtain the critical evaporation rate (e_c [kg/m^2/h]) according to environmental conditions and material properties, to mitigate the plastic shrinkage cracking:

$$e_c = \frac{C_B}{t_{FSB} - t_{cast}} \tag{2-1}$$
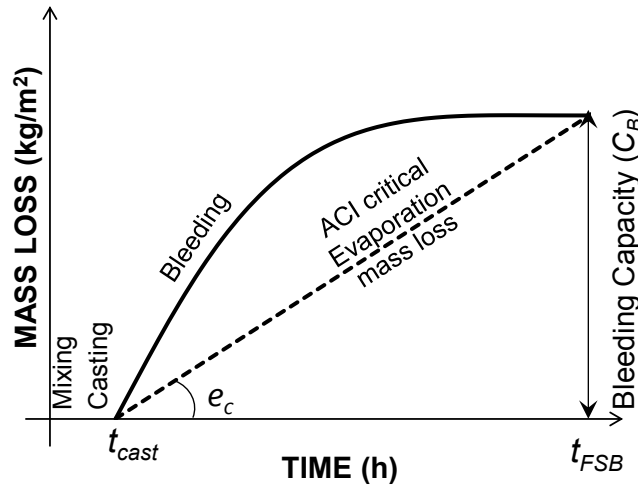
Fig. 2. 4. Estimation of the critical evaporation rate according to time of final set, time of casting and bleeding capacity

In eq. (2-1), C_B [kg/m^2] is the bleeding capacity, t_{cast} [h] is the time of casting, t_{FSB} [h] is the time of final set in the bleeding state (covered sample with no evaporation). Therefore, by estimating the evaporation rate of the free bleed water in a construction project environment according to the ACI nomograph (*Fig. 2. 3*), and comparing to the critical value of the evaporation rate (e_c), one could mitigate cracking, by postponing the casting to when the evaporation rate is less than the critical value. The bleeding capacity is a function of the coefficient of permeability, bulk modulus and the height of the element, determinable according to the relatively simple numerical model of consolidation proposed originally by Terzaghi [24] with input data obtained from a simple bleeding test, see Chapter 3.

Another method is to design the fresh concrete according to the estimated average evaporation rate of the casting-to-finishing period by *Fig. 2. 3*. In other words, according to eq. (2-2) one could obtain the required bleeding capacity that the concrete should possess. The design of a concrete mix with sufficiently high bleeding capacity determined with eq. (2-2) could be done by trial and error, employing a simple laboratory test for bleeding and the method proposed in Chapter 3. There are also models available for estimating the time of final set [51], which can be used in eq. (2-2), coupled with the maturity concept to incorporate the effect of temperature (see Chapter 5 and [52,53]).

$$C_B = e_c(t_{FSB} - t_{cast})$$ (2-2)

It is remarked that the setting time and the bleeding capacity are coupled, since both are a function of the mechanical properties. One practical approach would be to increase the coefficient of permeability (i.e. the bleeding rate) solely, since it is a function of the initial pore geometry independent of the evolution of mechanical properties (see Chapter 3), which can increase the bleeding capacity, while keeping the time of final set constant.

2.1.3. Closing remarks

The previous section proposed new approaches to extend the applicability of the well-known ACI nomograph to avoid the risk of plastic shrinkage cracking by considering the total bleeding capacity instead of the bleeding rate. The method is based on determining the actual concrete's bleeding capacity (capacity of self-curing with bleed water) and assuring that the bleed water is present at the surface at given environmental conditions sufficiently long, at least until the time of final set. The effect of environmental conditions on evaporation of bleed water can be estimated with the ACI nomograph.

If under any circumstances, it was not possible to design the concrete according to the procedures proposed in section 2.1.2, or place the concrete in the proper time, external curing needs to be started latest at the time of the intersection of the critical evaporation mass loss and the bleeding as shown in *Fig. 2. 2*. External curing methods include application of plastic sheets on the surface of concrete or spraying water on the whole surface [54]. The latter is necessary, since as mentioned by Lerch before, plastic shrinkage propagates very rapidly, and few minutes are enough for large cracks to occur. Furthermore, it must be assured that the whole concrete surface remains wet, otherwise cracking would occur in the zones with lack of external curing.

2.2. Effect of material properties on plastic shrinkage cracking

As explained in the previous section, the fresh concrete properties influence plastic shrinkage cracking. Thus, their effect needs to be understood precisely, in order to recommend the best appropriate mitigation method. In the literature, the effect on plastic shrinkage cracking of different parameters of the concrete mix design, including w/c (water-to-cement ratio), amount and type of SCM (Supplementary Cementitious Materials) in blended cements, chemical admixtures, internal curing and fibers, has been investigated. In the following, a brief literature review is presented.

2.2.1. Water-to-cement ratio

The w/c is an important factor for designing structural concrete, because it governs the evolution of the mechanical properties. ACI 302.1R-04: Guide for Concrete Floor and Slab Construction [54] specifies the following additional w/c specifications for enhancing the durability, which may increase the compressive strength to levels much higher than normally required for structural design:

w/c<0.5: Elements subjected to moderate and severe exposure to freezing and thawing

w/c<0.45: Elements subjected to deicing chemicals

w/c<0.4: Elements exposed to brackish water, seawater, deicing chemicals, or other aggressive materials

The specified limits consider the concrete's long-term behavior against ingress of harmful fluids and ions from the environment. Nevertheless, by knowing that: 1-Reinforced concrete floors and slabs are highly susceptible to plastic shrinkage cracking in the drying state, due to their high surface-to-volume ratio [55], and 2-Plastic shrinkage cracking facilitates the ingress of harmful species; one could conclude that the plastic shrinkage risk would also decrease by decreasing the w/c. However, no exclusive w/c limit for controlling the plastic shrinkage cracking is recommended by the standards, and as explained in the previous sections, the focus is just on the evaporation rate of free bleeding water [34].

In the literature, different conclusions were made regarding the effect of the w/c on plastic shrinkage cracking. Some studies stated that concretes with low w/c possess higher cracking risk due to less bleeding [56,57], while in other studies it was shown that higher w/c increases the cracking risk [46,57,58] (see *Fig. 2. 5*, *Fig. 2. 6* and *Fig. 2. 7*). Furthermore, according to Lura and Leemann [59] and Yang [60] (see *Fig. 2. 8* and *Fig. 2. 9*, respectively), concretes of medium w/c (around 0.5) showed the highest risk of plastic shrinkage cracking. On the contrary, some other studies concluded that the optimum w/c for minimizing the risk of

cracking is between 0.45 and 0.55 [57,58] (see *Fig. 2. 5* and *Fig. 2. 6*). The different conclusions can be related to the coupled effect of the evaporation rate (environmental conditions and concrete temperature) and concrete properties (i.e. mainly permeability and bulk modulus). For instance, in concretes with higher w/c, if the bleeding capacity is high enough to compensate for the evaporated water, and postpone the onset of capillary pressure after or close to the time of final set, cracking might not be observed. But if the evaporation rate is very high, so that those concretes cannot compensate the evaporated water during the bleeding state, they would crack more because of the longer dormant period and slower evolution of mechanical properties (see Chapter 4) caused by the high w/c. Therefore, the coupled effect of fresh concrete properties and environmental conditions needs to be considered. A poromechanics model would be able to estimate concrete behavior by considering both the environment and the material properties.
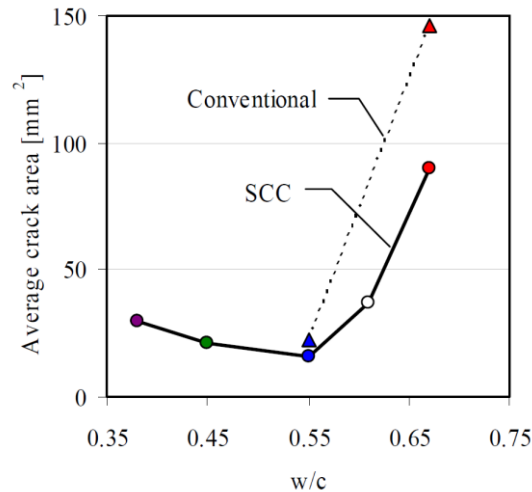
Fig. 2. 5. Influence of w/c on plastic shrinkage cracking in SCC (Self-Compacting Concrete) and conventional concretes [58]
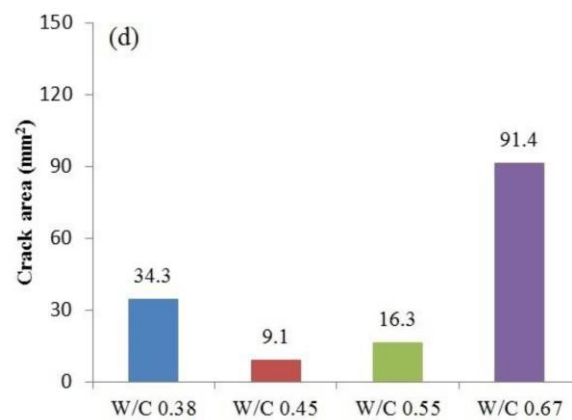
Fig. 2. 6. Influence of w/c on the crack area [61]
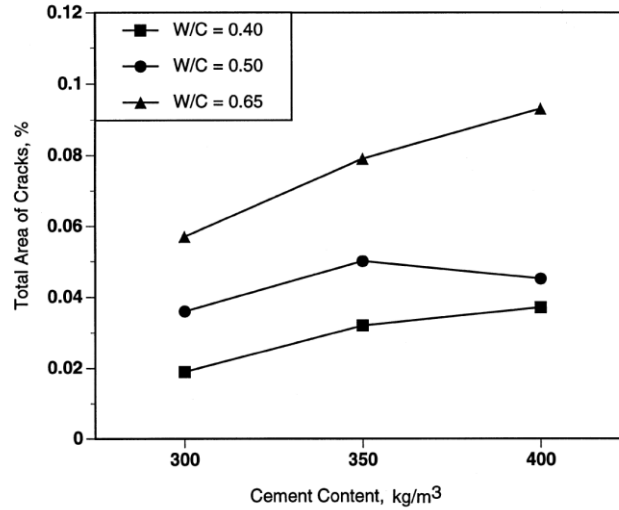
Fig. 2. 7. Effect of w/c and cement content on plastic shrinkage cracking [46]
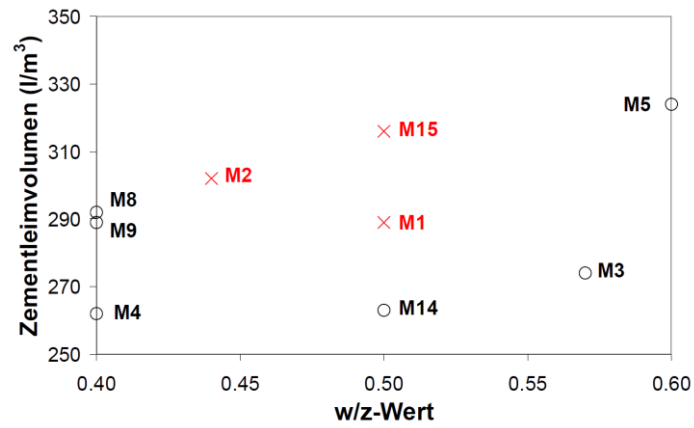
Fig. 2. 8. Cement paste volume (Zementleimvolumen) vs. w/c (w/z-Wert). The red crosses indicate concrete mixtures that cracked in ASTM C1579 [59]
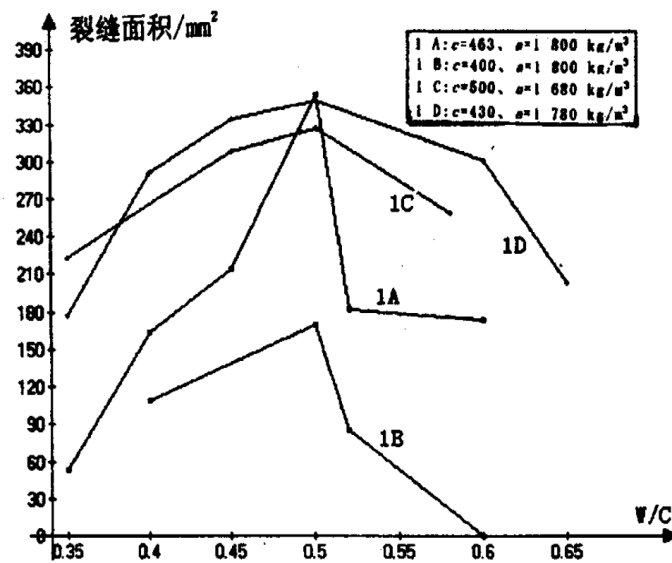
Fig. 2. 9. Crack surface area (vertical axis) vs. w/c (horizontal axis) [60]

2.2.2. SCMs

Since SCMs affect the fresh concrete's bleeding and setting time, standards have provisions regarding the utilization of SCMs in fresh concrete. It is specified in section 4.6 of ACI 234R-06: Guide for the Use of Silica Fume in Concrete [62] that utilizing silica fume in concrete mix design increases the probability of plastic shrinkage cracking. The latter was attributed to the significant reduction of bleeding caused by silica fume due to its high surface area which needs to be wetted. Therefore very little free water is left for bleeding [62]. Furthermore, silica fume physically blocks the pores in fresh concrete [62], i.e. it reduces the permeability.

ACI 233R-03 states that slag cement reduces the bleeding of concrete, and consequently it is considered to increase plastic shrinkage cracking, if its fineness is higher than the fineness of cement [63]. In ACI 232.2R-03 [64] it is mentioned that fly ash sometimes delays the setting time of fresh concrete and therefore it can increase the risk of plastic shrinkage cracks. According to Caldarone [65], metakaolin should be less susceptible to plastic shrinkage cracking compared to concretes with silica fume addition. Since metakaolin has average particle size 20 to 30 times larger than the average particles size of silica fume, metakaolin-containing concretes have lower water demand and less plasticizer is needed to compensate the workability [65].

The results presented in the scientific literature are generally in line with the above-mentioned standard provisions; however, the explanations are slightly different in some cases. For instance, according to Cohen et al. [32] the high specific surface area of silica fume increases the maximum capillary pressure and therefore increases the tendency of cracking. When cements with high fineness were used, the total bleeding water and the bleeding rate decreased [66,67]. For concretes with w/c 0.4, 0.5 and 0.6 in environmental conditions with free water evaporation rate 0.1 kg/m^{2}h, substitution of cement with fly ash of higher fineness decreased the horizontal plastic shrinkage due to the increased bleeding rate [68]. For mortars with equal w/c 0.35 and 0.45, inclusion of ground granulated blast furnace slag with higher fineness increased the bleeding rate and the bleeding capacity (i.e., the total amount of bleed water) [69]. Contrary to the abovementioned findings, other researchers found that the bleeding capacity decreased in blended-cement concretes containing fly ash, silica fume and blast furnace slag [70]. In a study by Slowik et al. [71], it was observed that increasing the fineness accelerated the air entry time for cement pastes with w/c of 0.26. Further, increasing the fineness decreased the vertical deformation and increased the developed capillary pressure. It was observed that both the magnitude of plastic shrinkage

[72] and the total area of plastic shrinkage cracks [70] increased in blended-cement concrete compared to OPC concrete. The latter increase in plastic shrinkage cracking was attributed to the lower bleeding and higher rate of evaporation observed in blended cement concretes [70]. Lura et al. [73] concluded that when cements of different mineralogical composition but similar fineness are employed, the influence of the cement type on the risk of cracking is small. In a recent study, authors concluded that increasing the cement fineness reduces the maximum crack width [74]. The effect of SCM and cement type on plastic shrinkage cracking is discussed extensively in Chapter 4.

2.2.3. Chemical admixtures

Chemical admixtures can increase or decrease the tendency of plastic shrinkage cracking, according to their effect on the concrete properties. Retarding admixtures extend the setting time of concrete and therefore they increase the cracking risk [58,75,76]. On the contrary, accelerators reduce the cracking risk [58,75,77]. It is mentioned that, with the application of water reducing admixtures, i.e. superplasticizers, the capillary pressure development starts almost immediately after placing [75]. The latter can increase the cracking tendency substantially, since some plasticizers retard cement hydration as well [58].

Shrinkage reducing admixtures (SRA), i.e. surfactants, have been shown to be very effective in controlling the plastic shrinkage cracking in the drying state [17,58,77–80] (see *Fig. 2. 10*). They reduce the surface tension of pore water (see *Fig. 2. 10*) and consequently, reduce the capillary pressure and plastic shrinkage. However, precautions are needed in using the SRA, since reduce the compressive strength and retard the development of mechanical properties at high dosages [21,80] and are generally expensive. Therefore, the dosage of SRA needs to be optimized.

Viscosity modifying agents (VMA) [81], i.e. stabilizers [77], primarily affect the viscosity of the pore fluid, while they also can reduce the surface tension of the pore fluid, but much less than SRA [77,81] (see *Fig. 2. 11*). When they contact water, they swell first, and then dissolve, forming a viscous solution [81].
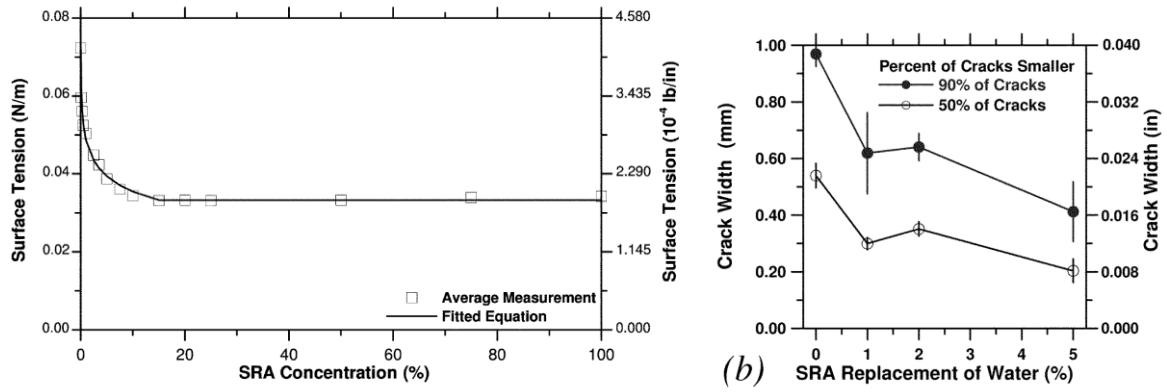
Fig. 2. 10. Effect of SRA on the surface tension of water (left) and the plastic shrinkage cracking in the drying state (right)[17]
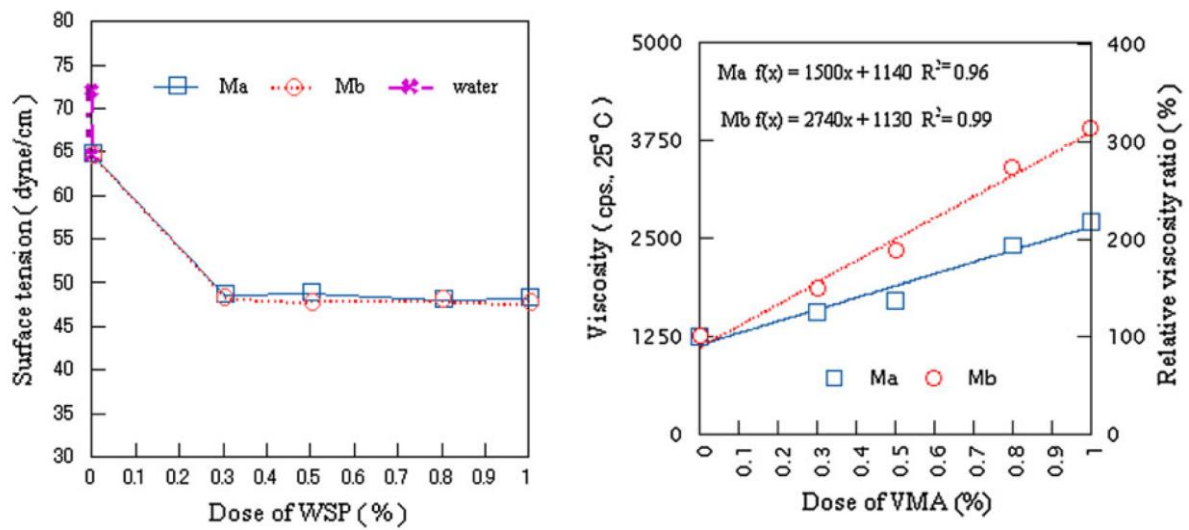
Fig. 2. 11. The effect of cellulose-based VMA on surface tension of pore solutions (left) and the viscosity of cement paste (right)[81]
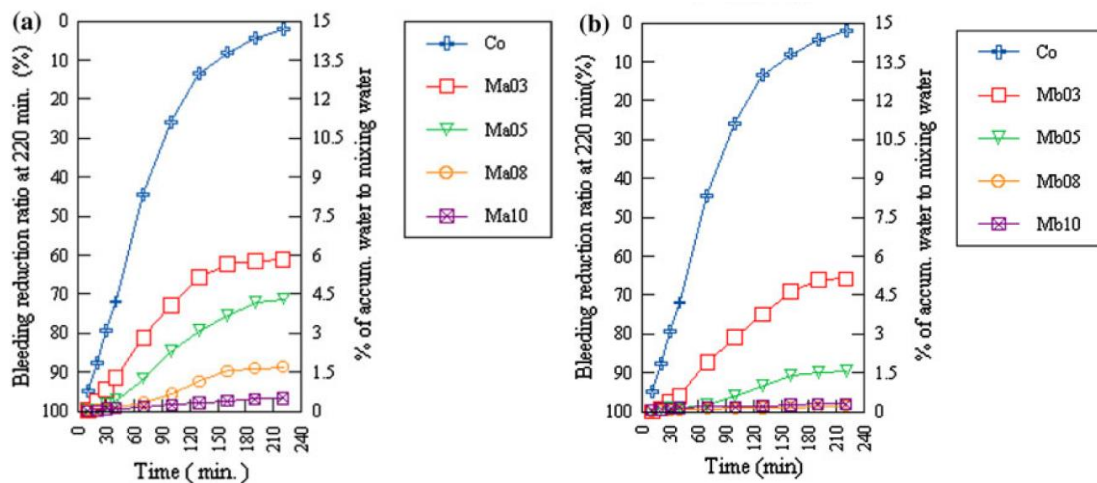
Fig. 2. 12. Left and right: effect of cellulose-based VMA on reduction of bleeding rate. In the legends, Co is the reference mix, and the numbers indicate the dosage of the admixture [81]

Since VMA decrease the coefficient of permeability significantly, by increasing the viscosity of pore fluid, they decrease the bleeding rate (i.e. rate of vertical/volumetric shrinkage), and consequently, they can be very effective in controlling the cracks in the bleeding state, in deep elements (see *Fig. 2. 12*). Please see Chapter 3 for the relationship between bleeding rate and coefficient of permeability. Similar to SRA, VMA also retard the evolution of mechanical properties [77], thus their dosage needs to be optimized.

Evaporation reducers [54] (i.e. curing compounds [77]), e.g. paraffin dispersion, can form a film on the surface of fresh concrete and reduce the evaporation of pore fluid, and plastic shrinkage cracking. Leemann et al. [77] showed that they can be used also as a concrete admixture, mixed in the volume of concrete, and not only as a curing compound applied on the surface, as proposed in ACI 302.1R-04 [54]. Moreover, if they are used as an admixture, it can be assured that the curing agent accumulates on the whole surface of the concrete by bleeding, and decreases the evaporation by forming a curing film on the surface of the concrete.

2.2.4. Internal curing

It has been shown that pre-wetted lightweight aggregates (e.g. expanded shales) with a fineness modulus of 3.1 higher than the fineness modulus of river sand 2.71 can reduce plastic shrinkage cracking in the drying state [82]. Smaller fineness modulus indicates a finer aggregate, therefore, utilized lightweight aggregate were coarser than utilized sand. The mechanism of action is by providing the water required for the evaporation (acting as a source term on the right hand side of the consolidation equation, see chapter 5), and thus preventing the increment of the capillary pressure. However, utilizing very fine lightweight aggregates (i.e. possessing lower fineness modulus comparing to the one for normal river sand) might not mitigate cracking, since the increment of the stiffness in the dormant hydration period, caused by the fine particles of the lightweight aggregates, can compensate the effect of the water provided by internal curing. See Chapters 5 and 6 for the effect of the stiffness in the dormant hydration period on plastic shrinkage cracking.

2.2.5. Fibers

Fibers (e.g. polypropylene fibers) have been utilized in fresh concrete to reduce the size and the area of plastic shrinkage cracks in many studies [18,50,83–97] and they are also recommended by ACI 302.1R-04 [54]. Their mechanism of action is by 1- Reduction of bleeding by enhancement of the concrete stiffness caused by the interlocking network of fibers [83], therefore beneficial against cracking in the bleeding state. However, the latter

accelerates the capillary pressure (i.e. stress) increase in the drying state (see Chapter 5). 2-Increment of the cohesion, and therefore tensile strength [83], which can prevent or retard the crack propagation in the drying state. Nevertheless, fibers are not able to prevent crack nucleation, as explained in [98].

2.3. Experimental methods for plastic shrinkage measurements

The eigenstrain (plastic shrinkage) is the source of eigenstress and early-age cracking. Therefore, the first step in studying plastic shrinkage cracking is to propose an accurate and robust method for shrinkage measurements. In the following sections, methods utilized for the measurement of plastic shrinkage and plastic shrinkage cracking are reviewed. Furthermore, the so-far available modeling approaches are briefly explained.

In the bleeding state, plastic shrinkage occurs solely in vertical direction, towards the direction of the gravity acceleration vector. However, in the drying state after the solid percolation, plastic shrinkage occurs also in the horizontal direction (please refer to Chapter 5 for a deeper description). Therefore, in the literature different methods have been utilized for the quantification of shrinkage of fresh concrete: 1-vertical displacement setups; 2-horizontal displacement setups; 3-setups for measuring both of vertical and horizontal displacements.

2.3.1. Vertical displacement (settlement)

Powers measured the settlement of cement paste and concrete by monitoring the displacement of a disk seated on the surface. The displacement was measured by a micrometer microscope (see *Fig. 2. 13*) [35].
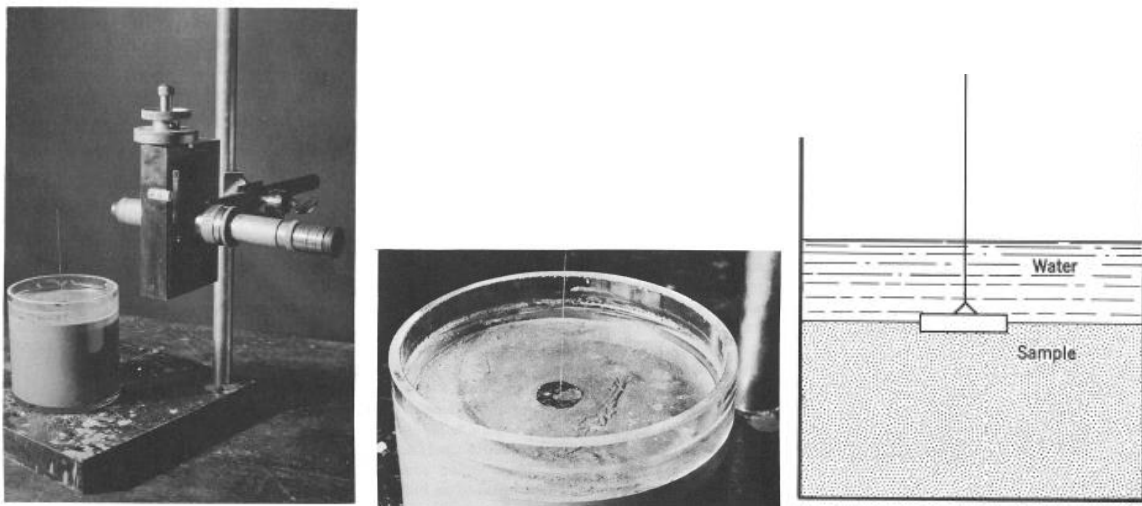
Fig. 2. 13. Powers' settlement measurement setup [35]

Fig. 2. 14 shows an optical apparatus according to ASTM C827-82 for measuring the vertical deformation of fresh concrete [99]. In following research, laser sensors were often utilized to measure vertical displacements (see *Fig. 2. 15* and *Fig. 2. 16*) [50,84], employing, e.g., cylindrical molds and conical molds, see *Fig. 2. 15* and *Fig. 2. 16*, respectively.
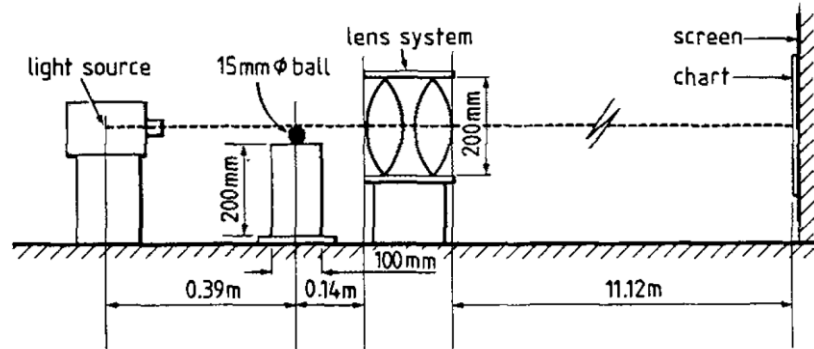
Fig. 2. 14. An optical setup for vertical deformation [99]
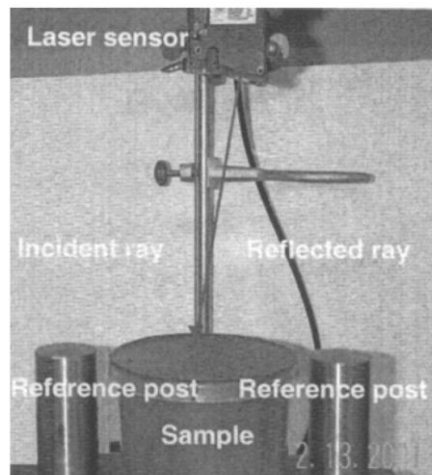
Fig. 2. 15. Laser sensor setup with cylindrical mold [50]
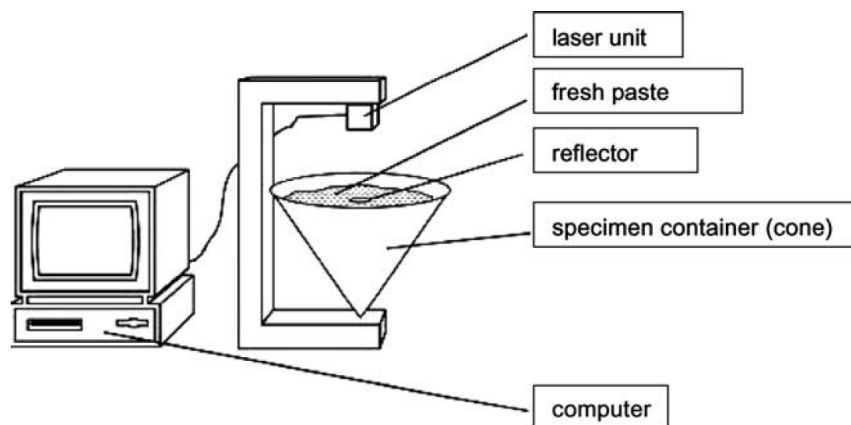
Fig. 2. 16. Laser sensor setup with conical mold [84]

Qi et al. [49], (see *Fig. 2. 17*) studied the effect of an embedded steel bar embedded in the concrete on the settlement. They mounted a laser sensor on a travelling table to measure the settlement of several points on a limited small area at the surface directly above the rebar. Each complete measurement over the studying area took approximately 5 minutes. It is noticed that concrete settles very rapidly in the first minutes to hours and the measurements should be as fast as possible to avoid introducing artifacts.
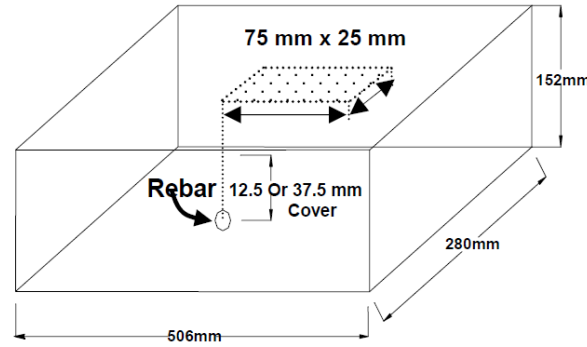
Fig. 2. 17. Area on which vertical shrinkage was measured with non-contact lasers [49]

In order to check the effect of the refraction brought by the bleeding water on the vertical displacement measurements, a test was performed during this PhD project, whose result is shown in *Fig. 2. 18*. A pattern was fixed at the bottom of a container (9 cm depth). Then, water was added on top, in different incremental amounts. While the target was completely fixed at the bottom of the container, laser sensors and DIC (Digital Image Correlation) system (see Chapter 4) showed false displacement, upwards. The experiment showed that, when the accumulated bleeding water thickness increases, the measurements can be affected by the refraction.
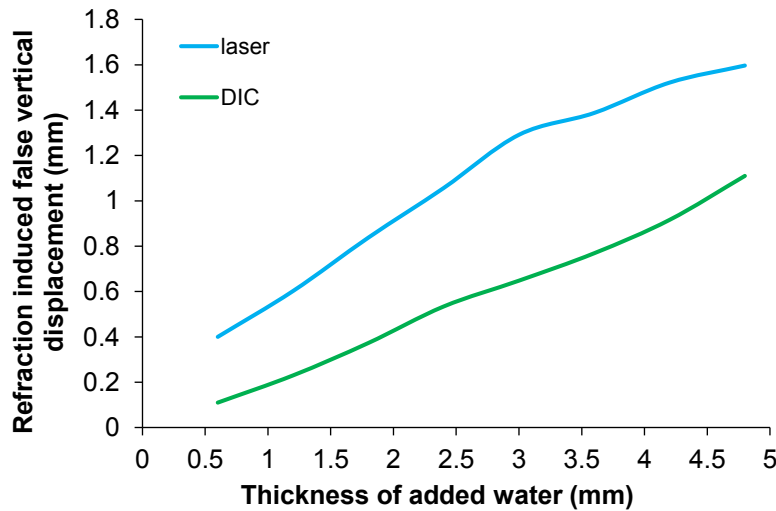
Fig. 2. 18. Effect of refraction on vertical displacement measurements

Accordingly, Kwak et al. [15], avoided the latter problem by using a wire mesh with the target above the water level (see *Fig. 2. 19*); this contrivance was also used in this PhD work (see Chapter 4) to measure the real displacements, avoiding the effect of refraction. Kwak et al. [15] (see *Fig. 2. 19*) measured the self-weight induced elastic displacement, excluding the chemical shrinkage, thermal expansion and the effect of refraction, by utilizing a Styrofoam floater for measuring the chemical shrinkage plus the thermal expansion. Furthermore, they mounted a wire mesh on the surface of the mortar to measure the total bulk deformation. All measurement targets were above the water level, avoiding the refraction problem. Subtracting the Styrofoam floater measurements from the wire mesh measurements led to the determination of the deformation induced by self-weight.
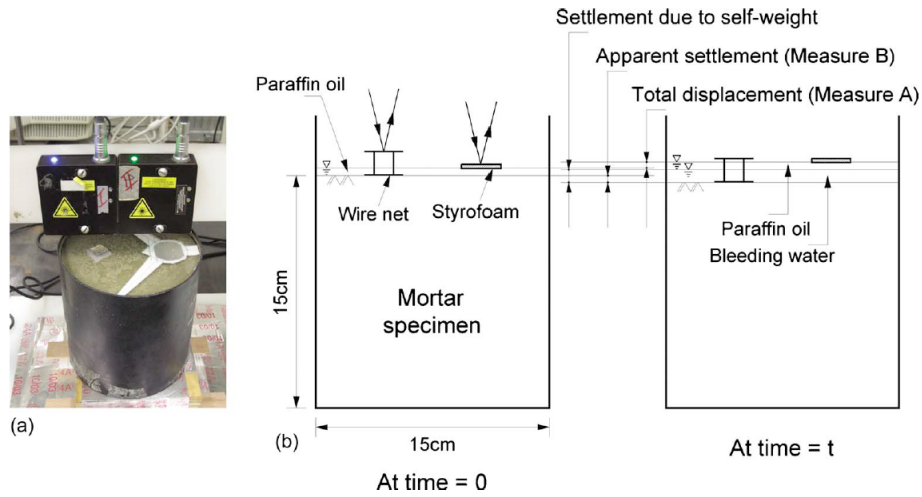
Fig. 2. 19. Setup to measure the vertical elastic deformation induced by self-weight [15]

2.3.2. Horizontal displacement

All proposed methods rely on the bond of rigid elements (e.g. cast-in studs) in the concrete, which might induce substantial artifacts in the measurements when the concrete is still plastic, due to the imperfect bonding and relative displacement of the rigid elements and the fresh concrete. Ravina and Shalon [29,100] assessed the horizontal shrinkage of fresh mortar by measuring the movement of studs inserted in both ends of the mold with mechanical gauges (*Fig. 2. 20*).
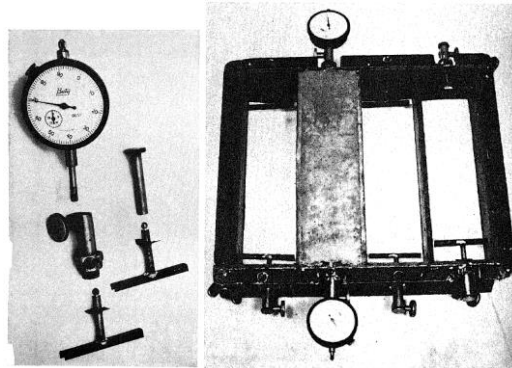
Fig. 2. 20. Setup for measurement of horizontal shrinkage according to Ravina and Shalon [29,100]

Cromarty and Bryden [101] and Orr and Haigh [102] measured the horizontal deformation of fresh cement paste and mortar with linear transducers and micrometers (Figure *Fig. 2. 21*). They used a mercury bed to reduce the effect of restraints from the bottom of the mold. However, the utilized grips (see *Fig. 2. 21*) are likely not able to restrain one end of the sample, while keeping the other end free, when the concrete is plastic before the time of final set.
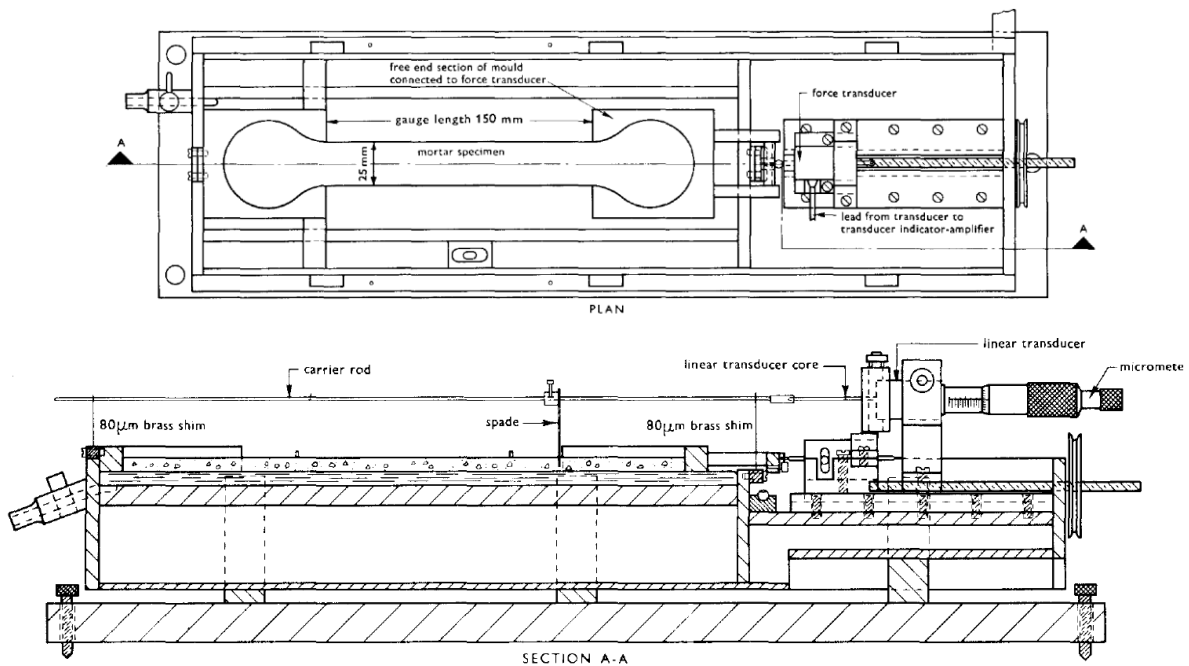
Fig. 2. 21. Setup for measurement of horizontal shrinkage according to Orr and Haigh [102]

Similar setups were utilized by Gowda [103] and by Scholer [104] except that a magnetic proximeter and a probe were used instead of linear transducers and micrometers. Displacement-induced voltage change was linked to horizontal shrinkage.

Jasiczak and Szymański used a potentiometer and relocating sensors to link the change in electrical current with length change (*Fig. 2. 22*) [105]. Later, accurate LVDTs were utilized to measure horizontal shrinkage [106–109,98,72,110]. Newlands et al. used LVDTs and movable stop ends instead of mounting pins inside the paste (see *Fig. 2. 23*) [110].
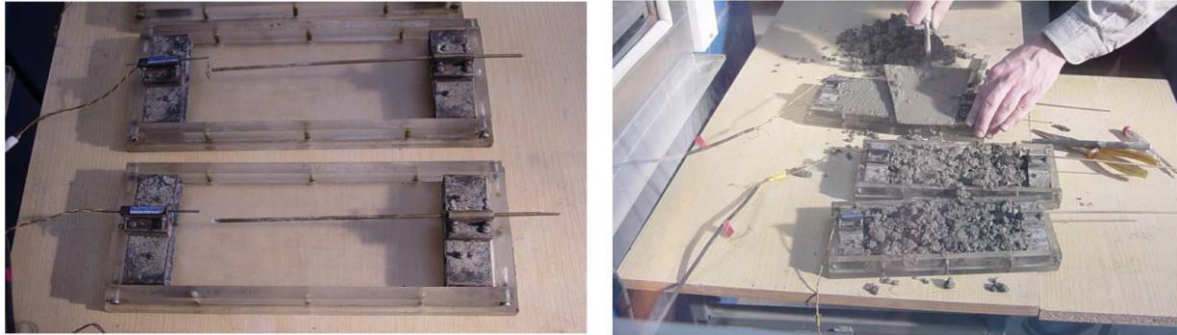
Fig. 2. 22. Potentiometers and relocating sensors for measurement of horizontal shrinkage [105]
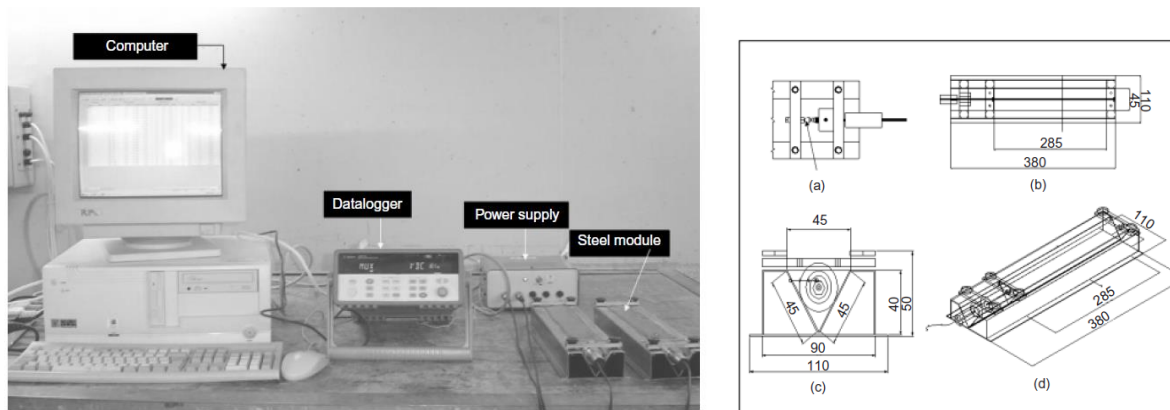
Fig. 2. 23. Left: experimental setup; Right: Dimensions and view of the linear test mould, (a) contact of LVDT and steel insert; (b) plan; (c) elevation; isometric view. All dimensions in mm [110]
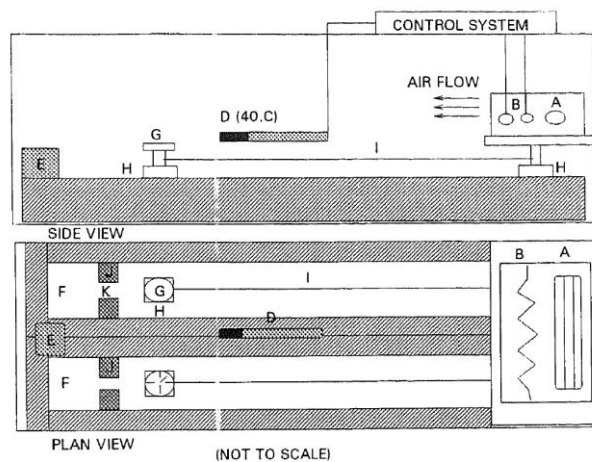
Fig. 2. 24. fan (A), electrical resistance (B), control system (C) connected to a thermometer (D), hygrometer (E), two specimens with dimensions of 20 mm X 150 mm X 1200 mm (F). The change of length over time is measured with strain gauges (G) located on steel plates (H) and connected to other steel plates by a steel rod (I) [111]

Dial gauge extensometers were used to measure shrinkage by Sanjuan et al (see *Fig. 2. 24*) [111–115].

Slowik et al. [116] investigated the early-age horizontal shrinkage of cement paste by optical fibers. They embedded fiber Bragg gratings inside cement paste. At each moment, the peak wavelength in the obtained reflection spectrum depends on the spacing of the lines forming the grating. The displacement of the grating is then used for measuring the shrinkage of the concrete (see *Fig. 2. 25*). In this method, enough bonding with the fresh cementitious material is needed to transmit the deformations to the sensors.
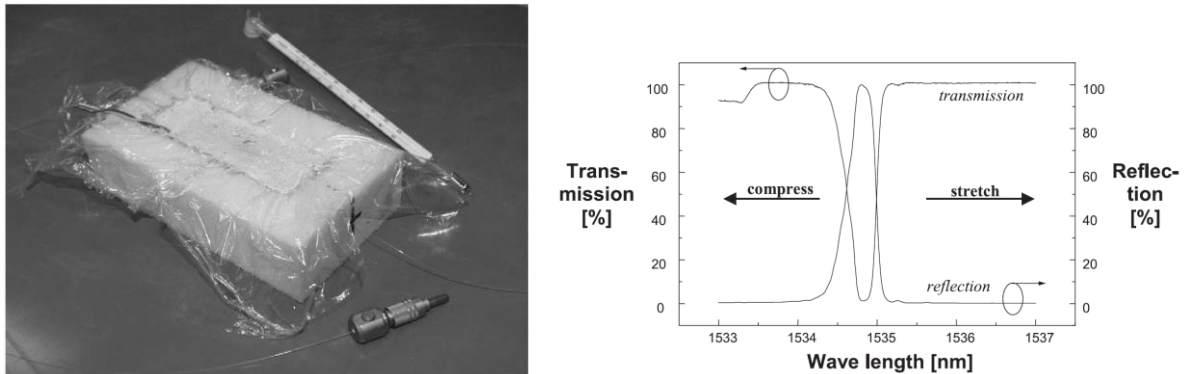
Fig. 2. 25. Left: cement paste specimen in form, sensor fiber and optical adapters. Right: transmission and reflection spectrum for fiber Bragg grating [116]

Also Wong et al. measured horizontal shrinkage and temperature variations by fiber Bragg grating sensors [117] (see *Fig. 2. 26*).
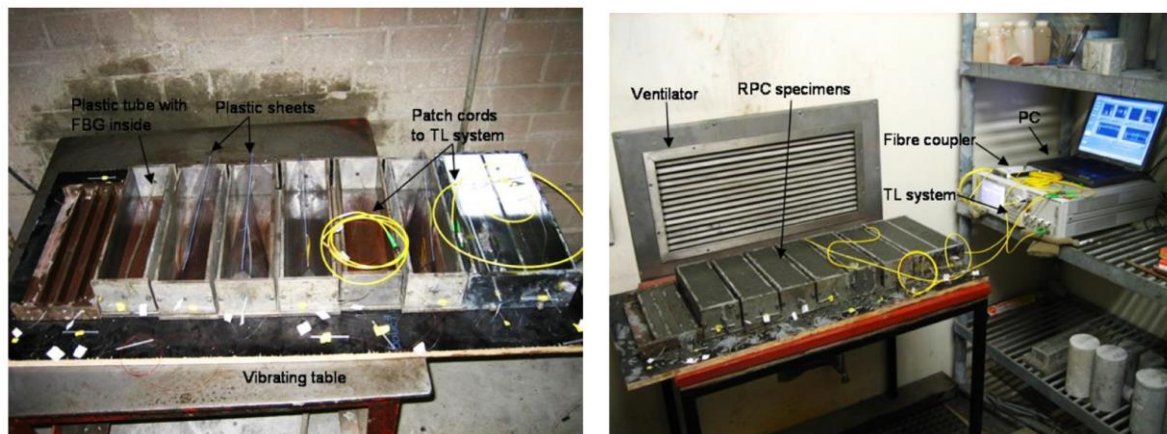
Fig. 2. 26. Left: Fiber Bragg grating sensor installation before casting, Right: final experimental setup inside a temperature- and humidity-controlled room [117]

Hanehara et al. and Baba et al. [118,119] measured early age horizontal shrinkage of fresh cement paste by inserting a strain gauge covered with waterproof silicone inside cement paste (see *Fig. 2. 27*). Also in this method sufficient bond is needed to transfer the deformations to the strain gauges, which would be likely difficult to provide in fresh cementitious materials.

Marioka et al. [120] and Bühler and Zurbriggen [121] used non-contact laser sensors to measure early age horizontal shrinkage of thick and thin mortar samples, respectively (see *Fig. 2. 28* and *Fig. 2. 29*).
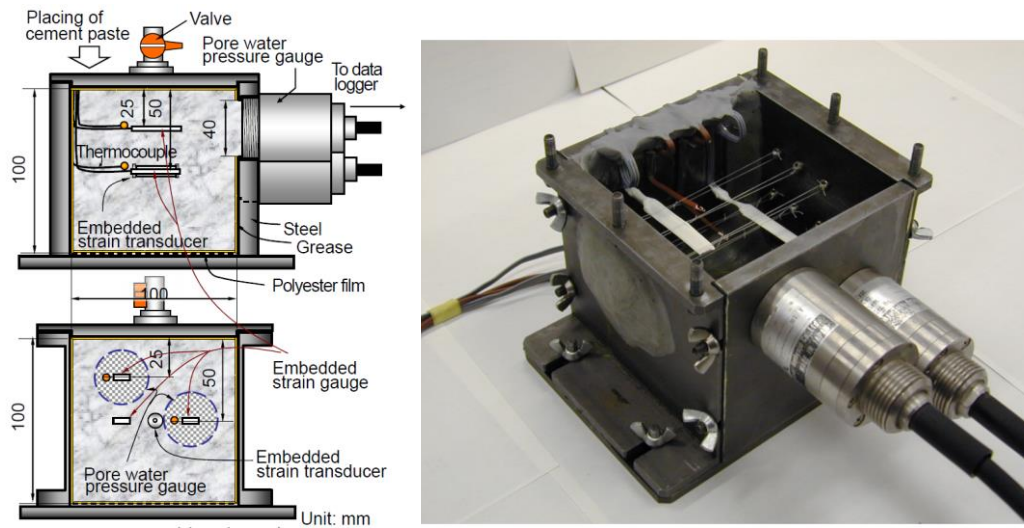
Fig. 2. 27. Left: setup plan, strain gauges were mount horizontally to measure the horizontal shrinkage; Right: appearance of the mold [119]
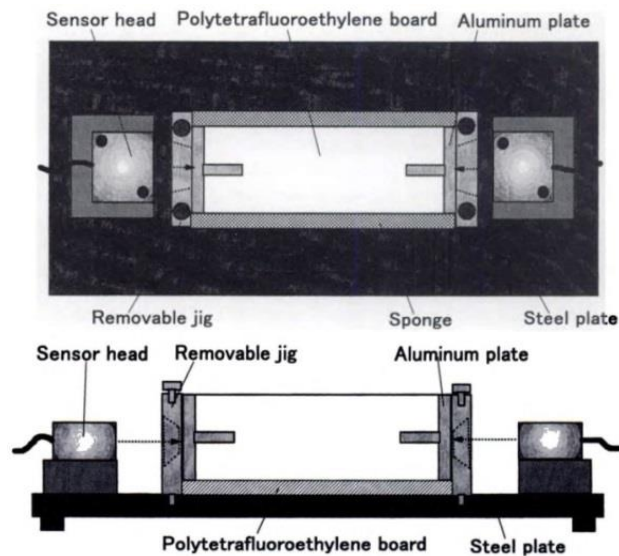
Fig. 2. 28. Test setup, including laser sensors which measure the movement of the aluminum plates bonded to the fresh concrete, Left: plan view, Right: side view [120]
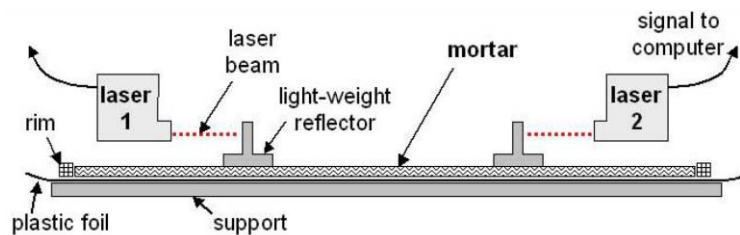
Fig. 2. 29. Setup for measuring the horizonzal shrinkage of thin mortar samples [121]

2.3.3. Setups for measuring both vertical and horizontal displacements

These setups consist of using LVDTs, laser sensors or combination of them. *Fig. 2. 30* and *Fig. 2. 31* show similar setups, in which LVDTs are employed for measuring both vertical and horizontal deformations [75,122–125].
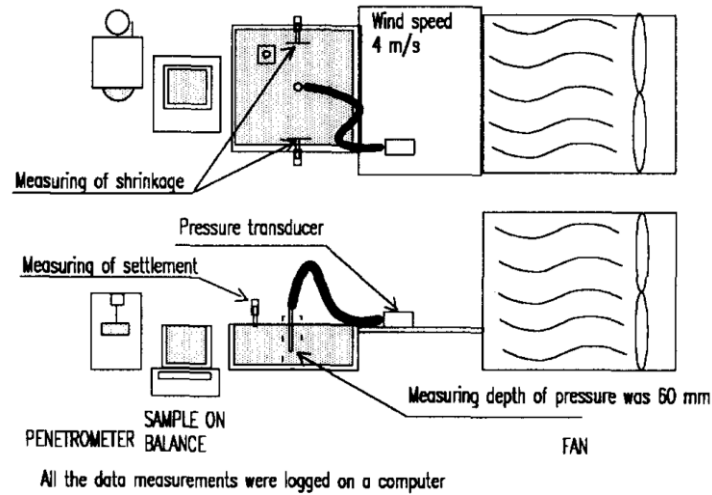
Fig. 2. 30. LVDTs for measuring both vertical and horizontal deformations [75,122]
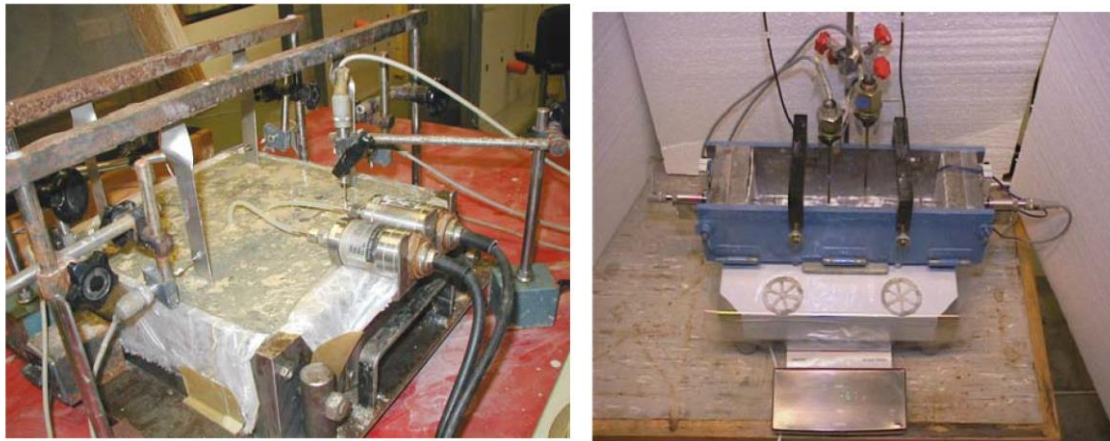
Fig. 2. 31. LVDTs for measuring both vertical and horizontal deformations. Left [123], Right [124,125]

Ghoddousi and Javid measured the shrinkage in two directions by using laser-beams induced magnified displacements, as shown in *Fig. 2. 32* [126].
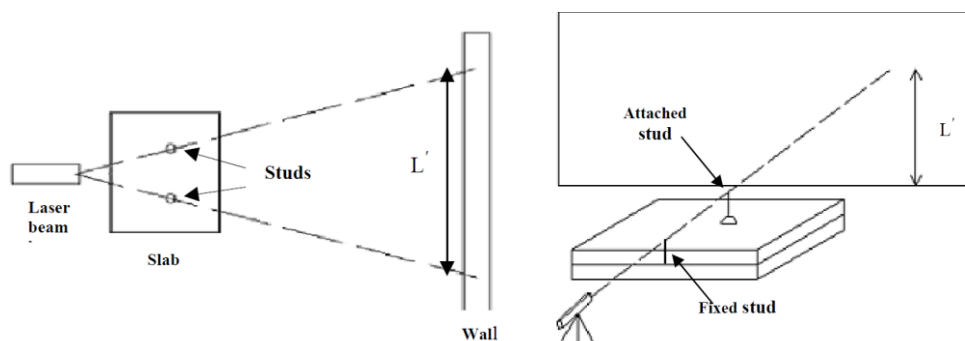
Fig. 2. 32. Left: horizontal shrinkage measurement; Right: setup for settlement measurement [126]

In *Fig. 2. 33*, setups are shown in which laser sensors are used for measuring both horizontal and vertical shrinkage [127].
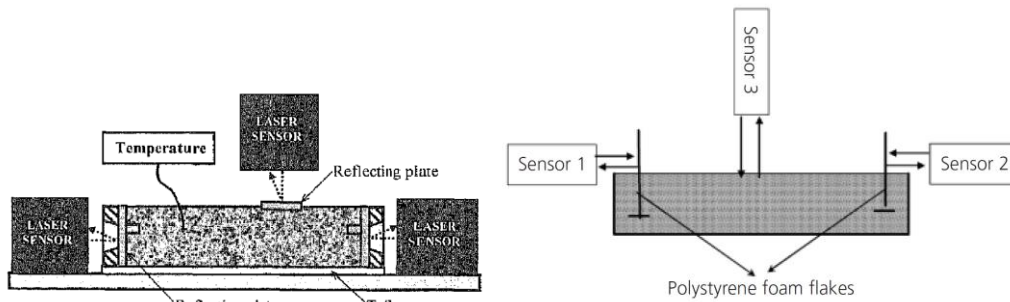
Fig. 2. 33 Laser sensors for measuring both vertical and horizontal deformations Left: [127], Right: [128]

Fontana et al. [129], used a laser sensor and LVDTs to measure the settlement and the horizontal shrinkage, respectively (*Fig. 2. 34*).
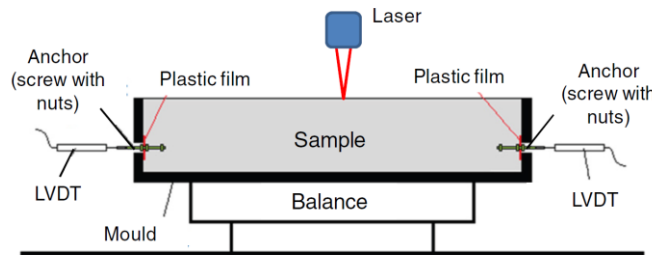
Fig. 2. 34. Combination of laser sensors and LVDTs for measuring both vertical and horizontal deformations [129]

2.3.4. Digital Image Correlation (DIC)

All of the mentioned methods measure either vertical or horizontal displacement of one point. As stated before, only Qi et al. [6] tried to measure a vertical deformation profile by mounting laser sensors on a moving table, but the displacement measurement was not simultaneous at all points. Furthermore, their measurements might have artifacts due to the improper bonding between the rigid embedded elements (e.g. studs) or sensors and the fresh concrete. Recently, a new measurement method was introduced, which is based on the correlation between images of a surface taken at specific time intervals. While this method is widely used to monitor the deformation of different materials [130], only few studies used this method for monitoring the deformation of fresh cementitious materials at early ages and before setting. None of them were dedicated to a detailed examination of plastic shrinkage of concrete. Nemoz-Gaillard et al. used a 2D image correlation system to study the effect of glass fibers on very early-age cracking [90]. In 2D image correlation systems, a single camera is used and only the in-plane deformation is measured. Nemoz-Gaillard et al. [90] monitored strain development on the surface of fiber-reinforced concretes within 24 h after casting. The

mixtures contained two aggregate size ranges, 0-3 mm and 0-6 mm. In the samples with finer aggregates, fibers (12 mm length was utilized) increased the homogeneity of the strains; however, they had a smaller impact on the deformations of concrete with coarser aggregates. Messen et al. used a 2D image correlation system to measure strain development of mortars containing cellulose ether during 25 h after casting [91]. Their study was based on comparing average values of measured strains, in which one pixel represented about 300 μm. They also followed a local approach to study the heterogeneity of the shrinkage at the surface, considering a gauge length equal to 30 mm divided into 100 pixels. For decreasing the boundary effects, they examined only a region of interest at the middle of specimen (*Fig. 2. 35*).
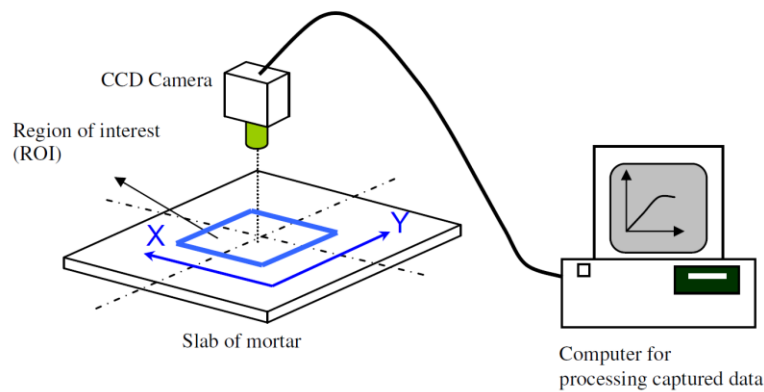
Fig. 2. 35. A schematic description of a 2D image correlation system [91]

Le-Bihan et al. used a 3D image correlation system to monitor deformations of mortars containing calcium sulfoaluminate cement up to 70 h after casting [131]. In 3D image correlation systems, two cameras are used, which allow both in-plane (horizontal) and out-of-plane (vertical) deformations measurements of at the surface of the specimen simultaneously. They compared the measurements with the 3D image correlation system with measurements with LVDTs and showed good agreement between these two methods. In this PhD thesis, a 3D image correlation system was used to monitor vertical and horizontal shrinkages simultaneously, during the plastic state (up to 6 hours after casting). Further details are explained in Chapter 4.

2.4. Experimental methods for plastic shrinkage cracking quantification

One of the most utilized test methods for quantifying the plastic shrinkage cracking is ASTM C1579 [17,50,74,77,82,85,86,92,129,132–136,136], "Standard Test Method for Evaluating Plastic Shrinkage Cracking of Restrained Fiber Reinforced Concrete (Using a Steel Form Insert)". The evaluation is based on the comparison of the final crack sizes with the one for the reference concrete, after the final setting time. As shown in *Fig. 2. 36*, the stress risers restrain the concrete. The crack appears on the top of the largest stress riser in the middle, and propagates to the surface. The specified temperature and relative humidity during the test are 36 ± 3 °C and 30 ± 10 %, respectively, and the wind velocity must be sufficient to maintain a minimum free water evaporation rate during the test of 1 kg/m²/h.
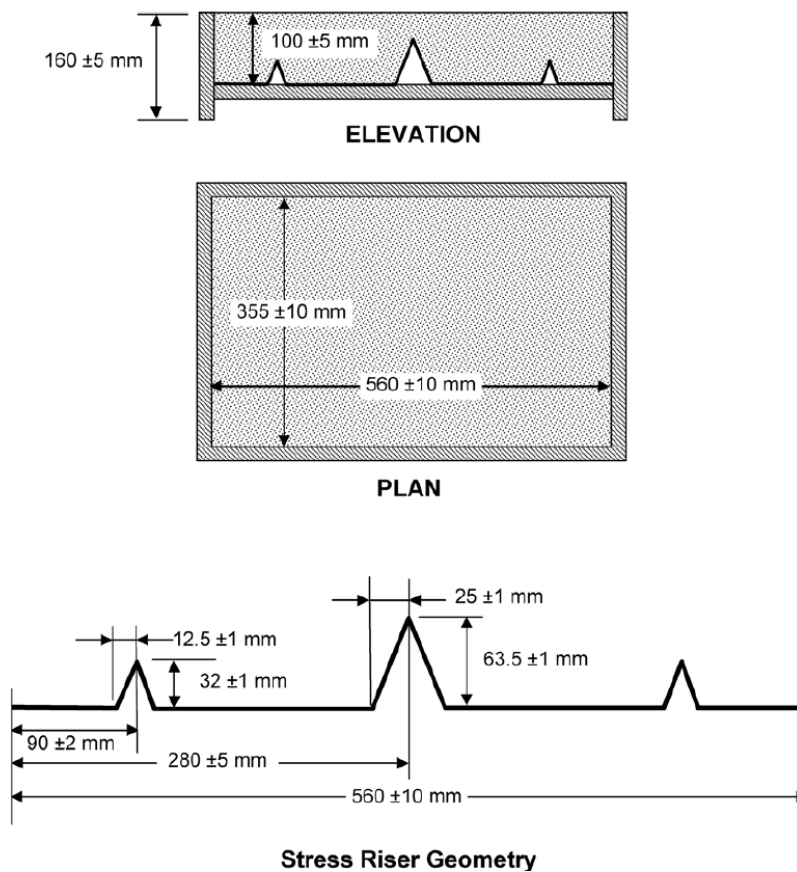
Fig. 2. 36. Specimen and stress riser geometry, according to ASTM C1579 [132]

A drawback of this method is that in some cases the initiated crack does not propagate to surface, or the size of the reference crack is less than 0.5 mm, the minimum specified crack width for the control concrete. Therefore, some researchers [55,78,89,93,137,138] tried to modify the ASTM standard by adding extra bolts and nuts, or arrangements at sides or reinforcing bars to increase the potential of cracking (see *Fig. 2. 37*).
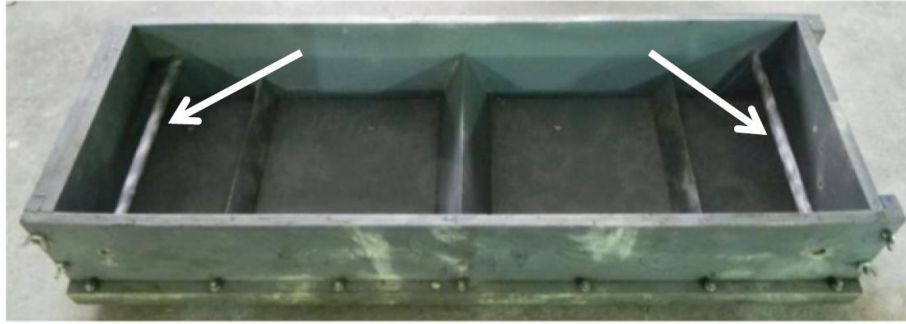
Fig. 2. 37. Addition of bars to the mold of the ASTM standard to increase the restraint [138]

Fig. 2. 38 shows the German DIBt (Deutsches Institut für Bautechnik) proposed mold [81,88,129,139–141]. It consists of a shallow cubic mold with threaded steel rebars to provide the boundary restraint and differential depth.
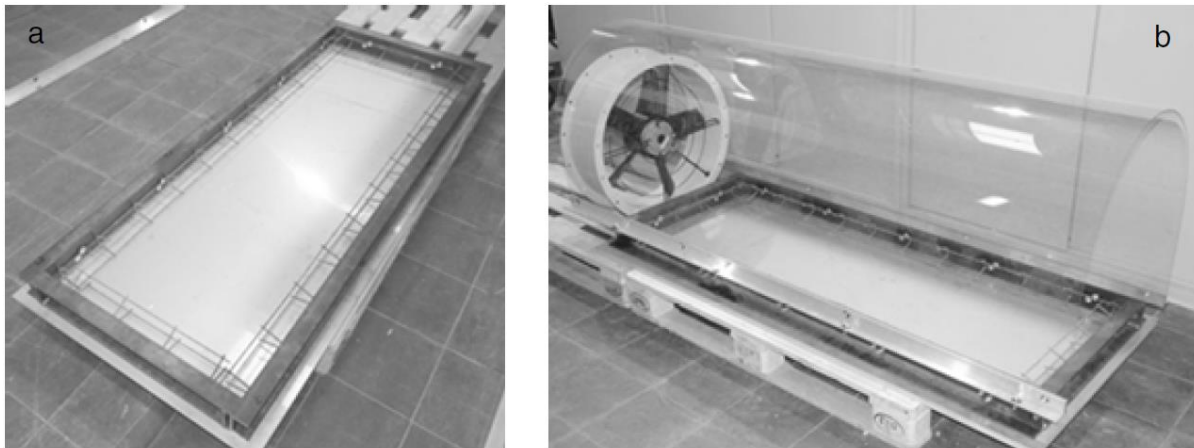
Fig. 2. 38. DIBt test setup [129]

Another standard test method is the ring test proposed by ÖVBB (Österreichische Vereinigung für Beton und Bautechnik) [129], and NORDTEST NT BUILD 433 [142] (see *Fig. 2. 39*). The ring shape provides the incompatibility of deformations. In addition, flat steel bars were added to increase the degree of restraint. The specified temperature and relative humidity during the testing period are 20 ± 1°C and 43 ± 3 %, respectively, and the wind speed is specified as 4.5 ± 0.3 m/s [142]. Ring tests have been utilized in several studies, e.g. [58,61,94,109,129,143–145].
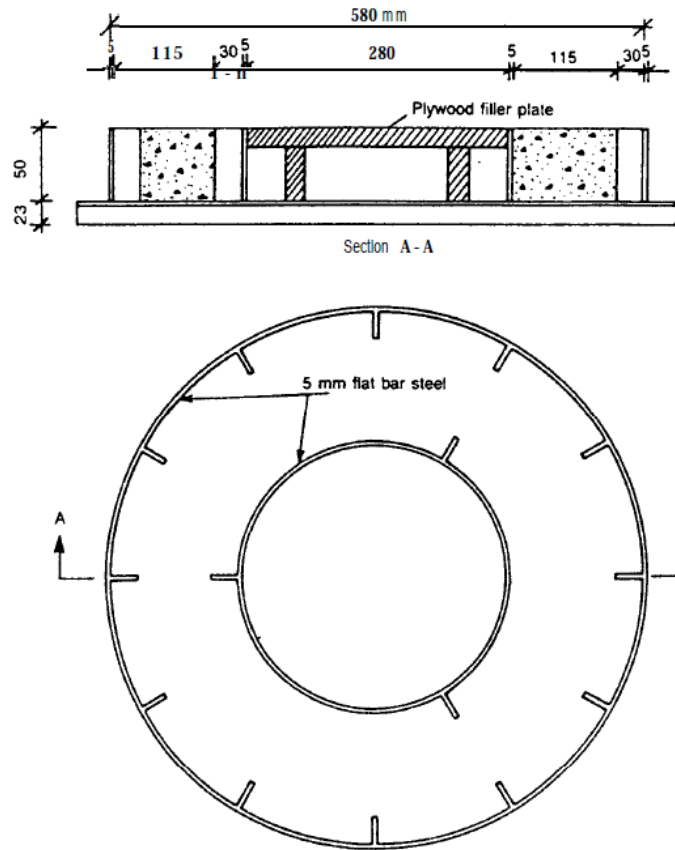
Fig. 2. 39. Ring test according to NORDTEST NT BUILD 433 [142]

The mold recommended in the Chinese GB/T 50082-2009 [146,147] standard is shown in *Fig. 2. 40*. The specified temperature and relative humidity during the testing period are 20 ± 2°C and 60 ± 5 %, respectively. The wind speed is specified as 5 ± 0.5 m/s [146].
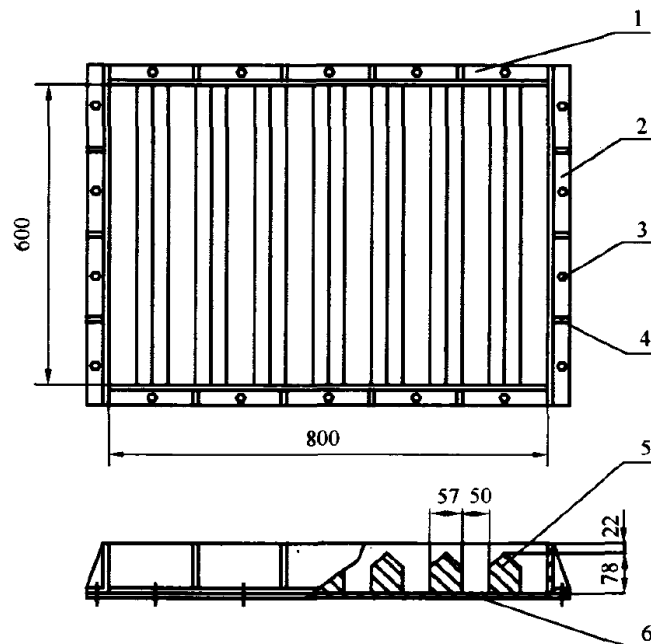
Fig. 2. 40. The mold according to GBT 50082-2009 (The dimensions are in mm)[146]

In addition, several other, non-standardized test methods can be found in the literature. According to one of them, concrete is placed on a substrate base with several knobs, exposed coarse aggregates or dents on the surface, which work as stress risers [95,96,126,148–151] (see *Fig. 2. 41*).
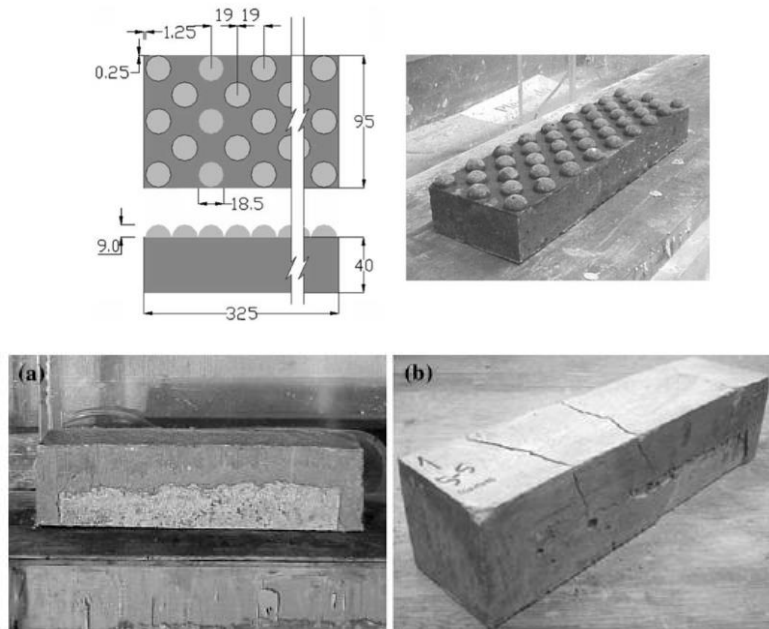
Fig. 2. 41. Up: substrate base with protuberances; Down: The specimen after demolding (a) and cracking (b) (The dimensions are in mm) [149]

In one study, a dumbbell shape mold was utilized [152]. The edges were designed to work as stress risers (see *Fig. 2. 42*).
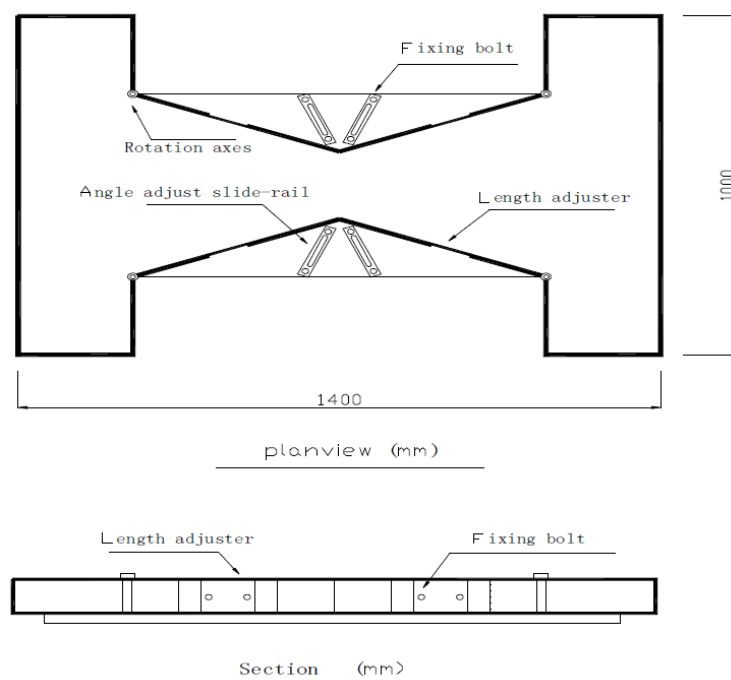
Fig. 2. 42. Dumbbell-shaped mold [152]

None of the methods described above is able to capture the crack initiation. Therefore, if the crack does not propagate to the surface, it is not possible to quantify the amount of cracking. In one study [48] (see *Fig. 2. 43*), transparent walls were utilized to study the crack initiation in the bleeding state. However, according to ASTM C1579 standard [132] the cracks observed within 2.5 cm from the walls should be neglected, due to the possible wall effect.
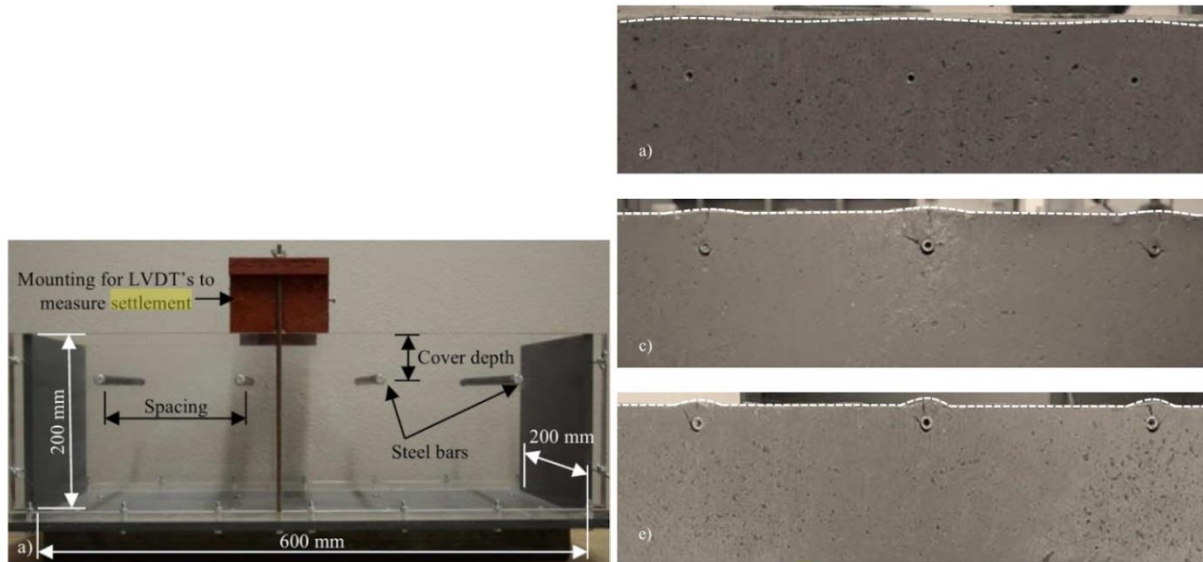
Fig. 2. 43. Left: mold with transparent walls; Right: observed cracks according to the elevation of the steel bars in the bleeding state [48]

In this PhD dissertation, the ASTM standard was utilized to study the effect of the cement type on plastic shrinkage cracking, as explained in Chapter 4. Furthermore, a novel method is proposed to capture the crack initiation by X-Ray radiography, as described in Chapter 6.

2.5. Analytical and numerical methods to model plastic shrinkage

The models are divided in two groups, according to the states of the plastic shrinkage: bleeding and drying (please see Chapter 1). The bleeding state is when the pore fluid does not completely evaporate before the time of final set, and the governing physic is self-weight consolidation. In the drying state, the pore fluid has evaporated completely before the time of final set, and the governing physic is capillary pressure development.

2.5.1. Bleeding state

In 1968, Powers [35] explained the phenomenon of bleeding according to the sedimentation theory (large strains). He determined the hydraulic gradient according to the unbuoyed weight of the solid materials. Bleeding was divided in two periods: constant initial bleeding rate and period of diminishing rate (see *Fig. 2. 44*). It was stated that the constant bleeding rate is an intrinsic property of fresh cement paste, and was related to the permeability, by utilizing Darcy's law and the previously-mentioned hydraulic gradient. Powers concluded that the bleeding capacity is a function of the height of the sample, and furthermore, that cement hydration arrests bleeding, in the period of diminishing rate.
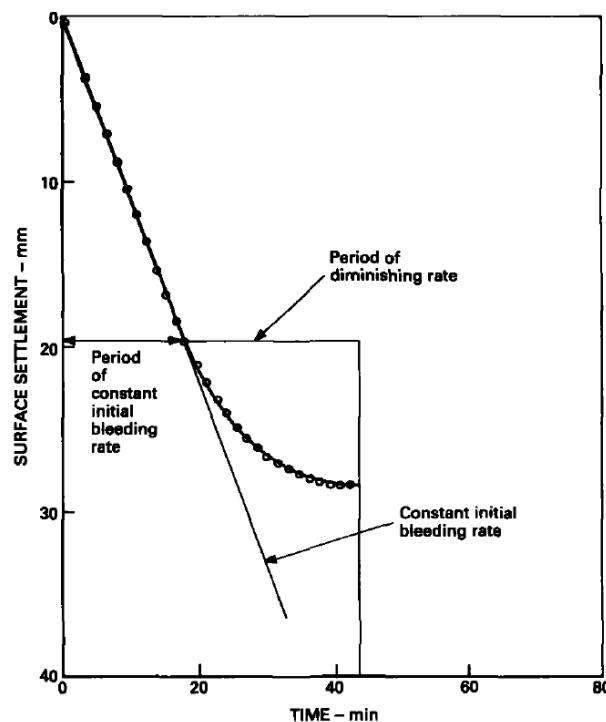
Fig. 2. 44. Periods of bleeding, according to Powers approach [153]

Later in 1987, Tan et al. [153], explained the bleeding of cement paste as a large-strain self-weight consolidation process, by using Terzaghi's principle of effective stress and consolidation equation. According to the assumed large-strain conditions (strain>10%) for

cement pastes, the bulk modulus was estimated as constant and the permeability was considered as a function of void ratio (i.e. porosity). The state variable was the void ratio.

Josserand, Coussy and De Larrard [154] modeled the bleeding of concrete as an ageing (cement-hydration dependent) large-strain consolidation process according to Terzaghi's approach, by considering an exponential evolution of bulk modulus. Furthermore, the permeability was assumed as a function of the solid volume proportion (i.e. porosity). The state variable was the solid volume proportion.

Morris and Dux [155] analyzed the bleeding of concrete as a small-strain consolidation phenomenon utilizing Terzaghi's principles. They utilized a function that takes into account the evolution of stiffness and permeability together. The determination of the variables was performed by fitting the analytical solution to experimental data. The state variable was the void ratio.

Kwak et al. [15], modeled the bleeding of mortars according to the small-strain approach, considering the pore pressure as the state variable. They applied the exponential evolution of the bulk modulus, proposed in the above-mentioned study by Josserand et al. [154], assuming the permeability as a function of the porosity.

In this PhD dissertation, Chapter 3 deals with the modeling of the bleeding state according to Terzaghi's small-strain consolidation process, using the pore pressure as the state variable. The materials properties (the permeability and the evolution of bulk modulus) were obtained by simulation of the bleeding tests performed on concrete specimens with different heights. The permeability was considered constant during the bleeding state, and was related to the experimentally-measured constant bleeding rate, in a similar manner as in the previously-mentioned approach by Powers [35]. Moreover, the hydration-dependent exponential function proposed by Josserand et al. [154] was utilized to obtain the bulk modulus evolution.

2.5.2. Drying state

In contrast to the bleeding state, only few studies about modeling of plastic shrinkage in the drying state have been published. In 1992, Radocea [156] proposed a model for predicting the plastic shrinkage and the capillary pressure development. Before him, just an estimation of the maximum capillary pressure exerted on the solid particles was available, being a function of the surface tension of the pore fluid, surface area of particles and porosity [30,32,35,156]. Radocea stated that the progress of the capillary pressure in fresh cementitious materials is not only a function of the evaporation rate and of the geometry of the pores at the surface, but also it is a function of the material's ability in transferring the pore fluid to the surface, e.g.

elastic modulus (see *Fig. 2. 45*). Accordingly, it was mentioned that, since fresh cementitious materials have low stiffness, their behavior in drying is similar to System B in *Fig. 2. 45*, rather than to System A. System A has a very high stiffness, in which the capillary pressure increases suddenly when a certain amount of water is removed, while system B, like a sponge, can provide some bulk water for evaporation, leading to a lower increment of capillary pressure compared to system B. Furthermore, he discussed that, if the cement particles have been compacted initially by settlement, larger horizontal shrinkage might be expected [31,156] because *E2>E1*, i.e. an orthotropic material behavior.
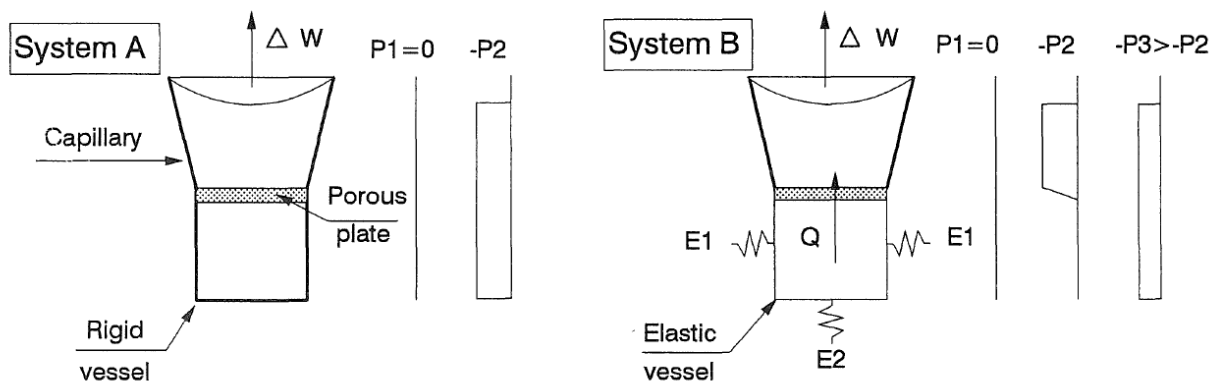
Fig. 2. 45. The effect of bulk stiffness on the increment of capillary pressure according to Radocea [156]

Nevertheless, two isotropic material property parameters were assumed, called plastic shrinkage modulus and pore structure function. Furthermore, no specific functions were derived for vertical and horizontal shrinkage and the gradient of pressure over the thickness of the sample was neglected.

It is worthwhile to mention that, although Powers did not develop a model for the development of capillary pressure, however he stated that [156]:

During the initial period of constant-rate settling, the top layer of particles descends faster than the underlying particles, because of capillary forces. Consequently, the top particles overtake the ones below, and a progressively thickening compression zone develops from the top downward.

This hypothesis by Powers is in line with the results shown in Chapter 5 of this dissertation, where it is shown that *capillary pressure stiffening* accelerates the evolution of the pore pressure. These findings agree also with Radocea's hypothesis, schematically shown in *Fig. 2. 45*. The rest of the analytical and numerical methods explained in section 2.7 are about modeling of plastic shrinkage cracking, without modeling the plastic shrinkage itself. It is

remarked that a comprehensive model, able to simulate the dynamics of the pore pressure and the plastic shrinkage development, has not been published so far.

2.6. Analytical and numerical methods to model plastic shrinkage cracking

Morris and Dux [157] developed a model for plastic shrinkage cracking in the drying state according to a fracture mechanics approach. The state of cracking was obtained by approximating the stress intensity factor, and its critical value, and then by comparing the latter factors. However, this model lacked experimental validation.

Slowik et al. [158,159] developed microscale models (discrete element models, DEM) for plastic shrinkage cracking by equilibrating the inter-particles forces acting on solid particles. The simulated cracking was not validated experimentally for cementitious materials, which are characterized by evolution of mechanical properties due to cement hydration. Slowik et al. utilized both an implicit solution scheme [158] and an explicit solution scheme [159]; the latter was mentioned to be more efficient from the computational point of view. Nevertheless, as explained before, the main source of the plastic shrinkage cracking is the self-equilibrated eigenstress brought by plastic shrinkage. The latter needs to be studied at the macroscale, according to the structural boundary conditions, as performed in this dissertation based on the poromechanics approach.

2.7. Conclusions

According to the presented literature review, it can be concluded that a comprehensive poromechanics model is needed to couple environmental and material properties for plastic shrinkage cracking estimation. The available methods of plastic shrinkage measurements are prone to significant artifacts. Therefore a robust method is needed to measure plastic shrinkage, as explained in Chapter 4. Furthermore, an accurate method is needed to detect the plastic shrinkage crack initiation, as explained in Chapter 6.

The analytical methods utilized in the literature to model plastic shrinkage and plastic shrinkage cracking were reviewed. A poromechanics approach needs to be utilized for the quantification of plastic shrinkage and plastic shrinkage cracking. As explained in Chapter 3, the bleeding state is in fact the manifestation of fresh concrete material properties. Accordingly, the modeling of the bleeding state can lead to the determination of the fresh cementitious materials properties (see Chapter 3).

This page is intentionally left blank.

Chapter 3. The bleeding test: A simple method for obtaining the permeability and bulk modulus of fresh concrete[2]

Abstract

This Chapter shows how the well-known bleeding test can be used as a simple and inexpensive method for measuring the permeability and the bulk modulus of fresh concrete, utilizing Darcy's law and a small-strain poromechanical approach. The permeability and the bulk modulus are two essential parameters for understanding the behavior of fresh concrete, in particular plastic settlement and plastic shrinkage cracking. The proposed methods are verified and validated by utilizing experimental data obtained from the literature.

Keywords: Bleeding; Fresh Concrete; Permeability; Shrinkage; Bulk modulus

3.1. Introduction

The intrinsic permeability [160] (also referred to as specific permeability [161]), κ [m^2], is a parameter of a porous medium describing transfer of fluids through its pore network [162–164]. It is an intrinsic property independent of pore fluid properties [162–164], while it depends on pore structure characteristics: total porosity, distribution of pore sizes, connectivity and tortuosity of pores, surface roughness of the flow paths [162]. After accounting for the properties of the pore fluid in addition to the intrinsic properties of the medium, the flow of a specific fluid through a particular porous medium can be characterized by means of the coefficient of permeability (also referred to as hydraulic conductivity), k [m/s] [26,162–164]:

$$k = \frac{\rho_f g}{\mu} \kappa \qquad\qquad (3\text{-}1)$$

where ρ_f [kg/m^3] is the density of the pore fluid, g [m/s^2] is the gravity acceleration, μ [Pa·s] is the dynamic viscosity of the pore fluid. In this study, *permeability* always refers to the coefficient of permeability expressed with eq. (3-1), similarly as in [165,166]. Mobility coefficient (K [m^2/Pa·s]) and diffusivity coefficient (C_d [m^2/s]) are other parameters describing the ability of a fluid to move within porous media. The mobility coefficient K

---

relates the pressure gradient to the fluid flux in Darcy's law and is analogous to the diffusivity coefficient in Fick's law [167]. It is expressed as:

$$K = \frac{\kappa}{\mu} \qquad (3\text{-}2)$$

The diffusivity coefficient C_d, also referred to as Terzaghi's consolidation coefficient, is related to the mobility coefficient K by the following equation [26,168]:

$$C_d = \frac{K}{\lambda + n\beta} \qquad (3\text{-}3)$$

where λ_b [1/Pa] and β [1/Pa] are the compressibility of the bulk and the pore fluid, respectively, and n [-] is the porosity. By assuming the pore fluid as incompressible [169] (i.e., assuming water as incompressible and considering negligible the effect of air content in the cementitious material [154]), eq. (3-3) simplifies to:

$$C_d = \frac{K}{\lambda_b} = KB \qquad (3\text{-}4)$$

where B [Pa] is the bulk modulus. Consolidation coefficient C_d derived from soil mechanics approach does not consider the evolution of material properties in time due to chemical processes [170]. However, in the particular case of cementitious materials considered here, we will also account for the hydration process by considering bulk modulus B as a function of time, see section 3.2.2.

Knowledge of the elastic properties and of the bulk modulus in particular is essential for predicting the early-age shrinkage (e.g. [171,172]). The plastic settlement, or the consolidation of fresh concrete while still fully saturated, is directly proportional to its permeability and bulk modulus (see eq. (3-4)). Also, as mentioned before, the permeability is an indicator of pore structure and pore fluid properties, which both affect the capillary pressure and the water transport in the unsaturated plastic shrinkage regime [116,125,173]. Additionally, in studies related to curing, permeability is a key factor which affects the curing water migration [174,175].

Besides determining the settlement and the horizontal shrinkage of fresh concrete, knowing the development of the bulk modulus is also essential to understand plastic shrinkage cracking, since crack propagation releases the stored elastic energy, which depends on the bulk modulus [176]. As permeability and bulk modulus are two key parameters for studying

the early-age concrete properties, in particular in the fresh, plastic state, the present study is dedicated to quantify these parameters with a simple and robust approach.

Although numerous studies devoted to measuring and modeling the permeability after hardening of concrete have been published (e.g. [174,177,178]), only a few are dedicated to the permeability at very early ages [35,165,166,179]. All of the developed methods for fresh cementitious materials are based on a soil-physics approach using Darcy's law. The pore pressure gradient either needs to be measured experimentally or it is obtained from available consolidation models. The latter is the most challenging issue for cementitious materials that, unlike soil, experience a rapid evolution of material properties due to cement hydration.

Picandet et al. [165] measured the permeability of cement pastes by a soil permeameter cell and a controlled oedometer with specimens of initial height 70 mm and 20 mm, respectively. Both methods work with a high constant water head. In the taller sample, Picandet et al. simulated the pressure gradient at each time instant by solving Terzaghi's consolidation equation for soil, neglecting hydration and the corresponding bulk modulus evolution. However, it will be shown later in this study that the latter parameter has a significant impact on the pore pressure profile and its evolution in time cannot be neglected. Additionally, the small sample sizes used in [165] are not easily applicable for studying concrete with normal aggregate sizes.

Assad et al. [166] opted for the falling pressure head method, which allowed faster stabilization of the flux within 4 to 10 min, depending on the mortar composition. Also in this study, the effect of bulk modulus evolution on the gradient of pore pressure was not accounted for in the analysis. Furthermore, in both previously-mentioned methods, the high pressure heads applied to the specimens may lead to changes in material properties, e.g. due to washing out of finest particles, the so-called leaching effect [165,166], or due to unusually high compaction of the material.

Methods for measuring the evolution of elastic properties at very early age are based on elastic wave propagation [180,181]: e.g. Ultrasound Pulse Velocity (UPV) and Ultrasound Wave Reflection (UWR). Such methods do not allow a direct measurement of the bulk modulus, rather of the two elastic moduli (Young's and shear). Since before solid percolation time, shear waves cannot properly propagate, the shear modulus cannot be measured, thus also excluding indirect monitoring of the bulk modulus evolution.

In this study, we propose to use the bleeding test [35] as a simple and easily accessible test for studying the properties of concrete in its fresh state, though of course limited to mixtures that experience bleeding. Bleeding is a consequence of self-weight consolidation

[15,39,154,182]; in some references, it was also referred to as an effect of a sedimentation process [35]. The bleeding rate in the constant rate period is an intrinsic property of cementitious materials [35] and can be used as a key value for obtaining the permeability. An approach to calculate the permeability of fresh concrete using the bleeding rate was previously proposed by Powers [35]. However, opposite to the present model, which assumes the existence of small strains, the latter was a large-strain model based on the sedimentation approach in which the hydraulic gradient was expressed in terms of the unbuoyed weight of the solids. Since the buildup of the bulk modulus in fresh cementitious materials arrests bleeding, modelling deformations of the fresh concrete and comparing them to the results of bleeding tests allows also to determine the evolution of the bulk modulus of concrete in the fresh state. The model was validated with experimental data on bleeding of concrete with samples of different height obtained from [154]. The permeability model was then used to calculate the permeability of concretes tested in [59], having different w/c and paste contents, to verify the robustness of the proposed model.

3.2. Poromechanics model

3.2.1. Analytical model for obtaining the permeability

Bleeding is a phenomenon taking place due to self-weight consolidation that manifests in water accumulating at the top surface of freshly-placed concrete. It takes place in the initial few hours after concrete mixing in the so-called dormant period of cement hydration. In the case the concrete layer is sufficiently deep, bleeding can also extend to the beginning of the acceleration period [35]. A schematic illustration of a bleeding test is shown in *Fig. 3. 1*.
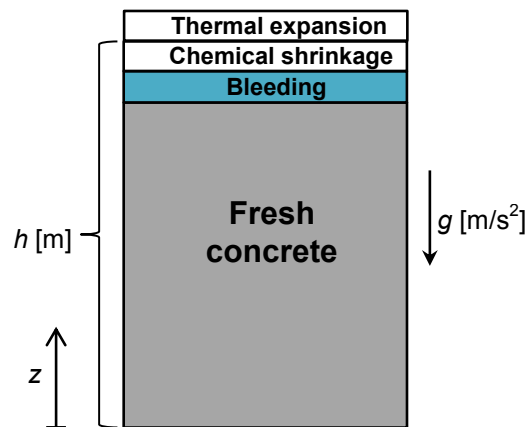
Fig. 3. 1. Schematic illustration of self-weight consolidation/bleeding. h [m] is the initial sample height

The total surface displacement of fresh concrete is the sum of vertical deformations due to chemical shrinkage, thermal expansion and self-weight consolidation/bleeding [173,183]. As discussed in [169], water flow and bleeding are caused by dissipation of excess pore water pressure as it is transferred from the fluid to the solid skeleton. Water flow in a porous medium can be described by Darcy's law. According to Darcy's law, the water flux q [m/s] is the consequence of the gradient of total pore fluid potential (Ψ_T [Pa]) in a porous material (concrete):

$$\vec{q} = -\frac{\kappa}{\mu} \nabla \psi_T \qquad (3\text{-}5)$$

Its component in the vertical direction for one-dimensional consolidation is:

$$q = -\frac{\kappa}{\mu} \frac{\partial \psi_T}{\partial z} \qquad (3\text{-}6)$$

Using a soil physics approach [162], one can define Ψ_T as:

$$\psi_T = \psi_z + \psi_p \qquad (3\text{-}7)$$

where Ψ_z is the gravitational potential [Pa], being the gravity-induced energy stored in the unit volume of pore fluid at certain height from a reference level, and Ψ_p [Pa] is the pressure potential (hydrostatic pressure or capillary pressure). According to Terzaghi's principle of effective stress one may write [184]:

$$\sigma = \sigma_{eff} + \psi_p \qquad (3\text{-}9)$$

where σ [Pa] is the total weight (total stress) and σ_{eff} [Pa] is the effective stress. In a non-consolidated concrete, it is assumed that the total weight is initially sustained by the pore fluid, and the effective stress is equal to zero [182,185]. The initial pore pressure is thus equal to:

$$\psi_p = \sigma = g\rho_C(h-z) \qquad (3\text{-}10)$$

where ρ_C [kg/m^3] is the density of concrete, g [m/s^2] is the gravity acceleration and h [m] is the height of the sample. It is assumed that the overall displacement of the concrete surface is always small compared to the height of the sample (small strain), so that changes in geometry

during consolidation can be neglected [185]. The gravitational potential of the pore fluid at a given height, taking the bottom of the container as reference point (see *Fig. 3. 1*), is:

$$\psi_z = g\rho_f z \tag{3-11}$$

where ρ_f [kg/m^3] is the pore fluid density. One can write the initial total potential as:

$$\psi_T = g\rho_C(h-z) + g\rho_f z = g\rho_C h - g(\rho_C - \rho_f)z \tag{3-12}$$

Substituting eq. (3-12) in eq. (3-6) leads to:

$$q = b = -\frac{\kappa}{\mu}\frac{\partial\psi_T}{\partial z} = \frac{\kappa}{\mu}g(\rho_C - \rho_f) \tag{3-13}$$

The pore fluid flux at the top surface of the concrete (eq. (3-13)) is equal to the constant initial bleeding rate b [m/s], a parameter conveniently determined experimentally. It should be noted that the measured bleeding rate is constant in the initial few hours after placing [35]. By simple transformation of eq. (3-13), the intrinsic permeability can be obtained as:

$$\kappa = -\frac{b\mu}{\dfrac{\partial\psi_T}{\partial z}} = \frac{b\mu}{g(\rho_C - \rho_f)} \tag{3-14}$$

Using eq. (3-1) and eq. (3-14), the coefficient of permeability can be written as:

$$k = \frac{b}{\rho_C/\rho_f - 1} \tag{3-15}$$

In eq. (3-15), the initial bleeding rate and the density of the fresh concrete are two inputs that can be easily determined with a bleeding test. The density of the pore fluid can be conveniently assumed as that of pure water. By combining eq. (3-2) and eq. (3-14), an equation for the mobility coefficient is derived:

$$K = \frac{b}{g(\rho_C - \rho_f)} \tag{3-16}$$

3.2.2. Evolution of bulk modulus

After obtaining the permeability as described in the previous section, one can determine the evolution of the bulk modulus by simulating a bleeding test with a one-dimensional consolidation equation [26]:

$$\frac{\partial \psi_p}{\partial t} = C \ \frac{\partial^2 \psi_p}{\partial z^2}, C = B \ \frac{k}{\rho_f g} \tag{3-17}$$

An exponential function proposed by Josserand et al. [154] is used to describe the evolution of the bulk modulus *B*:

$$B = B_0 \exp\left(t / t^*\right) \tag{3-18}$$

where B_0 [Pa] is the initial value of bulk modulus when bleeding starts and t^* [s] is a characteristic time governed by the kinetics of hydration.

It should be noted that the choice of the exponential function (eq. (3-18)) aims at describing the highly non-linear evolution of elastic properties in the early stages of hydration around the time at which percolation of solid microstructure takes place. Such approach has also been used by Kwak et al. [15]. It has also been used to describe the evolution in time of other hydration-driven properties related to the formation of solid microstructure, i.e. rheological properties, by Perrot et al. [186]. This is in agreement with the experimental observations in [187], where the highly non-linear in time evolution of yield stress and of ultrasound wave velocity (corresponding to the evolution of elastic properties) caused by percolation of solids was reported.

Morris and Dux [155] assumed a function which took into account the evolution of stiffness and permeability together and determined its variables by fitting the analytical solution to experimental data. On the other hand, Tan et al. [182] assumed constant permeability and a linear evolution for description of stiffness evolution.

Since eq. (3-17) using eq. (3-18) as an input has two independent variables (considering that the permeability is determined independently from eq. (3-15)), at least two bleeding tests on samples with different heights are required to fit the model (eq. (3-17)) to experimental data and estimate the evolution of the bulk modulus with eq. (3-18).

This approach can be summarized as follows: according to eq. (3-17), the gradient of pore pressure is affected by the evolution of bulk modulus and permeability. However, in a bleeding test the initial constant bleeding rate is controlled by the (constant) permeability alone according to eq. (3-15), while the bleeding capacity and therefore also the total deformation modelled with eq. (3-17) in the fresh concrete are influenced by the time at

which bleeding slows down and stops, and are therefore controlled both by permeability and bulk modulus. It should be noted that presented approach relies on assuming the constant permeability also in the diminishing rate period that follows the constant rate period. In this period, the decrease of bleeding rate is therefore solely an effect of the increasing bulk modulus. Such assumption stems from the observation that the very fast increase of bulk modulus in the initial stages of hydration brought about by the percolation of solid microstructure (see e.g. [187]) dominates over much slower evolution of permeability at that stages, that accelerates only later due to depercolation of porosity (see e.g. [188]); the latter is assumed negligible here. Another indication of the constant permeability is the constant evaporation rate observed in companion samples exposed to drying, see e.g. [59].

3.3. Model verification

For model verification, the experimental data obtained by Josserand et al. [154] was used where the authors performed bleeding measurements on samples with different heights. In [154], an approximately constant bleeding rate of 3.95×10^{-7} m/s was measured between 25 and 50 min after the beginning of the bleeding test. The concrete density was estimated as 2279 kg/m^3 based on the mixture compositions and the air contents reported in [154]. With the initially constant bleeding rate, a permeability of 3.09×10^{-7} m/s was calculated with eq. (3-15). Eq. (3-17) was solved using COMSOL Multiphysics$^{®}$. The initial condition is:

$$t = 0: \qquad \psi_p = \rho_c g (h - z) \qquad (3\text{-}19)$$

The boundary conditions are:

$$z = 0: \qquad \frac{\partial \psi_p}{\partial z} + \rho_f g = 0 \qquad (3\text{-}20)$$

$$z = h: \qquad \psi_p = 0 \qquad (3\text{-}21)$$

No friction along the vertical boundaries was assumed. According to [189] the effect of walls on bleeding can be considered negligible for the containers with diameter-to-height ratio above 0.24 (ratio of 1.0 was used in the analyzed case). The numerical analysis was run in 2-D, using a square geometry (25×25 cm^2) discretized with 922 triangular finite elements. The following parameters for the evolution of bulk modulus (eq. (3-18)) were found: B_0=31.5 KPa and t^*=35 min by fitting the modelled bleeding to experimental data shown in *Fig. 3. 2*. As can be seen, the assumed evolution of bulk modulus and a constant value of permeability allow to obtain a very good agreement of the simulated data with the experiment.
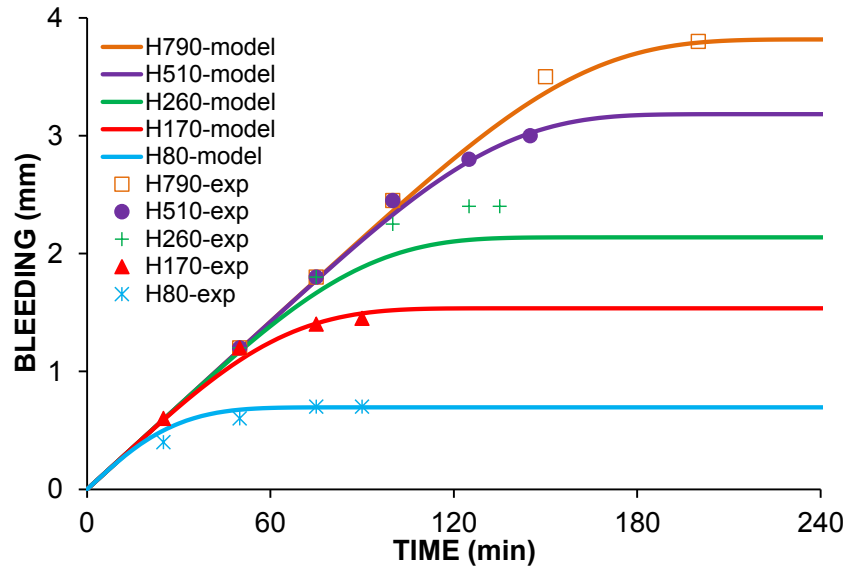
Fig. 3. 2. Comparison of experimental bleeding data with the simulated ones at different heights. The numbers refer to the height of samples in mm. The data were taken from reference [154]

3.4. A case study using the proposed model for permeability

In this section, a case study showing the applicability of the proposed approach is presented. The experimental results were taken from a previous study performed at Empa [59]. Two groups of concretes were analyzed, in which either w/c or cement paste content were systematically varied to study the effect of concrete porosity (affected by both parameters) on permeability. The w/c varied from 0.4 to 0.6 and the cement paste content from 263 to 316 l/m^3 [59]. Since the study [59] was published as a report in German and it deals with a much larger number of concrete mixtures, Appendix 3-A summarizes the information about the mixture compositions and the experiments that may be needed to understand fully the simulation results shown in this section.

3.4.1. Results

Experimental results of bleeding and calculated permeability values are presented in *Fig. 3. 3*, *Fig. 3. 4* and *Fig. 3. 5*, respectively. The permeability was calculated with eq. (3-15) using the measured density and bleeding rate, as shown in *Table 3. 1*. The slope of the experimental curve in the initial linear part is used as bleeding rate (see *Table 3. 1*). The names of the mixtures refer to the w/c and the paste volume; for example, "w/c 0.5-p289" means a concrete with w/c 0.5 and 289 l/m^3 of cement paste. *Fig. 3. 3* and *Fig. 3. 4* show that an increase in w/c has a substantially greater impact on the initial bleeding rate than an increase in the paste volume, considering a similar change in porosity brought about by varying the two parameters, *Fig. 3. 5*.
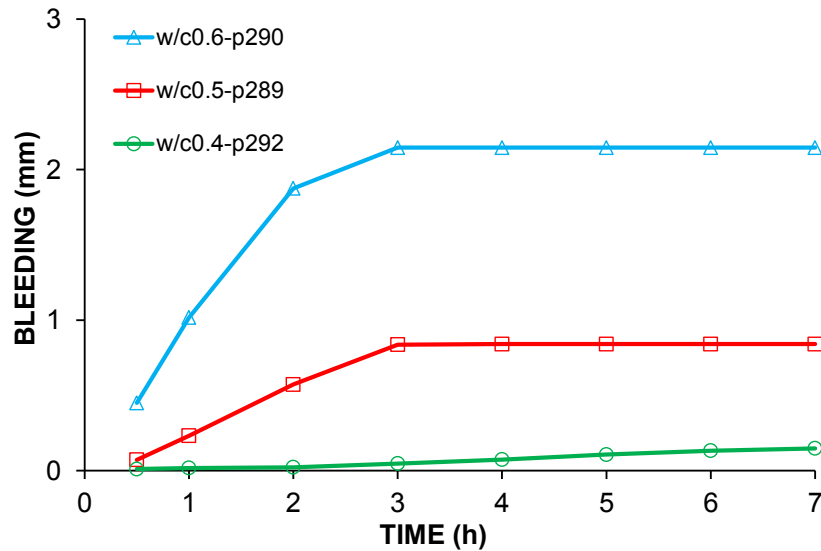
Fig. 3. 3. Bleeding for concretes with different w/c. Data from [59]
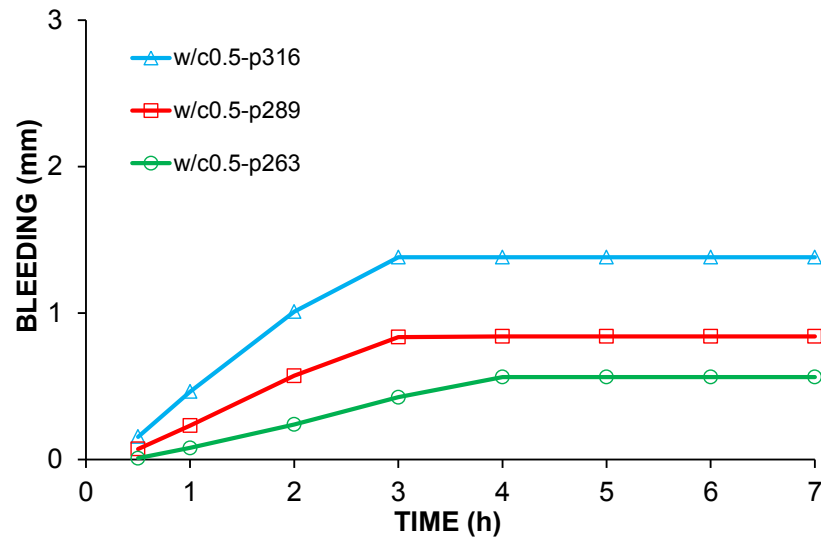
Fig. 3. 4. Bleeding for concretes with different paste content. Data from [59]
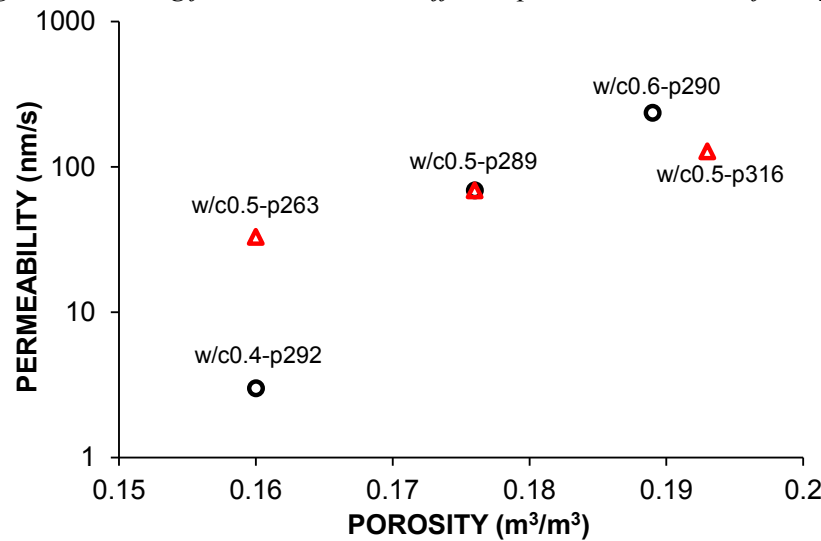
Fig. 3. 5. Permeability vs. porosity for the two groups of concretes. Circles correspond to concretes with different w/c and same paste content, triangles correspond to concretes with different paste content and same w/c.

Table 3. 1. Measured and calculated data

Concrete	w/c 0.5-p289	w/c 0.4-p292	w/c 0.6-p290	w/c 0.5-p263	w/c 0.5-p316
Bleeding rate (m/s)	$9.26 \cdot 10^{-8}$	$4.95 \cdot 10^{-9}$	$2.64 \cdot 10^{-7}$	$4.26 \cdot 10^{-8}$	$1.58 \cdot 10^{-7}$
Concrete measured density (kg/m³)	2338	2418	2341	2341	2333
Permeability- eq. (3-15) (nm/s)	69	3	197	32	119

The obtained values of permeability are in the range of 10^{-7} - 10^{-9} m/s, which is a reasonable range compared to previous studies on fresh concrete [166,190]. As expected, in both cases increasing the porosity of the whole concrete led to higher permeability, simply because the area for fluid flow increases by increasing the porosity. The two groups of concrete had similar extremes of porosities (see *Fig. 3. 5*); however increasing the porosity by increasing w/c was more effective in increasing the permeability rather than increasing the paste content for the same values of porosity. This finding can be explained by the fact that the size of the pores through which fluid flow takes place increases with higher w/c together with an increasing total porosity, while by increasing the paste content the size of the pores remains the same, and only the total porosity increases. In particular, both the surface area of the pores and the tortuosity of the fluid paths decrease with increasing pore size, and samples with larger pores would have shorter path lengths [191]. Lower tortuosity and lower specific surface area would result in higher permeability. A more detailed explanation is presented in section 3.4.2. As shown by the results in *Fig. 3. 5*, the model developed in this study is able to discriminate not only between concrete with different porosities, but also with different geometry of the fluid paths.

3.4.2. Permeability model verification

A frequently-used relationship for predicting the permeability of porous materials is the Kozeny-Carman equation (eq. (3-22)), which considers a porous material as an assembly of capillary tubes and is based on the Hagen-Poiseuille equation adapted for a granular porous medium [35,192]:

$$k = \frac{\rho_f g}{\mu F_S F_{TH} S^2} \frac{n^3}{(1-n)^2} \tag{3-22}$$

where μ [Pa·s] is the dynamic viscosity of the pore fluid, F_S [-] is the shape factor related to the cross section of the assumed tubes which transfer the fluid. F_{TH} [(m/m)²] is the hydraulic tortuosity or $(L_e/L)^2$, where L_e is the actual distance of flow in the direction of the traversing

thickness L. S [m^2/m^3] is the specific surface area of the wetted material, the total *surface area* of a material per unit of solid volume.

Although eq. (3-22) has been utilized for predicting the permeability of fresh cementitious materials [165,166], it does not take into account the immobile water, a quantity of water in the capillaries that does not take part in the flow, as proposed by Powers [35]. Experimental evidence [16] shows that during the initial hydration phase (the first minutes after the contact of the cement with water) nucleation and precipitation of initial hydration products may lead to increasing the surface roughness of cement grains and their interlocking, which can lead to immobilizing of part of the water. Powers [35] modified eq. (3-22) by defining the effective porosity (n_e):

$$n_e = n - \alpha_s(1-n) = ((n/(1-n)) - \alpha_s)(1-n) \tag{3-23}$$

where α_s [-] is a factor which accounts for the volumetric ratio of the stagnant water. Substituting eq. (3-23) in eq. (3-22), after some simple transformations, the modified Kozeny-Carman equation for cementitious materials is obtained (eq. (3-24)):

$$k = \frac{\rho_f g}{\mu F_S F_{TH} S_{ap}^2}[(n/(1-n)) - \alpha_s]^3(1-n) \tag{3-24}$$

where S_{ap} is the *apparent* specific surface equal to $S_h \cdot (1+\alpha_s)$ where S_h is the *hydrodynamic* surface area, the actual surface area per unit volume of solid plus stagnant liquid. According to [35], the values of α_s for cement paste (denoted as α_p) lie in the range of 0.26 to 0.58 for different cements. In lack of experimental evidence, in this study α_p is assumed to be 0.45 for all analyzed paste porosities (similarly as done in [35]), as the value providing the best fit of the Kozeny-Carman predictions and model calculations (see *Fig. 3. 6*). Additionally, the calculations were also run for the boundary values of 0.26 and 0.58 from [35] in order to estimate the effect of α_p on the predicted permeability. The latter coefficient for concrete (α_c) is calculated by eq. (3-25) assuming α_c as a function of paste content:

$$\alpha_c = \alpha_p \frac{V_p}{V_t} \tag{3-25}$$

where V_p [m^3] is the paste volume and V_t [m^3] is the total concrete volume. The values of apparent surface area were reported to be close to the fineness of dry cement measured by the

air permeability method [35]. Therefore the Blaine fineness is utilized here to estimate the apparent surface area of concretes by eq. (3-26), assuming that it is dominated by the surface area of cement:

$$S_{app} = \frac{M_{cem} V_t F_B}{(1-n)V_t} \qquad (3\text{-}26)$$
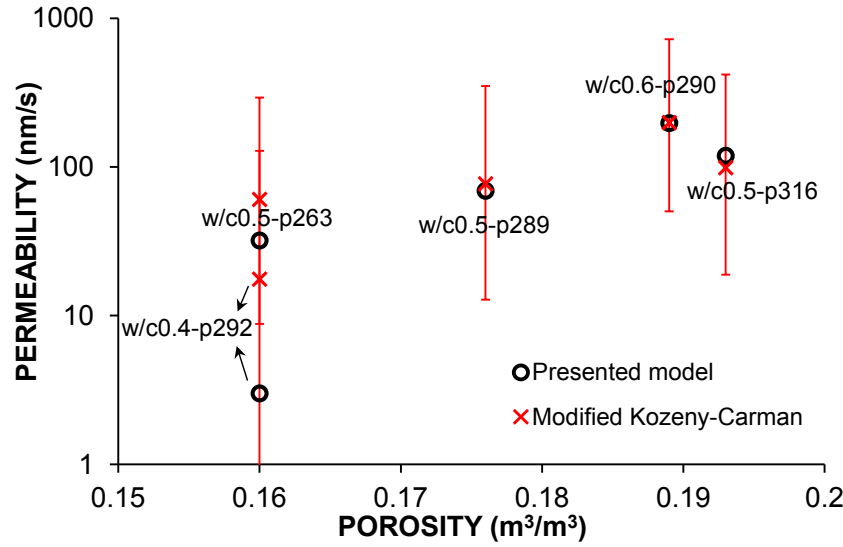
Fig. 3. 6. Comparison between the permeability values calculated with the model presented in this study and with the modified Kozeny-Carman model. The upper and lower limit of error bars refer to $\alpha_p=0.26$ and $\alpha_p=0.58$, respectively.

The numerator of eq. (3-26) gives the approximated total available surface area, where M_{cem} [kg/m^3] is the cement content of the concrete, F_B [m^2/kg] is the Blaine fineness of the cement, which was 315 m^2/kg in this study. The denominator of (26) gives the total volume of solids in the unit volume. The cross section of capillary tubes is assumed to be elliptic as used by Powers [35], leading to a value of 2.5 for F_s. The values of tortuosity is approximated by eq. (3-27) [193], by assuming that the hydraulic tortuosity is equal to the electric tortuosity as proposed in [193,194]:

$$F_{TH} = F_{TE} = n\frac{R_c}{R_f} \qquad (3\text{-}27)$$

where R_c [$\Omega \cdot$m] is the electrical resistivity of concrete and R_f [$\Omega \cdot$m] is the electrical resistivity of pore fluid. The concrete resistivity values were obtained from [195] by an empirical relationship which relates the resistivity to the aggregate content:

$$R_c = R_p \left(1 - (V_{agg}/V_t)\right)^{-1.5606} \qquad (3\text{-}28)$$

where R_p [Ω·m] is the electrical resistivity of paste which was reported to be around 1 Ω·m, 0.75 Ω·m, 0.5 Ω·m for w/c 0.3, 0.4, 0.5 respectively [195,196]. Having a decreasing trend for R_p with increased w/c, R_p for w/c 0.6 assumed to be 0.4 Ω·m. Electrical resistivity of pore fluid was assumed equal to 0.3 Ω·m [196,197]. The estimations for the afore-described coefficients of the modified Kozeny-Carman model are presented in *Table 3. 2*. The values of tortuosity are close to 2, a value which is normally used in the Kozeny-Carman equation [35,192]. As expected, the tortuosity increases when the w/c decreases, while the influence of different paste content on the tortuosity is only minor (as already mentioned in section 3.4.1).

Table 3. 2. Kozeny-Carman model coefficients for concretes with the same paste content and different w/c

Concrete	M_{cem} (kg/m^3)	n [m^3/m^3]	F_{TH} [(m/m)^2]	S_{app} [m^2/m^3]	α_c [m^3/m^3]	k (nm/s)
w/c0.4-p292	400	0.160	2.70	150000	0.131	18
w/c0.5-p263	320	0.160	2.14	120000	0.118	60
w/c0.5-p289	352	0.176	2.03	134563	0.130	77
w/c0.5-p316	385	0.193	1.94	150279	0.142	99
w/c0.6-p290	315	0.189	1.73	122349	0.131	199

As presented in *Fig. 3. 6*, the permeability results obtained with the present model are in a good agreement with the well-established modified Kozeny-Carman equation except for w/c0.4-p292, for which the modified Kozeny-Carman model (eq. (3-24)) predicts a much higher value. A (small) part of the observed difference could be related to the increased dosage of superplasticizer in w/c0.4-p292 (see *Table 3-A. 1* in Appendix 3-A), which could increase the viscosity of pore fluid [179], while in the calculations the viscosity of pore fluid for all concretes was assumed equal to the viscosity of pure water. According to *Fig. 3. 6*, the amount of stagnant water has a significant influence on the permeability of cementitious materials as estimated with Kozeny-Carman model; the experimental determination of the amount of stagnant water can be performed by a method presented in [35], which is however out of the scope of this study. It is worthwhile to mention that, although the value of permeability calculated with the modified Kozeny-Carman model is affected by the choice of α_s, the trend remains unchanged and it is in line with the trend of permeability values obtained from the model developed in this study.

An approach to determine permeability of fresh concrete based on the bleeding test was already proposed in the past by Powers [35] according to the sedimentation mechanism, i.e. based on the large strains approach. In the approach by Powers, the hydraulic gradient was expressed in terms of the unbuoyed weight of the solids. As shown in Appendix 3-B, when small strains are assumed, Powers' model becomes equivalent to the model presented here.

However, besides leading to the same results of permeability while being derived with a completely different approach (small vs. large strains), the model presented in this study still has two advantages. First, it needs as input the total density of the concrete, which includes the effect of air content and is easily measurable in a bleeding test, even if the mixture design and the density of components are not precisely known. On the contrary, Powers' approach requires the density of all components of the concrete as an input, with each of them prone to its determination error. Second, the approach presented here allows also determining bulk modulus based on the same bleeding test results.

3.5. Conclusions

In this study, the bleeding test was employed as a simple method to obtain early-age properties of cementitious materials: permeability and bulk modulus. These properties are key parameters for various aspects regarding the performance of early age concrete, e.g. water curing and plastic shrinkage.

The permeability was determined according to Darcy's law by writing the measured bleeding water flux as a function of the known gradient of total water potential. The robustness of the presented method was shown by comparing it to a modified Kozeny-Carman model according to Powers. The latter showed that the model developed in this study is sensitive not only to the changes in paste volume (which affect the total initial porosity only) but also to the changes in water-to-cement ratio (which affect both the total initial porosity and the pore structure).

Furthermore, by utilizing the permeability values in the one dimensional consolidation equation, and fitting the model to the experimental data obtained by standard bleeding test, the evolution of bulk modulus was obtained. The presented numerical model for obtaining the evolution of bulk modulus from bleeding measurements is extremely useful, since the available methods are not able to capture the evolution of bulk modulus before setting.

Acknowledgements

This page is intentionally left blank.

This page is intentionally left blank.

Chapter 4. Susceptibility of Portland cement and blended cement concretes to plastic shrinkage cracking[3]

Abstract

The market share of different types of blended cements is increasing year by year. Generally, blended cements are ground to higher fineness and exhibit a slower development of mechanical properties compared to Ordinary Portland Cement (OPC), which might affect the concrete performance in terms of shrinkage cracking at early ages.

In this study, the performance of concretes made with different cement types are compared according to the ASTM C1579-13 standard for plastic shrinkage cracking. The cracking behavior was further correlated to the deformations of both unrestrained and restrained specimens measured by a 3D image correlation system. The main factors influencing the cracking behavior were discussed based on poromechanics. It is concluded that the bulk modulus evolution has a dominant effect on controlling the plastic shrinkage cracking. Concretes made of more reactive cements, in particular with higher clinker content, are less susceptible to plastic shrinkage cracking. For cements with the same clinker content, increasing the cement fineness reduces the risk of plastic shrinkage cracking.

Keywords: Cement type; Blended cement; Plastic shrinkage cracking; Bulk modulus; Fineness; Capillary pressure

4.1. Introduction

Fresh concrete undergoes rapid volumetric deformations, also referred to as plastic shrinkage, directly after casting until the time of final set. Plastic shrinkage encompasses two regimes: saturated and unsaturated. In saturated regime, plastic concrete before set undergoes self-weight consolidation. Further, in unsaturated regime, drying of surfaces leads to buildup of capillary pressure in the pores. The action of capillary pressure leads to both vertical and horizontal deformations. When concrete is restrained, deformations may result in cracking. Cracking facilitates the ingress of harmful species through both diffusion and advection and consequently may reduce the service life of concrete structures [77].

Driven by concerns about the CO_2 emissions of cement production [198], the addition of mineral additives such as limestone, fly ash and blast-furnace slag to Ordinary Portland

---

Cement (OPC) clinker and the production of blended cements with decreasing clinker content are increasing year by year. To overcome the slow development of mechanical properties of blended cements, they are often ground to higher fineness than OPC [44].

Only a few studies have investigated the effect of the physical properties of cement, and in particular their fineness, on plastic shrinkage cracking. The use of fine cements or the addition of fillers with small particle size (in particular silica fume [32,199]) may increase the risk of plastic shrinkage cracking due to the smaller pore size and associated higher capillary pressure in the fresh concrete. When cements with high fineness were used, the total bleeding water and the bleeding rate decreased [66,67]. For concretes with water-to-cement ratio (w/c) 0.4, 0.5 and 0.6 in environmental conditions with free water evaporation rate 0.1 kg/m^{2}h, substitution of cement with fly ash of higher fineness decreased the horizontal plastic shrinkage due to the increased bleeding rate [68]. For mortars with equal w/c 0.35 and 0.45, inclusion of ground granulated blast furnace slag with higher fineness increased the bleeding rate and the bleeding capacity (i.e., the total amount of bleed water) [69]. Contrary to the abovementioned findings, other researchers found that the bleeding capacity decreased in blended-cement concretes containing fly ash, silica fume and blast furnace slag [70]. In a study by Slowik et al. [71], it was observed that increasing the fineness accelerated the air entry time for cement pastes with w/c of 0.26. Further, increasing the fineness decreased the vertical deformation and increased the developed capillary pressure. It was observed that both the magnitude of plastic shrinkage [72] and the total area of plastic shrinkage cracks [70] increased in blended-cement concrete compared to OPC concrete. The latter increase in plastic shrinkage cracking attributed to the lower bleeding and higher rate of evaporation noted in blended cement concretes [70]. Lura et al. [73] concluded that when cements of different mineralogical composition but similar fineness are employed, the influence of the cement type on the risk of cracking is small. In a recent study, authors concluded that increasing the cement fineness reduces the maximum crack width [74].

Another important factor in studying plastic shrinkage is the evolution of mechanical properties due to hydration of cementitious materials, which directly impacts the elastic properties and the strength of the concrete. It has been observed that retarding cement hydration increases plastic shrinkage cracking [58,76]. Furthermore, it appears that concrete with lower w/c and higher cement content is less susceptible to plastic shrinkage cracking due to the fast evolution of mechanical properties [200].

From this concise literature review it appears that no systematic study on the susceptibility of different cements (OPC and blended cements) to plastic shrinkage cracking, considering both

of the roles of cement fineness and evolution of mechanical properties, has been published so far.

Since the deformations are the source of cracking in plastic concrete, it is paramount to accurately measure the deformations, both for obtaining a better understanding about the acting mechanisms and for prescribing appropriate and effective mitigation methods. Several methods have been utilized in the literature for measuring plastic shrinkage (see *Table 4. 1*). One main drawback of several of the methods listed in *Table 4. 1*, items **d** to **p**, is that when embedded probes, studs, sensors or external grids are used, the measurements are not reliable due to improper bond between the measuring system and the still workable concrete [90]. The mentioned problems led to the development of new non-contact, optical methods, which have the advantage of limiting or fully avoiding the disturbance to the fresh concrete. Nemoz-Gaillard et al. [90] used a 2D image correlation system to study the effect of glass fibers on plastic shrinkage cracking. The limitation of the utilized method was that single measurements in the horizontal direction only were performed. In 2D image correlation systems, a single camera is used and only the in-plane deformation is measured. Furthermore, the light refraction caused by bleeding water was not taken into account in the image correlation analysis; this can induce artifacts that will inevitably affect the obtained deformations (see Chapter 2). Messan et al. [91] used a 2D image correlation system to measure strain development of mortars containing cellulose ether during the first 25 h after casting. Since the specimens were bleeding-free, refraction did likely not influence their measurements.

In the present study, a 3D image correlation system was utilized, allowing for both in-plane and out-of-plane strain measurements simultaneously. Furthermore, the refraction problem was avoided through a contrivance based on a method proposed in [15], by using a small and light wire mesh sitting on the concrete surface (see *Fig. 4. 4*). The detailed description of the setup is provided in the methods section of this study (see *Fig. 4. 2*). The deformations are linked to the final crack widths obtained by ASTM C1579-13 [132] test where the crack width after conclusion of the tests is measured on high-resolution photographs. The susceptibility of concrete mixtures to plastic shrinkage cracking is discussed utilizing a poromechanical approach.

Table 4. 1. Classical methods for measuring the horizontal and vertical plastic shrinkage

Item	Researchers	Method	Deformation
a	Powers [35]	Displacement of disk seated on surface monitored in vertical direction by micrometer microscope	vertical
b	Mangat and Azari [99]	ASTM C827 [201], magnified image of indicator ball on surface of specimen produced by projected light source cast on displacement-indicating chart. Surface displacement measured by comparing magnified images	vertical
c	Qi et al. [49,50], Kaufmann et al.[84], Lura et al. [17], Leemann et al. [77]	Surface displacements measured by laser sensors	vertical
d	Ravina and Shalon [29,100]	Movement of studs inserted in both ends of mold measured with mechanical gauges	horizontal
e	Cromarty and Bryden [101] and Orr and Haigh [102]	Mortar samples externally connected to linear transducer and micrometer	horizontal
f	Gowda [103] and Scholer [104]	Mortar samples connected to magnetic proximeter and probe. Voltage change linked to shrinkage	horizontal
g	Jasiczak and Szymański [105]	Potentiometer and relocating sensor embedded in mortar samples. Change in electrical current linked to length change	horizontal
h	Several researchers [106–109,98,72,110]	Movement of embedded objects (e.g. strips, pins) measured by Linear Variable Differential Transformers (LVDTs)	horizontal
i	Sanjuan et al. [111–115]	Displacement measured by extensometers located on steel plate and connected to other steel plate by steel rod	horizontal
j	Slowik et al. [116] and Wong et al.[117]	Embedded Fiber Bragg gratings used to measure displacements	horizontal
k	Hanehara et al. [118] and Baba et al.[119]	Embedded strain gauges used to measure displacements	horizontal
l	Marioka et al. [120] and Bühler and Zurbriggen [121]	Movement of embedded pins or surface lightweight reflectors monitored by laser sensors	horizontal
m	Kronlöf et al. [75], Holt et al. [122,123] Hammer et al. [124,125]	Movement of embedded nails measured by LVDTs	vertical and horizontal
n	Ghoddusi and Javid [126]	Reflection of laser beam on tips of embedded studs correlated to displacements	vertical and horizontal
o	Turcry, A. Loukili [127] and Liu et al.[128]	Laser sensors used to monitor movement of embedded pins and reflecting plate for horizontal and vertical deformation, respectively	vertical and horizontal
p	Fontana et al. [129]	Laser sensors used to measure vertical surface displacements and LVDTs used to measure horizontal movement of embedded pins	vertical and horizontal

4.2. Materials and methods

4.2.1. Materials

Ten types of cement were tested with the characteristics shown in *Table 4. 2*, *Table 4. 3* and *Fig. 4. 1*. The actual clinker contents in *Table 4. 2* were obtained by QXRD measurements according to *Table 4. 3*. The mixture compositions of the concretes are presented in *Table 4. 4*. The name of the concrete mixtures reflects the cement type used according to EN 197-1 [202]. For CEM I 42,5 N and CEM II/A-LL 42,5 N, cements from two different plants were tested, which is indicated by numbers 1 and 2 after the standard name. The alluvial sand and gravel used as aggregates were added as separate fractions (by mass of all aggregates, 0–1 mm: 31%, 1–4 mm: 19%, 4-8 mm: 20%, 8–16 mm: 30%). A polycarboxylate-based

superplasticizer was added in an amount allowing for obtaining similar workability for all analyzed mixtures. The paste volume and w/c were kept constant, accounting for differences in density of cements, leading to a small change in the cement content per m^3 of concrete. Prior to concrete mixing, all components were stored at 22 ± 2 ˚C, the same temperature at which concrete production took place. After premixing cement and dry aggregates, 90% of the mixing water was added. The rest of the mixing water was poured into the mixer together with the superplasticizer. The concrete was mixed within 90-180 s in a 80 l pan-type Eirich mixer. The produced concrete quantity for each test was 80 l.

Table 4. 2. Characteristics of tested cements

Cement type (according to EN 197-1[202])	Density (kg/m^3)	Blaine fineness (m^2/kg)	Normative composition (%-mass)	Actual clinker content normalized per powder without gypsum (%-mass)	Actual clinker content of the cement (%-mass)
CEM I 42,5 N-1	3120	363	Portland cement clinker 95-100 %	94.7	89.5
CEM I 42,5 N-2	3130	319	Portland cement clinker 95-100 %	95.1	91.6
CEM II/A-S 42,5 R	3100	379	Portland cement clinker 80-94 %, blast furnace slag 6-20 %	86.1	79.0
CEM II/A-LL 42,5 N-1	3050	427	Portland cement clinker 80-94 %, limestone 6-20 %	80.2	76.5
CEM II/A-LL 42,5 N-2	3070	391	Portland cement clinker 80-94 %, limestone 6-20 %	83.9	79.0
CEM II/B-M (S-T) 42,5 R	3060	421	Portland cement clinker 65-79 %, blast furnace slag and burnt oil shale 21-35 %	68.4	67.0
CEM II/B-M (T-LL) 42,5 N	3040	404	Portland cement clinker 65-79 %, burnt oil shale and limestone 21-35 %	75.1	73.0
CEM III/A 42,5 N	3020	385	Portland cement clinker 35-64 %, blast furnace slag 65-36 %	54.8	51.8
CEM III/B 42,5 N	2960	466	Portland cement clinker 20-34 %, blast furnace slag 80-66 %	29.1	28.5
CEM III/B 32,5 N	2940	415	Portland cement clinker 20-34%, blast furnace slag 80-66 %	30.1	28.0
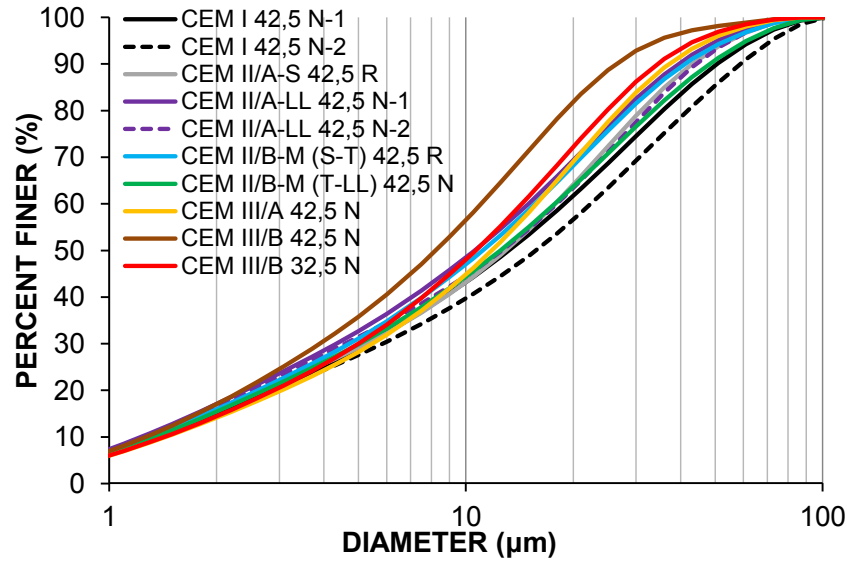
Fig. 4. 1. Particle size distribution of the cements

Table 4. 3. Cement components (including clinker phases obtained by QXRD and other components)

Cement	C_3S	C_2S	C_3A	C_4AF	Gypsum	Limestone	Slag	Kiln dust	Other
CEM I 42,5 N-1	65.3	9.8	4.7	9.8	5.3	-	-	5.0	-
CEM I 42,5 N-2	66.8	9.5	11.0	4.3	3.7	3.7	-	1.0	-
CEM II/A-S 42,5 R	57.6	8.2	9.5	3.7	4.0	-	12.8	-	-
CEM II/A-LL 42,5 N-1	55.8	8.4	4.0	8.4	4.6	14.8	-	4.0	-
CEM II/A-LL 42,5 N-2	59.3	6.2	4.9	8.6	4.6	13.6	-	1.6	-
CEM II/B-M (S-T) 42,5 R	48.9	7.3	3.5	7.3	2.3	-	18.3	-	12.6
CEM II/B-M (T-LL) 42,5 N	53.2	8.0	3.8	8.0	2.7	10.8	-	-	13.4
CEM III/A 42,5 N	37.8	5.4	6.2	2.4	4.3	2.0	40.2	-	0.6
CEM III/B 42,5 N	20.8	3.0	3.4	1.3	-	1.5	67.6	-	0.4
CEM III/B 32,5 N	20.4	3.1	1.5	3.1	6.8	-	65.0	-	-

Table 4. 4. Mix design of tested concretes

Concrete	Cement (kg/m³)	water (kg/m³)	Sand [0-4 mm] (kg/m³)	Gravel [4-16 mm] (kg/m³)	Superplastic-izer (kg/m³)	w/c (-)	Estimated density (kg/m³)
CEM I 42,5 N-1	352	176	927	928	1.056	0.5	2384
CEM I 42,5 N-2	353	177	927	928	0.988	0.5	2386
CEM II/A-S 42,5 R	350	175	927	928	1.258	0.5	2381
CEM II/A-LL 42,5 N-1	348	174	927	928	1.253	0.5	2378
CEM II/A-LL 42,5 N-2	348	174	927	928	1.183	0.5	2378
CEM II/B-M (S-T) 42,5 R	348	174	927	928	1.362	0.5	2378
CEM II/B-M (T-LL) 42,5 N	347	174	927	928	1.215	0.5	2377
CEM III/A 42,5 N	347	174	927	928	1.323	0.5	2377
CEM III/B 42,5 N	346	173	927	928	1.28	0.5	2375
CEM III/B 32,5 N	343	172	927	928	1.366	0.5	2374

4.2.2. Methods

Flow and slump of concretes were measured right after concrete production according to EN 12350-5 [203], EN 12350-2 [204], respectively. Bleeding was determined according to EN 480-4 [205]: 10 min after producing the concrete, a cylindrical steel vessel with diameter 250 mm and height 250 mm was filled with concrete and the concrete was compacted using a needle vibrator. Since the cylinder has known volume (12 l), the density of the fresh mixture can be obtained at the same time by determining the mass of the filled cylinder. The vessel was covered by a lid to prevent evaporation and was moved to the plastic shrinkage test room to store the sample in the same temperature as the plastic shrinkage test. The bleeding water was collected with a pipette after 15, 30 and 60 min and afterwards every hour after mixing. The last measurement took place six hours after mixing.

The susceptibility of the concrete mixtures to plastic shrinkage cracking was measured according to ASTM C1579-13 [132] (see *Fig. 4. 2*). The evaluation is performed by comparing the developed average crack widths. At each test, two restrained samples of size $560 \times 355 \times 90$ mm^3 with stress risers per concrete mixture were tested (see *Fig. 4. 2* and *Fig. 4. 3*). A stress riser is an object which restrains the concrete leading to the incompatibility of deformations and cracking as explained in *Fig. 4. 14*. In addition to two specimens with stress risers, a third specimen for free-shrinkage measurement of size $560 \times 225 \times 100$ mm^3 was prepared. The molds were filled with concrete on a vibrating table (vibration time 10-12 s) and the top surface was finished using a darby tool. According to ASTM C1579-13, the temperature must be maintained at 36 ± 3 °C, the relative humidity must be 30 ± 10 %, and the wind velocity must be sufficient to maintain the minimum evaporation rate for free water (1 kg/m^{2}h) during the test. Therefore, a climate-controlled chamber was used to maintain stable temperature and humidity conditions (33 ± 1 °C and 38 ± 8% RH) and sufficient wind velocity during the measurements. An air blower was used to produce a wind speed of 7.5 ± 0.5 m/s over the top surface of the specimens, blowing in a channel purposefully designed to obtain uniform wind speed on the specimens [206]. The measured evaporation rate of pure water in the mentioned environment was higher than 1 kg/m^{2}h, the minimum specified evaporation rate for free water. The capillary pressure development was monitored by pressure sensors connected to capillary pipes mounted at the bottom of the free deformation sample. The temperature evolution was monitored by thermocouples of resolution ± 0.1 ºC mounted on the free-deformation sample: two thermocouples at the bottom of the free sample and two at about 10 mm from the top surface. Additionally two thermocouples were utilized for measuring the air temperature directly above the surface of the samples. The relative

humidity of air was monitored by a relative humidity sensor. The evaporation rate was monitored by recording the mass change of the free-deformation sample.
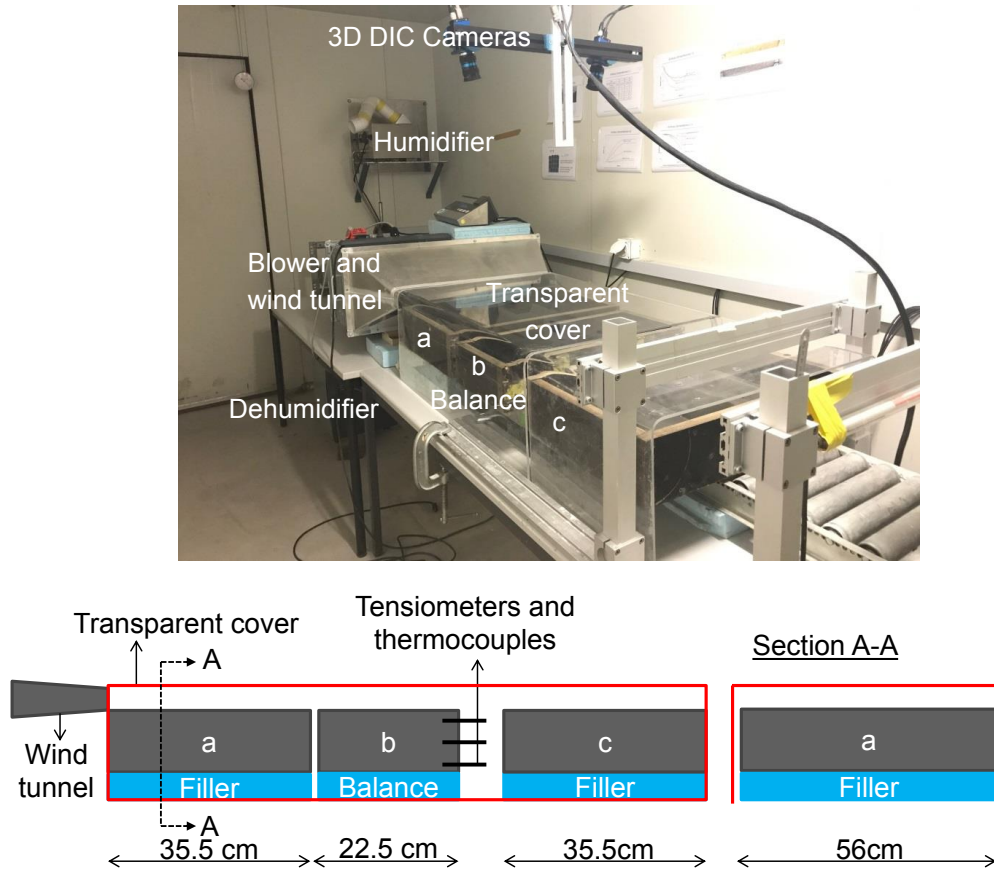
Fig. 4. 2. Climate controlled chamber and plastic shrinkage test setup. a and c are restrained samples according to ASTM C1579-13 [132], and b is an unrestrained sample for measuring mass change, free shrinkage, capillary pressure and temperature evolution
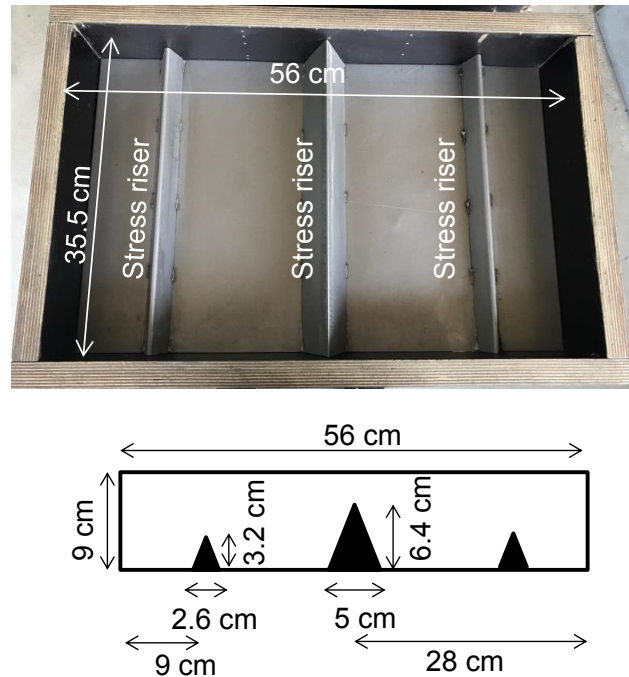
Fig. 4. 3. Restrained mold according to ASTM C1579-13 [132]

A 3D Digital Image Correlation (DIC) system was used to measure deformations. 3D correlation allows for measuring the in-plane and out-plane deformations simultaneously. In this method, images of the area of interest are taken at predefined time intervals (e.g. 5 min here) by two 8-Megapixel cameras. According to the intensity of the reflected light by the surface of the target, each pixel stores a grey scale value ranging from 0 to 255 [130]. For measuring the deformations, the gray patterns of subset of pixels on the reference image are compared with the same on the deformed specimen by a software. The displacement result, expressed in the center point of the subset, is an average of the displacements of the pixels inside the subset. In this study, the target was a small pattern drawn on miniature wire meshes (*Fig. 4. 4*) placed at the top surface of the concrete directly after casting [15]. The latter allows to measure the deformation of concrete while avoiding the refraction effect, since the mesh keeps the pattern above the bleeding water layer. Furthermore it allows for maintaining constant reflected light intensity, since the drying of the wet concrete surface affects the surface color and consequently it changes the subset properties. In a restrained concrete sample, the patterned meshes were placed at opposite sides of the stress riser for determining in particular the deformations leading to crack formation. In the unrestrained sample, the meshes were placed along the longitudinal axis for determining the free shrinkage deformations (see *Fig. 4. 4*). The vertical deformation was measured by monitoring the vertical deformation of wire meshes on the free sample. Based on the average mass of the wire meshes (2.37 g) and contact area between wire mesh and concrete surface (12×10^{-5} m^2), the applied pressure by a wire mesh was about 0.2 kPa, which is negligible compared to the pore pressure resulting from environmental conditions (see *Fig. 4. 12*). No settlement of the wire meshes into the concrete was observed.

Each experiment lasted for 6.5 ± 0.5 hours after mixing time; the crack widths were measured at the end of the experiments. For measuring the crack width, multiple high resolution pictures (2413 ± 50 dpi) of the crack along its length were taken. The crack width was then determined on the images by measuring the width with resolution of 0.01 mm at 10 ± 1 mm intervals along the length of the crack. To avoid possible effects of mold boundaries on measured crack widths, the 25 mm of the cracks next to the edges of the molds were not taken into account [132].
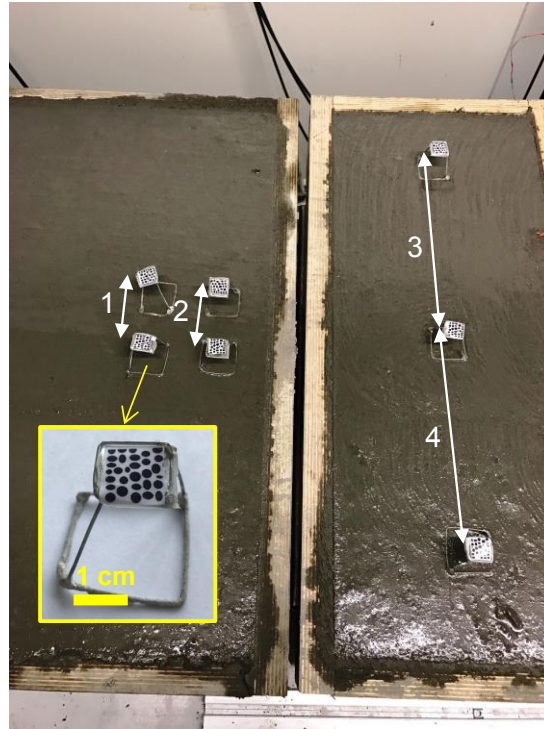
Fig. 4. 4 . Wire meshes placed on the concrete surface across and above the stress riser (working as virtual strain gauges 1&2) for measuring across-crack deformation, or placed in the mold without stress riser for measuring free shrinkage (strain gauges 3&4). The insert shows the wire mesh in detail.

4.2.3. Statistical data analysis

In order to explain the effects of different properties of cement and mix compositions on deformations and cracking of concretes, a standard statistical analysis was performed. The linear correlations between experimentally-determined quantities, i.e. deformations and crack widths, and between crack widths and cement or concrete properties have been quantified by means of Pearson's correlation coefficient r.

To assess the significance of the effect of different cement or concrete properties on crack widths, a multiple linear regression model was used [207]. In this model, crack widths were considered as dependent variables, whereas different parameters of cement or concrete were considered as explanatory variables. Couplings between all explanatory variables were assumed. The significance of the explanatory variables was quantified by means of P-values obtained from testing the null-hypothesis of no significant effect of a given variable or set of variables.

4.3. Results

4.3.1. Bleeding

Fig. 4. 5 shows the experimentally-determined bleeding development as a function of time for all concretes. An initial steep branch with almost constant bleeding rate is followed by a plateau, which indicates the final setting time and is dominated by stiffening of the concrete that arrests bleeding (see Chapter 3). The coefficient of permeability (simply called permeability in this study) of the fresh mixtures was calculated according to the method presented in Chapter 3. The method is based on assuming that the initial, constant bleeding rate is equal to the flux of pore fluid in the concrete that feeds the bleeding water. The latter can be described with Darcy's law. Thus, by substituting the experimentally-determined bleeding rate to Darcy's law, the permeability can be conveniently determined. In this study, the required bleeding rate was obtained from *Fig. 4. 5* and is shown in *Table 4. 5*. According to the calculated data, CEM I 42,5 N-2 had the highest permeability, probably due to coarser cement particles, (see *Fig. 4. 1*) (manifested also by the relatively low Blaine fineness of 319 m^2/kg). Concretes with other cements show similar rate of bleeding and consequently similar values of permeability were found, even though considerable differences between the fineness of different cements were shown in *Fig. 4. 1*. It is however worthwhile to mention that the liquid permeability may also be affected by the viscosity of the pore fluid, that may have been affected differently by different cements and by the different amount of superplasticizer (see Chapter 3).

As long as the initial bleeding rate is governed by the permeability according solely to Darcy's law, the total amount of bleeding water is affected also by the stiffening of the mixture that leads to a reduction of the bleeding rate in accordance with Terzaghi's description of the consolidation process [26]. This is based on assuming that the volume of bleeding water is equal to the volumetric deformation that fully translates into vertical deformation in a consolidation process. Therefore, by fitting the experimentally-obtained bleeding curve with the one-dimensional Terzaghi's consolidation equation [26], the evolution of the bulk modulus of the medium can be estimated. This method is described in detail in Chapter 3.

Similarly as in Chapter 3, the exponential function proposed originally by Josserand et al. [154] was used to approximate the evolution of bulk modulus in time (B [Pa]): $B=B_0\exp(t/t^*)$, where B_0 [Pa] is the initial bulk modulus and t^* [s] is the characteristic time of bulk modulus evolution, correlated to the kinetics of the initial stages of cement hydration. Since the goal

was to compare the evolution of bulk modulus of concretes, it is assumed that all concretes have the same initial bulk modulus, due to identical paste and aggregate content. The initial bulk modulus was taken equal to 50 kPa, a value close to the value determined in Chapter 3 for a fresh concrete. The characteristic times of bulk modulus evolution obtained from fitting the experimental data (see Chapter 3 for details) are presented in *Table 4. 5*. Please note that a smaller characteristic time means a faster evolution of bulk modulus.
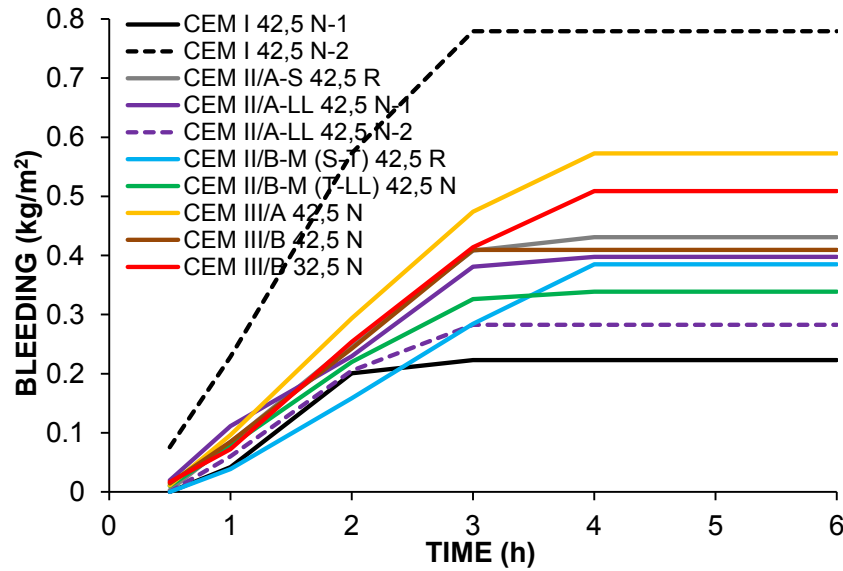
Fig. 4. 5. Experimental results of bleeding test

Table 4. 5. Experimental results from the bleeding test and density and calculated permeability and characteristic time of bulk modulus evolution (see Chapter 3)

Concrete	bleeding rate (kg/m²h)	Measured density (kg/m³)	Permeability (m/s)	Characteristic time of bulk modulus evolution (min)
CEM I 42,5 N-1	0.134	2316	2.82×10^{-8}	19
CEM I 42,5 N-2	0.331	2338	6.86×10^{-8}	43
CEM II/A-S 42,5 R	0.165	2321	3.46×10^{-8}	41
CEM II/A-LL 42,5 N-1	0.162	2355	3.31×10^{-8}	37
CEM II/A-LL 42,5 N-2	0.145	2340	3.00×10^{-8}	26
CEM II/B-M (S-T) 42,5 R	0.12	2352	2.46×10^{-8}	45
CEM II/B-M (T-LL) 42,5 N	0.142	2306	3.01×10^{-8}	30
CEM III/A 42,5 N	0.188	2354	3.85×10^{-8}	51
CEM III/B 42,5 N	0.158	2332	3.29×10^{-8}	38
CEM III/B 32,5 N	0.182	2334	3.79×10^{-8}	45
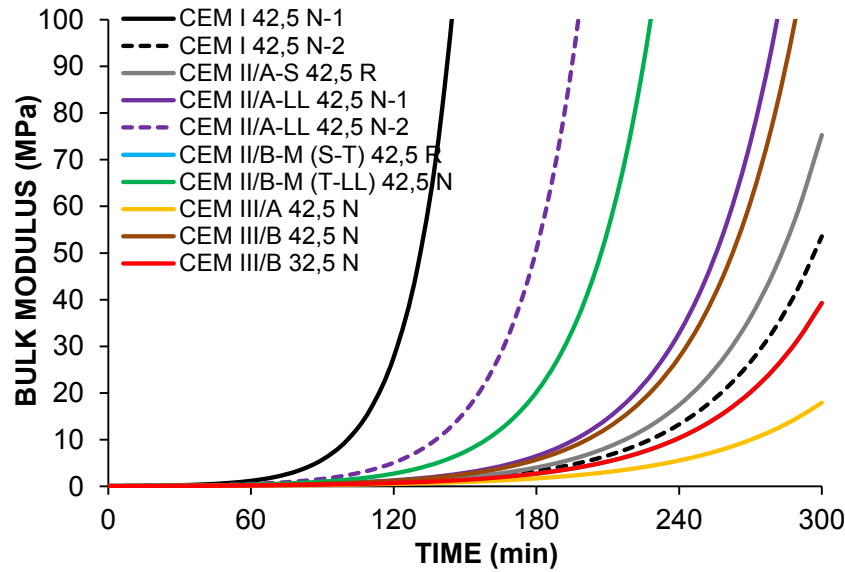
Fig. 4. 6. Simulated evolution of bulk modulus for tested concretes, according to Chapter 3

According to *Fig. 4. 6*, the evolution of bulk modulus does not depend only on cement type. For example, CEM III/B 42,5 N had 28.5% clinker content but showed faster evolution of bulk modulus compared to other cements with higher clinker content due to its higher fineness (466 m^2/kg). It is noted that the latter cement does not contain any gypsum (see *Table 4. 3*), which may lead to rapid hydration of C$_3$A [208]. Indeed, the evolution of bulk modulus agrees well with the evolution of the early hydration processes, as indicated also by the temperature evolution in *Fig. 4. 7* and by the estimated length of the dormant period in *Table 4. 6*.

4.3.2. Temperature evolution

Fig. 4. 7 shows the temperature evolution in the concrete mixtures during the plastic shrinkage test. The initial temperatures of the mixing water and of the fresh concretes were 20±1 ˚C and 22±2 ˚C, respectively. The curve WATER shows the temperature evolution of pure water placed in the same environment; the water temperature initially increased at a progressively lower rate, due to the competing effects of the higher room temperature and cooling due to evaporation. The water temperature then stabilized at around 25˚C, which is a couple of degrees higher than the dew point temperature of 22˚C for the test room environment, *T*=33˚C and *RH*=50%. In the beginning, the temperature of all concretes increased at a progressively lower rate, similarly to pure water. However, after a couple of hours the temperature started to increase in the concrete mixtures due to cement hydration entering the acceleration period. In order to determine the start of the acceleration period (or in other words the end of dormant period), the inflection point of the temperature evolution curves were calculated and are shown in *Table 4. 6*. The latter is in line with the data

provided in *Table 4. 5*: concretes with longer dormant period also had slower evolution of bulk modulus (estimated with the higher values for the characteristic hydration time calculated from the bleeding results).
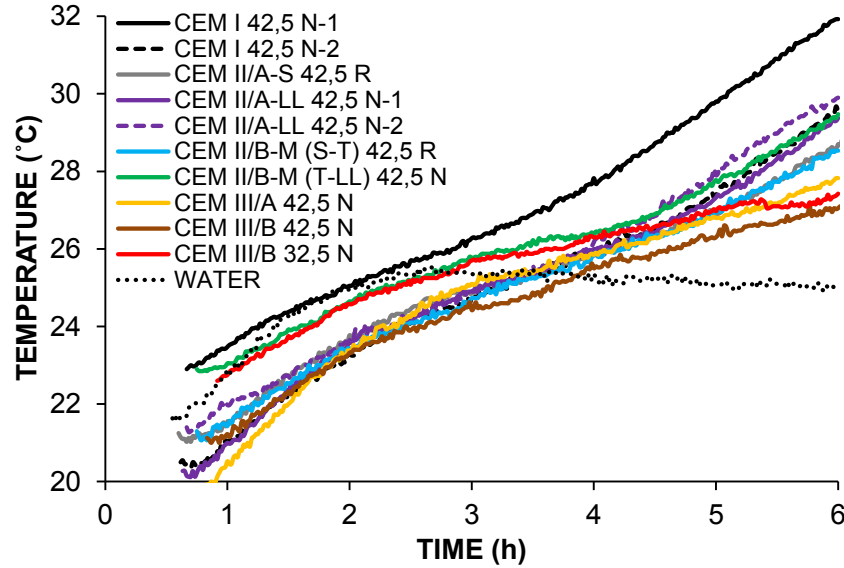
Fig. 4. 7. Temperature development of concretes in the plastic shrinkage test

Table 4. 6. Dormant periods obtained from the inflection points of the temperature evolution curves

Concrete	Dormant hydration period duration including the pre-induction period (h)
CEM I 42,5 N-1	2.50
CEM I 42,5 N-2	3.57
CEM II/A-S 42,5 R	3.42
CEM II/A-LL 42,5 N-1	3.65
CEM II/A-LL 42,5 N-2	2.95
CEM II/B-M (S-T) 42,5 R	3.88
CEM II/B-M (T-LL) 42,5 N	3.62
CEM III/A 42,5 N	3.98
CEM III/B 42,5 N	3.32
CEM III/B 32,5 N	3.82

4.3.3. Deformations

Since the shrinkage induced by the capillary pressure is the source of plastic shrinkage cracking [17,30,71,138,156], the deformations from the onset of the capillary pressure manifested by the horizontal shrinkage initiation point were investigated in this study. The results are reported in *Fig. 4. 8* to *Fig. 4. 10*. High fluctuations were observed in the measured vertical deformation, probably due to the presence of large aggregates. As shown in next Chapter and in another study [209], it has been observed that the scatter was substantially lower for mortars.
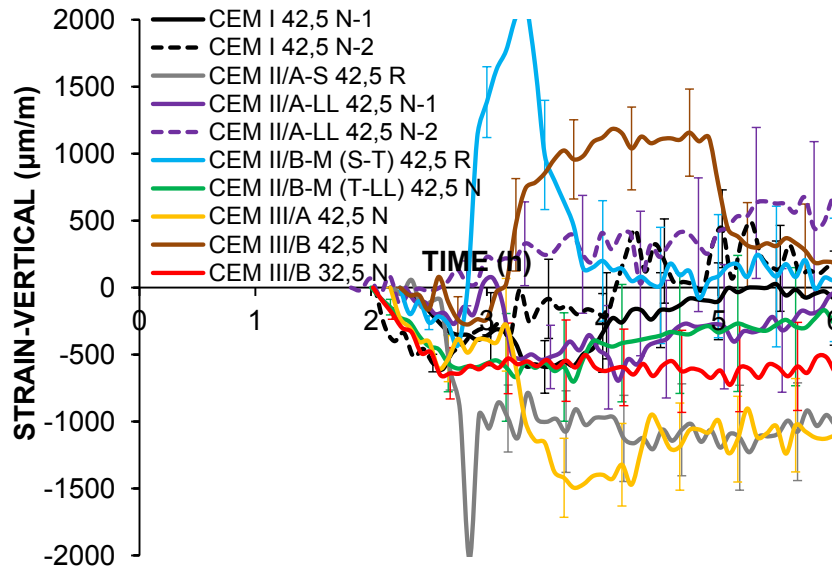
Fig. 4. 8. Vertical deformations of free specimens. The bars show the standard deviation obtained from three points on the same sample.
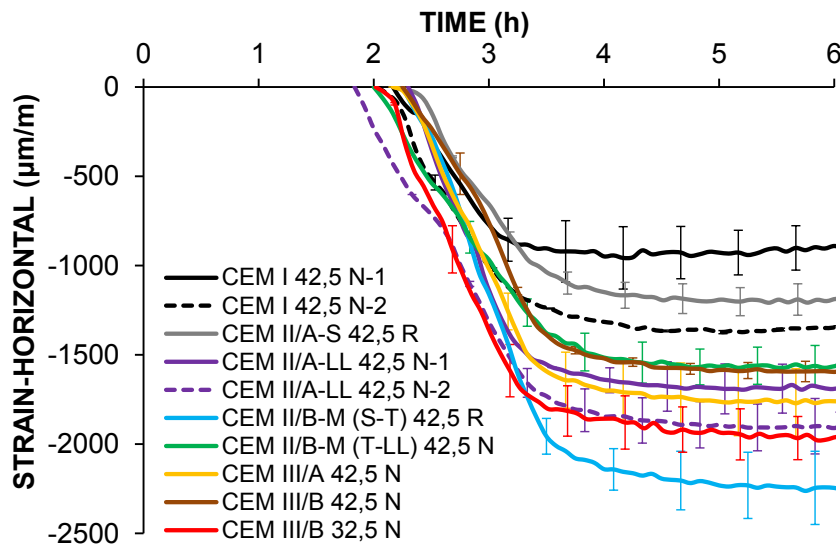
Fig. 4. 9. Horizontal deformations of free specimens. The bars show the standard deviation obtained from two positions measured on the same sample.

In *Fig. 4. 10*, the sudden jump in the horizontal deformation measured across the crack happens when the crack originating at the stress riser propagates to the surface. Afterwards, the crack opens steadily until it reaches a plateau starting around final set, when the rate of both the horizontal and the vertical deformation slow down considerably.
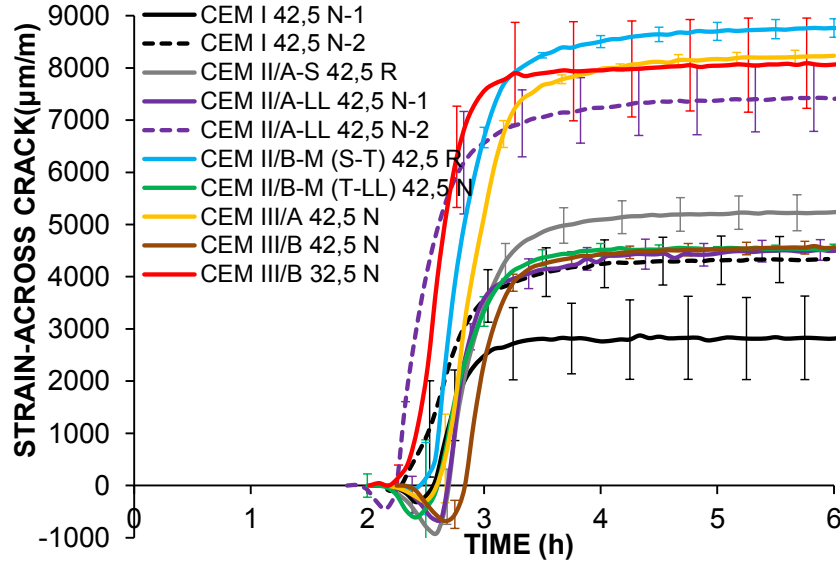
Fig. 4. 10. Horizontal deformations measured across the crack in the restrained specimens. The bars show the standard deviation obtained from two positions measured on the same sample

4.3.4. Evaporation rate

The evaporation rates are shown in *Fig. 4. 11*, calculated using mass loss data by Origin software and applying the Savitzky-Golay smoothing of polynomial order 2 and points of window 100. The initial evaporation rates are in the range 0.45-0.65 kg/m^2 h. The initial evaporation rate in the constant rate period depends on several factors, including surface and air temperature, air relative humidity, wind velocity, porosity and mean value of pore radius [37]. The predicted evaporation rate for the environment of this study according to the ACI 305R-10 nomograph [33] is indeed around 0.5 kg/m^{2}h, which lies in between the measured initial evaporation rates. The initial constant rate period was followed by the falling rate period, that started 2.5 to 4 h after mixing. This transition in evaporative regimes is primarily due to the increased air entry value and reduced pore size resulted by cement hydration. Furthermore after the air entry, the effective permeability (kk_r [m/s]) starts to decrease, due to the unsaturation of concrete, and consequently according to the Darcy-Buckingham's law [210] (eq. (4-1)) the evaporation rate decreases:

$$e = -\frac{kk_r}{\rho_w g}\left(\frac{\partial p}{\partial z} + \rho_w g\right) \tag{4-1}$$

where *e* [m/s] is the evaporation rate, *k* [m/s] is the saturated coefficient of permeability, k_r [-] is the relative permeability, *p* [Pa] is the pore pressure, ρ_w [kg/m^3] is the water density and *g* [m/s^2] is the gravity acceleration. Furthermore it is pointed out that a faster hydration accelerates the pore size reduction which leads to faster reduction of intrinsic permeability.

Also it accelerates the evolution of bulk modulus. According to the one-dimensional consolidation equation, a faster evolution of concrete stiffness accelerates the pore pressure development (see Chapter 3) or the desaturation and consequently it leads to faster reduction of effective permeability and shorter constant rate period.

By comparing *Fig. 4. 11* and *Fig. 4. 10*, it can be understood that cracking occurred during the constant evaporation rate period some time after the initial setting, when the capillary pressure develops rapidly due to the increasing stiffness.
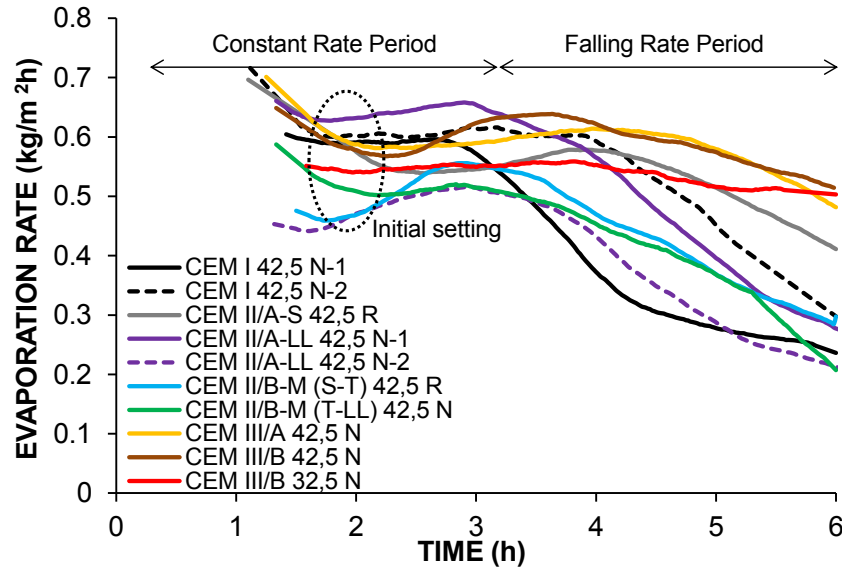
Fig. 4. 11. Evaporation rate vs. time. Initial setting was estimated to occur at a time instant when pore pressure development started.

4.3.5. Pressure development

Fig. 4. 12 shows the change in pore pressure after the initial setting. Due to the low accuracy of the pressure sensors (±6 kPa) and their positions (bottom of the mold), it is not possible to distinguish different trends in pore pressure evolution. The results allow however to follow a general trend of pressure development. The initial value of pressure at the bottom of the container is positive, indicating the presence of pore pressure derived from evaporative flux and self-weight. Then concrete consolidates tending to decrease the pore pressure. For cementitious materials, the evolution of stiffness accelerates the consolidation, according to the one dimensional consolidation equation (see Chapter 3). With growing stiffness, the concrete cannot deform enough to provide water for evaporation. Therefore menisci radius on top of concrete decreases and capillary pressure develops (negative pore pressure) [71]. The latter is followed by decreased pore size and permeability reduction resulted by hydration. At this point, the evaporative demand leads to further pressure reduction while evaporation rate starts to decrease. The end point of the curve is when air penetrates the sensor. This depends on the local condition where the capillary tube connects to the pressure sensor, see also [71].

The capillary pressure increased before the end of the constant rate period around 2 h after mixing, followed by an accelerated evolution due to bulk modulus evolution and reduction of pore sizes due to cement hydration.
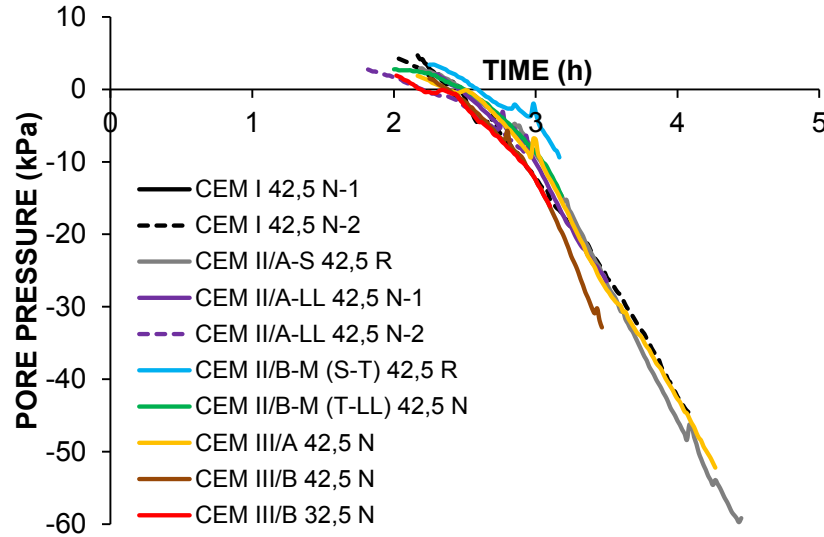
Fig. 4. 12. Capillary pressure development at the bottom of the molds

4.3.6. Crack width

Fig. 4. 13 and *Table 4. 7* show the crack width cumulative frequency and the average crack widths and total crack areas, respectively; the crack widths were measured at 6.5 ± 0.5 hours after mixing with the method described in section 4.2.2. CEM I 42,5 N-1 had the smallest crack width, with all blended cements showing wider cracks. CEM I 42,5 N-1, with higher fineness, had smaller crack width than CEM I 42,5 N-2. Also CEM III/B 42,5 N showed smaller crack width compared to other CEM III concretes made with cement of lower fineness.

Table 4. 7. Average crack width and total crack area

Concrete	Average crack width (mm)	Average total crack area (mm^2)
CEM I 42,5 N-1	0.316±0.016	101±5
CEM I 42,5 N-2	0.526±0.037	168±12
CEM II/A-S 42,5 R	0.509±0.015	163±5
CEM II/A-LL 42,5 N-1	0.723±0.236	231±75
CEM II/A-LL 42,5 N-2	0.504±0.098	161±31
CEM II/B-M (S-T) 42,5 R	0.718±0.162	230±52
CEM II/B-M (T-LL) 42,5 N	0.506±0.062	162±20
CEM III/A 42,5 N	0.841±0.212	269±68
CEM III/B 42,5 N	0.635±0.038	203±12
CEM III/B 32,5 N	0.786±0.207	252±66
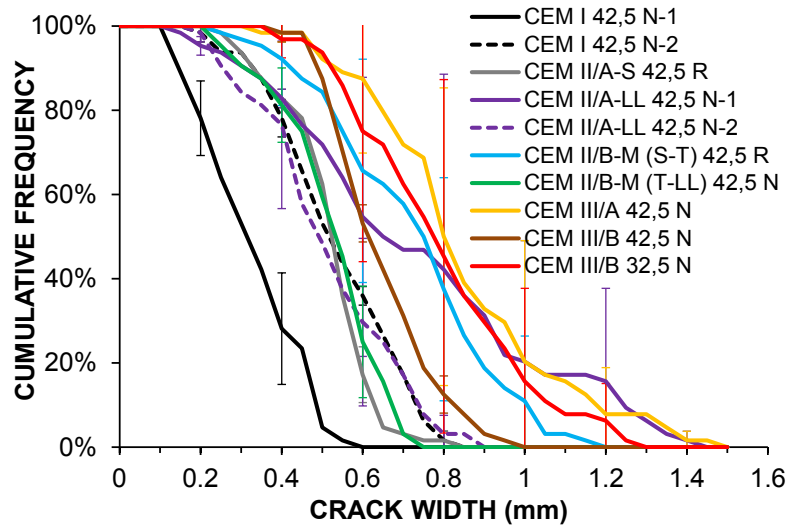
Fig. 4. 13. Cumulative frequency of crack widths. Crack widths were measured on crack opening above the central stress riser. The bars show the standard deviation obtained from two restrained samples

4.4. Discussion

Fig. 4. 14 (to be read from left to right) shows a schematic explanation of plastic shrinkage cracking. In the unsaturated regime, pore pressure develops due to the evaporative flux. As a consequence of the pore pressure, an effective stress develops on the solid particles and the material deforms. Since the volume changes of structural concrete are normally restrained by other structures, by the subgrade and by the reinforcement, a restraint stress (eigenstress) builds up. However, fresh and young concrete has very limited strain capacity or strength in tension (e.g., only about 10 kPa at the age of 3 hours and less than 100 kPa at ages of 5 or 6 h, for tensile strength [211,212]) to withstand restraint stresses which results in crack initiation and propagation.
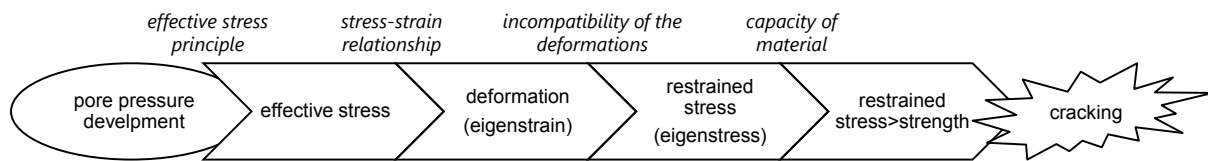
Fig. 4. 14. Schematic explanation of localized plastic shrinkage cracking. From left to right, each item is the source of the item on its right hand side.

According to the explanation outlined above, the crack opening at the exposed surface is expected to be dependent on the deformations of the mixture. Therefore although the performance of concrete mixes can be evaluated by comparing the final crack widths only,

for a better understanding about the involved mechanisms deformations were followed by means of DIC and further correlated to the final crack width.

Since the sample is restrained both horizontally and vertically by means of the stress risers, both the horizontal strain occurring after the development of capillary pressure and the vertical strain are relevant; they can be considered together by means of volumetric strain. The volumetric strain (ε_{vol} [-]) is calculated according to eq. (4-2):

$$\varepsilon_{vol} = \varepsilon_v + 2\varepsilon_h \qquad (4-2)$$

where, ε_v [-] is the vertical deformation and ε_h [-] is the horizontal deformation, measured by DIC. Following this approach, at given environmental conditions, the crack widths measured on restrained samples, dependent both on material properties and geometric constraints (i.e. restraint), are plotted against the free volumetric strain measured on unrestrained samples, thus dependent only on material properties (considering similar evaporation regimes), *Fig. 4. 15*. It should be noted that this dependence could be generalized to other environmental conditions within the range normally encountered in concrete practice, e.g., [40].
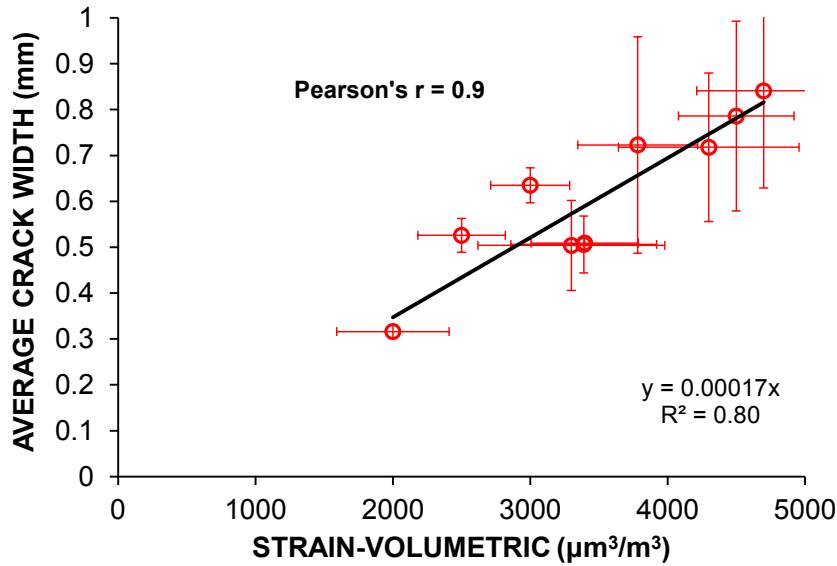
Fig. 4. 15. Average crack width vs. average final volumetric strain (final values at the conclusion of a test, measured from the onset of capillary pressure), see Fig. 4. 8 and Fig. 4. 9. The bars show the standard deviation of two measurements each obtained from one free shrinkage sample or one sample with stress riser.

For the data presented in *Fig. 4. 15*, the Pearson correlation coefficient is $r = 0.9$, which shows that the measured crack width in restrained samples is very strongly correlated to the volumetric deformation of free samples. Considering this dependence, the factors that govern free strain need to be investigated regarding their influence on crack widths for different cements studied here.

In order to understand the factors influencing the volumetric deformation, one can consider the incremental stress-strain relationship (eq. (4-3)) for a hypo-elastic material like fresh concrete:

$$\frac{\partial \varepsilon_{vol}}{\partial t} = -\frac{1}{B}\frac{\partial \sigma_{eff}}{\partial t} \tag{4-3}$$

where ε_{vol} [-] is the volumetric strain, B [Pa] is the bulk modulus, σ_{eff} [Pa] is the effective stress and t [s] is time. Utilizing the effective stress principle, $\sigma = \sigma_{eff} + S_w p$, for the unsaturated regime after some simple transformation one obtains:

$$\frac{\partial \varepsilon_{vol}}{\partial t} = \frac{1}{B}\left(\frac{\partial S_w}{\partial t}p + \frac{\partial p}{\partial t}S_w\right) \tag{4-4}$$

where S_w [-] is the saturation degree, p is the pore pressure and σ [Pa] is the total stress. As shown in *Fig. 4. 11* and *Fig. 4. 12*, for the concrete mixtures in this study before the time of final set no significant differences were observed in the evolution of the evaporation rate and of the pore pressure, respectively. Therefore, considering that these evolutions depend on the pore structure, it can be assumed that the water retention curves do not differ considerably between the concretes tested, before the time of final set. An evidence for the latter is the similar permeability for all mixtures calculated from the bleeding measurements (see section 4.3.1). At the same time, as shown in *Fig. 4. 6* (derived from bleeding results), there is a significant difference in the evolution of the bulk moduli. Consequently, we can conclude that for the tested concretes, the observed differences in the rate of volumetric strain (and consequently, in cracking) are primarily due to changes in bulk modulus, which strongly depends upon hydration of cement. In fact, it was found that the crack width shows a strong, positive correlation with the length of the dormant period estimated based on temperature data in *Table 4. 6* ($r = 0.72$) and with the characteristic time of the bulk modulus evolution, see *Fig. 4. 6* ($r = 0.70$). When a linear regression model (see section 4.2.3) is applied with crack width as aim variable and either the dormant period or the characteristic time as explanatory variables, in both cases the explanatory variables are highly significant, with P-values below 0.001.

The following parameters of the tested cements are relevant considering the discussed effect of bulk modulus evolution on the crack width:

- plasticizer content (strongly positively correlated to crack width, $r = 0.65$),

- cement composition (represented by clinker content from *Table 4. 2* as the part of cement responsible for fast reaction, moderately-strongly negatively correlated to crack width, $r = -0.56$),
- fineness of cement (represented by Blaine fineness, moderately positively correlated to crack width, $r = 0.39$).

It should be noted that these parameters are all mutually strongly correlated ($|r| > 0.70$), e.g. with increasing fineness the plasticizer content required to reach the reference workability increases, or, with decreasing clinker content cement producers mill the cements to higher fineness to increase their reactivity. Due to this mutual correlation between different parameters, referred to as collinearity, it is not possible to use a multiple regression model to explain the role of the individual parameters [213]. Nevertheless, a multiple linear regression model can be still used to check their combined effect. The linear regression model with crack width as dependent variable and the afore-described parameters as explanatory variables (with coupling) was applied showing that at least one of the parameters is significant as predictor of the crack width, yielding a P-value of 0.012, with multiple $R^2 = 0.72$ (adjusted $R^2 = 0.56$).

From this analysis it becomes evident that decreasing clinker content, which requires grinding the cement to higher fineness and consequently using more plasticizer, leads to higher cracking risk. This is primarily due to delayed hydration, and consequently delayed bulk modulus evolution brought about by lower clinker content and higher plasticizer dosage. For the same clinker content, higher fineness leads to faster hydration (faster bulk modulus evolution), and consequently smaller cracks; this effect apparently dominates over the effect on capillary pressure. This is confirmed by comparing the results of the cements with similar clinker contents and similar plasticizer amount but different fineness, i.e. both for the two types of CEM I and the two types of CEM III/B tested here. Naturally, the positive effect of higher fineness will be partially lost due to higher plasticizer necessary for workability. This suggests that, when using blended cements, plastic shrinkage cracking may be reduced by selecting cement with higher fineness and possibly using hydration accelerators [209].

4.5. Conclusions

The susceptibility of concretes made of OPC and blended cements to plastic shrinkage cracking was studied according to ASTM C1579-13. A good correlation was observed between the total volumetric deformation measured by a novel 3D image correlation system and the measured average crack width at the end of the test.

According to the presented model based on poromechanics, the main factors that affect the magnitude of the volumetric shrinkage in the plastic phase are discussed; it was found that the crack widths are mainly affected by the evolution of the bulk modulus governed by the cement hydration process, whereas the pore structure governed by cement fineness is less important. Consequently, the dependence of cracking upon cement properties has been studied by means of statistical analysis.

The results clearly indicate that, due to the decreasing clinker content, the susceptibility to plastic shrinkage cracking increases in concretes with blended cements. This is due to slower evolution of hydration and consequently slower evolution of bulk modulus that leads to larger deformations in concrete exposed to early-age evaporation. This effect is further magnified by the higher amount of plasticizer required in concrete produced with blended cements, which further delays hydration. At the same time, the high fineness of the cement allows to partially overcome this negative effect, leading to higher initial hydration rate. The results also indicate that the accelerating effect of cement fineness on limiting crack widths dominates over that on higher capillary pressures. Therefore, to overcome the negative effects of blended cements on plastic shrinkage cracking, measures should be taken to accelerate early hydration, e.g. by using cements with higher fineness or using accelerators.

Acknowledgements

This page is intentionally left blank.

Chapter 5. A poromechanics model for plastic shrinkage of fresh cementitious materials[4]

Abstract

When fresh cementitious materials are exposed to evaporation, drying of the pore fluid leads to capillary pressure development and plastic shrinkage. Plastic shrinkage occurring after the solid percolation threshold plays an important role in the initiation and propagation of plastic shrinkage cracks, which may compromise the durability and decrease the service life of concrete structures.

In this study, a poromechanics approach to plastic shrinkage is developed. Novel experimental methods are utilized to quantify the material properties used as model input. An independent set of measurements is further used to validate the developed model. It is shown that the bulk modulus evolution plays a prominent role in controlling the plastic shrinkage of cementitious materials.

Keywords: Fresh concrete; Characterization; Shrinkage; Finite Element Analysis; Bulk modulus.

5.1. Introduction

In fresh concrete, similarly as in soils, the pore pressure changes due to the effects of gravity and evaporation [24], see also Chapter 3 for the case of concrete. The pore pressure evolution is accompanied by an increase of effective stress [24,26]. The resulting volumetric contraction, when occurring in concrete after placement and before final set, is referred to as *plastic shrinkage* [28]. When plastic shrinkage is restrained (for example, by the subgrade, by the reinforcement or by self-restraint in a concrete slab, or by the presence of the stress risers in the ASTM standard [132]), deviatoric stresses due to restrained deformations arise. Eventually, the fresh concrete cracks when the stress surpasses the failure limit. Plastic shrinkage cracks are preferred pathways for the penetration of harmful ions, liquids and gases into concrete structures and they may jeopardize their durability and ultimately reduce their service life [11,214]. In order to mitigate plastic shrinkage cracking, a thorough understanding of the mechanisms of plastic shrinkage is needed.

Plastic shrinkage is generally considered to occur in two regimes or states: bleeding state (also referred to as saturated state, where it is also called *plastic settlement,* see Chapter 3 and [15]) and drying state (where saturation degree can drop below 1 due to external drying).

5.1.1. Bleeding state

The process of water flowing from the bulk of fresh concrete towards its surface, due to effect of gravity, and the accumulation of water (or, more precisely, pore fluid) on the surface is referred to as *bleeding* [35]. During bleeding of fresh concrete, the accumulated surface free water evaporates; therefore, all pores of concrete remain saturated with pore fluid. Initially after placement, the concrete self-weight, i.e. the weight of the solid particles suspended in the pore fluid, generates the pore pressure. At a certain time instant, the solid particles percolate and can therefore transfer the stress due to their weight through the freshly formed solid network. As a consequence, the minimum absolute value of pore pressure is reached due to self-weight of the pore fluid itself, eq. (5-1). At this point, the gradient of total pore fluid potential (the pressure potential plus the gravitational potential, see Chapter 3) becomes zero and, according to Darcy's law, the upward water flow stops and bleeding ceases. Therefore, eq. (5-1) can be referred to as the suspension threshold or the solid percolation threshold [180], when bleeding ceases:

$$\psi_p \ at \ suspension \ threshold = \rho_f g(h - z) \tag{5-1}$$

In eq. (5-1), ψ_p [Pa] is the pore fluid's pressure potential, ρ_f [kg/m^3] is the density of the pore fluid, assumed equal to the density of water, $g = 9.81$ [m/s^2] is the gravity acceleration, h [m] is the height of the concrete layer (sample) and z [m] is the elevation from the bottom of the sample. The pore fluid pressure potential takes positive values for fluid under compression and negative for fluid under tension (capillary pressure). In fresh cementitious materials, the solid percolation is caused in the bleeding state primarily by cement hydration [180]. In other words, cement hydration forms a solid network and arrests the bleeding process [35]. The process of bleeding was discussed in Chapter 3, in which relationships for the permeability and bulk modulus evolution for saturated fresh concrete were derived. The literature about bleeding of fresh concrete (e.g., [15,155,154,182]) has been discussed in depth in Chapter 3.

5.1.2. Drying state

In the drying state (i.e., when the rate of evaporation of free water from the concrete surface is higher than the rate of bleeding, and eventually the pore fluid starts to evaporate), the water

flow is governed by the external environmental drying (evaporation flux). In these conditions, the water flow will continue after the limitation stated in eq. (5-1) due to the gradient of negative pore pressure (capillary pressure, p_c [Pa]).

Furthermore, after the solid percolation threshold, (i.e. the transition between suspension of solid particles in pore fluid and solid body), chemical shrinkage also contributes to the pore pressure evolution in the process of self-desiccation [215], acting as a sink term for the reduction of the degree of saturation [172] (see eq. (5-13) and eq. (5-16)).

In the drying state, since the evaporative flux is higher than the bleeding flux, the rate of water expulsion from the pores is higher and therefore the solids percolate faster than in the case of pure self-weight consolidation. Also as explained in this study, according to the consolidation equation, the direct contribution of the capillary pressure (i.e. isotropic stress) on the distances between the solid particles (and therefore on the stiffness) accelerates this process.

Although several experimental investigations have been dedicated to plastic shrinkage in the drying state (e.g., [17,28,29,50,57,71,75,77,216]), only few authors developed analytical and numerical models of plastic shrinkage.

5.1.3. Previous approaches to modelling plastic shrinkage

The primary studies related to the mechanism of the plastic shrinkage in the drying state [35,30,32], proposed an estimation of the maximum capillary pressure exerted on the solid particles. It was a function of the surface tension of the pore fluid, surface area of particles and porosity. Later, Radocea [31,128,156] modeled the plastic shrinkage of cement-based materials by relating the total volumetric deformation to the evaporated water and to the water transferred to the surface, with the latter as a function of the bulk stiffness. A relationship was derived for the evolution of the capillary pressure by defining two isotropic material property parameters, called *plastic shrinkage modulus* and *pore structure function*. No distinct functions were derived for vertical and horizontal shrinkage. Radocea concluded that the stiffening of the cement paste brought about both by consolidation and cement hydration contributes to increase the rate of capillary pressure development. A drawback of this method is that the gradient of pressure over the thickness of the sample is neglected. On the contrary, the present study shows that both the coefficient of permeability and the gradient of pore pressure (which are coupled) govern the water flux. Moreover, Radocea included into the plastic shrinkage modulus the effect of both parameters, permeability and

stiffness, while they need to be utilized separately in order to obtain the evolution of pore pressure more accurately (as discussed both in Chapter 3 and in this study).

In other studies, prediction methods of plastic shrinkage cracking were generally developed without explicitly modeling the plastic shrinkage, e.g., (as mentioned above) by predicting the maximum pressure [32,35], approximating the stress intensity factor, and its critical value [157], or by simulating the coupled effect of forces acting on solid particles [158,159]. However, as explained before, the eigenstresses (caused by restrained deformations) play a dominant role in localized plastic shrinkage cracking (see Chapters 4, 6 and [138]). Therefore, developing a predictive model of the plastic shrinkage of unrestrained cementitious materials, as performed in this study, is the first step in modeling cracking and failure.

The classical poromechanical model for studying drying and consolidation of inert porous materials, e.g. soil, considering the pore fluid pressure as the state variable, follows the extended Richards equation [217,218], utilizing the mass conservation of pore water:

$$\left(\frac{S_w}{B} + n_{cap}\frac{\partial S_w}{\partial \psi_p}\right)\frac{\partial \psi_p}{\partial t} = \nabla \cdot \left[\frac{\vec{k}_{eff}}{\rho_f g}\cdot(\nabla \psi_p + \rho_f \vec{g})\right]$$ (5-2)

where S_w [-] is the saturation degree, B [Pa] is the bulk modulus, n_{cap} [m³/m³] is the capillary porosity and, $\vec{g}$ [m/s²] is the gravity acceleration vector. In writing eq. (5-2) here, the pore fluid's compressibility is neglected. Furthermore, as derived in [217], the transfer of moisture due to the gradient of the vapor pressure is neglected owing to high saturation degrees. For $S_w=1$, eq. (5-2) becomes Terzaghi's consolidation equation for saturated soils [26]. The drawback of eq. (5-2) when applied to fresh concrete is that it does not consider the effect of the chemical shrinkage on the evolution of the pore pressure, since it was derived for chemically-inert materials, e.g. soils [217].

5.1.4. New modelling approach and experimental validation

The goal of the work presented here is to provide a comprehensive description of plastic shrinkage, based on the consolidation equation (eq. (5-2)), by including the chemical shrinkage term. The bulk modulus evolution was determined according to the approach proposed in Chapter 3 for the bleeding state. The latter is extended to the drying state by considering also the effect of suction (capillary pressure) on the stiffness of fresh cement-based materials, according to the model proposed for soils by Alonso et al. [219]. Furthermore, the Water Retention Characteristic Curve (WRCC) of the fresh cementitious

materials was obtained experimentally according to the Tempe cell method [220], further incorporating the quantification of the effect of self-desiccation on the WRCC by tensiometer measurements. For the dynamics of the pore pressure evolution, comprising the chemical shrinkage term, a generalized consolidation equation was derived by a poromechanics approach that utilized the mass conservation equation of solids and pore fluid (originally proposed by Gawin et al. [173]), Terzaghi's effective stress principle [23,217] and the incremental stress-strain relationship. The whole model was verified and validated by the experimental data obtained by performing plastic shrinkage measurements on unrestrained specimens utilizing a 3D digital image correlation system (DIC) (see Chapter 4) on both an ordinary cement-based mortar mix and a mortar with partial replacement of cement with silica fume. Finally, the mechanisms involved in plastic shrinkage of fresh cementitious materials in the drying state are extensively discussed on the basis of the poromechanics model and of the experimental results presented in this study.

5.2. Model derivation

5.2.1. Bulk modulus evolution

The bulk modulus evolution was determined experimentally according to the method presented in Chapter 3 first for the bleeding state B_b [Pa] (eq. (5-3)), i.e. with no influence of capillary pressure on stiffness. In eq. (5-3), B_0 [Pa] is the initial bulk modulus, mainly related to the initial porosity, aggregate content [154,221] and the surface area of the binders, as shown in this study, and t^* [min] is the characteristic time related to the kinetics of the hydration process (see Chapter 4 and [154]):

$$B_b = B_0 \exp(t / t^*) \tag{5-3}$$

The latter is extended to the drying state B_e [Pa] (eq.(5-4)), by including the effect of the negative pore pressure (capillary pressure) [27], on the stiffness of fresh concrete according to the non-linear empirical model proposed in [219]:

$$B_e = B_b[(1-\xi)\exp(-\omega|p_c|)+\xi] \tag{5-4}$$

In eq. (5-4), ξ [-] is a parameter defining the maximum effect of the capillary pressure on the fresh concrete stiffness and ω [1/Pa] is a parameter controlling the rate of increase of fresh concrete stiffness with the capillary pressure. According to eq. (5-4), in the absence of the capillary forces compressing the body, $p_c=0$ and the bulk moduli in the two states are

identical. In this study, for the final plastic shrinkage model validation, a function is used independent from the experimental pressure and shrinkage data, possessing the same evolution regime as proposed in eq. (5-4). Its parameters were calibrated according to the Vicat needle measurements in two regimes: bleeding and drying (see section 5.4.1.2).

5.2.2. Water Retention Characteristic Curves (WRCC) of fresh concrete

The Water Retention Characteristic Curve (WRCC) relates the water content in the pores of a porous body to the capillary pressure [220,222]. The initial total porosity n_{tot} [-] is the initial volumetric water content (equal to the volume of mixing water per volume of fresh concrete). Although entrapped air voids are present in fresh concrete, they are not explicitly considered in the present model; their effect is however taken into account in the calculation of the saturated permeability and of the bulk modulus (see Chapter 3). The evolution of the capillary porosity n_{cap} [-] was obtained by the classical model by Powers [223] as a function of the degree of hydration α [-] and utilizing all parameters according to [224]:

$$n_{cap} = n_{tot} - 1.32 \left(\frac{M_{cem}}{\rho_{cem}} \right) \alpha \tag{5-5}$$

Mind that all water in fresh concrete is assumed to be present as free and capillary water. Conceptualizing the pores of fresh concrete as a bundle of circular cylindrical capillary tubes [225], the capillary pressure is related to the radius of water-air menisci r [m] according to the Young-Laplace equation [17]:

$$p_c = -\frac{2\gamma \cos\theta}{r} \tag{5-6}$$

where γ [Pa·m] is the surface tension of the pore fluid, and θ [rad] is the contact angle. When applying eq. (5-6) to cementitious materials, perfect wetting is usually assumed ($\cos\theta=1$) (see e.g., [17]). The air entry pressure, p_{ae}, is defined as the value of capillary pressure that starts to drain the internal pores. While at capillary pressures lower than the air entry pressure the porous body remains saturated, for larger capillary pressures the overall saturation degree drops below one.
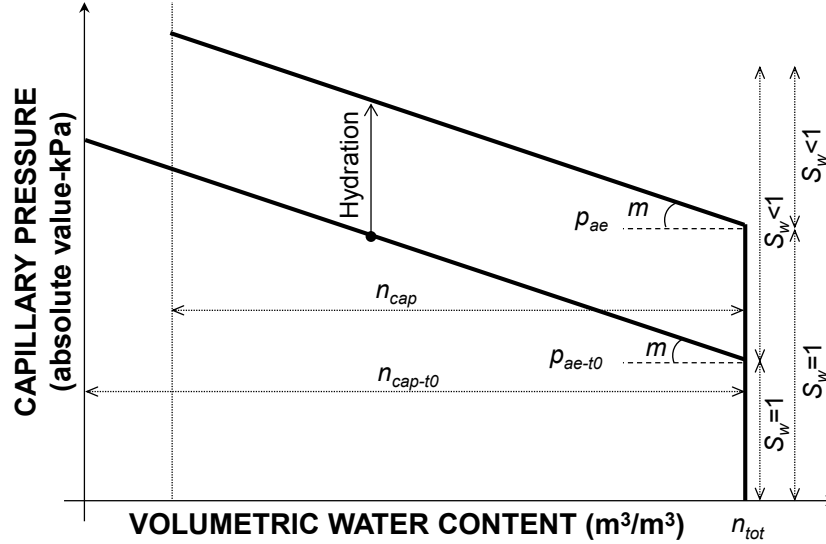
Fig. 5. 1. Schematic figure showing the evolution of the Water Retention Characteristic Curve (WRCC) for fresh cementitious materials, assuming small strains (see Chapter 3). The vertical axis is in the logarithmic scale. The subscript t0 denotes the initial values at the time of mixing. The air entry pressure (p_{ae}) was determined according to the Brooks and Corey method [220,226]. S_w [-] is the saturation degree.

According to the Kelvin-Laplace equation, the drainage starts from the largest pores within the systems and smaller pores are gradually drained with increasing capillary pressure [227,228]. Therefore, as shown in *Fig. 5. 1*, in cementitious materials the air entry pressure increases with cement hydration [222], due to the refinement of the pores that are emptied by evaporation. After the air entry, the capillary pressure increases according to the pore size distribution index [229] indicated as *m* [-] in *Fig. 5. 1*. The pore size distribution index was assumed to remain constant as in [222].

Eventually, according to the above-explained WRCC, we can establish a protocol (similar to [220]) for the volumetric capillary water content $W_{v\text{-}cap}$ [m^3/m^3]:

If $|p_c| < p_{ae}$:
$$W_{v\text{-}cap} = n_{cap} - \varepsilon_{vol} \qquad (5\text{-}7\text{-}1)$$

If $|p_c| \geq p_{ae}$:
$$W_{v\text{-}cap} = n_{cap} - \varepsilon_{vol} - (1/m)\log(|p_c|/p_{ae}) \qquad (5\text{-}7\text{-}2)$$

The saturation degree is equal to:
$$S_w = W_{v\text{-}cap}/(n_{cap} - \varepsilon_{vol}) \qquad (5\text{-}8)$$

The mentioned parameters are obtained experimentally in the results section.

5.2.3. Coefficient of permeability

The saturated coefficient of permeability (k_{sat} [m/s]) is denoted as the saturated permeability in this study. Its initial value ($k_{sat\text{-}t0}$ [m/s]), until the evolution of the air entry pressure, can be determined according to the method proposed in Chapter 3. The method is based on the fact that the experimentally-determined constant bleeding rate is equal to the upward constant flux of water and hence the transport property (saturated permeability) can be determined via Darcy's law describing the flux. When the air entry pressure rises, eq. (5-9) can be utilized as a function that relates the change in the pore size to the change in the permeability before the air entry for the saturated state, according to the model proposed in [230], assuming constant slope of the retention curve *m*:

$$k_{sat} = \left(\frac{p_{ae-t0}}{p_{ae}} \right)^2 k_{sat-t0} \tag{5-9}$$

with $p_{ae\text{-}t0}$ [Pa] being the initial air entry pressure. According to the Darcy-Buckingham equation [210] (eq. (5-10)) for pore fluid flux q [m/s], the effective coefficient of permeability is $k_{eff}=k_{sat}k_r$, where k_r [-] is the relative permeability, which includes the effect of desaturation on permeability.

$$\vec{q} = -\frac{k_r \vec{k}_{sat}}{\rho_f g} \cdot (\nabla \psi_p + \rho_f \vec{g}) \tag{5-10}$$

For studying plastic shrinkage, the effective permeability is considered as approximately equal to the intrinsic permeability (permeability in the saturated state) for saturation degrees close to 1 (>0.99) [231] encountered in fresh concrete (see section 5.4.2.1). As explained in this study, the effect of hydration on the intrinsic permeability is dominant for studying the plastic shrinkage of cementitious materials.

5.2.4. Generalized consolidation equation incorporating chemical shrinkage

In order to obtain a governing equation for the dynamic pressure development in fresh cementitious materials, the mass balance equation of fluid and solid skeleton for a porous medium in the form proposed by Gawin et al. [173] is utilized (eq. (5-11)). In the derivation of eq. (5-11), the gradient of the water vapor pressure is neglected as in eq. (5-2) (the extended Richards equation for soils), due to the fact that in a fresh concrete with saturation degree close to 1, the gas relative permeability is close to zero [231]. Furthermore, when the water permeability is high, liquid water transport dominates, due to the much higher density

of water compared to vapor. Finally, it is considered that the change in density of concrete with the temperature change is negligible.

$$n_{cap}\rho_f \frac{\partial S_w}{\partial \psi_p} \frac{\partial \psi_p}{\partial t} - \rho_f S_w \frac{\partial \varepsilon_{vol}}{\partial t} = \frac{\rho_f}{\rho_s} S_w \dot{m}_{hydr} - \dot{m}_{hydr} + \nabla \cdot \left[\rho_f \frac{\vec{k}_{eff}}{\rho_f g} \cdot (\nabla \psi_p + \rho_f \vec{g}) \right] \qquad (5\text{-}11)$$

$$\text{with } \frac{\partial \varepsilon_{vol}}{\partial t} = -\nabla \cdot \frac{\partial \vec{u}}{\partial t} \qquad (5\text{-}12)$$

In eqs. (5-11) and (5-12), $\vec{u}$ [m] is the displacement vector of the solid skeleton, S_w [-] is the saturation degree, ε_{vol} [-] is the volumetric strain, $\dot{m}_{hydr}$ [kg/m³·s] the rate of water consumption during the hydration process, ρ_s [kg/m³] and ρ_f [kg/m³] are the densities of the solid and of the pore fluid, respectively. The terms on the left hand side (LHS) of eq. (5-11) are the accumulation terms due to changes in the saturation degree, and the solid medium elastic deformation, respectively. The right hand side (RHS) of eq. (5-11) describes the source and sink terms, where the first term is the actual source of skeleton due to the decrease of pore volume caused by the buildup of hydration products ($\dot{m}_{hydr}/\rho_s$) and the following terms are the actual sinks due to the mass of water consumed by hydrating cement [172] and lost to the environment by evaporation according to the Darcy-Buckingham law. Dividing both sides of eq. (5-11) by $n_{cap}\rho_f$ yields:

$$\frac{\partial S_w}{\partial \psi_p} \frac{\partial \psi_p}{\partial t} = \frac{1}{n_{cap}} \nabla \cdot \left[\frac{\vec{k}_{eff}}{\rho_f g} \cdot (\nabla \psi_p + \rho_f \vec{g}) \right] - \frac{\dot{m}_{hydr}}{n_{cap}} \left(\frac{1}{\rho_f} - \frac{S_w}{\rho_s} \right) + \frac{S_w}{n_{cap}} \frac{\partial \varepsilon_{vol}}{\partial t} \qquad (5\text{-}13)$$

According to eq. (5-13), the pore fluid saturation degree is a function of water transport in the fresh concrete (due to the drying), chemical shrinkage and elastic volumetric deformation of the solid medium, from left to right of the RHS of the equation, respectively. It should be remembered that the volumetric deformation is a function of the bulk modulus. Therefore, eq. (5-13) needs to be coupled with eq. (5-15), obtained by coupling Terzaghi's effective stress principle, eq. (5-14) [23,217], and the incremental stress-strain relationship, as shown in eq. (5-19). In this study, the general convention is: strains and stresses positive for shrinkage and compression of the solid.

$$\sigma_{eff} = \sigma_{sw} + \sigma_{ex} - \psi_p \qquad (5\text{-}14)$$

$$\frac{\partial \sigma_{eff}}{\partial t} = -\frac{\partial \psi_p}{\partial t} = B \frac{\partial \varepsilon_{vol}}{\partial t} \tag{5-15}$$

In eq. (5-14), σ_{ex} [Pa] is the external load, which in this study is zero, and σ_{sw} [Pa] is the self-weight stress, which is constant in time. The effect of desaturation on effective stress is usually considered by means of assuming the pore pressure as an average between pressures of different components occupying the pores. However, for saturation degrees close to 1 (in fact, in all simulations carried out in this work, $S_w > 0.9995$) the effect of desaturation on the average pore pressure can be neglected and the pressure of pore fluids exerted on the skeleton can be approximated with the capillary pressure, i.e. $\psi_p = p_c$. Further, it should be noted that the compressibility of the solid grains is neglected since the latter have bulk modulus B_s [Pa] orders of magnitude higher than the fresh concrete, and consequently the so-called Biot coefficient, $(1 - B/B_s)$ [232] can be assumed as equal to 1.

After some transformations, the generalized consolidation equation (eq. (5-16)) is obtained:

$$\left(\frac{\partial S_w}{\partial \psi_p} n_{cap} + \frac{S_w}{B} \right) \frac{\partial \psi_p}{\partial t} = \nabla \cdot \left[\frac{\vec{k}_{eff}}{\rho_f g} \cdot (\nabla \psi_p + \rho_f \vec{g}) \right] - \dot{m}_{hydr} \left(\frac{1}{\rho_f} - \frac{S_w}{\rho_s} \right) \tag{5-16}$$

Eq. (5-16) is equivalent to eq. (5-2) with the addition of the chemical shrinkage term. According to eq. (5-16), both the evaporative flux (the gradient of pore pressure for a concrete under evaporation is negative upwards) and cement hydration (chemical shrinkage) decrease the pore pressure (i.e. they both lead to an increase in the absolute value of capillary pressure).

A higher slope of the water retention curve (lower value of the $\partial S_w / \partial \psi_p$ term) and a higher value of the air entry pressure (corresponding to finer pores) both accelerate the evolution of the pore pressure. Furthermore, as also mentioned by Radocea [31,156], for a plastic concrete when the evaporation rate (i.e. the first term on the RHS of eq. (5-16)) is constant, stiffening of concrete by cement hydration and capillary pressure (the latter was referred to as the effect of consolidation by Radocea [31,156]) accelerate the rate of increase of the absolute value of capillary pressure.

The second term on the RHS of eq. (5-16), which defines the chemical shrinkage rate, can be replaced by the chemical shrinkage term according to the classical Powers' model [223], with all parameters according to [224]:

$$\dot{m}_{hydr} \left(\frac{1}{\rho_f} - \frac{S_w}{\rho_s} \right) = 0.2 \left(\frac{M_{cem}}{\rho_{cem}} \right) \frac{\partial \alpha}{\partial t} \tag{5-17}$$

In eq. (5-17), α [-] is the hydration degree, ρ_{cem} [kg/m^3] is the cement density, M_{cem} [kg/m^3] is the initial mass of cement in the mixture. The rate of hydration obtained in isothermal conditions can be extended to non-isothermal conditions utilizing the maturity approach (see next section).

5.2.5. Maturity concept

In order to consider non-isothermal conditions, the maturity concept is used, assuming an Arrhenius-type temperature-dependent evolution for the rate of the hydration degree [53]:

$$\frac{\partial \alpha(T_c)}{\partial t} = \frac{\partial \alpha(T_{iso})}{\partial t} \exp\left[-\frac{E_a}{R}\left(\frac{1}{T_c} - \frac{1}{T_{iso}}\right)\right] \tag{5-18}$$

where T_{iso} is the reference isothermal temperature [K], and T_c is the actual concrete temperature, respectively. E_a [$\approx$ 39 kJ/mol] [233] is the apparent activation energy of concrete and R [8.314 J/mol K] is the gas constant.

5.2.6. Horizontal and vertical shrinkage

The volumetric shrinkage is calculated by determining the effective stress, according to the simulated pore pressure development and the effective stress principle. After casting and before the solid percolation or suspension threshold (see eq. (5-1)), concrete can be considered as a suspension of (heavier) solid particles in the (lighter) pore fluid. In the presence of gravity, the solid particles move down and an upward bleeding water flux takes place. Since before the percolation of the solids the gravitational load of the solid particles is exerted on the pore fluid, it results in a hydrostatic pressure. At the same time, since the deformations of the solid part of fresh concrete in *drained* conditions are considered (i.e. excluding bleeding water), the body is compressible and concrete consolidates in the vertical direction [24]. The deformations are calculated as follows:

$$\psi_p \geq \rho_f g(z-h) \rightarrow \Delta\varepsilon_{xx} = \Delta\varepsilon_{yy} = 0 \quad \& \quad \Delta\varepsilon_{zz} = \Delta\varepsilon_{vol} = \frac{\Delta\sigma_{eff}}{B} \tag{5-19}$$

The correctness of describing the consolidation process in 1-D following the approach by Terzaghi [24] is supported by the DIC data, which show negligible strains in the horizontal direction before the percolation of the solids, see e.g. *Fig. 5. 15*.

After the solid percolation, the deformations for an isotropic concrete under isotropic stress, for small-strains, can be obtained:

$$\psi_p < \rho_f g(z-h) \rightarrow \Delta\varepsilon_{xx} = \Delta\varepsilon_{yy} = \Delta\varepsilon_{zz} = \frac{\Delta\varepsilon_{vol}}{3} = \frac{\Delta\sigma_{eff}}{3B} \qquad (5\text{-}20)$$

The incremental values at each time step were integrated over time to obtain the final evolution curves. The time step was 1 min.

It is worth underlining that, as long as the initial value of stress tensor considers the gravitational load in the downward direction (-z direction, see *Fig. 5. 2*), the increments of the effective stress tensor in absence of any external loads are isotropic and result solely from the decrease of pressure (in the bleeding process) or due to drying.

5.2.7. Boundary conditions and initial values

Fig. 5. 2 shows the boundary conditions of the plastic shrinkage problem. In this study, the experimentally-measured evaporation flux was used for the boundary condition, by monitoring the mass change of the specimens. No flux in *Fig. 5. 2* means that the flux towards the normal direction of the surface ($\vec{n}$) is equal to zero:

$$-\vec{n} \cdot \nabla(\psi_p + \rho_f \vec{g}) = 0 \qquad (5\text{-}21)$$
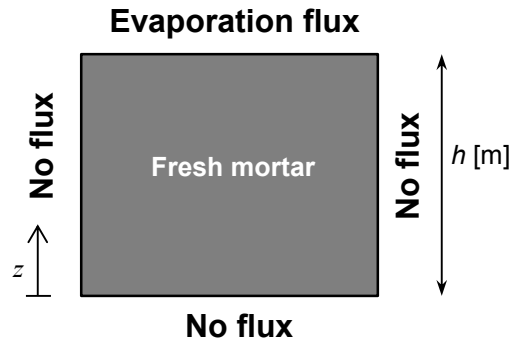
Fig. 5. 2. Boundary conditions of the plastic shrinkage problem. The friction between the mold walls and fresh concrete is neglected (pure volumetric free deformation)

The initial value of the state variable is:

$$\psi_p = \rho_C g(h-z) \qquad (5\text{-}22)$$

5.2.8. Numerical method and meshing

COMSOL Multiphysics® [234] was utilized to obtain the solution, by implementing eq. (5-16). The utilized finite element mesh is shown in *Fig. 5. 3*. The model (eq. (5-16)) was discretized in space and time, using Finite Element Method (FEM) and Backward Differentiation Formula (BDF) methods [234], respectively.
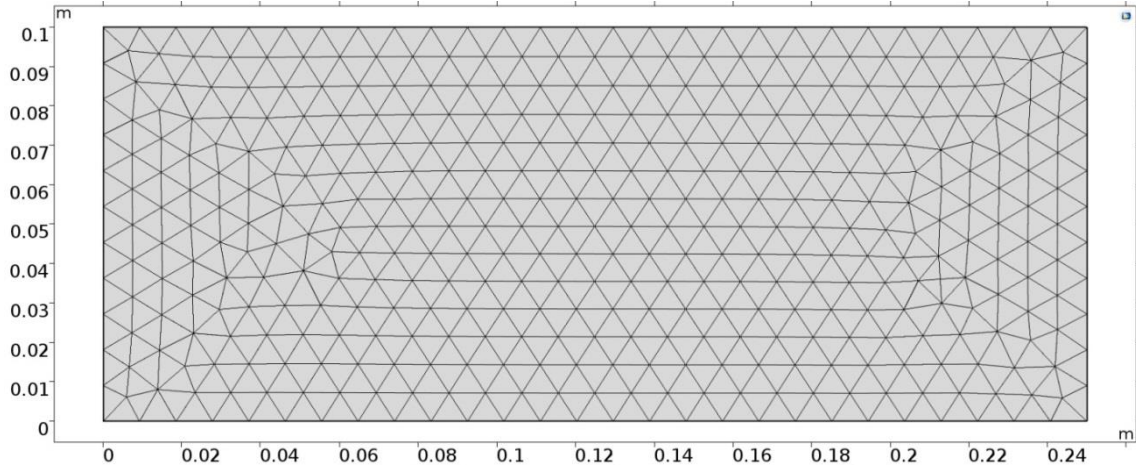
Fig. 5. 3. Details of the implemented mesh consisting of 760 triangular finite elements.

5.3. Materials and experimental methods

5.3.1. Materials and mixture compositions

Cement mortar was prepared using CEM I 42.5N with a modified Bogue-calculated composition (by mass %) C_3S: 61.7, C_2S: 10.1, C_3A: 4.3, C_4AF: 11.6, free CaO: 0.5, Na_2O: 0.2 [235]. The mix designs for the reference plain mortar (REF) and the mortar with 20% volumetric substitution of cement with silica fume (SF20%) are shown in *Table 5. 1*. The volumetric portions of paste (including 3% air content by mortar volume [236]) were identical in the two mortars (paste 49%, aggregate 51%), to study exclusively the effect of binder replacement. In SF20%, the water-to-binder ratio (w/b) by mass was increased to 0.48 due to the lower density of the silica fume compared to the cement. Furthermore, SF20% had higher water-to-cement ratio (w/c). Consequently, as silica fume does not react at very early ages [237], it is expected that SF20% will show a delayed evolution of mechanical properties.

Table 5. 1. Mix designs and physical properties of mortars

Mortar	Water (kg/m³)	Cement (kg/m³)	Silica fume (kg/m³)	Sand [0-1mm] (kg/m³)	Sand [1-4mm] (kg/m³)	Measured air content (%)	w/b (-)	w/c (-)	Estimated density (kg/m³)	Measured density (kg/m³)	Spread diameter (cm)
REF	270	600	0	810	540	3	0.45	0.45	2220	2243	21.5
SF20%	270	480	84	810	540	3	0.48	0.56	2184	2164	15.5

A 12-l Hobart mixer was used to mix the components. The dry constituents were first premixed during 30 s, and next wet mixing continued for another 1 min. The workability was measured according to EN 1015-3 [238], by measuring the spread diameter after 15 drops. The densities were calculated by filling a 350 ml cylindrical container and measuring the mass of mortar after compacting on a vibrating table until no large air bubbles escaping the mix could be seen. The spread diameter and densities are presented in *Table 5. 1*.

5.3.2. Methods

5.3.2.1. Bleeding
The bleeding test was performed to determine the permeability and the bulk modulus evolution in saturated conditions according to Chapter 3. The test was performed at 20 ± 1°C. The materials were kept in a temperature-controlled room at the testing temperature for 24 h prior to mixing. After mixing, the mortar was placed in three 105 mm-diameter cylinders with known mass. The cylinders were filled up to three different heights, namely 60 mm, 100 mm and 140 mm, and compacted on a vibrating table until no large air bubbles escaping the mix could be seen (about 12 s vibration). The bleeding test started 20 min after mixing for all specimens. The samples were covered with a lid to prevent water evaporation. The bleeding water was collected with a pipette every 15 min during the first 30 min and every 30 min afterwards until no further bleeding water was found at the surface. Since the collected water unavoidably contained some solid particles, after the initial determination of the mass of the collected fluid, the fluid was evaporated in an oven at 100 °C for 30 min to measure and account for the mass of the dry residue.

5.3.2.2. Vicat setting time
The setting times were determined by the Vicat needle for mortars adapted from ASTM C807-13 [239]. The needle had 2 mm diameter and 300 g mass. Cylindrical molds with inner diameter 76 mm were filled with mortar and placed in the climate-controlled room, where the plastic shrinkage test was performed (see section 5.3.2.5). Two types of samples were used: opened to drying in a wind channel (the same as for plastic shrinkage measurements, section 5.3.2.5) and covered with a plastic lid to avoid evaporation. Hence, setting times were defined in two states: bleeding and drying (see Introduction). The penetration tests were performed at 10 min intervals. The time at which the needle failed to penetrate down to the bottom of the cylinder was reported as the initial set and the time at which the needle did not penetrate into the surface was reported as the final set.

5.3.2.3. Isothermal calorimetry

The heat flow was measured with a Thermometric TAM Air conduction calorimeter. Tests were performed on mortars and on pastes with no aggregates to assess any possible effect of aggregates on the measurements. The mixes were mixed inside the calorimeter with a miniature mixing paddle staying inside the calorimeter and attached to an external mixing engine. Before mixing, all components were allowed to reach thermal equilibrium inside the calorimeter for several hours. From the time of water addition and mixing, the heat flow was measured for 1 day. During the experiment, isothermal conditions (20 ± 0.02 °C) were maintained in the measuring cells. The hydration heat flow and the cumulative hydration heat, normalized to the cement mass in the samples, are shown in the results section starting from the time of water addition. The presented results are the average from two measuring cells each, with the difference in cumulative heat not exceeding 2%.

5.3.2.4. WRCC measurements

WRCC was measured with a Tempe cell as explained in section 5.3.2.4.1. Furthermore, the effect of self-desiccation on WRCC was measured by tensiometers as explained in section 5.3.2.4.2. The capillary pressure measured with the tensiometers was added to the Tempe cell measurements to obtain the final WRCC, shown in *Fig. 5. 11* and *Fig. 5. 12*. The self-desiccation and Tempe cell measurements were mutually independent, since self-desiccation is uniform in the whole sample and thus does not influence the pore pressure gradient. The test room temperature was 19±1 ℃.

5.3.2.4.1. Tempe cell method

As shown in *Fig. 5. 4*, a cylinder with diameter of 47 mm was used as a Tempe cell [220] to determine the pore size distribution index and the air entry pressure for the WRCC. The test started 10 min after mixing. 80 to 100 g of mortar were placed in the cylinder and compacted in the vertical direction with a 45-mm-diameter cylindrical rod. A paper filter with pore size 8 μm was inserted at the bottom of the cylinder, to ensure high enough permeability for the pore fluid, while blocking almost all cement particles. Different constant air overpressures (p_{over} [Pa]) were applied for 10 min each and the mass of the filtered pore fluid was recorded. A period of 10 min was enough to reach equilibrium at each pressure step (in fact, no more pore solution droplets were extracted already after 5 min). The gradient of total pore fluid potential led to the desaturation of the mortar. At the equilibrium one can calculate the capillary pressure according to its definition, eq. (5-23). $p_{non\text{-}wetting\ phase}$ is equal to $p_{over} + p_a$

and $p_{wetting\ phase}$ is equal to p_a [Pa] (air pressure), since the pore water is connected to the air at the outlet.

$$p_c = -\left(p_{non\text{-}wetting\ phase} - p_{wetting\ phase}\right) = -\left(p_{over} + p_a - p_a\right) = -p_{over} \tag{5-23}$$

The Tempe cell measurements were run two times for each mix design. The applied air overpressures (kPa) were 200, 130, 100, 70, 40 and 20 and they were applied at 10, 20, 30, 40, 50, 60 min after mixing, respectively. Then the test was continued at 90, 120, 150, 240 and 300 min after mixing, the first time with 130 kPa and the second time with 70 kPa, to monitor the evolution of the water retention curve with cement hydration. All samples were manually compacted before the time of initial set measured by Vicat on sealed samples (110±10 [min]).
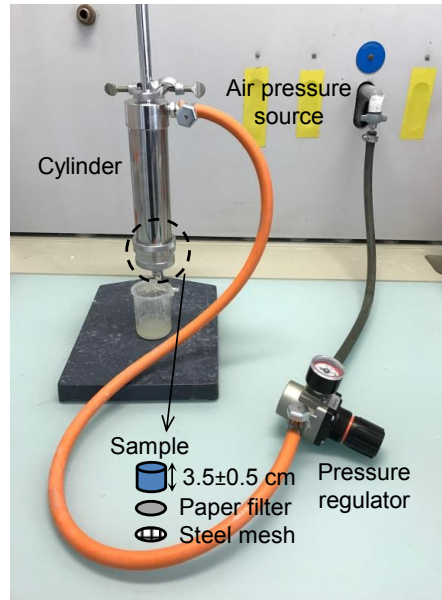
Fig. 5. 4. Tempe cell test setup

5.3.2.4.2. Tensiometer method

The capillary pressure caused by self-desiccation was measured by tensiometers (see also [222]) on thin sealed samples (height=2 cm) as shown in *Fig. 5. 5*. The tensiometer's head was mounted horizontally in the middle of the sample. The fresh mortar was poured into the mold and compacted on a vibrating table for 12 sec. The mold was then sealed with plastic foil to avoid evaporation and hence measure pore fluid pressure only due to capillary effects during self-desiccation. The measurements were repeated twice and the average value was added to the capillary pressure measurements by the Tempe cell. The air entry point of the porous ceramic head of the tensiometer was 200 kPa.

Fig. 5. 5. Tensiometer measurements setup

5.3.2.5. Plastic shrinkage

As shown in *Fig. 5. 6*, a mold with dimensions of $250\times250\times100$ mm^3 was filled with mortar and compacted on a vibrating table for 12 sec. Then the mold was placed in a climate controlled room at 32.5±2.5 %RH and temperature 25.5±0.5 °C. The temperature of the room was chosen in order to obtain an initial temperature of the evaporating concrete close to 20 °C (due to evaporative cooling). 20 °C is the temperature at which the material properties of the mortars have been measured.

A wind channel was used to produce a uniform wind velocity of 7.5±0.5 m/s over the sample to accelerate evaporation. Two tensiometers were embedded into the sample horizontally at depth of about 85 mm from the top surface to measure the pressure development. Thermocouples were utilized to measure the temperature evolution of the surface and at depths of about 10 mm, 50 mm and 95 mm. A balance was used to obtain the change in mass of the mortars due to evaporation. A digital image correlation system (DIC) was used to measure the horizontal and vertical deformations by following the movement of light chairs placed on the mortar surface, on which a pattern with sufficient contrast was painted, as described in Chapter 4 (see *Fig. 5. 6. b*). The test started 20 min after mixing. For each mix design, two measurements were performed, and the average between repetitions (after having averaged between different sensors during each test) and the related standard deviation were reported.
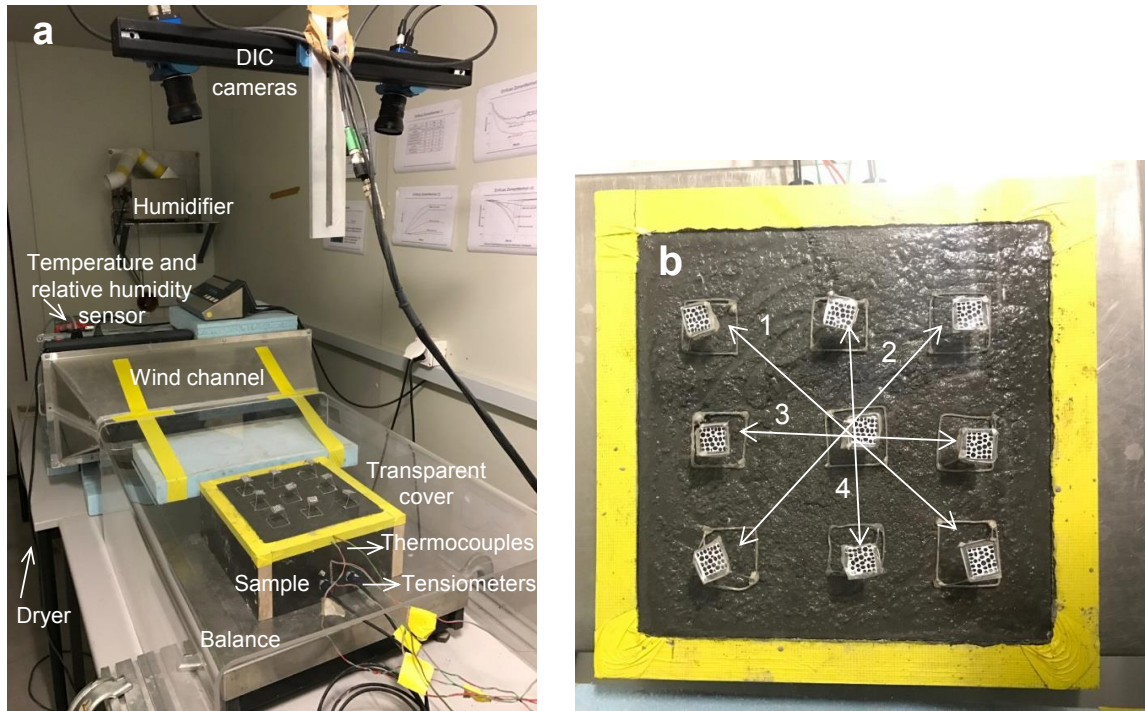
Fig. 5. 6. a) test setup, b) position of 4 virtual strain gauges for measuring the horizontal shrinkage and 9 wire meshes for measuring the vertical shrinkage.

5.4. Results and discussions-model verification and validation

Experimental results are divided in two groups: model input experimental results and model output experimental results. The former are the experimental results that are used as input to run the model (mostly used to calculate material properties) and the latter are the results obtained from independent tests used to verify the predictions made by the model.

5.4.1. Model input experimental results

5.4.1.1. Bulk modulus in the bleeding state and initial permeability

Fig. 5. 7 shows bleeding vs. time for the tested mixes. The bleeding rate and the calculated initial permeability are shown in *Table 5. 2*. The bulk modulus for the bleeding state (B_b) and the initial permeability (k_{sat-t0}) were calculated according to Chapter 3. As expected, SF20% had lower permeability due to the fineness of the silica fume and the consequent finer pore size distribution of the fresh mortars (see *Fig. 5. 11*), which had been also observed in, e.g., [166,221]. The bulk moduli were approximated with the exponential relationship proposed in Chapter 3, for the bleeding state, utilizing the exponential function presented in eq. (5-3). The determined values are presented in *Table 5. 2*. Higher bulk modulus in the bleeding state was obtained with silica fume, due to the higher fineness of the used silica fume compared to the

cement it partially replaced, which was in line also with the lower workability of these mixes (see *Table 5. 1*).

The characteristic hydration time, being a proxy of the inverse of hydration rate in the initial stages of the reaction, is mainly related to the cement clinker content and to the effect of plasticizers on retarding the hydration process [154] and is very relevant to the pre-induction plus dormant hydration duration (see Chapter 4). SF20% had a higher hydration characteristic time due to the lower cement (clinker) content, or higher w/c, since silica fume does not react at very early ages [237].
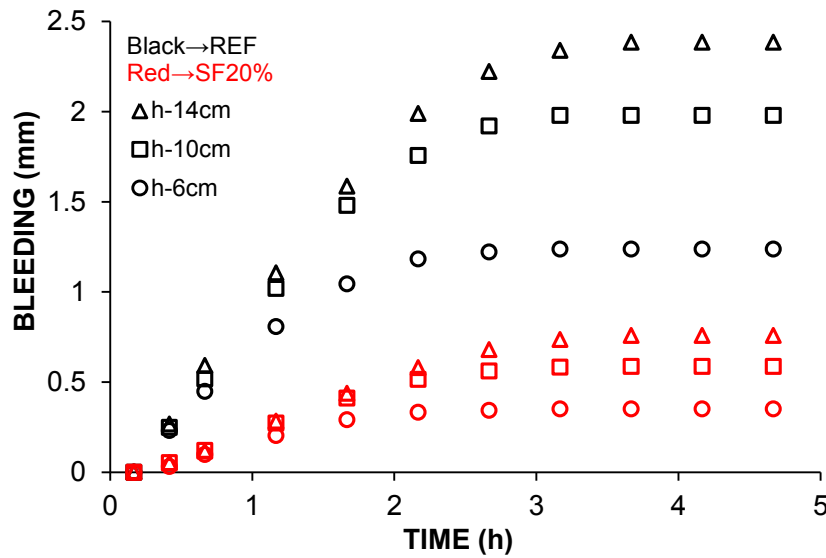
Fig. 5. 7. Bleeding vs. time for REF and SF20%

Table 5. 2. Measured and calculated properties

Mortar	b [nm/s]	$k_{sat\text{-}t0}$ [nm/s]	B_0 [kPa]	t^* [min]	t_{ISD} [min]	t_{FSD} [min]	t_{FSB} [min]	ω_V [1/h]	ξ_V [-]	$p_{ae\text{-}t0}$ [kPa]	m [-]
REF	310	250	4.6	43.5	90	125	200	4	5.8	16±7	7.5
SF20%	85	73	18.8	50	70	107	210	4	7.9	16±7	10.2

5.4.1.2. Bulk modulus in the drying state

To obtain the bulk modulus in the drying state for the model validation, a function (see eq. (5-24)) is proposed, possessing the same non-linear exponential evolution regime as in eq. (5-4). Its parameters (ξ_V [-] and ω_V [1/h]) were calibrated according to the Vicat needle measurements in two regimes: bleeding and drying. This was based on the assumption that final setting times at different regimes correspond to the same values of bulk modulus. In eq. (5-24), t_{ISD} [h] is the Initial Vicat Setting Time at the Drying State, when drying expels the inter-particle water and solids percolate.

$$t < t_{ISD} \qquad\qquad\qquad B_e = B_b \qquad\qquad\qquad (5\text{-}24\text{-}1)$$

$$t \geq t_{ISD} \qquad\qquad B_e = B_b[(1 - \xi_V)\exp(-\omega_V(t - t_{ISD})) + \xi_V] \qquad (5\text{-}24\text{-}2)$$

As shown in *Fig. 5. 8*, the time of final set in the drying state (FSD-point 2) occurred earlier than the time of final set in the bleeding state (FSB-point 1). Assuming that a) mortars had the same bulk modulus at the time of final set (both in the bleeding and drying states), and b) that after the time of final set the bulk modulus evolution was dominated by hydration, the maximum effect of the capillary pressure on the stiffness to be used in eq. (5-24-2) is obtained by eq. (5-25):

$$\xi_V = \frac{B_b(t_{FSB})}{B_b(t_{FSD})} \qquad\qquad\qquad (5\text{-}25)$$
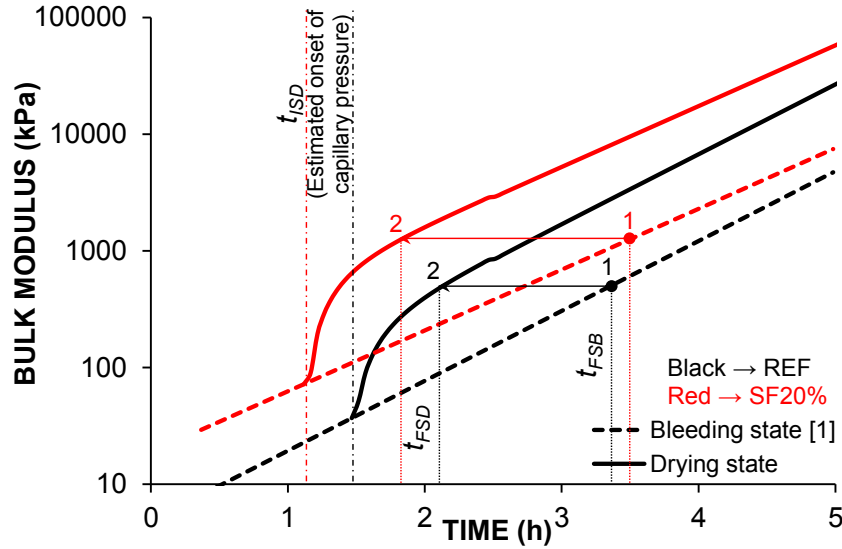
Fig. 5. 8. Vicat setting times and estimated evolution of bulk modulus in the drying state

The onset of the capillary pressure was assumed to be around t_{ISD}, when the solids percolate. The parameter that controls the rate of the evolution (ω_V [1/h]) was obtained by fitting the curve to reach to the maximum capillary pressure effect at t_{FSD}. Obtained parameters are shown in *Table 5. 2*.

5.4.1.3. Temperature

Fig. 5. 9 shows the average temperature of the bulk (measured with thermocouples at depths of 10 mm, 50 mm and 95 mm) to be used for the maturity transformation. The difference of measured temperatures along the height of the sample was negligible. When the hydration acceleration period started, the temperature started to increase. The difference between the temperature evolution of REF and SF20% was not significant.
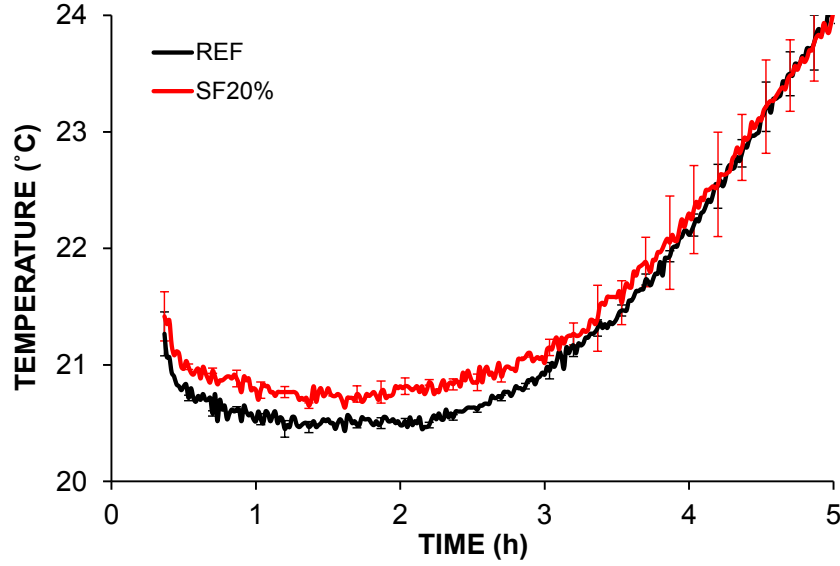
Fig. 5. 9. Bulk temperature vs. time

5.4.1.4. Hydration degree

The isothermal heat fluxes are shown in *Fig. 5. 10. a* for mortars. The difference between the measured heat fluxes for mortars and pastes were negligible. The isothermal hydration degree was calculated (see *Fig. 5. 10. b*) according to the measured heat flux $\dot{Q}$ [J/(s g cement)]. The theoretical heat at full hydration of the cement was estimated based on the cement composition as 423 J/g [208]. The dormant period ends when the isothermal heat flux $\dot{Q}$ reaches a minimum, which is the inflection point of the hydration degree vs. time curve (see *Fig. 5. 10* and eq. (5-26)):

$$\frac{\partial \dot{Q}}{\partial t} = \frac{\partial^2 \alpha}{\partial t^2} = 0 \qquad (5\text{-}26)$$

SF20% had slightly longer dormant period, 2.18 h (including the pre-induction period), comparing to REF, 2.03 h, due to the lower cement content and higher w/c [208], which is in line with the higher estimated value of t^* for SF20% in section 5.4.1.1. According to *Fig. 5. 10*, the end of the dormant period occurred at hydration degree (calculated with respect to the mass of cement reacted) 3.9% and 4.6% for REF and SF20%, respectively. The non-isothermal hydration degree was estimated according to the maturity concept explained in section 5.2.5 and *Fig. 5. 9* data, and presented in *Fig. 5. 10. b*. Note that for the temperature change in non-isothermal conditions considered here (increase by about 3 degrees until 5 h, see *Fig. 5. 9*), the effect of temperature on hydration was minor in the first 3-4 hours of hydration.
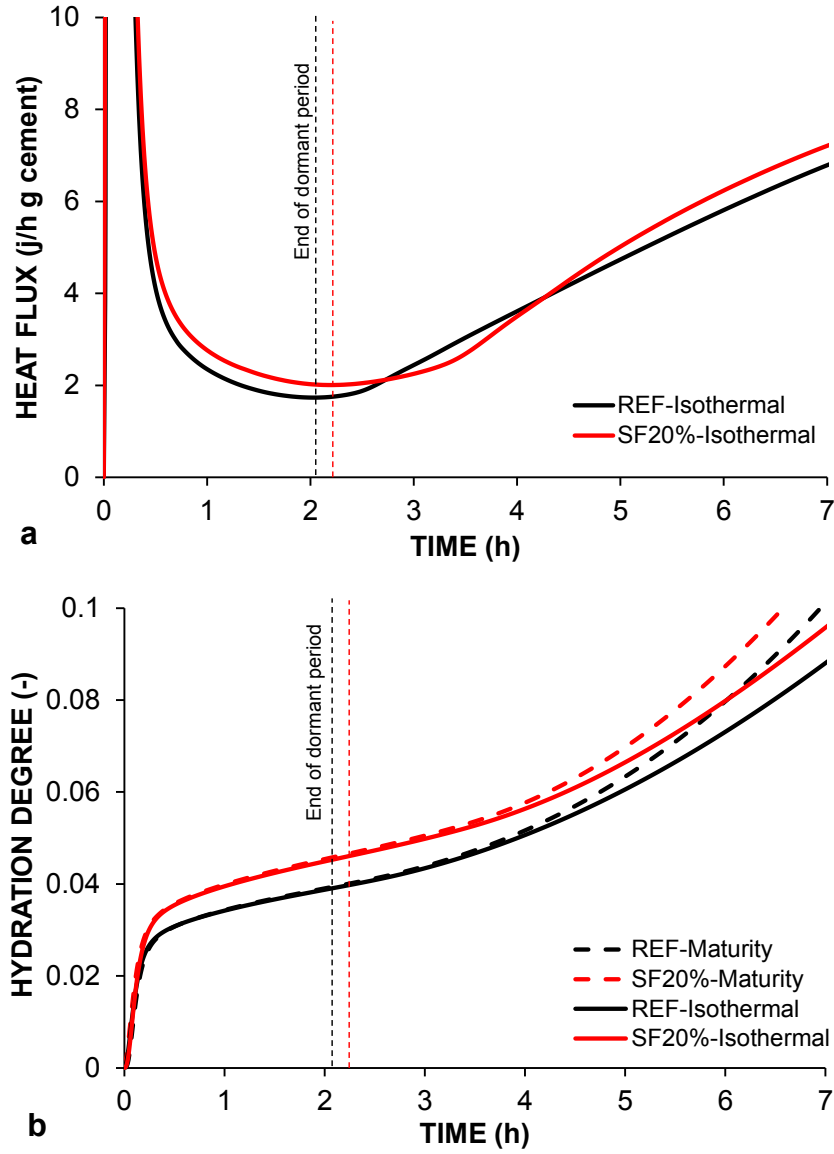
Fig. 5. 10. a) Isothermal heat fluxes vs. time for mortars. b) Hydration degree vs. time for isothermal condition and with maturity transformation. Time zero is the mixing time.

5.4.1.5. Pore size distribution index and air entry pressure

As shown in *Fig. 5. 11,* SF20% had a higher pore size distribution index due to partial substitution of cement particles with finer silica fume particles, which increased the surface area of the binder and decreased the average pore size. The capillary pressure measured with tensiometers on sealed samples were -16±7 kPa and -12±7 kPa for REF and SF20%, respectively, at 300 min after mixing. Considering that similar capillary pressure developed due to self-desiccation in the samples used in WCCR measurements (Tempe Cell), the absolute values of capillary pressure measured in sealed conditions were added to the overpressure applied on the samples for determination of the WRCC at 300 min. No capillary pressure increment due to self-desiccation was recorded at 120 min and 180 min after mixing, in the test mentioned in section 5.3.2.4.2. The air entry pressure was obtained according to

the Brooks-Corey method [220,226] as shown in *Fig. 5. 1*, considering small-strain assumptions (i.e. deformations do not affect the pore size). The standard deviation of the Tempe cell measurements was ± 7 kPa, obtained from the scatter of the duplicate water loss measurements. There was no substantial difference in the initial air entry pressure between the two mortars; this was likely due to the fact that silica fume possibly affected primarily pores in the small size range, and not the largest pores. The characteristic air entry value evolved slightly later in SF20%, due to the lower cement content and longer dormant period. The hydration degree in which air entry pressure changed agrees well with the hydration degree at the end of dormant period obtained in the previous section. The estimated pore size distribution index remained approximately constant in both mortars, i.e. the points after air entry fell on approximately parallel lines (see *Fig. 5. 11*), while the air entry pressure increased due to the hydration of cement (see *Fig. 5. 12*), as also obtained in [222].
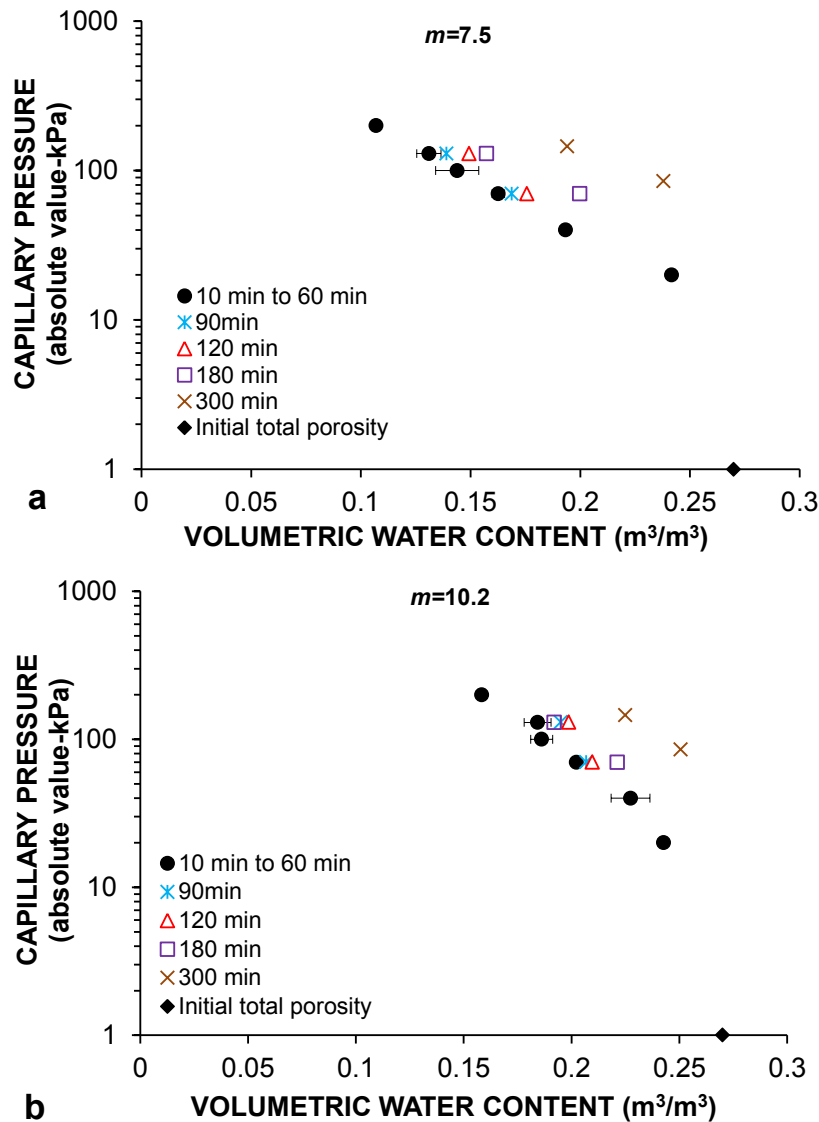
Fig. 5. 11. WRCC evolution for a)REF and b)SF20%. Error bars refer to the standard deviations of volumetric water content measurements.
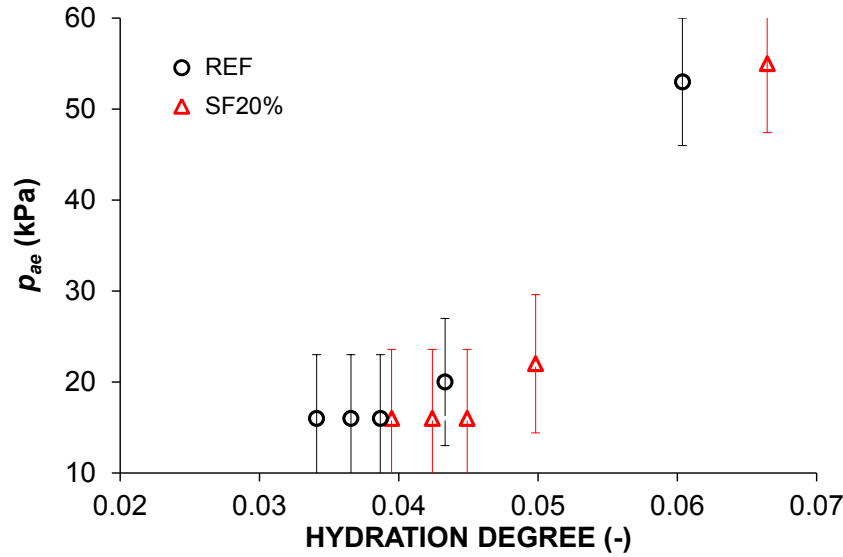
Fig. 5. 12. Evolution of the characteristic air entry pressure. Error bars refer to the standard deviations.

5.4.1.6. Evaporation rate

The evaporation rate plotted vs. the hydration degree is shown in *Fig. 5. 13*. It was calculated from the mass change data by applying Savitzky-Golay smoothing of polynomial order 2 and windows of 30 points. In the pre-induction and dormant period, the evaporation rate was constant (Constant Rate Period-CRP). In the hydration acceleration period, the evaporation rate decreased (Falling Rate Period-FRP), due to the increased air entry pressure and reduction of the intrinsic permeability caused by cement hydration. SF20% had longer CRP, due to the lower clinker content (see Chapter 4). The hydration degree obtained for the beginning of the FRP period agrees well with the obtained hydration degree for the end of the dormant rate period in section 5.4.1.4 and also with the hydration degree at which the air entry pressure changed, which was obtained in the previous section. Therefore, it can be concluded that: a) during the dormant hydration period the intrinsic permeability remains constant (in agreement with Chapter 3) and, accordingly, the evaporation rate remains constant; b) at the end of dormant period, the pore sizes start to decrease, the intrinsic permeability decreases and the evaporation rate falls in the hydration acceleration period; c) retarding hydration by any method, e.g. reducing the clinker content or utilizing retarders, makes the CRP longer.
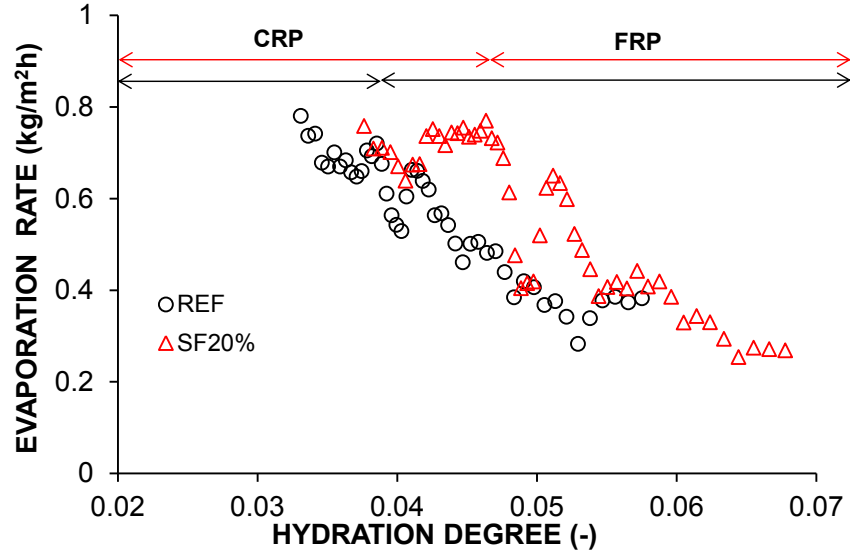
Fig. 5. 13. Evaporation rate vs. hydration degree

5.4.2. Model output results

5.4.2.1. Pore pressure

Fig. 5. 14 shows the simulated evolution of the capillary pressure vs. time. The standard deviation shown on the curve was obtained by running the model with higher and lower boundaries of the characteristic air entry values shown in *Fig. 5. 12*.

Considering that the rate of evaporation of the free water was higher than the rate of bleeding of mortars, the capillary pressure increased. The higher initial stiffness of the mortar with SF causes faster solid percolation and faster onset of the capillary pressure. Furthermore, the pore size reduction at the beginning of the hydration acceleration period contributed to the acceleration of the capillary pressure increment. After the air entry time, the simulated pressure increased with lower rate, since as shown in *Fig. 5. 1*, the slope of the WRCC decreases after the air entry.

When the upper limit of the characteristic air entry values (see *Fig. 5. 12*) were used for the simulation, the air entry in *Fig. 5. 14* was postponed (see the upper limit of the deviations shown on the model curve). The latter is due to the fact that, according to the Young-Laplace equation (see eq. (5-6)), higher capillary pressure is needed to evacuate smaller pores [227,228]. Despite the increasing deviations between model and experiments after the air-entry point, the model agrees well with the experimental pressure data in the time period in which plastic shrinkage cracking occurs [17,77]. The effect of chemical shrinkage on the pressure development was negligible, (< 1kPa), because the evaporation rate was found to be much higher than rate of chemical shrinkage. Nonetheless, the chemical shrinkage may have a more pronounced effect in cementitious materials with lower w/c. The saturation degree

decreased slightly after the air entry, however it remained higher than 0.9995 for both mortars.
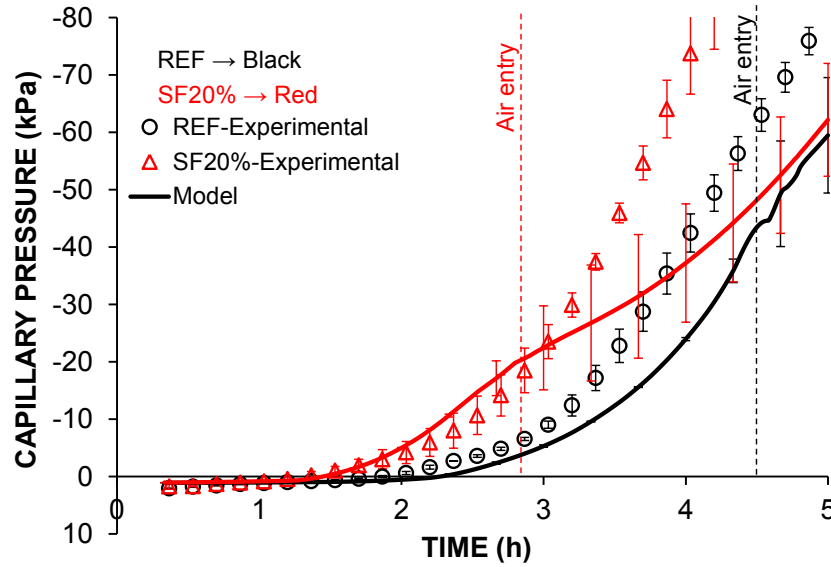
Fig. 5. 14. Capillary pressure development vs. time. The deviations on the model curves show the effect of upper and lower bounds of characteristic air entry on the pore pressure evolution

5.4.2.2. Volumetric, horizontal and vertical plastic shrinkage

Fig. 5. 15 and *Fig. 5. 16* show the simulated and experimental 3D plastic shrinkage. The standard deviation shown on the model curve was obtained by running the model with higher and lower boundaries of the characteristic air entry values, shown in *Fig. 5. 12*. The model agrees well with the experimental data and the scatter in the values of air entry did not influence the simulated plastic shrinkage significantly. SF20% had faster onset of the horizontal shrinkage, at early stages of the dormant hydration period, caused by the higher initial bulk modulus and faster solid percolation. The latter led to less vertical and volumetric shrinkage, and higher horizontal shrinkage in SF20%, as already observed in [240,241] and [72,199], respectively. The rate of volumetric shrinkage evolution decreased dramatically at the air entry time (so-called critical point), when vertical and horizontal shrinkage practically stopped. This is due to the increased stiffness of the mortar [17,30,77,156], caused by the coupled effect of cement hydration and capillary pressure, as mentioned in the previous section.

The addition of silica fume moved the onset of the capillary pressure to the dormant period, when the mortar does not possess significant strength, while the effective stress increment was accelerated. Moreover, the addition of silica fume also prolonged the dormant period. Therefore, it can be concluded that increment of initial bulk modulus during the dormant period, and also the later evolution of mechanical properties, by substitution of cement with fine inert materials, e.g. silica fume, increase the cracking risk. On the other hand, faster

stiffening caused by the addition of reactive materials, e.g. cement clinker, or by accelerating cement hydration (see Chapter 4) causes a shift of the capillary pressure increase towards the acceleration period of cement hydration, when the strength grows rapidly. Consequently, concretes with accelerated cement hydration, or in other words, shorter dormant period and lower hydration characteristic time (t^* in eq. (5-3)), are less susceptible to plastic shrinkage cracking. The latter conclusion also emerged from Chapter 4.
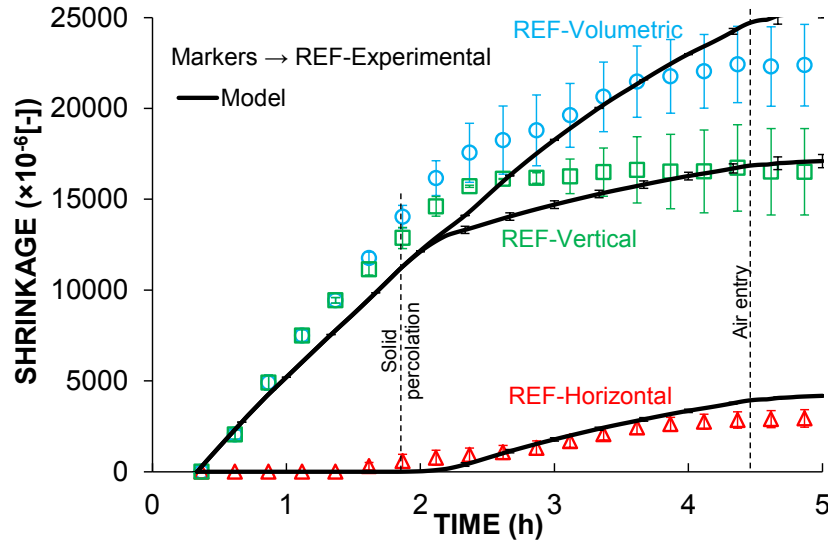
Fig. 5. 15. Volumetric, horizontal and vertical plastic shrinkage for REF. The deviations on the model curve show the effect of upper and lower bounds of characteristic air entry on plastic shrinkage.
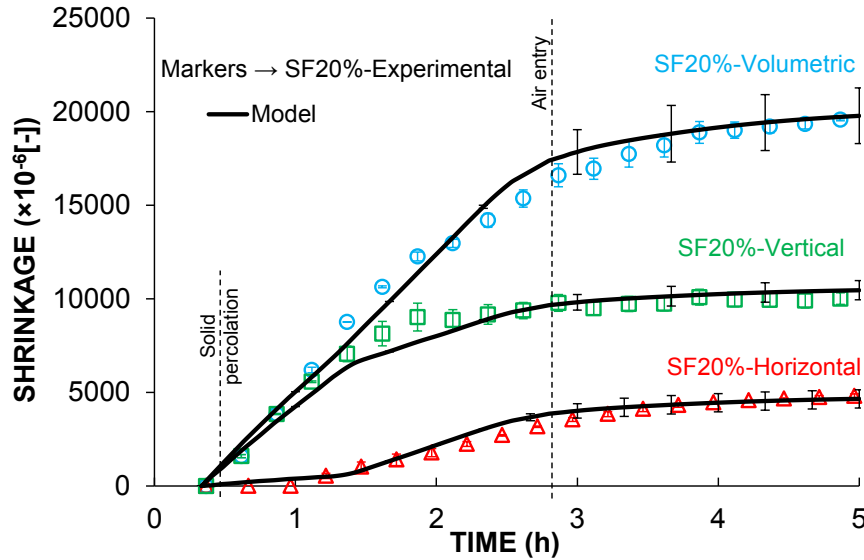
Fig. 5. 16 Volumetric, horizontal and vertical plastic shrinkage for SF20%. The deviations on the model curve show the effect of upper and lower bounds of characteristic air entry on plastic shrinkage.

5.5. Conclusions

A poromechanics model was proposed for the plastic shrinkage of cementitious materials. The governing consolidation equation, which includes a chemical shrinkage term, was derived by coupling the mass conservation of solids and pore fluid, Terzaghi's effective stress principle and an incremental stress-strain relationship.

The material properties utilized in the model were determined in a genuine set of experiments independent from those used for model validation. These were: hydration degree, coefficient of permeability, bulk modulus in the bleeding and drying states and WRCC.

The model validation was performed according to independent experimental measurements of pore pressure evolution and 3D plastic shrinkage during drying of mortars in a wind tunnel. It was found that the effect of the bulk modulus is dominant in controlling the plastic shrinkage and the capillary pressure development. The inclusion of ultrafine inert materials, e.g. silica fume at very early ages, moves the capillary pressure and stress development to early stages of the hydration dormant period, while simultaneously prolonging the duration of the dormant period. Since concretes do not possess significant strength in the dormant period, it can be concluded that addition of fine fillers such as silica fume makes concrete more susceptible to plastic shrinkage cracking.

This page is intentionally left blank.

Chapter 6. On the mechanism of plastic shrinkage cracking in fresh cementitious materials[5]

Abstract

In this study, a continuum poromechanics approach is presented to model the plastic shrinkage cracking of fresh cementitious materials. The boundary conditions are according to the modified ASTM C1579-13 standard for mortars. The restrained deformations are linked to the restraint stresses according to the Cauchy-Navier equations of elasticity, assuming an incremental stress-strain relationship. The Bresler-Pister and Rankine failure criteria are utilized to model failure. The material parameters are adapted according to the Drucker-Prager and Griffith criteria. The crack initiation and propagation is verified experimentally by X-ray radiography. Eventually, the cracking mechanism is discussed and a safe capillary pressure limit is proposed. It is found that capillary pressure stiffening occurring before air entry, when deformations take place in the saturated state, is the predominant cause of plastic shrinkage cracking in the drying state.

Keywords: Fresh Concrete; Crack Detection; Shrinkage; Mechanical Properties; Finite Element Analysis

6.1. Introduction

One of the issues that may jeopardize the service life of concrete structures is early-age cracking, which often occurs as a consequence of restrained deformations, including plastic shrinkage [45,157,242]. Plastic shrinkage is the volumetric deformation of fresh concrete before final set [28,35,36]. Plastic shrinkage may lead to localized, macroscopic cracking in the case of concrete elements with differential depth or in the presence of restraints such as reinforcing bars, knobs and dents on the substrate base and friction between the substrate base and the layer of fresh concrete [70,125,149]. Failure occurs due to the local magnitude of the deviatoric stresses exceeding the failure limit of the fresh concrete. Plastic shrinkage, both in bleeding [35,153] and drying [31–33] states, has been estimated to be the source of about roughly 80 % of early-age cracks in concrete structures [15]. The large economic impact of plastic shrinkage cracking motivates the necessity of a thorough understanding of its mechanisms, which is a prerequisite for developing and prescribing suitable mitigation methods. Nevertheless, the majority of studies about plastic shrinkage cracking is purely

---

experimental (see *Table 6. 1*), and very few analytical and numerical models are available. Kwak et al. [15] modeled the self-weight consolidation of saturated fresh mortars restrained by rebars using the three dimensional small-strain consolidation theory for soil. However, their approach neglects the non-linearity due to time evolution of stiffness. The evolution of the elastic properties in fresh concrete in the drying state is caused both by cement hydration and by capillary-pressure stiffening. A truly robust and accurate model needs to consider an incremental stress-strain relationship for fresh cementitious materials, as explained in this study and in Chapter 5. For the drying state, Morris and Dux modeled plastic shrinkage cracking by approximating the stress intensity factor and its critical value, however without presenting an experimental validation [157]. Furthermore, Slowik et al. [158,159] modeled the plastic shrinkage cracking of an inert material without cement hydration by simulating the interaction of the forces acting on the solid particles in the microscale. However, in order to develop solutions to mitigate cracking, plastic shrinkage cracking need to be modeled at the macroscale, by considering the development of stresses due to restrained deformations.

Various experimental methods for studying plastic shrinkage cracking of concrete and mitigation methods have been developed, as summarized in *Table 6. 1*. Virtually all methods rely on the measurement of the features of the final crack(s) apparent on the concrete surface; this measurement is thus an effect of crack initiation (i.e. failure, which may happen far from the surface) and propagation to the surface. Consequently, if a crack does not propagate to the surface, no meaningful results can be obtained in those methods. Apart from the latter, according to classical engineering failure criteria [243], the damage is defined (and the measures are taken to avoid it) in terms of the crack initiation, when the stress goes beyond the strength envelope, rather than by considering further crack propagation. The fib Model Code for Concrete Structures 2010 [244], classifies any local damages (which do not affect structural safety but may influence the efficiency of structural or non-structural components) as the "serviceability limit state criteria". Local damage (i.e. crack inititation) needs to be avoided, since dormant cracks can propagate further when the required conditions are satisfied, due to the stress concentration existing at the tip of the crack [245]. The latter criteria are in line with the experimental and analytical studies [11,214,246–248] showing the effect of localized cracking and distributed microcracking on increasing fluid and ion transport in concrete, ultimately leading to decreased serviceability. Therefore, crack initiation, which can be considered as local damage influencing the durability of concrete structures, should be chosen as a criterion for comparing the performance of different concrete mixtures, rather than the final crack characteristics. Consequently, experimental

methods which can detect the damage (crack) before propagation are desirable. In [48], a mold with two transparent walls allowed detecting of the crack initiation. However, a drawback of this method is that the observed behavior can be affected by the wall effect. In fact, according to the ASTM C1579-13 standard [132], the cracks observed within 25 mm from the walls should be neglected in the measurements of the crack width distribution.

Based on the arguments discussed above, it is evident that an appropriate experimental set-up and an analytical model are necessary to detect the plastic shrinkage damage initiation; this is the main objective of the present study. For the experimental detection of crack initiation, X-ray radiography was carried out on a sample cast in a modified ASTM C1579-13 [132] mold for mortars. X-ray radiography allowed to detect the crack before its propagation to the surface. This is a clear advantage compared to a standard method where only crack opening at the surface can be assessed. For the numerical procedure, a previously-developed model for simulating free plastic shrinkage explained in Chapter 5 was used as input to the structural mechanics module in COMSOL Multiphysics®.

Tensile strength is a key material property in studies related to concrete's failure, and particularly plastic shrinkage cracking [29,32,55,157]. Even though tensile strength is related to cohesion commonly measured in soils, the experimental measurements are very challenging for fresh concrete, due to a low strength at very early ages. The drawbacks of available methods are extensively discussed in [249]. Although many efforts have been made to measure the strength properties of fresh concrete, the outcome is limited, and might be affected by a series of artifacts [249]. In this study, an attempt is made to present an indirect method for predicting the cohesion and tensile strength of fresh cementitious materials, according to the available multiaxial failure envelopes for porous materials, i.e. soil and concrete. In a multiaxial failure envelope, all strength properties are related according to the equation of the failure limit. In other words, by the measurement of a strength property, e.g. the pseudo-elastic limit, one can estimate the tensile strength. The pseudo-elastic compressive isotropic stress limit [250], which separates the elastic and plastic zones in the mechanical response of fresh cementitious materials, was determined by utilizing the experimentally-validated approach by Casagrande [251] on the modeled stress-strain curves, according to the isotropic, stress-dependent bulk modulus evolution determined in Chapter 5.

The Bresler-Pister failure criterion [243,252,253] was applied for predicting crack initiation. This model was chosen due to the fact that it covers the failure zones of multiaxial stresses, from pure hydrostatic failure (which can happen for porous geomaterials, referred to as cap failure) to shear and tensile failures. Thanks to this approach, it was possible to relate the

pseudo-elastic limit (which relates to pure hydrostatic failure), to the failure envelope in shear and tension, to study plastic shrinkage cracking. Additionally, after modeling the uniaxial tensile strength, the Rankine (maximum tensile principal stress) failure criterion for brittle materials [243,254] was also utilized to study the failure initiation. The material parameters for the cohesion strength used in the Bresler-Pister criterion were adapted according to the Drucker-Prager model at pure shear failure [252,255,256] and the Grrifith's model for tensile failure as explained in Appendix 6-A. Relating the Bresler-Pisler model to the latter two models allowed to utilize an already-available eastimation of the internal friction angle of fresh mortar and to relate the pseudo-elastic stress limit to the tensile strength, by explaining the evolution of cohesion as a linear function of the evolution of the pseudo-elastic limit. Eventually, the model was validated by comparing the predicted crack inititation with X-ray radiography data. A safe limit was proposed for the development of capillary pressure as a benchmark for avoiding plastic shrinkage cracking in the drying state.

Table 6. 1. Methods used for quantifying plastic shrinkage damage

Item	Authors	Test method	Measured quantity
a	Lura et al. [17], Leemann et al. [77], Fontana et al. [257], Norfleet [92], Sivakumar [133], Rahmani et al. [85], Qi et al. [50], Ranjbar [134], Combrinck and Boshof [135], Hossain et al. [136,258], Henkensiefken et al. [82], Yang et al.[74], Soroushian et al. [86]	ASTM C1579 [132]: Cubic mold with three lateral stress risers (triangular section)	Crack length, width, area
b	Berke and Dallaire[93], Sivakumar and Santhanam[55,137], Shao and Mirmiran [89], Mora-Ruacho et al. [78], Boshoff and Combrinck [138]	Modified ASTM C1579 with extra bolt and nut or arrangements at sides or reinforcing bars in both directions to increase the potential of cracking	Crack length, width, area
c	Fontana et al. [257], Löfgren et al. [58], Hwang et al. [143], Branch et al.[109], Esping [144], Sayahi et al. [61], Toledo Filho and Sanjuan [145], Balaguru and Shah [94]	ÖVBB [257], and NORDTEST NT BUILD 433[142]: Ring shape mold with perimeter restraints by expanded metal lath-Ring shape mold, and with rebars positioned at the mid-height of the mold [145]	Crack area
d	Liu [152]	Dumbbell shape mold	Crack width
e	Fontana et al. [257], Lin et al. [20,139,140], Shen et al. [88], Ruiz-Ripoll et al. [141]	DIBt method [257], Shallow cubic mold with threaded steel rebars to provide the boundary restraint and differential depth.	Crack area, width, and length
f	Banthia et al. [148], Banthia and Gupta [95,149,216], Ghoddousi and Javid [126], Malathy et al. [96], Senthilkumar and Natesan [150], Nabil et al. [151]	Concrete was placed on a substrate base with several knobs, exposed coarse aggregates or dents on the surface working as stress risers	Crack area, width, length
g	Li and Qian [147]	GB/T 50082-2009[259]: Cubic mold with seven composite shape lateral stress risers	Crack width, area
h	Kraai[260], Shaeles et al.[261], Soroushian et al.[86], Eren et al.[262], Ramakrishnan et al. [263], Gunasekaran[264], Pelisser et al. [265], Medina et al. [266]	Shallow flat cubic mold with perimeter restraints by L-shaped hardware cloth or expanded metal lath	Crack length, width, area
i	Hosoda [97]	Shallow flat cubic mold with eight lateral rebar stress risers welded to bottom of the mold	Crack area
j	Alhozaimi and Al-Negheimish [76]	Slabs were reinforced in both directions with four steel bars spaced at the middle height	Crack width, area

6.2. Model derivation

In Chapters 3 and 5, the bulk modulus of a fresh plastic concrete (B_e [Pa]) was found to be non-linearly dependent upon: 1- cement hydration, as explained in Chapter 3, and 2- the applied isotropic compressive stress [27] (i.e. capillary pressure), after the solid percolation threshold, according to the relationship proposed by Alonso et al. [219]:

$$B_e = B_b[(1-\xi)\exp(-\omega\sigma_{eff})+\xi]$$
(6-1)

Where B_b [Pa] is the bulk modulus in absence of capillary pressure (in bleeding conditions), dependent only upon hydration of cement. In eq. (6-1), ξ [-] is a parameter defining the maximum effect of the capillary pressure on the fresh concrete stiffness and ω [1/Pa] is a parameter controlling the rate of increase of fresh concrete stiffness with the capillary pressure. In this study, the parameters of eq. (6-1) were obtained by fitting the incremental stress-strain relationship:

$$d\varepsilon_{vol}=d\sigma_{eff}/B_e$$
(6-2)

to the experimentally-obtained incremental effective stress, $d\sigma_{eff}$ [Pa], vs. volumetric strain, $d\varepsilon_{vol}$ [-]. The experimental data comes from the plastic shrinkage experiment performed in Chapter 5 for the same mortars as tested in this study.

Now let us consider the quasi instantaneous (compared to the kinetics of hydration) stress-strain relationship at a given (fixed) time instant, i.e. for a constant B_b. It can be readily seen that, even when excluding the evolution of hydration in the B_b term in eq. (6-1), the stress-strain relationship is still nonlinear due to the dependence of stiffness upon stress. Thus, an incremental form eq. (6-2) is used also at a fixed time. Combining eq. (6-1) and (6-2) one obtains:

$$d\varepsilon_{vol} = \frac{d\sigma_{eff}}{B_b[(1-\xi)\exp(-\omega\sigma_{eff})+\xi]}$$
(6-3)

Integration of both sides of eq. (6-3), assuming the initial values of stress and strain equal to zero, leads to the stress-strain relationship at a given time instant:

$$\varepsilon_{vol} = \frac{\ln(\xi[\exp(\omega\sigma_{eff})-1]+1)}{B_b\xi\omega}$$
(6-4)

The stress-strain relationship described with eq. (6-4) is presented in *Fig. 6. 1* for two exemplary degrees of hydration (two different time instants). The stress-strain curves are used for estimating the compressive pseudo-elastic limit (p_{pel-c} [Pa]) [250,267] at time t, which separates the elastic and plastic domains for the mechanical response of fresh cementitious materials, according to Casagrande's graphical method [251]. The method is based on finding the pseudo-elastic limit as corresponding to the intersection between the slope of the stress-strain curve in the plastic domain (referred to as the *virgin compression line* in [251]) and the bisector of the tangent at maximum curvature with the vertical line. As presented in *Fig. 6. 1*, p_{pel-c} becomes higher with increasing hydration degree of cement. In fact, the pseudo-elastic limit can be referred to as the strength of fresh concrete for the hydrostatic stress (i.e. isotropic stress), which increases with hydration.
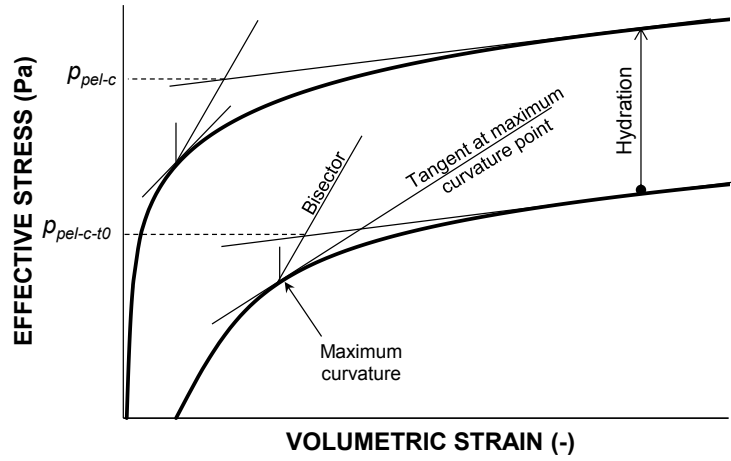
Fig. 6. 1. Schematic evolution of isotropic effective stress vs. volumetric strain curves in fresh cementitious material. The compressive pseudo-elastic stress limit (p_{pel-c}), which increases with hydration, was determined according to Casagrande's graphical method [251,267]. The vertical axis is in the logarithmic scale. The subscript t0 denotes the initial value at the time of mixing.

6.3. Analytical and numerical methods

6.3.1. Effective stress tensor

According to Terzaghi [24], the effective stress is the stress in a porous body that resutls in deformations or contributes to failure resistance and is expressed as:

$$\boldsymbol{\sigma}_{eff} = \boldsymbol{\sigma} - \psi_p \mathbf{I} \tag{6-5}$$

where $\mathbf{I}$ is a 3×3 identity matrix, and ψ_p [Pa] is the pore water pressure. $\boldsymbol{\sigma}$ [Pa] is the total stress tensor. The latter (in absense of external loads) is only due to self-weight, which in a non-consolidated fresh concrete (before percolation of solids) can only be transferred through

the pore fluid and hence is an isotropic stress equal to $\rho_c g(h\text{-}z)\mathbf{I}$ where h [m] is the total height of concrete layer, ρ_c [kg/m^3] is the concrete density, g [m/s^2] is the gravity acceleration, and z [m] is the elevation from the sample's bottom (see Chapter 3). Since in the model presented here an incremental form of the equations is used, it is worth noting that the changes of effective stress are only due to changes of pore water pressure, the latter being initially due to consolidation, and after onset of drying due to capillary pressure (see Chapter 5). Hence, the stress tensor is always isotropic for the plastic shrinkage problem. In eq. (6-5), the pore pressure is assumed to be exerted by the pore water only also after desaturation. This neglects the contribution of the gaseous phase, based on the fact that the saturation degree is always close to 1 (>0.9995) during plastic shrinkage, see Chapter 5. In this study, the compressive stress and the shrinkage are assumed positive. The pore water pressure is assumed positive for compression of the fluid (hence, capillary pressure corresponds to negative pore pressure, i.e. suction). The pore pressure and the resulting effective stress development were modeled in Chapter 5 utilizing the generalized consolidation equation. The free horizontal and vertical shrinkage were calculated by the effective isotropic stress development model as explained in Chapter 5 and were utilized here in an incremental form as input for the model of restraint stress.

The equations of equilibrium [26] for an increment of the restraint stress $d\boldsymbol{\sigma}_r$ reads:

$$\nabla \cdot (d\boldsymbol{\sigma}_r) = 0 \tag{6-6}$$

Assuming x (out-of-plane) and y (in-plane) as horizontal directions and z the vertical direction, for a plane strain problem in the yz plane, and considering the symmetry of the stress tensor, the incremental stress-strain relationship for an isotropic material under plane strain condition is [268]:

$$\begin{bmatrix} d\sigma_{yy} \\ d\sigma_{zz} \\ d\sigma_{yz} \end{bmatrix}_r = \frac{3B_e}{(1+\upsilon)} \begin{bmatrix} 1-\upsilon & \upsilon & 0 \\ \upsilon & 1-\upsilon & 0 \\ 0 & 0 & \frac{1-2\upsilon}{2} \end{bmatrix} \begin{bmatrix} d\varepsilon_{yy} \\ d\varepsilon_{zz} \\ d\varepsilon_{yz} \end{bmatrix}_r \quad \& \quad d\sigma_{xx\text{-}r} = \upsilon(d\sigma_{yy\text{-}r}+d\sigma_{zz\text{-}r}) \tag{6-7}$$

where B_e [Pa] is the bulk modulus, and υ [-] is the Poisson's ratio. Based on the strain compatibility equation, the restrained strain increment is the total strain increment $d\varepsilon$ [-], minus the free strain increment $d\varepsilon_{fr}$ [-]:

$$d\varepsilon_r = d\varepsilon - d\varepsilon_{fr} \tag{6-8}$$

The free strain increments $\Delta\varepsilon_{yy\text{-}fr}$ and $\Delta\varepsilon_{zz\text{-}fr}$ obtained from the plastic shrinkage model in Chapter 5, were utilized in eq. (6-8). Solving the coupled equtions (6-8), (6-7), and (6-6) with the structural boundary conditons (see *Fig. 6. 3*), yields the restraint stress increments. The equations were solved using the structural mechanics module of COMSOL Multiphysics®. The evolution of stresses in time was calculated by integrating $(\Delta\boldsymbol{\sigma_r}/\Delta t)$ over time. Δt [s] is the time increment, which in this study was 1 min. Eventually, the principal restraint stresses were added to the principal (hydrostatic) effective stresses, to obtain the overall effective stress tensor [220]. Failure thus includes the effect of effective stress as postulated originally by Terzaghi [24], see also [220]. Failure occurs when the stress path goes beyond the failure limit, which is explained in the next section.

The experimental determination of the Poisson's ratio of fresh concrete is a very challenging task. In a study on 3-D consolidation of saturated clay, a value of Poisson's ratio of 0.4 was found at the solids percolation threshold [269]. A similar value was reported for saturated clays also by Bowles [270]. Lower values of Poisson's ratio are reported for unsaturated clays (0.1-0.3) or sandy clays (0.2-0.3) [270]. Also, values around 0.3 were reported for early-age cement paste after setting [271]. In lack of direct experimental evidence, in particular considering the effect of drying and capillary pressure stiffening, a constant Poisson's ratio equal to 1/3 was assumed in the simulations.

6.3.2. Failure criteria

Failure is assessed based on two criteria: Bresler-Pister and Rankine. Here, the applied failure criteria are briefly presented, while the derivation of the equation describing the failure curves is presented in Appendix 6-A.

6.3.2.1. Bresler-Pister criterion

The Bresler-Pister criterion [243,252,253] (see *Fig. 6. 2* and eq. (6-9)) was initially developed to model the resistance of hardened concrete under multiaxial stresses. It was developed as an extension of Drucker-Prager shear failure model for soils [252,256]. Similarly as in the Drucker-Prager model with cap failure [255,272], the Bresler-Pister criterion used here also accounts for the hydrostatic model of failure (corresponding to the *cap* in the failure curve). The derivation of the equation of the failure curve of the Bresler-Pister model presented in *Fig. 6. 2* and eq. (6-9) based on the experimentally-determined compressive pseudo-elastic stress limit explained in section 6.2 and fresh concrete's shear strength propertiesis is presented in Appendix 6-A. According to the Bresler-Pister criterion with parameters derived in Appendix 6-A, the failure can be written in terms of stress invariants:

$$\sqrt{J_2} = \left(-\frac{C + 3p_{pel-c}\tan\phi}{9p_{pel-c}^2} \right)I_1^2 + I_1\tan\phi + C \qquad (6\text{-}9)$$

where, J_2 [Pa^2] and I_1 [Pa] are the principal stress invariants (see Appendix 6-A)*, C* [Pa] and ϕ [Pa] are the shear strength material properties in the Drucker-Prager failure criterion that are related to *c* [Pa] (cohesion) and φ [degree] (angle of internal friction) in the Mohr-Coulomb criterion [243,272] (see eqs. (6-A-10) and (6-A-11)). The angle of internal friction for fresh mortar was found to be 11° to 42° [273]. Here, the angle was assumed as equal to 27°, close to the value of 31.5° proposed for sand-to-cement (s/c) ratio of 2 and water-to-cement ratio of 0.45 in [273]. Increasing the aggregate content increases the friction angle [273,274]. Furthermore, based on the conclusions of [275], it was assumed that the friction angle remains constant, while cement hydration increases the cohesion.
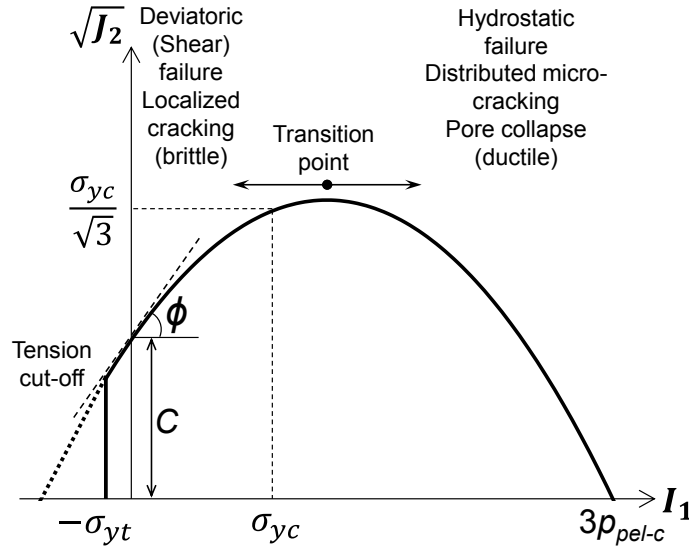
Fig. 6. 2. Bresler-Pister failure model for cementitious materials with material parameters adapted according to the Drucker-Prager model including the tension cut-off and cap failure. The axes are not scaled equally. Compressive stresses are assumed positive.

Mind that *C* and p_{pel-c} evolve, due to the hydration and capillary pressure. The effect of capillary pressure (i.e. isotropic stress) on the cohesion [220] was taken into account, since the pseudo-elastic limit was obtained by considering the effect of the isotropic stress on the stress-strain curve (see section 6.2). The evolution of the compressive pseudo-elastic limit was estimated in section 6.2 according to the data presented in Chapter 5. The evolution of the cohesion can be linked to the development of the compressive pseudo-elastic limit by assuming a linear relationship between the increments of p_{pel-c} and the cohesion. In lack of experimental data, ratios between the two increments dC/dp_{pel-c} equal to (0.2, 0.3, 0.4) were employed in this study. Higher values for the latter ratio would imply that the tensile strength of concrete becomes too high

compared to the compressive strength. The initial value of the cohesion was assumed zero, as stated in [275].

6.3.2.2. Rankine criterion

Rankine's failure theory states that a brittle material fails when the maximum principal normal stress exceeds the tensile strength during a uniaxial stress test [254,276]. The tensile strength was estimated according to Griffith's failure envelope, as explained in the previous section, and was compared with the tensile principal stress.

6.3.2.3. Boundary conditions and mesh size

Fig. 6. 3 shows the mesh and boundary conditions. To avoid the stress singularity, the sharp edges were substituted by fillets of radius 2 mm. The radius was chosen equal to half of the maximum aggregate diameter (D=4 mm). In *Fig. 6. 3*, the first and second word written on the boundaries in the figure belong to the boundary condition of the structural mechanics (explained in this study) and moisture transfer (explained in Chapter 5) modules, respectively. The mesh was generated by the utilized FEM (Finite Element Method) software, COMSOL Multiphysics®.
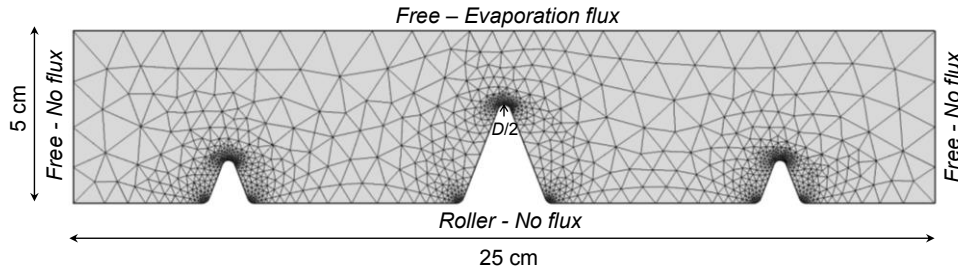
Fig. 6. 3. Mesh sizes and boundary conditions. D is the maximum aggregate diameter. The implemented mesh consists of 1994 triangular finite elements.

In the free boundary condition, the displacement is allowed in all directions. In roller, the displacement is not allowed in the direction normal to the surface:

$$\textbf{\textit{n.u}}=0 \tag{6-10}$$

where $\textbf{\textit{u}}$ is the displacement vector and $\textbf{\textit{n}}$ is the vector normal to the surface. No flux means that the flux according to the Darcy-Buckingham equation towards the normal direction of the surface is equal to zero:

$$\textbf{\textit{-n.}}\nabla(\psi_p+\rho_f gy)=0 \tag{6-11}$$

where y [m] is the elevation and ρ_f [kg/m^3] is the pore fluid density. The evaporative flux is the evaporation rate obtained experimentally by measuring the mass changes of the sample. Initially, when the bleeding rate (b) is higher than the evaporation rate of free water (e), water accumulates

at the surface (surface pores stay saturated) and Dirichlet boundary condition are applied on the wet surface, eq. (6-12):

$$\psi_p = 0 \qquad\qquad (6\text{-}12)$$

After the cumulative bleeding and evaporated water curves intersect as shown in *Fig. 6. 4* (pores of the surface start desaturating), the latter boundary condition is replaced with the flux determined from mass measurements (Neumann boundary condition).

The initial values are:

If $e \geq b$ $\qquad\qquad\qquad\qquad\qquad\qquad\qquad\qquad\qquad\qquad (6\text{-}13\text{-}1)$

$\psi_p = \rho_c g(h-z)$ immediately after casting and $\psi_p = \rho_f g(h-z)$ immediately at the end of the bleeding state

If $b > e$: $\qquad\qquad\qquad\qquad\qquad\qquad\qquad\qquad\qquad\qquad (6\text{-}13\text{-}2)$

$$\psi_p = \rho_c g(h-z)$$

6.4. Bleeding and drying states

Fig. 6. 4 shows the plastic shrinkage physical states after concrete casting at t_c [min]. The end of the bleeding state can be estimated as the time instant when the cumulative bleeding intersects the mass loss due to evaporation. In this study, the evaporation rate was measured experimentally and bleeding was simulated according to the procedure described in Chapter 3.

The evaporation rate of mortars in the constant rate period was found to be very close to the evaporation of free water [17]. The evaporation rate of free water and mortars or concretes during the constant rate period, when draining of surface pores starts, can be estimated according to the analytical method proposed in [37]. After the constant rate period, the evaporation rate falls primarily due to the change in the intrinsic permeability caused by cement hydration, see Chapters 4 and 5.

In this study, first the onset of the drying state was determined. Then the restraint stresses were determined from the casting time until the end of the bleeding state, based on the free volumetric deformations. The latter stresses were added to the stresses determined in the drying state as the initial values.

The evaporation rate in the specific environmental conditions and specific concrete applied here was estimated based on the initial rate in the constant rate period applied here and

assuming that the effect of hydration-dependent microstructure (permeability) is as found for the same mortar tested in Chapter 5. The initial rate of evaporation considered here was about 0.9 of that in Chapter 5. Consequently, the evaporation rate used in the simulations was the one in Chapter 5 multiplied by 0.9.
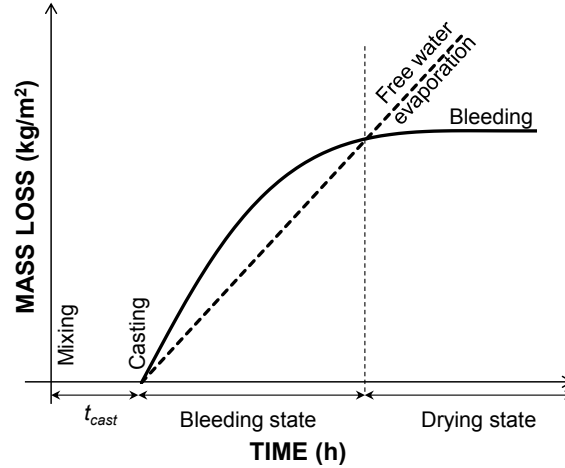
Fig. 6. 4. States of plastic shrinkage in a fresh cementitious material

6.5. Experimental methods

6.5.1. Mix design

The mortars investigated in this study, based on a Portland cement CEM I 42.5N, are shown in *Table 6. 2*; they are identical to the ones tested in Chapter 5. Two mortars were studied: a reference (REF) with Portland cement and a mortar with 20% by volume reduction of cement by silica fume (SF20%). Both mortars had the same volume of aggregates (51 %) and similar water-to-binder ratio (w/b) by mass, with a small difference in the latter resulting from different densities of silica fume and cement, see *Table 6. 2*. The volumetric water content was the same. Mixing took place in a 2-l Hobart mixer. The dry materials were mixed for 30 s. Then water was added and mixing was continued for a further 1 min. The air content and consistency were determined according to EN 12350-7 [236] and EN 1015-3 [238], respectively. The densities were measured by filling a 350 ml cylindrical bowl with mortars and weighing after compaction for 12 s on a vibrating table.

Table 6. 2. Mix designs and physical properties of mortars

Mortar	Water (kg/m³)	Cement (kg/m³)	Silica fume (kg/m³)	Sand [0-1mm] (kg/m³)	Sand [1-4mm] (kg/m³)	Measured air content (%)	w/b (-)	w/c (-)	Estimated density (kg/m³)	Measured density (kg/m³)	Spread diameter (cm)
REF	270	600	0	810	540	3	0.45	0.45	2220	2243	21.5
SF20%	270	480	84	810	540	3	0.48	0.56	2184	2164	15.5

6.5.2. Restrained plastic shrinkage test and X-ray radiography

X-ray radiography carried out on mortars cast in a HD polyethylene mold with geometry in the imaging plane based on that prescribed in ASTM C1579 [132] (plane dimensions of the sample 50×250 mm^2), but thinner in the out of plane direction (80 mm) as to enable sufficient X-ray transmission, see *Fig. 6. 5*. The fan placed over the top surface provided air flow with speed 0.9±0.2 m/s. The room temperature and relative humidity were 25 °C and 27 %, respectively. The mold was filled with mortar and was compacted by manual shaking for 12 s. The tests started 40 min after mixing.
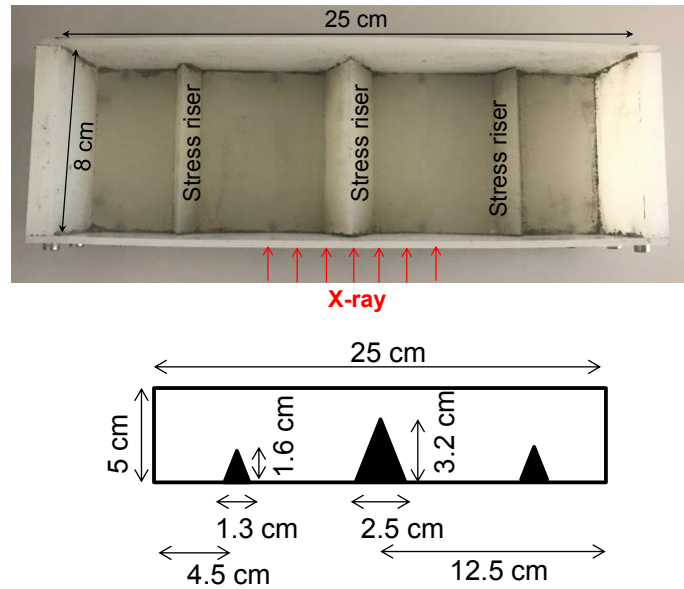
Fig. 6. 5. Details of mold for imaging of plastic shrinkage cracking and direction of X-ray beam.
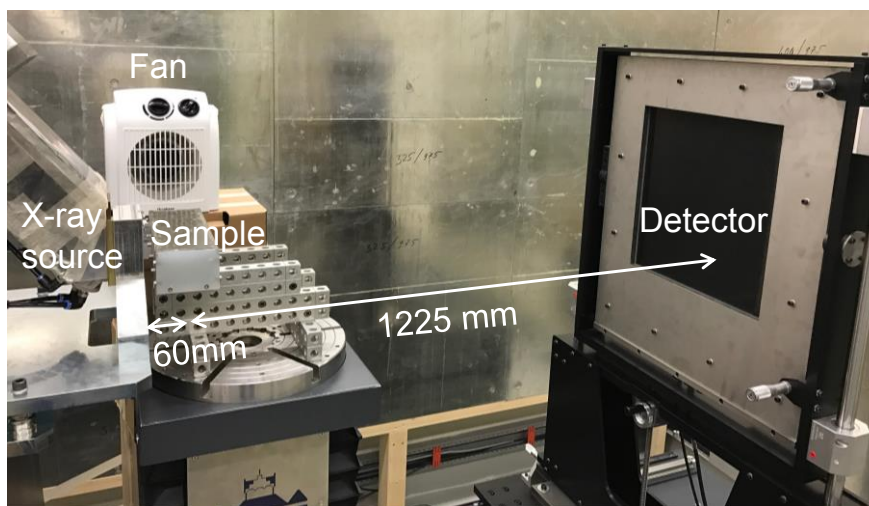
Fig. 6. 6 X-ray radiography set-up

The specimens were imaged in radiography with the X-ray µDETECT setup at Empa (see *Fig. 6. 6*) with no rotation. In this instrument, the X-ray radiation is generated by a micro-focus X-ray tube from Finetec (model FOMR 300.03Y RT) operating at an acceleration

voltage of 280 kV and a tube current of 70 µA. A flat panel detector from Perkin Elmer (model XRD 1611-CP3) acquired the projection images, in its full-resolution mode, corresponding to pixels of 100×100 µm². An acquisition time of 2 s was employed, and a total of 15 images were averaged per time frame. The sample was placed as close as possible to the source, at roughly 60 mm from the focus, and the detector was located at a distance of 1225 mm from the sample.

6.5.3. Determination of the pseudo-elastic limit

To determine the pseudo-elastic limit according to the method proposed in section 6.2, first the parameters of eq. (6-1) were obtained with the following method. The experimental bulk modulus was calculated utilizing the experimentally-measured volumetric plastic shrinkage and pore pressure in Chapter 5 (equal to the effective stress in a thin sample with negligible effect of gravity) and the incremental stress-strain relationship:

$$B_e = \frac{\Delta\sigma_{eff}}{\Delta\varepsilon_{vol}} \qquad (6\text{-}14)$$

The time increment (Δt) was identical to the time increment in the DIC measurements, 3 min, as performed in Chapter 5. Then eq. (6-15), which takes into account the effect of negative pore pressure on stiffness after the solid percolation, was fitted to the experimental data by the least squares method (see *Fig. 6. 7*).

$$\psi_p \geq \rho_f g(h\text{-}z) \qquad\qquad\qquad B_e = B_b \qquad\qquad (6\text{-}15\text{-}1)$$

$$\psi_p < \rho_f g(h\text{-}z) \qquad B_e = B_b[(1-\xi)\exp(\omega[\psi_p - \rho_f g(h-z)])+\xi] \qquad (6\text{-}15\text{-}2)$$

The determined parameters were: ξ=8.1 [-] identical for both mortars and ω=1.3 and 0.6 [1/kPa], for REF and SF20%, respectively. The latter is in line with the experimental evidences for soils [277], where it is shown that ω decreases by moving from coarser to finer particle size distribution, while ξ remains constant.

Following to the above-mentioned parameter calibrations, the evolution of the pseudo-elastic limit was obtained by the method proposed in section 2, yielding the evolution presented in *Fig. 6. 8*. As it is presented in *Fig. 6. 8*, reducing the clinker content retards the evolution of the pseudo-elastic limit.
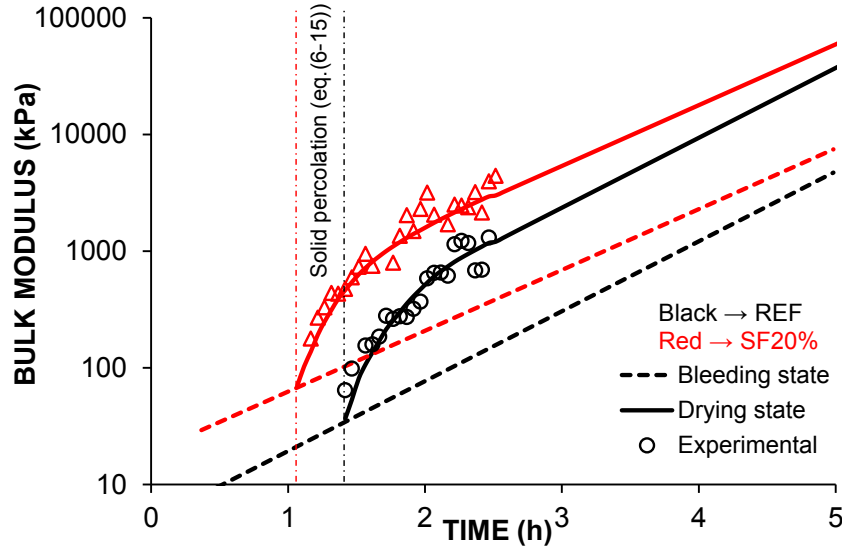
Fig. 6. 7. Evolution of bulk modulus in the drying state, according to the experimental plastic shrinkage test data and eq. (6-15), performed on samples of size $250 \times 250 \times 100 \ mm^3$ in Chapter 5.
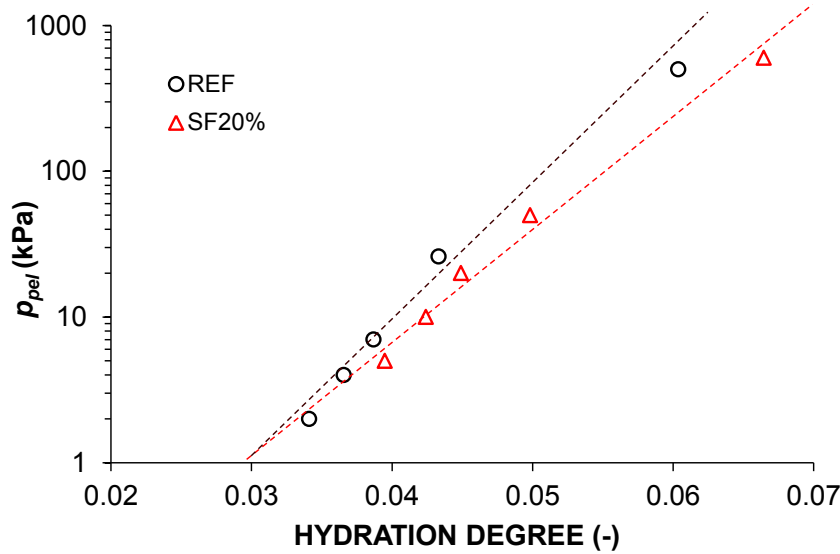
Fig. 6. 8. Evolution of pseudo-elastic limit vs. hydration degree.

It should be mentioned that the method proposed here calculates the average values of the parameters of eq. (6-1) during the performed plastic shrinkage test in Chapter 5 by fitting the experimental data. As an alternative, one could explicitly determine the dependence of bulk modulus upon capillary pressure along the hydration by repeating the plastic shrinkage test on thin samples (to enable faster equilibration of pressure) at certain time intervals, similar to Chapter 5. At each test, high wind speed needs to be provided to accelerate the evaporation. The pore pressure or the effective stress evolution can be measured by tensiometers. Furthermore, the volumetric deformation can be measured with the DIC system described in Chapter 5.

6.6. Model verification

6.6.1. Evaporation and bleeding rates

Fig. 6. 9 shows the simulated bleeding curves and measured evaporation rate (0.65 ± 0.03 kg/m^{2}h). t_{cast} was equal to 0.67 h for both tested mortars. The REF mortar experienced bleeding during 1.7 h, due to the higher bleeding rate compared to the evaporation rate, while SF20% entered the drying state right after the beginning of the test. *Fig. 6. 10* shows the utilized evaporation rates.
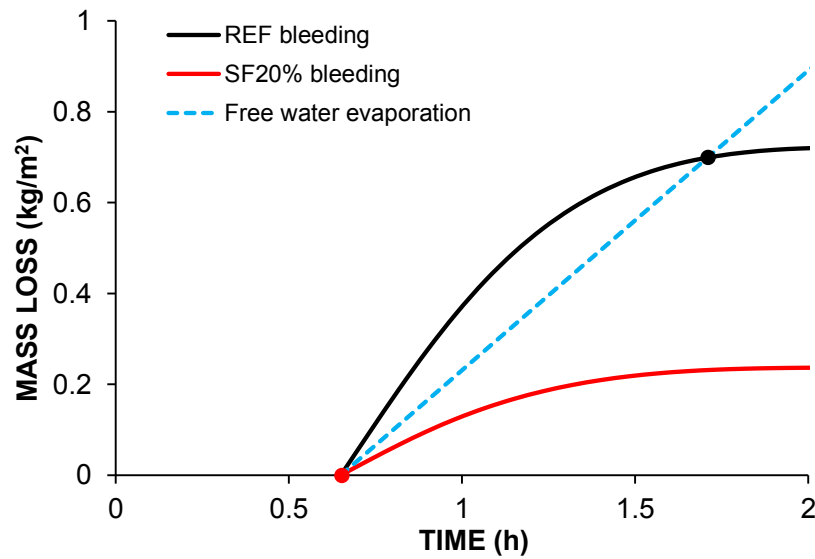
Fig. 6. 9. Simulated bleeding and experimentally measured evaporation mass loss vs. time. Black and red dots show the beginning of the drying state for REF and SF20%, respectively.
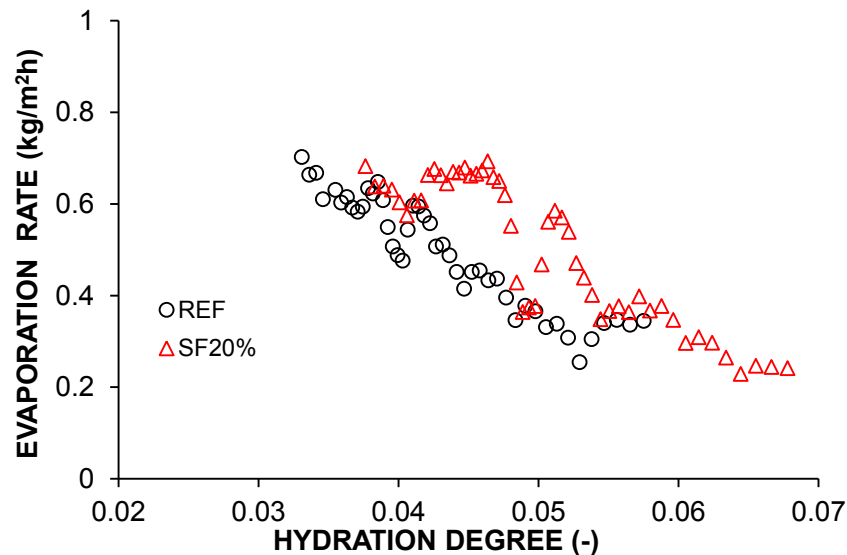
Fig. 6. 10. Evaporation rate vs. hydration degree used in the model

6.6.2. Failure

6.6.2.1. Experimental crack detection

Fig. 6. 11 shows the crack initiation at the tip of the stress riser in the middle of the mold obtained by X-ray radiography. The time shown in the pictures is from mixing time. SF20% cracked earlier at 2.33 h comparing to REF at 2.75 h. After crack initiation, the cracks propagated rapidly to the top surfaces. At the end of the test, in SF20% a substantially larger crack was evident.
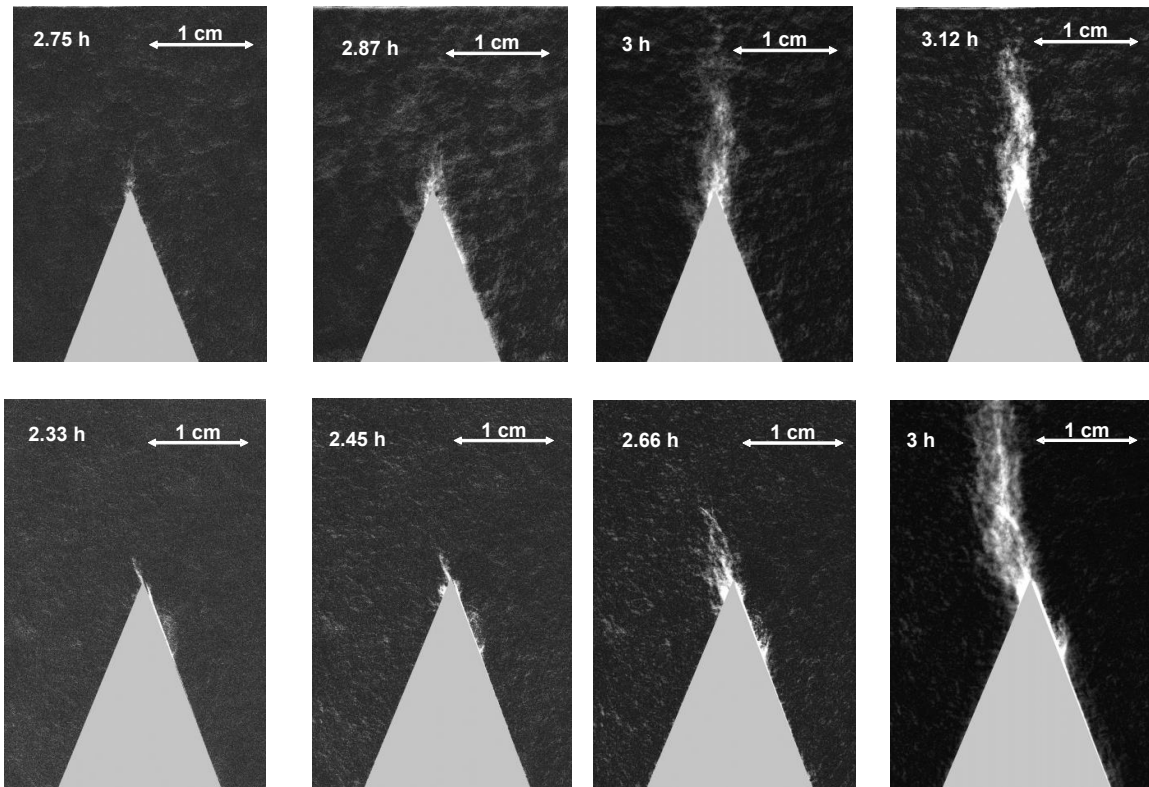
Fig. 6. 11. Plastic shrinkage cracking initiation and propagation in the drying state for REF (above) and SF20% (below), detected by X-ray radiography. The values on top left corner show the time after mixing.

6.6.2.2. Modeled crack initiation

The free shrinkage was obtained according to the model explained in Chapter 5, and was applied as input to the structural mechanics model to obtain the restraint stresses. *Fig. 6. 12* shows the restrained deformation of SF20% (note that the deformations were qualitatively similar) and the position of failure initiation. As expected, the failure occurred at the tip of the largest stress riser, due to the restraint stress concentration. Both failure criteria (Bresler-Pister and Rankine, see section 3.2) showed the same position and time of failure initiation.
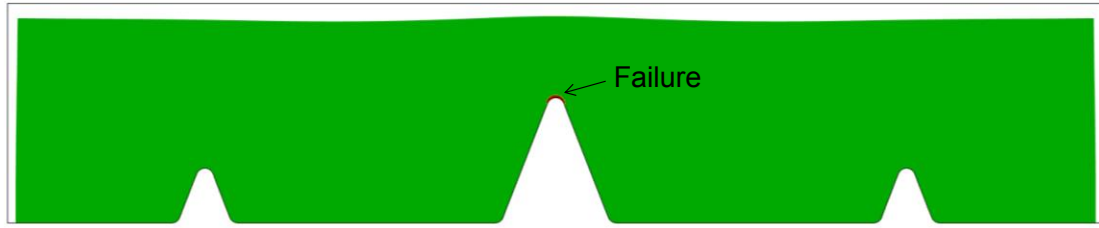
Fig. 6. 12. Deformation of the SF20% mortar in restrained conditions and position of failure initiation. The deformations are overscaled for better visibility.

The failure is explained in detail in the next section by extracting the related average values of principal stresses and comparing them with the failure criteria.

Crack propagation has not been modeled in this work. As explained in the introduction, the failure is defined to occur due to the crack initiation. Crack propagation could be modeled by FEM remeshing techniques and XFEM (Extended Finite Element Method) to simulate the occurred discontinuity [245,278] or by the phase-field method, which reproduces the crack paths without introducing discontinuities on a fixed mesh [279].

6.6.2.2.1. Crack initiation according to Bresler-Pister's criterion

Fig. 6. 13 and *Fig. 6. 14* show the stress development and the strength envelope at the time of failure according to the Bresler-Pister criterion. The time interval between markers is fixed at 5 min. The rate of increment of stresses increased dramatically in the drying state, due to increase of capillary pressure that further leads to a stiffening of the bulk according to eq. (6-1) as also shown in *Fig. 6. 15*. The failure occurs when the stress path intersects the strength envelope. Increasing the value of the strength ratio dC/dp_{pel-c} did not influence the failure time significantly. As explained in Chapter 5, the capillary pressure stiffens the bulk before the air entry, when high deformations take place in saturated conditions, accompanied by high capillary pressure at the evaporating surface (see *Fig. 6. 15*). The high deformations together with stiffening accelerate the stress progress, and lead to cracking. The latter has been identified as the main mechanism of plastic shrinkage cracking in the drying state.

The model underestimated the crack initiation time for both mortars, which could be due to the over-estimated evaporation rate, since the applied wind was not uniform on the sample. The latter shows the importance of having uniform wind velocity on the samples in plastic shrinkage tests in order to obtain meaningful comparable experimental results [206]. Another possible reason could be the resolution of the utilized X-ray setup, which may not be able to capture the failure right at the time of initiation. Failure occurred earlier for SF20%, which agrees well with the experimental data.
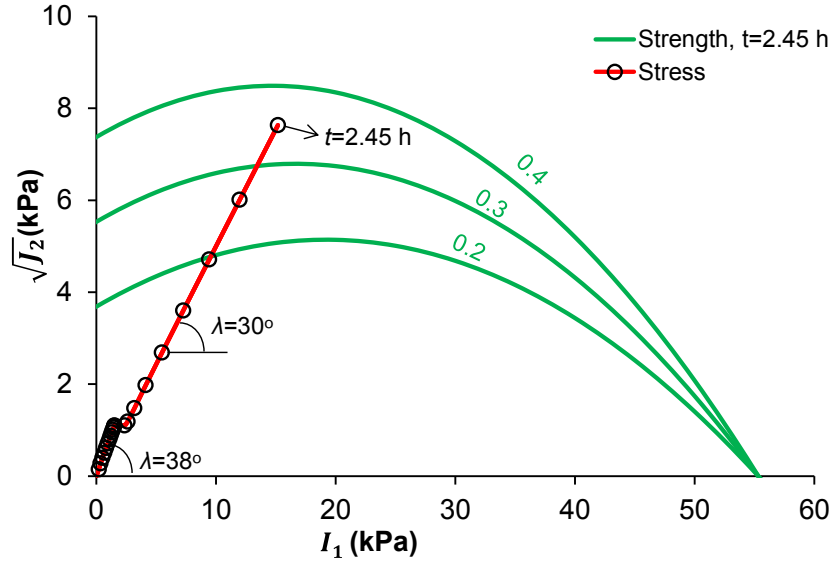
Fig. 6. 13. Stress path and the strength envelopes for REF at the time of failure according to Bresler-Pister Criterion. The numbers next to the curves refer to the ratio dC/dp_{pel-c} (see section 6.3.2.1)
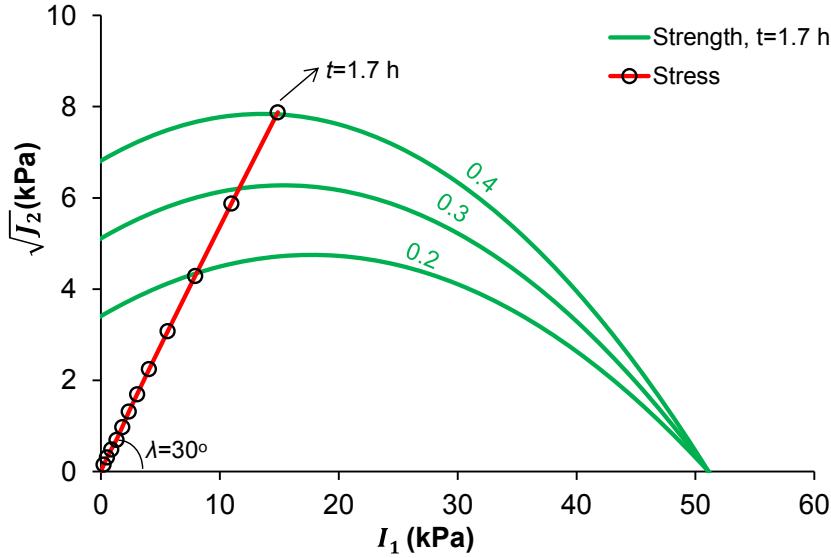
Fig. 6. 14. Stress path and the strength envelopes for SF20% at the time of failure according to Bresler-Pister Criterion. The numbers next to the curves refer to the ratio dC/dp_{pel-c} (see section 6.3.2.1)

The angle of stress path (λ [degree]) was identical for both mortars during the drying state equal to about 30°. The angle was higher for the bleeding state for the REF mortar, 38°. The latter is due to the fact that in the bleeding state the deformations are solely in vertical direction. Therefore, higher cohesion increment is needed in order to move the failure to the pore collapse regime, compared to the drying state.
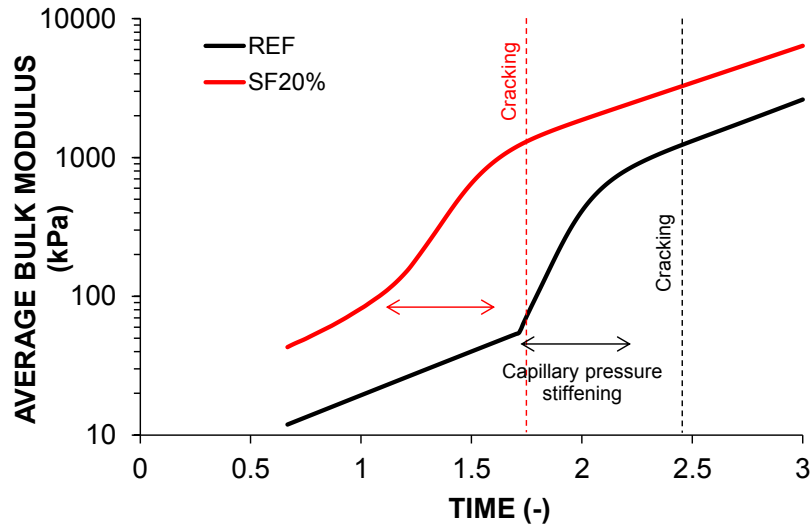
Fig. 6. 15. Simulated bulk modulus evolution. The shown periods indicate the secondary exponential evolution of bulk modulus due to the capillary pressure stiffening in the drying state.

6.6.2.2.2. Crack initiation according to Rankine's criterion

Fig. 6. 16 and *Fig. 6. 17* show the development of the principal stresses over time and their direction at the position of the failure on the tip of the largest stress riser. The principal tensile stress developed in the horizontal direction, leading to the initiation of the brittle crack, perpendicularly to the horizontal axis [157], as also obtained in the experimental failure test. The time of failure indicated by the Rankine's criterion agrees well with the Bresler-Pister criterion. The crack initiation occurring earlier in the SF mortar (while still in the dormant period of hydration) may further lead to wider crack opening compared to the REF mortar, in which crack initiation occurred in the acceleration period. This is in agreement with the findings of Chapter 4 where it was observed that faster hydration (in cements with higher clinker content or finer cements) leads to smaller crack opening.
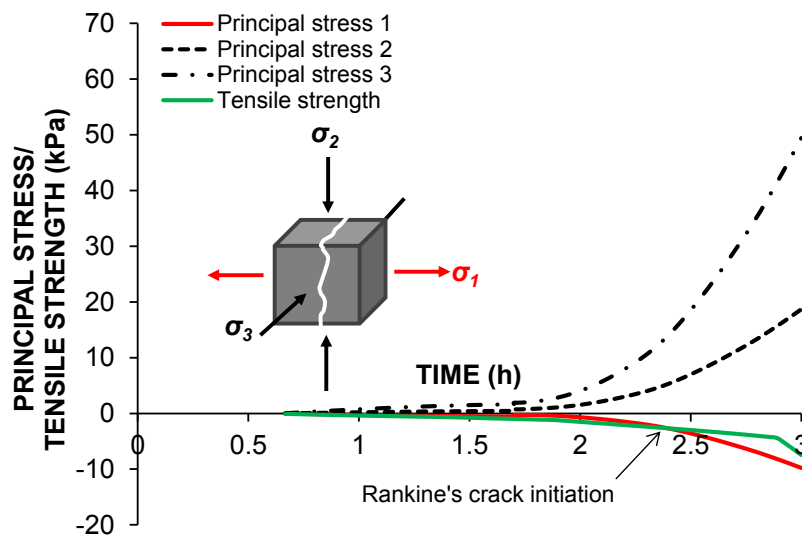
Fig. 6. 16. Principal stresses vs. time for REF.
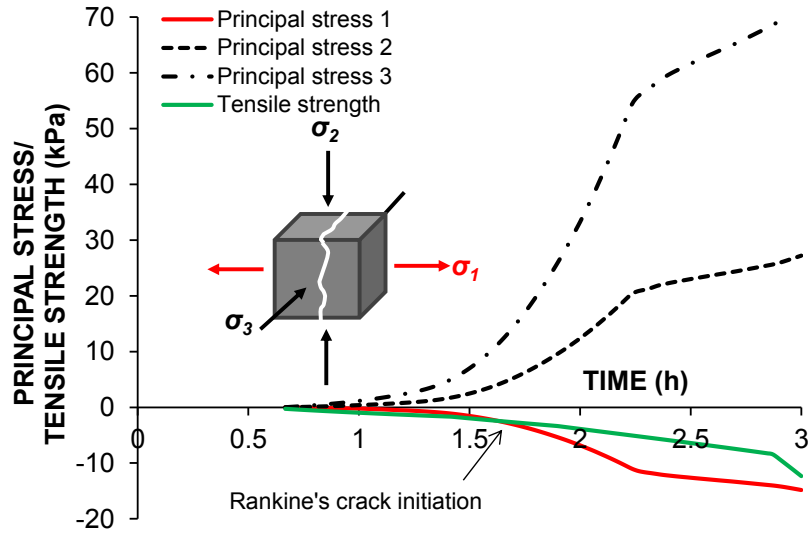
Fig. 6. 17. Principal stresses vs. time for SF20%.

6.6.3. Horizontal and vertical shrinkage

Fig. 6. 18 shows the simulated free plastic shrinkage for both mortars, with in addition a line that indicates the predicted time instant of crack initiation. REF had delayed failure initiation due to the initial bleeding, which delayed the initiation of the capillary pressure and horizontal shrinkage. The crack initiation was sometime after the onset of horizontal shrinkage as obtained in Chapter 4. According to the simulated shrinkage, crack initiation occurred when the horizontal shrinkage was 0.003 [-] for both mortars. The latter implies that the strength does not play an important role in the initiation of plastic shrinkage cracking. The plastic shrinkage crack initiation is controlled by the capillary pressure or in the other words the horizontal shrinkage. Therefore, the best method for controlling the plastic shrinkage is to reduce the capillary pressure or the horizontal shrinkage development. On the contrary, crack opening should be reduced in cements with faster evolution of hydration.
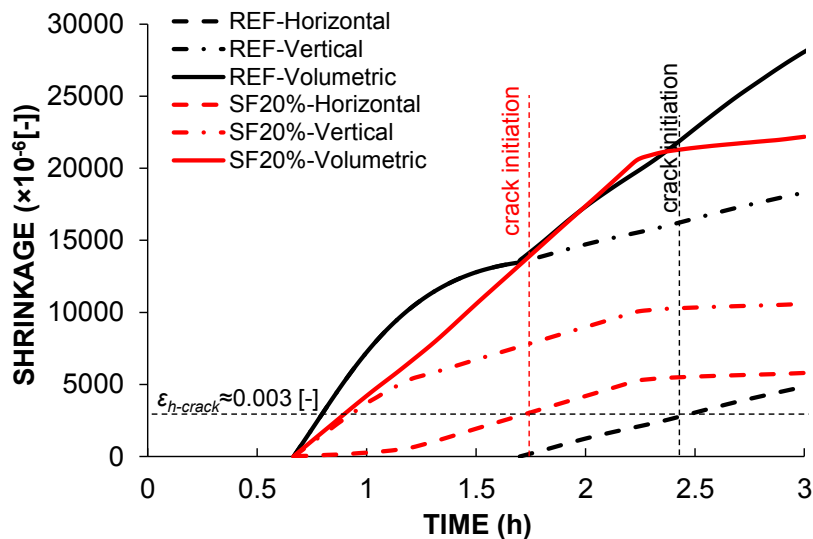
Fig. 6. 18. Simulated free plastic shrinkage vs. time.

6.7. Discussion

As shown in the previous section, the angle of stress path in the Bresler-Pister criterium was similar for both mortars in the drying state. Furthermore the failure occurred close to the von Mises envelope, in the maximum distortion energy due to the confinement brought by the capillary pressure (see *Fig. 6. 19*). Reminding that the horizontal axis in *Fig. 6. 19* represents solely the isotropic stresses (i.e. capillary pressure according to eq. (6-5)) and the I_1 invariant is zero for the deviatoric stress tensor (i.e. traceless) [280], one can derive a safe pressure limit ($p_{c\text{-}safe}$ [Pa]), based on the utilized ASTM geometry, considering that the failure occurs when:

$$p_c > p_{c-safe} = \frac{\sigma_{cy}}{3} \tag{6-16}$$
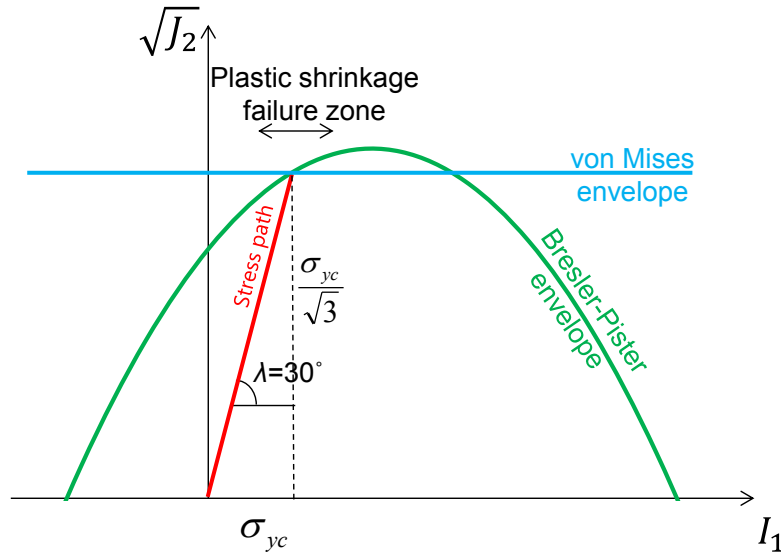
Fig. 6. 19. Plastic shrinkage failure zone

σ_{cy} is obtainable by eq. (6-A-12) and is related to the compressive pseudo-elastic limit and cohesion or tensile strength. By monitoring the capillary pressure development at the construction site [281] and applying the necessary actions (e.g., external curing), it is possible to keep the capillary pressure always below the safe limit to avoid plastic shrinkage cracking (see *Fig. 6. 20*). It is worthwhile to mention that the stated limit does not cover the cracks due to bleeding, which might occur in deep elements.
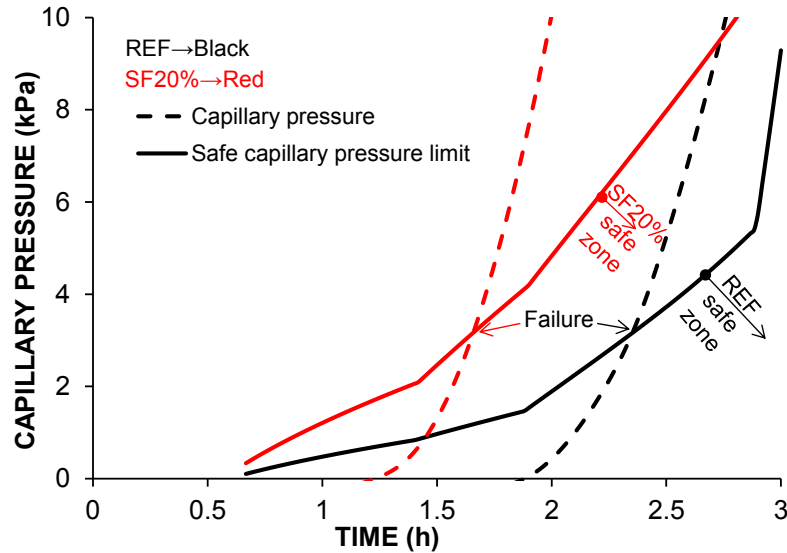
Fig. 6. 20. Evolution of safe capillary pressure limit and simulated capillary pressure vs. time.

6.8. Conclusions

The simulated capillary pressure increment in fresh cementitious materials and the resulting plastic shrinkage (see Chapter 5) were used to model the overall effective stress development in a modified ASTM test. The failure was modeled utilizing the Bresler-Pister and Rankine failure criteria. The material parameters were adapted according to the Drucker-Prager and Griffith's model. The modelled crack initiation was validated against experiments, in which the crack initiation was identified by X-ray radiography.

The mechanism of plastic shrinkage failure (cracking) in the drying state can be summarized as follows. The rapid evaporation of water from surface pores, while the whole body is still saturated, results in corresponding high deformations. Evaporation from the surface pores causes formation of menisci in these pores and the rise of capillary pressure. The capillary pressure causes a dramatic increment of the stiffness, which further leads to a corresponding increase of stresses. When these stresses exceed the failure limit, cracking initiates.

A safe capillary pressure limit was proposed according to the obtained stress path for plastic shrinkage failure and the strength properties at failure time to be used as a safe pressure limit benchmark. It is found that substitution of cement with silica fume moves the failure time to the dormant period, making the concrete more susceptible to plastic shrinkage cracking.

Acknowledgements

This page is intentionally left blank.

This page is intentionally left blank.

Chapter 7. Performance of passive methods in plastic shrinkage cracking mitigation[6]

Abstract

The occurrence of plastic shrinkage cracking in fresh concrete may significantly compromise their service life. Therefore, it is essential to reduce the crack width with appropriate, efficient and effective methods. This study is dedicated to comparing the ability of passive mitigation methods including: Shrinkage Reducing Admixtures (SRA), accelerators based on Calcium Silicate Hydrate seeding agents and curing compounds, in controlling the plastic shrinkage cracking in the drying state. The performance of the different admixtures was evaluated according to the ASTM C1579-13 standard. Furthermore, a series of complementary test methods were utilized to study the mechanism of action of the different admixtures. Among the crack mitigation methods that were studied in this study, SRA were the most effective.

Keywords: Fresh Concrete; Plastic Shrinkage Cracking; Mitigation Methods; Admixtures; Additives

7.1. Introduction

Fresh concrete undergoes volumetric shrinkage, referred to as *plastic shrinkage*, due to the effects of the gravity (in the bleeding state) [35,153] and pore water evaporation (in the drying state) [31,33], from casting to the time of final set. Since structural concrete is always restrained (e.g., by reinforcement, differential depth or knobs and dents on the substrate base, and friction between fresh concrete and substrate base), incompatibility of deformations occurs, which leads to the buildup of restraint stresses. During the above-mentioned period, concrete is plastic, possessing insignificant strength, which makes it highly susceptible to cracking when the stresses increase beyond the strength limit (see Chapter 6). Accordingly, it is mentioned that plastic shrinkage is the source of roughly 80% of the early-age cracking of reinforced concrete structures [15]. The cracks that appear on the surface may grow to widths larger than 1 mm and lengths of 50 to 1000 mm, and may be spaced in an irregular pattern from 50 to 700 mm apart [18]. In shallow elements (e.g. concrete slabs) they can even grow throughout the whole element depth (see *Fig. 7. 1* and [28]). The cracks are unsightly [28],

---

[6] This Chapter was submitted for publication in: *Ghourchian S, Wyrzykowski M, Baquerizo L, Lura P. Performance of passive methods in plastic shrinkage cracking mitigation. submitted to Cement and Concrete Composites, 2018 Jan.*

and furthermore accelerate the ingress of harmful substances (e.g. chloride ions) into the hardened concrete [11], leading to the reduction of serviceability. Therefore, they need to be eliminated or at least their width needs to be reduced with effective methods [17,77,282].

Fig. 7. 1. Plastic shrinkage cracking in the drying state in a reinforced concrete slab. Photo courtesy of Dr. Andreas Leemann, Empa.

The mitigation methods available in the engineering practice are divided into two groups: active and passive solutions. The active solutions, e.g. the ACI method, are mainly based on the evaporation rate of the free bleeding water [34]. When the rate of water evaporation is higher than the proposed critical evaporation rate (the latter derived based on a typical bleeding rate of concrete), necessary actions need to be taken. Examples of possible actions are external curing, i.e. by wetting of the concrete surface, or covering the surface by plastic sheets [54]. An improved method was proposed in Chapter 2 to complement the ACI approach to mitigate plastic shrinkage cracking in the drying state, which is based on ensuring that the total amount of bleed water is larger than the amount of evaporated water until the time of final set, instead of evaluating the evaporation/bleeding rates only.

On the other hand, passive solutions to mitigate plastic shrinkage cracking rely on modifying the material properties (e.g. by chemical admixtures), regardless of the environmental parameters, i.e. the evaporation rate. It was observed that accelerators tend to reduce the cracking risk [58,75,77], while on the contrary, retarders extend the time of set, extending the time window when cracking may appear [43],and therefore generally tend to increase the cracking risk [58,75,76]. It was also found that, with the reduction of mixing water (made possible by the use of water reducing admixtures, i.e. plasticizers), the capillary pressure development starts almost immediately after placing [75]. The latter can increase the cracking tendency considerably, since some plasticizers are also known to retard cement hydration

[58]. Shrinkage reducing admixtures (SRA), i.e. surfactants, have been shown to be very effective in controlling plastic shrinkage cracking in the drying state [17,58,77–80]. They reduce the surface tension of pore water and consequently, reduce the capillary pressure and plastic shrinkage. However, precautions are needed in using the SRA, since they may reduce the compressive strength and retard the development of mechanical properties at high dosages [21,80] and they are in general expensive. Therefore, the dosage of SRA needs to be optimized. Viscosity modifying agents (VMA) [81], i.e. stabilizers [77], primarily affect the viscosity of the pore fluid, while they also can reduce the surface tension of the pore fluid, but much less than SRA [77,81]. When they contact water, they swell first, and then dissolve, producing a viscous solution [81]. Since VMA decrease the coefficient of permeability significantly, by increasing the viscosity of pore fluid, they decrease the bleeding rate (i.e. the rate of vertical/volumetric shrinkage) [81], and consequently, they can be very effective in controlling the cracks in the bleeding state in deep elements. Reference is made to Chapter 3 for the relationship between bleeding rate and coefficient of permeability. Similar to SRA, VMA also can retard the evolution of mechanical properties [77], thus their dosage needs to be optimized. Evaporation reducers [54,283] (i.e. curing compounds [77]), e.g. paraffin dispersion, can form a film on the surface of fresh concrete and reduce the evaporation of pore fluid, and plastic shrinkage cracking. Leemann et al. [77] confirmed that they are effective also as a concrete admixture, mixed in the volume of concrete, and not only as a curing compound applied on the surface, as proposed in ACI 302.1R-04 [54]. Moreover, if they are used as an admixture, it can be assured that the curing agent accumulates on the whole surface of the concrete by bleeding, and decreases the evaporation by forming a curing film on the surface of the concrete.

It has been shown that pre-wetted lightweight aggregates (e.g. expanded shale, used in coarser fraction that the river sand they substituted) can reduce plastic shrinkage cracking in the drying state [82]. The mechanism of action is by providing the water required for evaporation [79] and thus preventing the increment of the capillary pressure. However, utilizing very fine light-weight aggregates (i.e. finer than the sand they substitute) might not mitigate cracking, since the negative aspect of the increment of the stiffness in the dormant hydration period, caused by the fine particles of the lightweight aggregates, may compensate the effect of the water provided by internal curing. See Chapters 5 and 6 for the effect of the stiffness in the dormant hydration period on plastic shrinkage cracking.

Fibers (e.g. polypropylene fibers) have been utilized in fresh concrete to reduce the size and the area of the plastic shrinkage cracks in many studies [18,50,83–97] and they are also

recommended by ACI 302.1R-04 [54]. Their mechanism of action is by: 1- Reduction of bleeding by enhancement of the concrete stiffness caused by the interlocking network of fibers [83], therefore beneficial against cracking in the bleeding state. However, the latter accelerates the capillary pressure (i.e. the effective stress) increase in the drying state (see Chapter 5). 2- Increment of the cohesion, and therefore tensile strength [83], which can prevent or retard crack propagation in the drying state. Nevertheless, fibers are not able to prevent crack nucleation, as explained in [98]. Similar conclusions can be made according to the simulations performed in Chapter 6, as well.

It has been shown that Calcium Silicate Hydrate (C-S-H) seeds act as cement hydration accelerator [284–286], shortening the dormant period and increasing the rate of hydration. According to Nicoleau [286], the efficiency of C-S-H seeding is less sensitive to the cement composition than other conventional accelerators. While no results have been published so far, it is expected that C-S-H seeding may be able to mitigate plastic shrinkage cracking, similarly as for the accelerators mentioned above [77].

In order to choose the most efficient and robust mitigation method, the performance of the above-mentioned passive solutions needs to be compared and discussed. Therefore, in this study the performance of different passive solutions, including a curing compound, SRA and C-S-H seeding, were compared. The crack size distribution was obtained with the ASTM C1579-13 standard [132], while a DIC (Digital Image Correlation) system was used to measure the free and restrained deformations in the plastic state. The temperature evolution was monitored by a semi-adiabatic temperature measurement device, in the bleeding state on mortar samples corresponding to the tested concretes. Furthermore, thermocouples and Vicat needle were utilized to record the temperature change and setting times, respectively, in the drying state. Finally, the mechanism of action of the above-mentioned additives was explained extensively, according to the novel poromechanics model proposed in Chapter 5, utilizing the above-mentioned complementary data and pore pressure measurements.

7.2. Materials and methods

7.2.1. Materials and mix compositions

The used cement was a CEM II/A-LL 42.5 N with density and Blaine fineness, 3060 kg/m^3 and 401 m^2/kg, respectively. The mix compositions are presented in *Table 7. 1*. The names of the concrete mixes indicate the type of utilized crack-reducing additive. CURE is the concrete with a paraffin-based curing agent (BASF Masterlife IC100), added in the mixer as an admixture. CSRA is the concrete containing SRA (Sika Control 60). SEED is the concrete

with the C-S-H seeds (X-Seed 100 by BASF). The amounts of the additives were based on the values recommended by the producers. A polycarboxylate-based superplasticizer was added in an amount allowing for obtaining similar consistency for all analyzed mixtures, see *Table 7. 1*. The amount of required superplasticizer increased considerably for the CURE concrete. In this case, adjusting the needed amount in steps produced no satisfactory slump until a rapid increase in slump (110 mm compared to 61 mm on average for other concretes), while the differences in flow were much lower. The individual mixes had flow different by 28 mm at most from the average of 468 mm, see *Table 7. 1*. The particle sizes of sand and gravel used as aggregates were 0-4 mm and 4-16 mm, respectively. The same cement content and water-to-cement ratio (w/c) were used in all concretes. All the constituents were stored in a climate-controlled room at 20±0.3 °C for a minimum of 12 h prior to mixing. All mixtures were prepared and tested within a 4-days' time window. Slump and flow were measured according to EN 12350-2:2009 [287] and EN 12350-5:2009 [288], respectively. The density of the fresh concrete was also determined using a 13-l cylinder.

Table 7. 1. Mix compositions

Concrete	REF	SEED	CURE	CSRA
Cement (kg/m^3)	348	348	348	348
Water (kg/m^3)	174	163.8	171	176
Sand [0-4 mm] (kg/m^3)	927	927	927	927
Gravel [4-16 mm] (kg/m^3)	928	928	928	928
Superplasticizer (kg/m^3)	1.88	1.66	3.132	1.89
Additive amount (% bwoc)	0	3.7	1.5	1.5
Additive amount (kg/m^3)	0	12.87	5.22	5.22
w/c [-]	0.5	0.5	0.5	0.5
Slump (mm)	59	60	110	65
Flow (mm)	460	440	490	480
Measured density (kg/m^3)	2321	2280	2348	2300

7.2.2. Plastic shrinkage

7.2.2.1. Environmental conditions

A climate-controlled room was utilized to maintain stable temperature and humidity conditions (33±0.5 °C and 40±5 %RH) during the test. An air blower was utilized to produce wind velocity of 7.5 ± 0.5 m/s over the top surface of the specimens. A purposefully-designed channel was utilized to obtain uniform wind speed on the samples (see Chapter 4). The mass change and the temperature of pure water in the above-mentioned environment, placed in a pan with 90 mm depth with initial temperature of 21 °C, is shown in *Fig. 7. 2*. The surface had higher initial temperature because it was in direct contact with 33 °C air, while the temperature at the bottom of the pan was lower. At first, the temperature of the water started to increase until a temperature of about 25 °C (which was lower than the room temperature

but substantially higher than the dew point temperature of 16 °C). After about 2 h, the temperature remained almost stable (with only a slow decrease over time) and the rate of evaporation increased and then remained almost constant. The overall evaporation rate of pure water in the above-mentioned environment was 1.1 kg/m²/h. This fulfills the conditions of the necessary evaporation rate prescribed in the ASTM standard (minimum 1.0 kg/m²/h). A pan with lower depth would likely reach constant evaporation rate faster, because of faster temperature equilibration.
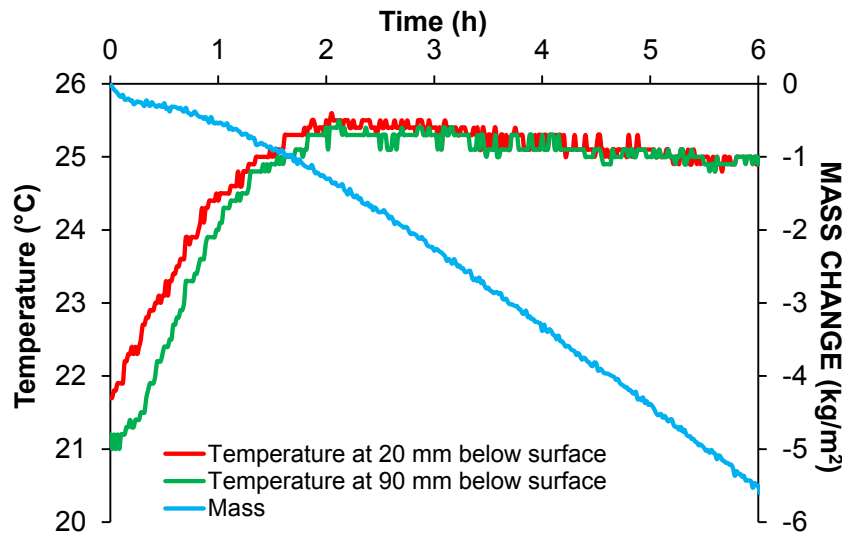
Fig. 7. 2. Mass change and temperature evolution of pure water in the test environment, placed in a pan with 90 mm depth.

7.2.2.2. Measurements of plastic shrinkage and cracking

The susceptibility of concrete mixtures to plastic shrinkage cracking was studied according to ASTM C1579-13 [132], as explained in Chapter 4. The assessment was performed by comparing the developed average crack widths. Furthermore, the free horizontal and vertical shrinkage, and the horizontal deformation across the crack was measured by DIC (see also Chapter 4). The molds were filled with concrete on a vibrating table (12 s vibration time) and the top surface was finished using a trowel. At each test, two restrained samples per concrete mixture were tested. Every experiment lasted for 6 h after the air blower was started; the cracks were measured at the conclusion of each test. For measuring the crack size, multiple high-resolution pictures (2413±50 ppi) of the crack throughout its length were taken. The crack width was then quantified by an operator with image processing software by measurements of a distance in pixels at resolution 0.01 mm at 10±1 mm intervals throughout the length of the crack. To prevent possible wall-effects on the measured crack widths, cracks widths within 25 mm of the sample edges were not taken into account.

The capillary pressure development in the free shrinkage specimen (additional specimen without the stress risers) was monitored by pressure sensors connected to capillary pipes mounted in a mold. The temperature evolution was monitored by thermocouples of resolution ±0.1 °C: two thermocouples at the bottom, two at the surface and two thermocouples at the middle of the free shrinkage samples. The evaporation rate was measured by recording the mass change of the free shrinkage sample. The complete test setup was discussed in detail in Chapter 4.

7.2.3. Bleeding

Bleeding tests were performed according to EN 480-4:2005 [289]. A cylindrical container with diameter of 250±10 mm and height of 250±10 mm was filled with concrete, which was compacted by a needle vibrator. The container was kept in the climate-controlled chamber during the parallel plastic shrinkage test and covered to avoid evaporation and desaturation. The water accumulated on the samples was collected at 15 min, 30 min, 1 h, and then every hour until 6 h from mixing. The mass of collected water was measured directly after collecting. Next, the containers were dried at 105 °C and weighed again to account for the mass of solid particles collected together with the bleeding water.

7.2.4. Semi-adiabatic temperature evolution and Vicat setting times

The measurements of the semi-adiabatic temperature evolution of mortars were performed in a climate-controlled room at 20±0.3 °C, within a thermally isolated box, with sample openings containing the cylindrical mortar samples with thermocouples placed underneath the samples (HolcimHeat®). The measurements were performed on mortars obtained by sieving the corresponding concretes on a 3.2 mm sieve. This procedure was employed in order to obtain higher content of the cement paste in the material and therefore higher signal, assuming that the removed coarse aggregates had negligible effect on heat release during hydration. 1300 g of the mortar were poured into the containers of the device and two samples were tested for each mixture. The measurements started 80±10 min after mixing.

The Vicat test was performed on the mortars obtained in the same way as for the semi-adiabatic calorimetry according to ASTM C807-13 [239] in the same room and conditions as in the plastic shrinkage tests, in the drying state. The needle had 2 mm diameter and mass of 300 g. A cylindrical mold with inner diameter 76 mm was filled with the sieved mortar and was placed in the climate-controlled room under evaporative conditions similar to the samples for plastic shrinkage. Starting at 30 min from the start of mixing, the needle was released every 10 min and its penetration depth was recorded. Before release, the needle was

brought in contact with the surface of the mortar. The time that the needle failed to penetrate up to the bottom of the sample was reported as the initial set and the time at which the needle did not penetrate into the surface was reported as the final set.

7.2.5. Compressive strength

The compressive strength test was performed on $150 \times 150 \times 150$ mm^3 samples, two samples for each test. They were stored in a climate-controlled room (20±0.3 °C, RH>95%) and were tested after 7 days and 28 days of curing.

7.3. Results

7.3.1. Bleeding

As shown in *Fig. 7. 3*, very small bleeding was measured on the REF and CURE concretes, while no bleeding could be measured on the SEED and CSRA concretes. The small bleeding is due to the low coefficient of permeability, caused by the increment of viscosity of pore fluid due to the admixtures, and by the high initial stiffness (see Chapter 3).
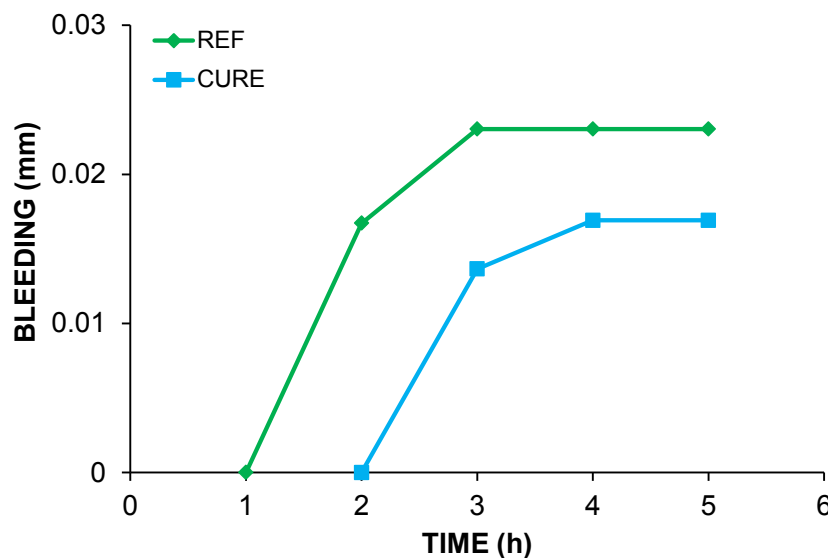
Fig. 7. 3. Bleeding vs. time measured on the REF and CURE concretes. For the other concretes, no bleeding was observed

7.3.2. Temperature evolution

The temperature evolution of concretes at the bottom of the samples (temperatures of the bulk) and at the surfaces is shown in *Fig. 7. 4*. The presented results are the average from 2 thermocouples with standard deviation of less than 0.5 °C. The bulk temperature of the samples became almost identical within the first 4 h after mixing. A very interesting trend of temperature evolution could be observed at the surface of the CURE concrete (concrete with paraffin-based curing agent) at around 4 h from mixing. Before the mentioned time, the

surface temperature increased due to the lack of surface water evaporation, while the temperature dropped later, due to a sudden increment of evaporation. The latter is discussed further in the discussion section.
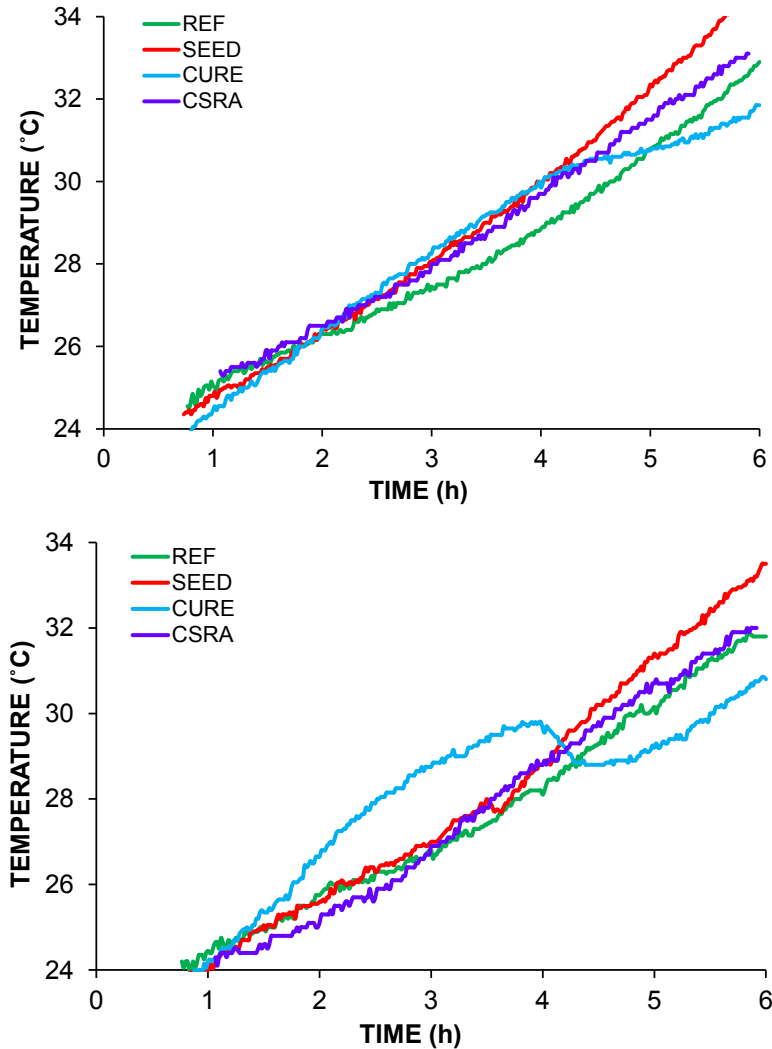
Fig. 7. 4. Average temperatures at the surface of the samples (above) and at the bottom of the samples (below).

7.3.3. Semi-adiabatic temperature evolution and Vicat setting times

Fig. 7. 5 shows the semi-adiabatic temperature evolutions measured with HolcimHeat®. The influence of the additives on the hydration kinetics was evident. The seeding agent considerably accelerated cement hydration. SRA addition only slightly delayed hydration (CSRA mixture), while the curing agent (CURE mixture) delayed hydration considerably.
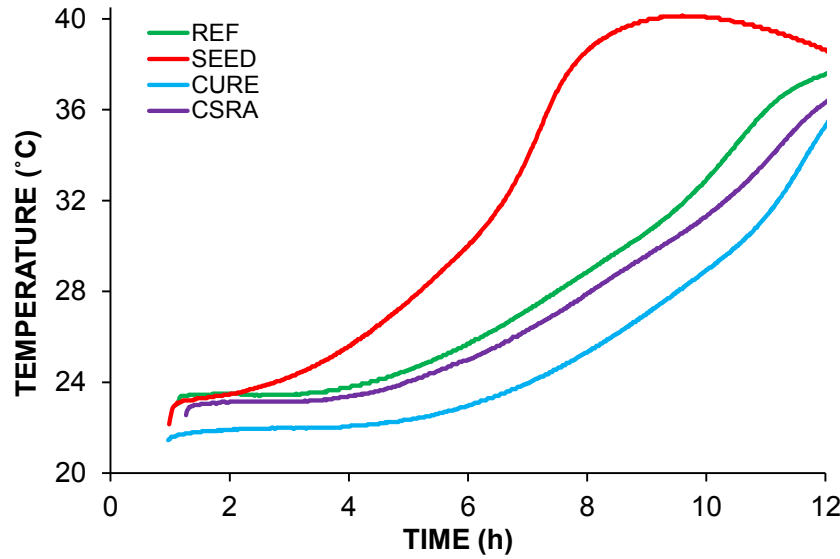
Fig. 7. 5. Semi-adiabatic temperature evolution of concrete mixtures with and without admixtures

The obtained setting times by Vicat test are shown in *Table 7. 2*. The trend is similar to that revealed in *Fig. 7. 5*. However, the capillary pressure stiffening also accelerates setting in the drying state (see Chapter 5). The initial set measured by Vicat correlates well with the onset of horizontal shrinkage as measured by DIC (see section 3.6), as also found before in Chapters 4 and 5.

Table 7. 2. Setting times determined by Vicat test on samples open to drying.

Sample	Initial	Final
REF	1h 07 min	2h 00 min
SEED	0h 55 min	1h 40 min
CURE	1h 15 min	2h 40 min
CSRA	1h 10 min	2h 20 min

7.3.4. Pore pressure development

Fig. 7. 6 shows the pore pressure development in the samples. The sudden random jump and pressure release visible in the curves are artifacts due to penetration of air into the capillary tubes of the pressure sensors. However, it is pointed out that the latter might not necessarily show the correct air-entry time, since air might not enter the capillary tube of the pressure sensor exactly at the air entry time. The capillary pressure developed in SEED earlier than in other concretes. CSRA had slower pressure progress.
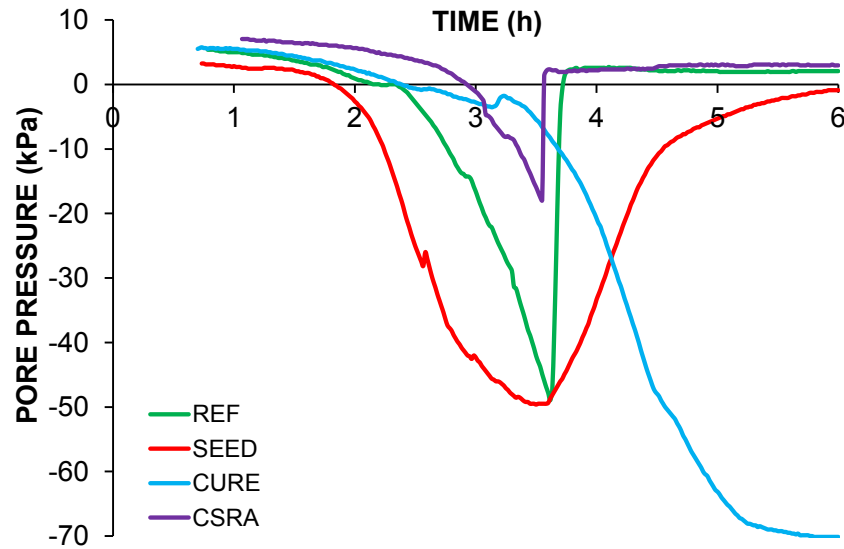
Fig. 7. 6. Pore pressure development vs. time of concrete mixtures with and without admixtures. The curves were utilized to monitor the rate of progress of capillary pressure, while the initial values might not be calibrated.

7.3.5. Mass change

The mass change vs. time is plotted in *Fig. 7. 7*. All concretes had the same initial evaporation rate, due to the same initial volumetric water content (mixing water) and environmental conditions. The different trends are discussed in the discussion section.
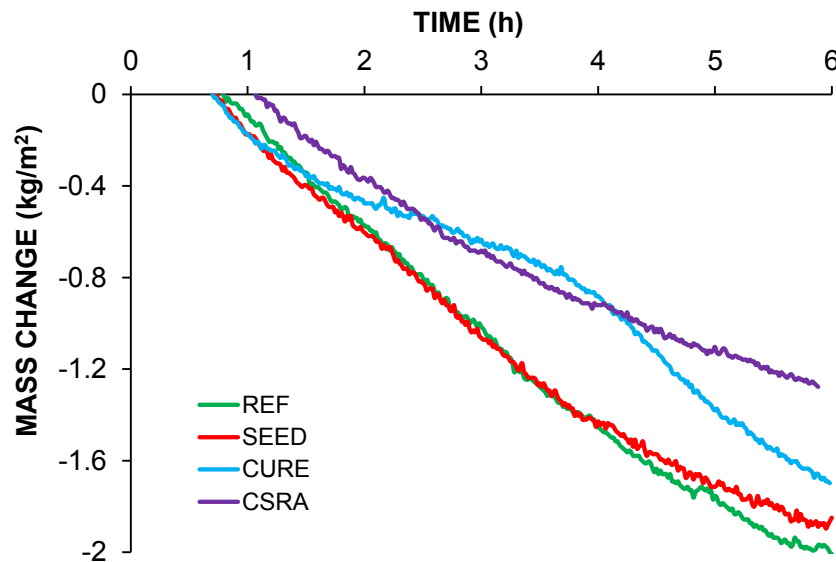
Fig. 7. 7. Mass change vs. time of concrete mixtures with and without admixtures.

7.3.6. Deformations

Strains measured with DIC are shown in *Fig. 7. 8* to *Fig. 7. 11*. The slight initial expansion observed in some samples is likely due to thermal expansion. The order of the times of final set from earlier to later was: 1-SEED 3h, 2- REF 3.5 h, CSRA 3.7 h, CURE 4.5 h. This confirms that hydration was significantly delayed and accelerated in the CURE and SEED

concretes, respectively, (see also *Fig. 7. 5*). The black dots on the across-crack deformation curves show the crack initiation time. Due to a technical problem, the standard deviations for horizontal deformations are not available, however, as shown in Chapter 4, standard deviation of the horizontal shrinkage measurements by the DIC method is below 250×10^{-6} [-].
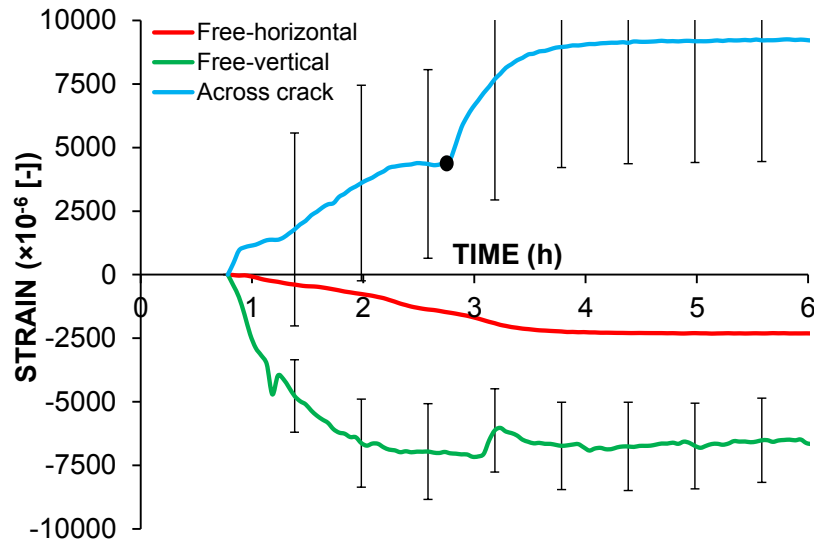
Fig. 7. 8. Strain vs. time for REF concrete. The error bars in across crack and free-vertical curves show the standard deviation between two and three measurements, respectively.
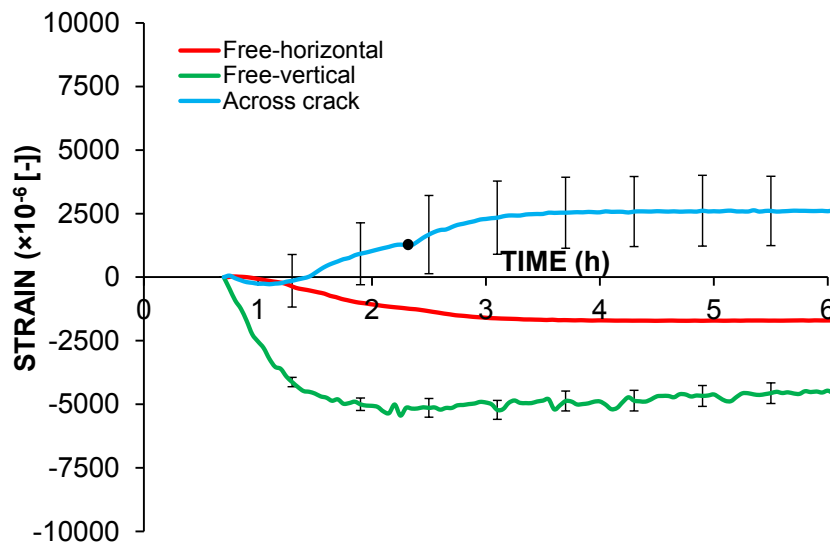
Fig. 7. 9. Strain vs. time for SEED concrete. The error bars in across crack and free-vertical curves show the standard deviation between two and three measurements, respectively.
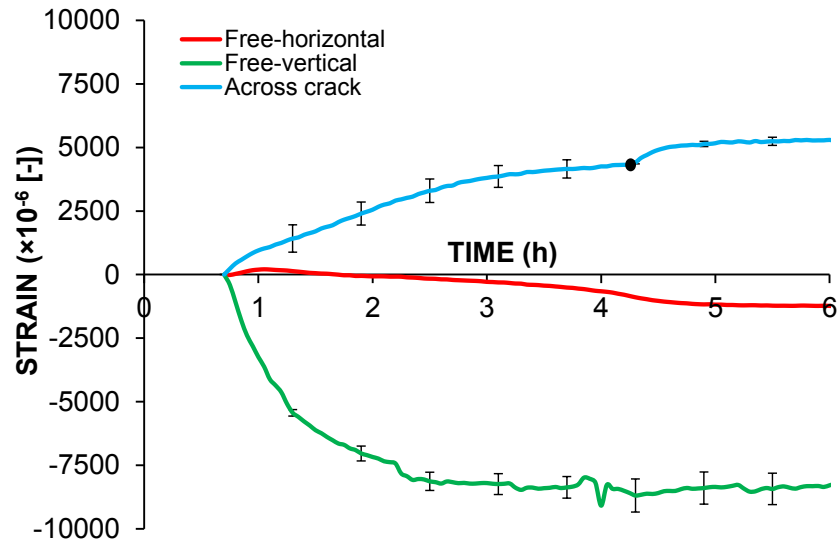
Fig. 7. 10. Strain vs. time for the CURE concrete. The error bars in across crack and free-vertical curves show the standard deviation between two and three measurements, respectively.
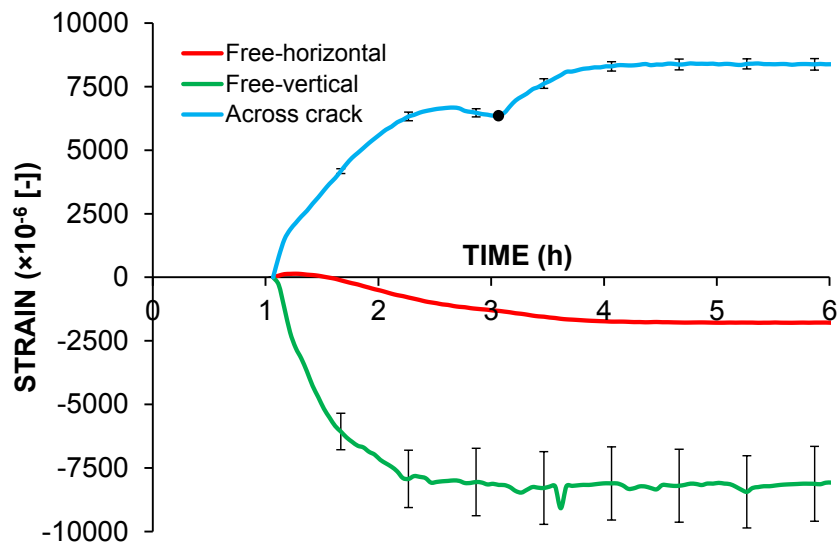
Fig. 7. 11. Strain vs. time for the CSRA concrete. The error bars in across crack and free-vertical curves show the standard deviation between two and three measurements, respectively.

7.3.7. Crack width

The cumulative crack width as a function of crack size and the average crack width for the different mixtures are shown in *Fig. 7. 12* and *Table 7. 3*, respectively. All of the additives led to reduction of the crack width compared to the reference concrete REF.
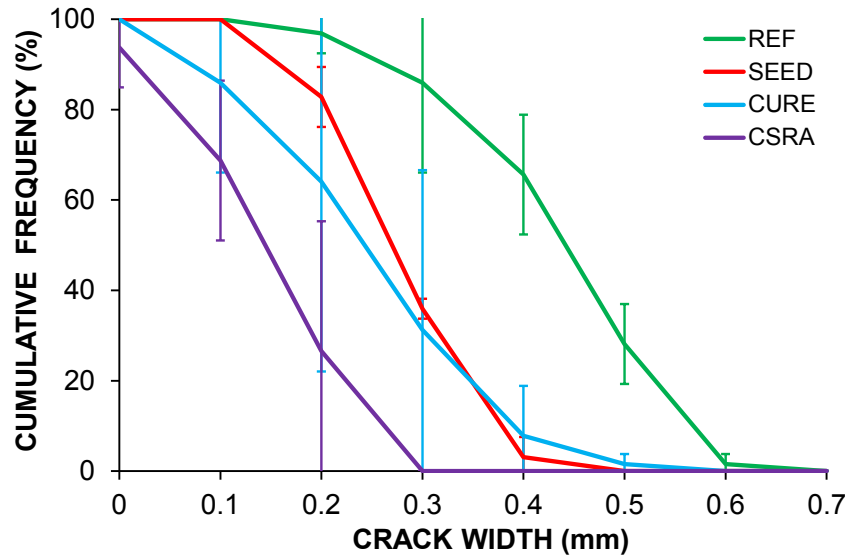
Fig. 7. 12. Cumulative crack widths of concrete mixtures made with different crack-reducing additives. The error bars represent the range of the measured values from the two samples tested in parallel.

Table 7. 3. Average crack widths of concretes made with different crack-reducing additives. Results denoted as 1 and 2 were measured on separate samples tested in parallel.

Sample	average crack width 1 (mm)	average crack width 2 (mm)	total average (mm)
REF	0.389	0.466	0.428
SEED	0.263	0.279	0.271
CURE	0.318	0.159	0.239
CSRA	0.182	0.108	0.145

7.3.8. Compressive strength

Compressive strength results are presented in *Table 7. 4*. The reported values are the average of two samples. No considerable differences could be observed between the REF, CURE and CSRA concretes, while the SEED concrete had substantially lower 28-days compressive strength.

Table 7. 4. Compressive strength results (average±standard deviation)

Sample	7-day (MPa)	28-day (MPa)
REF	45.0±0.2	51.3±0.0
SEED	40.7±0.6	46.6±0.3
CURE	42.9±0.1	50.5±0.3
CSRA	42.6±0.5	51.0±1.1

7.4. Discussions

The concretes did not bleed significantly, as shown in section 3.1. The latter was manifested also by the onset of the pressure evolution and horizontal shrinkage, right after or very close to the beginning of the plastic shrinkage test (see sections 3.4 and 3.6). See Chapter 3 and Chapter 5 for the effect of the initial stiffness on bleeding and horizontal shrinkage, respectively. The latter is in line with the conclusions of [75], according to which in mixtures with high water demand requiring superplasticizers, the onset of capillary pressure is accelerated and occurs almost immediately after placing.

During the constant rate evaporation period, the curing agent accumulated on the surface pores of CURE, forming a paraffin film that was apparently able to block the surface pores and reduce the surface coefficient of permeability, which led to lower evaporation rate (see also eq. (2)) [77,282,283]. However, at around 3.5 h to 4 h after mixing, the evaporation (see *Fig. 7. 7*) and consequently the pressure evolution (see *Fig. 7. 6*) were accelerated. The latter can be related to the evaporation of the layer of the water between the film and the surface of the concrete, when the evaporation rate decreased and less water was supplied from the bulk to keep the curing layer wet. Consequently, when the layer of water finally disappeared from the surface, most likely the film became discontinuous (i.e. pores opened again) and the rate of evaporation increased dramatically (at about 3.5 h from the start of mixing). After the opening, the evaporation rate was even higher than in the CRP, since the surface temperature had increased more than for other concretes beforehand (see *Fig. 7. 4*), due to the lack of evaporation, leading to an increased gradient of vapor pressure on the surface. The stability [50] and shrinkage and cracking [51] of the films created by curing compounds are important factors which need to be investigated further under different climatic conditions.

In CSRA, the evaporation was reduced, due to the effect of the SRA on the pore fluid's surface tension [17]. According to the Young-Laplace equation (eq. (1)), the characteristic air entry pressure decreases in CSRA concretes, i.e. the pore drainage starts with lower capillary pressure (see *Fig. 7. 13* and Chapter 5). Therefore, as shown in *Fig. 7. 13*, lower capillary pressure develops with the same amount of lost water in CSRA concretes (see also [290] for soils).

$$p_c = -\frac{2\gamma \cos\theta}{r} \tag{7-1}$$

In eq. (7-1), p_c [Pa] is the capillary pressure, γ [Pa·m] is the surface tension of the pore fluid, θ [rad] is the contact angle and r [m] is the radius of water-air menisci.
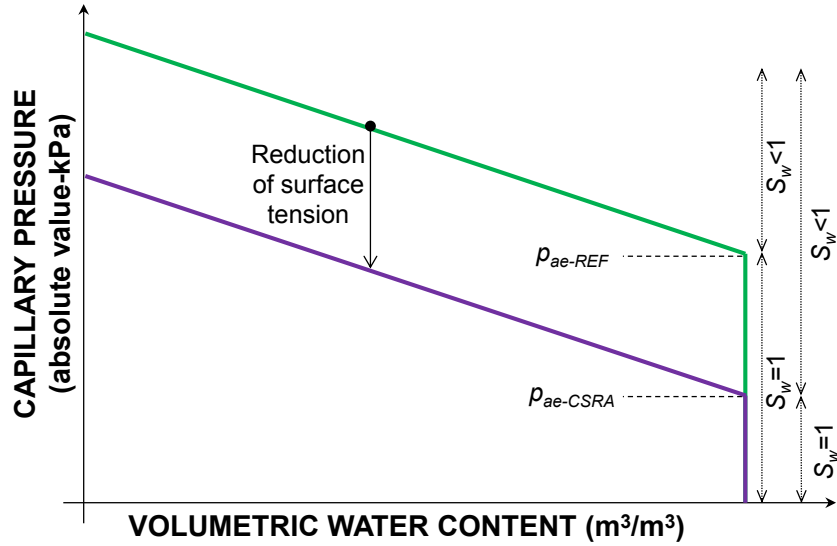
Fig. 7. 13. Schematic conceptual diagram showing the effect of SRA on the Water Retention Characteristic Curve (WRCC) of reference concrete, right after mixing. p_{ae} [kPa] indicates the characteristic air entry of concretes. S_w [-] is the saturation degree. It is assumed that after mixing all water is present in the capillary pores.

Furthermore, CSRA concretes enter the Falling Evaporation Rate Period (FRP) earlier than the reference concrete (see [17] for the effect of SRA dosage on the onset of FRP). The latter can be explained by *Fig. 7. 13*. When air enters the surface pores of CSRA, with a lower value of capillary pressure compared to REF, the resulted desaturation decreases the relative hydraulic conductivity (k_r [-]) (see [229]), leading to a reduction of the effective coefficient of permeability ($k_r k_{sat}$) in eq. (7-2). At the same time, with lower capillary pressure, the driving force for the transport of water from the bulk towards the surface is reduced, see equation 2. This leads to earlier onset of FRP (Falling Evaporation Rate Period), for CSRA compared to REF and SEED, according to the Darcy-Buckingham equation (eq. (7-2)) (see *Fig. 7. 7*). In eq. (7-2), k_{sat} [m/s] is the saturated coefficient of permeability. The latter explanation is in line with the observations of a preceding study by neutron tomography [79]. In mortars possessing identical mixing water content, the SRA-containing mortar had lower water content at the top surface, already few minutes after the beginning of the evaporation [79]. Also see [37] for the effect of surface volumetric water content and hydraulic conductivity on the evaporation rate of soils. In addition, the resulted slower progress of capillary pressure in the CSRA concrete also results in a smaller contribution of the capillary pressure to the stiffness (see Chapters 5 and 6) for the effect of stiffness on the progress of capillary pressure in the plastic shrinkage problem).

$$\vec{q} = -\frac{k_r \vec{k}_{sat}}{\rho_f g} \cdot (\nabla \psi_p + \rho_f \vec{g}) \qquad (7\text{-}2)$$

The evaporation decreased in SEED earlier than in REF, due to shorter dormant period and earlier reduction of the pore sizes in SEED, and consequently earlier reduction of intrinsic permeability as a consequence of faster hydration (see Chapter 5).

Except for the CSRA mixture, the air entry occurred primarily due to the increased stiffness of the bulk, which is due to the simultaneous reduction of pore size and evaporation rate in the hydration acceleration period, and slight progress of shrinkage, while the saturation degree most likely remained very close to 1 (see Chapter 5). However, as explained before, in CSRA the air entry was due to the effect of the SRA on the surface tension during the dormant hydration period, when pore sizes are constant (see Chapter 5). Therefore, the shrinkage proceeded even after the air entry, when the concrete was not stiff enough, and eventually stopped at around the time of final set, when the coupled effect of hydration and capillary pressure increased the stiffness of the bulk. Accordingly, CSRA had lower horizontal shrinkage, due to the effect of SRA on the WRCC (see *Fig. 7. 13*), which also was manifested by later crack initiation time comparing to REF.

The capillary pressure started to develop in SEED at an earlier time, also manifested by faster crack initiation (see *Fig. 7. 9*), due to faster evolution of the bulk modulus as a consequence of faster hydration (see *Fig. 7. 5* and *Table 7. 2*). However, accelerating cement hydration decreases the volumetric plastic shrinkage after the solid percolation. It was shown in Chapter 4 that the final crack size correlates well with the magnitude of the volumetric plastic shrinkage after solid percolation. Therefore it can be concluded that, although acceleration of cement hydration accelerated the crack initiation in this study, the reduction of shrinkage due to rapid increase of stiffness led to smaller final crack sizes. Furthermore, a faster evolution of mechanical properties (i.e. stiffness and strength), can possibly arrest the crack propagation and decrease the final crack size (see Chapters 4 and 6). It is reminded here that, opposite to the effect of cement hydration accelerators, increasing the initial values of bulk modulus with inert materials (just by increasing the solid fraction or using finer particle size distribution) may on the contrary accelerate the crack initiation and also significantly increase the final crack size (see Chapters 4 and 6).

Although CURE had initially slower capillary pressure progress, the later sudden increase of the evaporation rate (possibly due to the previously-mentioned film breakage), led to development of high capillary pressure, crack initiation and propagation. Since the intrinsic permeability was still likely high at the time of film breakage, the shrinkage caused by severe evaporation together with already high stiffness induced restraint stresses high enough to cause cracking. Since cement hydration was delayed in the CURE concrete, one hour from

the increase in evaporation rate (corresponding to possible paraffin film breakage) to the time of final set was enough for the crack to propagate to the surface (see *Fig. 7. 7* and *Fig. 7. 10*). The latter reminds the fast progress of plastic shrinkage cracking [28], and the necessity of the curing up to the time of final set, as also mentioned in Chapter 2. Finally, the CSRA concrete showed the smallest overall crack width, since 1- SRA delayed the capillary pressure progress and therefore effective stress progress (see Chapter 6), 2- SRA did not retard the hydration (i.e. strength and stiffness) significantly.

Based on the above-mentioned discussion, it can be speculated that a combination of passive methods could be even more effective. For instance, the combination of SRA or evaporation reducers with an accelerator (e.g. seeding agents), would be very effective, since the former changes the WRCC and reduces the evaporation rate, respectively, and the latter accelerates the evolution of mechanical properties. At the same time, the use of SRA would be even more effective than the use of evaporation reducers, since SRA can modify the WRCC (i.e. reduce the characteristic air entry pressure), while at the same time they also reduce the evaporation rate.

According to the compressive strength data, it can be concluded that, except for SEED, all concretes had similar 7-day and 28-day strength. Although C-S-H seeding accelerates strength enhancement up to 24 h after mixing [291], which is beneficial in controlling the plastic shrinkage cracking, they might reduce to a certain extent the later strength, as also shown in [291]. This is somewhat surprising, since contrary to other accelerators C-S-H seeds, when properly stabilized, should cause homogenous nucleation of C-S-H in the pore fluid, rather than heterogeneous nucleation on the cement grains [292]. While this is only of marginal interest for the present study, the long-term effect of C-S-H seeding on the mechanical properties of concrete needs further investigation.

7.5. Conclusions

The performance of passive plastic shrinkage cracking mitigation methods was compared according to the ASTM standard, by comparing the final crack sizes. Furthermore, complementary tests were performed to explain the mechanisms of action of passive methods according to an approach based on poromechanics.

Calcium Silicate Hydrate seeding accelerated both the pressure evolution and the mechanical properties evolution at very early ages. The fast hydration, accompanied by rapid stiffness and strength increase, arrested the crack propagation and decreased the final crack size.

However, it was also observed that Calcium Silicate Hydrate seeding slightly reduced the 7-day and 28-day compressive strength.

A curing compound (paraffin suspension) admixed into the concrete also was shown to be initially effective in reducing plastic shrinkage. However, after a couple of hours the evaporation rate of the concrete suddenly increased (possibly as a consequence of the breaking of the paraffin film at the surface). In addition, the curing compound also retarded cement hydration.

A shrinkage-reducing admixture delayed the increase in capillary pressure by reducing the characteristic air entry value, and the evaporation rate, without substantially retarding the evolution of mechanical properties (no effect on time of set). Therefore, the shrinkage-reducing admixture was found to be the most effective admixture in this study.

Moreover, it was hypothesized that the combination of different passive methods, to target both the water retention curve and the acceleration of evolution of mechanical properties, could represent a robust solution for mitigation of plastic shrinkage cracks.

This page is intentionally left blank.

This page is intentionally left blank.

Chapter 8. Conclusions

Plastic shrinkage cracking in fresh concrete might occur in both the bleeding state and the drying state. In the bleeding state, cracking is solely the consequence of the fresh concrete properties, manifesting as vertical shrinkage (settlement) before the solid percolation, which leads to the development of deviatoric stresses and cracking. This type of cracking is especially probably in deep concrete elements experiencing large settlement deformations. On the other hand, in concrete elements with higher surface to volume ratio, cracking caused by the development of capillary pressure in the drying state is more probable. For this type of cracking, the environmental factors play a fundamental role. Thus, to address plastic shrinkage cracking in both states, a thorough knowledge is required, spanning from the determination of material properties to shrinkage mechanisms, and from the latter to mitigation strategies, taking into account the climatic factors.

Although many efforts have been made to mitigate cracking in the drying state, mostly starting from rough estimations of the bleeding rate and its comparison with the recommended critical evaporation rates, they are reported to lack robustness and they possess a number of drawbacks (see Chapter 2). A robust method needs to couple the environmental factors with the material properties of the fresh concrete and needs to include the element's geometry, in order to: 1- determine the development of plastic shrinkage 2- estimate the cracking risk according to the plastic shrinkage. Therefore, this PhD project aimed to combine all above-mentioned factors and in particular the material properties, to reach to a robust method in quantifying the risk of plastic shrinkage cracking, and furthermore to recommend the most appropriate mitigation method.

The determination of the material properties started with developing a model able to simulate the bleeding process as governed by the fresh concrete's permeability and bulk modulus evolution in the bleeding state, as explained in depth in Chapter 3.

In studies dealing with cracking, and in particular cracking of fresh concrete, proper methods for quantification of the free shrinkage (the driving mechanism) and cracking (the consequence) are vital. However, the available methods possessed several drawbacks and limitations. Therefore, a novel method based on Digital Image Correlation (DIC) was introduced, combined with the well-known ASTM C1579 – 13 standard, to study the plastic shrinkage cracking mechanism. It was found that, for concretes in the same environmental conditions and similar properties right after mixing (namely water retention characteristic curve 'WRCC', permeability and bulk modulus), the cracking magnitude correlates well with

the total measured plastic shrinkage after the solid percolation. The latter was related to the hydration characteristic time (see Chapter 3), which has a good correlation with the dormant hydration period. Consequently, concretes with lower clinker content and retarded hydration were found to be more susceptible to plastic shrinkage cracking. See Chapters 3 and 4 for more details.

Once the material properties were determined accurately and robust plastic shrinkage quantification methods were developed and implemented, free plastic shrinkage was modeled by a newly-derived, modified consolidation equation, which includes a chemical shrinkage term to incorporate the effect of self-desiccation. Moreover, quantification methods were proposed for the WRCC, which can play an important role in studying the behavior of different concretes in the drying state. COMSOL$^{®}$ Multiphysics software package was utilized for numerical modelling of plastic shrinkage. Two mortars were studied with the model and in a set of genuine experiments, a reference mortar with only Portland cement and a mortar with 20% volumetric substitution of the cement with silica fume. The model was validated successfully, and it was found that in the drying state the bulk modulus, which is affected also by the capillary pressure, plays a predominant role in controlling the plastic shrinkage, and the stiffness increment accelerates the pressure progress. The inclusion of fine inert materials (e.g. silica fume), which increases the initial stiffness during the dormant hydration period, anticipates the capillary pressure progress, with high pressures developing already during the dormant period. Furthermore, inert fillers prolong the dormant hydration period, so that the concrete experiences horizontal plastic shrinkage for a longer period. The above-mentioned modeling is detailed in Chapter 5.

The knowledge regarding the evolution of concrete's cohesion and in particular of the tensile strength is essential for studying the cracking of brittle materials, i.e. fresh concrete. However, methods for the measurement of the tensile strength of fresh concrete are extremely complex and prone to artifacts. In this PhD thesis, an indirect method for the estimation of the evolution of cohesion and tensile strength was developed. This method consisted in modeling the pseudo-elastic limit in the ductile failure regime and finding the mentioned strength properties in the brittle regime using a multiaxial strength envelope, possessing cap failure together with shear and tensile failures. It was found that the strength enhancement can be described as a function of the hydration-dependent evolution of the bulk modulus in the bleeding state. After the determination of the strength evolution, the total effective stress increment was obtained by coupling the consolidation equation proposed in Chapter 5 with the solid mechanics equations. The latter approach allowed for considering a more realistic

incremental stress-strain relationship more apt for materials with non-linearity due to evolving properties, while virtually all other available consolidation theories assume linear stress-strain relationships. The crack initiation was predicted and validated successfully by a crack detection based on X-ray radiography. In line with the findings of Chapter 5, it was concluded that addition of silica fume shifts the capillary pressure progress to the dormant hydration period, when the concrete's strength is insignificant, causing faster crack initiation and more severe damage. Moreover, a safe capillary pressure limit was proposed to be utilized as a benchmark for predicting the plastic shrinkage crack initiation. Please refer to Chapter 6 for more details.

After validating the modeling approaches and shedding light on the driving mechanisms of plastic shrinkage cracking, the performance of different passive methods for plastic shrinkage cracking mitigation in the drying state was investigated in Chapter 7. It was found that some accelerators (e.g. C-S-H seeding agents) can accelerate the crack initiation time, however since they also accelerate the growth of mechanical properties in parallel, eventually they reduce the final crack size. Furthermore, it was found that utilizing SRA in the mix design is an efficient mitigation method, since they can reduce the characteristic air entry pressure, while at the same time having only minor impact on the development of the mechanical properties. It was also noticed that mitigation methods which rely on curing techniques (by active or passive elimination of the surface pore water evaporation) need to be available and stable until the time of final set, when the concrete is free from plastic shrinkage cracking risk. Otherwise, if curing is stopped to early, cracking can occur and propagate rapidly to the surface. In addition to a common risk of too early stopping of water spraying, another case may be e.g. when the curing film provided by a curing agent (passive method) breaks during evaporation. It was also recommended to combine different passive mitigation methods to obtain more robust and efficient crack mitigation. An example is utilizing the SRA or evaporation reducers in combination with hydration accelerators.

Outlook

This PhD project established and validated a poromechanics model, together with experimental and analytical methods, from material properties to mechanisms and mitigation strategies, to be utilized in future research about plastic shrinkage cracking of fresh cementitious materials. The final aim of this model is to be utilized in construction projects, helping civil engineers and contractors to avoid or reduce plastic shrinkage cracking and thereby to design and execute more sustainable concrete infrastructure.

To reach the above-mentioned goal, further research is needed to validate the model in predicting the effect of: e.g. water-to-cement ratio, paste content, cement type, admixtures and passive mitigation methods. Furthermore, the latter needs to be studied in different environmental conditions, to assess the coupling between the material properties and environmental factors. Once the validation has been performed, a database of material properties linked to mix design could be established, including: permeability, evolution of bulk modulus, WRCC, cement isothermal hydration and maturity concept parameters. Additionally, further research is needed on determining the evolution of Poisson's ratio of fresh concrete, in particular in presence of capillary pressure stiffening. This database would allow to run the model for different mix designs and for different climatic conditions to assess the risk of cracking. Thanks to the robust numerical techniques available nowadays, e.g. COMSOL$^{®}$ Multiphysics used in this thesis, it is also possible to optimize the mixes for every climatic conditions and element geometries to reach to the most efficient and economically most feasible result. Moreover, the expert systems based on this model could be used to develop apps to be installed on smart phones or laptops, to assess the cracking risk at the construction site and specify the necessary curing and mitigation technique in real time. The latter is very promising, since it could be implemented in a very simple and practical framework. It is worthwhile to mention that many models are already available to predict the water evaporation, and evaporation from the surface of porous materials, which can be coupled with the material based model proposed in this PhD project, making it truly comprehensive.

Furthermore, it is worthwhile to mention that the above-mentioned model has the potential to be extended to the simulation of the crack propagation, utilizing e.g. the phase-field method and XFEM, which include the mesh discontinuities after the crack initiation.

This page is intentionally left blank.

Appendixes

3-A: a case study using the proposed model for permeability (Chapter 3)

This appendix is a short description of concrete mixtures and measurements of fresh concrete properties and bleeding translated and adapted from [59].

The mix design is shown in *Table 3-A. 1* and *Table 3-A. 2* for concretes having different w/c and different paste content, respectively. The used cement was CEM I 42.5 N with density 3130 kg/m^3 and Blaine fineness 315 m^2/kg. A polycarboxylate-based superplasticizer was utilized to adjust the spread in the range 42 ± 4 cm. The alluvial sand and gravel used as aggregates were added as separate fractions, by mass (0-1 mm: 31%, 1-4mm: 19%, 4-8mm: 20%, 8-16mm: 30%). The density of aggregates was 2670 kg/m^3. Storage of the components and mixing took place at 20±1.5 ºC. After premixing cement and dry aggregates, 90% of the mixing water was added. The rest of the mixing water was poured into the mixer together with the admixture. For w/c0.5-p316 and w/c0.6-p290 concretes all water was added after the premixing. The concrete was mixed for approximately 90 s in a pan-type Eirich mixer. The capacity of the mixer was 80 l and each time 60 l of concrete were produced.

Flow and air content were measured right after concrete production according to EN 12350-5 [288] and EN 12350-7 [236], respectively. The bleeding test method was based on the standard EN 480-4:2005. Other standardized bleeding tests are specified in e.g.: ASTM C232 / C232M-14, EN 480-4:2005, AS 1012.6–1999, JIS A 1123:2012, ISIRI 3820, IS 9103 and RILEM CPC 16 [289,293–298].

According to the standard applied here, a cylindrical mold with height of 25 cm and diameter to height ratio equal to 1 was used. After filling the container, the concrete was compacted with a needle vibrator. Since the cylinder has known volume (12 l), the density of the fresh mixture can be obtained at the same time by determining the mass of the filled cylinder. The bleeding test started 10 min after the start of mixing for all specimens. The bleeding water was collected with a pipette at given time intervals (markers in *Fig. 3. 3* and *Fig. 3. 4* refer explicitly to the time of measurement, which was performed every 30 min during 1 h after casting and then every 1 h until bleeding ceased). Since the collected water unavoidably contained some solid particles, after the initial determination of the mass of the collected fluid, the fluid was evaporated in an oven at 100 ˚C for 24 h to determine the mass of dry residue. Directly after mixing, the concrete was moved to a controlled-climate room at 30 ± 1 ºC; all tests were performed at this temperature. During the measurements, the cylinders were covered in order to eliminate the loss of water due to evaporation.

Table 3-A. 1. Mix design of group 1 with different w/c and same paste content. The names of the mixes refer to the w/c and paste volume

Concrete	w/c0.4-p292	w/c0.5-p289	w/c0.6-p290
Aggregate (kg/m^3)	1850	1855	1857
CEM I 42,5 N (kg/m^3)	400	352	315
Water (kg/m^3)	160	176	189
Superplasticizer (%)	1.2	0.2	0
Paste volume (l/m^3)	292	289	290
w/c	0.4	0.5	0.6
Flow (cm)	46	40	44
Air content (Vol-%)	3.9	3.9	2.2

Table 3-A. 2. Mix design of group 2 with same w/c and different paste content. The names of the mixes refer to the w/c and paste volume

Concrete	w/c0.5-p263	w/c0.5-p289	w/c0.5-p316
Aggregate (kg/m^3)	1928	1855	1787
CEM I 42,5 N (kg/m^3)	320	352	385
Water (kg/m^3)	160	176	193
Superplasticizer (%)	0.2	0.2	0
Paste volume (l/m^3)	263	289	316
w/c	0.5	0.5	0.5
Flow (cm)	38	40	46
Air content (Vol-%)	3.3	3.9	3.6

3-B: Powers' classical model vs. the model presented in this study (Chapter 3)

Powers considered bleeding of concrete as the result of sedimentation of a thick suspension of solid materials in a liquid and expressed the total potential gradient (eq. (3-B-1)) as a value dependent on the unbuoyed weight of the solid materials, during constant rate bleeding [35]:

$$\nabla \psi_T = -(\rho_s - \rho_f)(1-n)g \tag{3-B-1}$$

where ρ_s [kg/m^3] is the density of solids. Substitution of eq. (3-B-1) in eq. (3-13) leads to:

$$k = \frac{b}{(1-n)(\rho_s / \rho_f - 1)} \tag{3-B-2}$$

ρ_s can be replaced by eq. (3-B-3) assuming that the strains are small and ρ_c remains constant:

$$\rho_s = \frac{\rho_c V_t - \rho_f V_f}{(1-n)V_t} \tag{3-B-3}$$

where V_f [m^3] is the fluid volume. Consequently, the denominator of the right hand side of eq. (3-B-2) can be simplified to what is proposed in this study:

$$(1-n)(\rho_s / \rho_f - 1) = \frac{(\rho_C / \rho_f)V_t - V_f}{V_t} - 1 + n = \rho_C / \rho_f - 1 \tag{3-B-4}$$

Eq. (3-B-4) shows that, when the small strain assumption is valid, sedimentation and consolidation approaches give the same formulation for the permeability of fresh concrete. Furthermore, it can be concluded that when the strains are small, the effect of change in porosity due to consolidation, thermal expansion and chemical shrinkage on the permeability of fresh concrete is negligible.

6-A: Failure envelope parameters (Chapter 6)

To link the material properties of the Bresler-Pister model (eq. (6-A-1)) [252] to the compressive pseudo-elastic limit that was obtained experiemntally in this study (see section 6.2), first the shear strength parameters of fresh concrete were determined by considering the analogy of pure shear failure with the Drucker-Prager model [255,272], and further assuming that the failure under isotropic stress corresponds to the pseudo-elastic limit.

The Bresler-Pister criterion is expressed in eq. (6-A-1)

$$\sqrt{J_2} = A_1 I_1^2 + A_2 I_1 + A_3 \tag{6-A-1}$$

where and A_1 [1/Pa], A_2 [-] and A_3 [Pa] are the material parameters and J_2 [Pa^2] and I_1 [Pa] are the principal stress invariants:

$$J_2 = \frac{1}{6}[(\sigma_1 - \sigma_2)^2 + (\sigma_2 - \sigma_3)^2 + (\sigma_3 - \sigma_1)^2] \tag{6-A-2}$$

$$I_1 = \sigma_1 + \sigma_2 + \sigma_3 \tag{6-A-3}$$

where σ_1 [Pa], σ_2 [Pa] and σ_3 [Pa] are the principal effective stresses.

In order to determine the parameters of eq. (6-A-1), consider the Drucker-Prager failure criterion with the parameters commonly used in failure of soils:

$$\sqrt{J_2} = I_1 \tan\phi + C \tag{6-A-4}$$

with C [Pa] and ϕ [Pa] being the shear strength material properties.

Assuming that the failure limit of Bresler-Pister (eq. (6-A-1)) and Drucker-Prager (eq.(6-A-4)) match when the material is purely under shear stress (pure distortion, $I_1=0$), one can write (see also *Fig. 6. 2*):

$$I_1 = 0 \Rightarrow \sqrt{J_2} = A_3 = C \tag{6-A-5}$$

$$I_1 = 0 \Rightarrow \frac{\partial \sqrt{J_2}}{\partial I_1} = A_2 = \tan\phi \tag{6-A-6}$$

The remaining parameter A_1, is obtained considering that the material fails under pure compressive isotropic stress ($J_2=0$) at the compressive pseudo-elastic limit (p_{pel-c} [Pa]):

$$\sqrt{J_2} = 0 \Rightarrow 0 = A_1 (3p_{pel-c})^2 + 3p_{pel-c} \tan\phi + C = 0 \Rightarrow A_1 = -\frac{C + 3p_{pel-c} \tan\phi}{9p_{pel-c}^2} \tag{6-A-7}$$

Therefore the final form of the Bresler-Pister criterion used in modelling of failure takes the form as presented also in eq. (6-9):

$$\sqrt{J_2} = \left(-\frac{C + 3p_{pel-c} \tan\phi}{9p_{pel-c}^2} \right) I_1^2 + I_1 \tan\phi + C \tag{6-A-8}$$

The shear failure material properties in the Drucker-Prager model are related to the ones in Mohr-Coulomb criterion according to the following equations [243,299]:

$$C = \frac{6c\cos\varphi}{\sqrt{3}(3 + \sin\varphi)} \tag{6-A-9}$$

$$\phi = \tan^{-1}\left(\frac{2\sin\varphi}{\sqrt{3}(3 + \sin\varphi)} \right) \tag{6-A-10}$$

In the failure curve in *Fig. 6. 2*, σ_{yc} [Pa] represents the uniaxial compressive (yield) strength [300] for which the material has the maximum capacity for deviatoric stresses close to vertex yielding [255], the transition surface where the von Mises criterion ($\sqrt{J_2} = \frac{\sigma_{yc}}{\sqrt{3}}$) [301,302] intersects with the Bresler-Pister envelope. At the left and right side of the vertex yielding, shear and cap failure occurs, respectively. The shear failure is a brittle failure in the form of discrete cracking. The cap failure is dominated by hydrostatic stresses and is a ductile failure in which pore collapse occurs in the form of distributed microcracking [303,304]. Accordingly, the uniaxial compressive strength, eq. (6-A-12) can be obtained by solving eq. (6-A-11):

$$\frac{\sigma_{yc}}{\sqrt{3}} = A_1 \sigma_{yc}^2 + \sigma_{yc} \tan\phi + C \tag{6-A-11}$$

$$\sigma_{yc} = -\frac{3\tan\phi - \sqrt{3} + 3\sqrt{(\tan\phi)^2 - (2/3)\sqrt{3}\tan\phi - 4A_1 C + (1/3)}}{6A_1} \tag{6-A-12}$$

The uniaxial tensile strength (σ_{yt} [Pa]) at the tension cut-off [255,305] can be determined according to Griffith's failure envelope [211,306]:

$$\sigma_{yt} = \frac{c}{2} \tag{6-A-13}$$

Therefore the hydrostatic tensile strength [255,305] is:

$$p_{pel-t} = \frac{\sigma_{yt}}{3} = \frac{c}{6} \tag{6-A-14}$$

Bibliography

[1]   K.F. Haven, 100 greatest science inventions of all time, Libraries Unlimited, 2006.

[2]   C. Shi, A.F. Jiménez, A. Palomo, New cements for the 21st century: the pursuit of an alternative to Portland cement, Cem. Concr. Res. 41 (2011) 750–763.

[3]   P. Lura, M. Wyrzykowski, M. Griffa, Shrinkage and Cracking of Concrete: Mechanisms and Impact on Durability-Course at ETH Zurich, (2017).

[4]   L. Holzer, F. Winnefeld, B. Lothenbach, D. Zampini, The early cement hydration: a multi-method approach, in: Proc. 11th Int. Congr. Chem. Cem. ICCC Durb., 2003: pp. 236–248.

[5]   R.J. Flatt, N. Roussel, C.R. Cheeseman, Concrete: an eco material that needs to be improved, J. Eur. Ceram. Soc. 32 (2012) 2787–2798.

[6]   G.P. Peters, G. Marland, C. Le Quéré, T. Boden, J.G. Canadell, M.R. Raupach, Rapid growth in CO2 emissions after the 2008-2009 global financial crisis, Nat. Clim. Change. 2 (2012) 2–4.

[7]   R.M. Andrew, Global CO2 emissions from cement production, Earth Syst Sci Data Discuss. (2017).

[8]   J. Davidovits, Global warming impact on the cement and aggregates industries, World Resour. Rev. 6 (1994) 263–278.

[9]   M.S. Imbabi, C. Carrigan, S. McKenna, Trends and developments in green cement and concrete technology, Int. J. Sustain. Built Environ. 1 (2012) 194–216.

[10]   D.P. Bentz, A review of early-age properties of cement-based materials, Cem. Concr. Res. 38 (2008) 196–204.

[11]   D.P. Bentz, E.J. Garboczi, Y. Lu, N. Martys, A.R. Sakulich, W.J. Weiss, Modeling of the influence of transverse cracking on chloride penetration into concrete, Cem. Concr. Compos. 38 (2013) 65–74.

[12]   E. Fehling, M. Schmidt, J. Walraven, T. Leutbecher, S. Fröhlich, Ultra-high Performance Concrete UHPC: Fundamentals, Design, Examples, John Wiley & Sons, 2014.

[13]   N.B. Winter, Understanding cement: An introduction to cement production, cement hydration and deleterious processes in concrete, Microanalysis Consultants, 2012.

[14]   F. Goetz-Neunhoeffer, J. Neubauer, P. Schwesig, Mineralogical characteristics of Ettringites synthesized from solutions and suspensions, Cem. Concr. Res. 36 (2006) 65–70.

[15]   H.-G. Kwak, S. Ha, W.J. Weiss, Experimental and numerical quantification of plastic settlement in fresh cementitious systems, J. Mater. Civ. Eng. 22 (2010) 951–966.

[16]   A. Zingg, L. Holzer, A. Kaech, F. Winnefeld, J. Pakusch, S. Becker, L. Gauckler, The microstructure of dispersed and non-dispersed fresh cement pastes—new insight by cryo-microscopy, Cem. Concr. Res. 38 (2008) 522–529.

[17]   P. Lura, B. Pease, G.B. Mazzotta, F. Rajabipour, J. Weiss, Influence of shrinkage-reducing admixtures on development of plastic shrinkage cracks, ACI Mater. J. 104 (2007).

[18]   S.H. Kosmatka, B. Kerkhoff, W.C. Panarese, Design and control of concrete mixtures, Portland Cement Assoc., 2011.

[19]   D. Bentz, P. Lura, J. Weiss, A Series of Workshop Lectures on Reducing Early-Age Cracking in Concrete Today (REACCT) at Purdue University, (2008).

[20]   S.-T. Lin, R. Huang, Effect of viscosity modifying agent on plastic shrinkage cracking of cementitious composites, Mater. Struct. 43 (2010) 651–664.

[21]   F. Rajabipour, G. Sant, J. Weiss, Interactions between shrinkage reducing admixtures (SRA) and cement paste's pore solution, Cem. Concr. Res. 38 (2008) 606–615.

[22]   G.H. P.-C. Aitcin and R. Morin, Controlling Plastic and Autogenous Shrinkage in High-Performance Concrete Structures by an Early Water Curing, Spec. Publ. 220 (2004). doi:10.14359/13150.

[23]   K. Terzaghi, Erdbaumechanik auf bodenphysikalischer Grundlage, (1925) 390.

[24]   K. Terzaghi, Theoretical soil mechanics, Chapman And Hali, Limited John Wiler And Sons, Inc; New York, 1944.

[25]   R.E. Goodman, Karl Terzaghi: The engineer as artist, in: American Society of Civil Engineers, 1999.

[26]   A. Verruijt, Computational geomechanics, Springer Science & Business Media, 1995.

[27]   A. Verruijt, An Introduction to Soil Mechanics, Springer International Publishing, 2018.

[28] W. Lerch, Plastic shrinkage, in: ACI 52nd Annu. Conv., Journal of the American Concrete Institute, Philadelphia, 1957: pp. 797–802.

[29] D. Ravina, R. Shalon, Plastic shrinkage cracking, in: ACI J. Proc., ACI, 1968.

[30] F.H. Wittmann, On the action of capillary pressure in fresh concrete, Cem. Concr. Res. 6 (1976) 49–56.

[31] A. Radocea, A model of plastic shrinkage, Mag. Concr. Res. 46 (1994) 125–132.

[32] M.D. Cohen, J. Olek, W.L. Dolch, Mechanism of plastic shrinkage cracking in portland cement and portland cement-silica fume paste and mortar, Cem. Concr. Res. 20 (1990) 103–119.

[33] P.J. Uno, Plastic shrinkage cracking and evaporation formulas, ACI Mater. J. 95 (1998) 365–375.

[34] ACI Committee 305, ACI 305R-10: Guide to Hot Weather Concreting, Am. Concr. Inst. (2010).

[35] T.C. Powers, Properties of Fresh Concrete, John Wiley and Sons, Inc N. Y. (1968) 301.

[36] C.A. Menzel, Causes and prevention of crack development in plastic concrete, Proc. Portland Cem. Assoc. (1954) 130–136.

[37] E. Haghighi, E. Shahraeeni, P. Lehmann, D. Or, Evaporation rates across a convective air boundary layer are dominated by diffusion, Water Resour. Res. 49 (2013) 1602–1610.

[38] M. Al-Fadhala, K.C. Hover, Rapid evaporation from freshly cast concrete and the Gulf environment, Constr. Build. Mater. 15 (2001) 1–7.

[39] H.-G. Kwak, S.-J. Ha, Plastic shrinkage cracking in concrete slabs. Part I: a numerical model, Mag. Concr. Res. 58 (2006) 505–516.

[40] A.A. Almusallam, Effect of environmental conditions on the properties of fresh and hardened concrete, Cem. Concr. Compos. 23 (2001) 353–361.

[41] P. Ghoddousi, A. Raiss ghasemi, T. Parhizkar, A comparison between plastic shrinkage of concrete containing silica fume and the normal concrete, Int. J. Civ. Eng. IUST. 5 (2007) 266–273.

[42] O.M. Jensen, Monitoring water loss form fresh concrete, in: Int. RILEM-JCI Semin. Concr. Durab. Serv. Life Plan., RILEM, 2006: pp. 197–202.

[43] C.A. Menzel, A tribute to "Causes and Prevention of Crack Development in Plastic Concrete," ACI Spec. Publ. 249 (2008) 161–172.

[44] D.P. Bentz, G. Sant, J. Weiss, Early-age properties of cement-based materials. I: Influence of cement fineness, J. Mater. Civ. Eng. 20 (2008) 502–508.

[45] S.P. Shah, W.J. Weiss, W. Yang, Shrinkage Cracking--Can It Be Prevented?, Concr. Int. 20 (1998) 51–55.

[46] A.A. Almusallam, M. Maslehuddin, M. Abdul-Waris, M.M. Khan, Effect of mix proportions on plastic shrinkage cracking of concrete in hot environments, Constr. Build. Mater. 12 (1998) 353–358.

[47] H.-G. Kwak, S.-J. Ha, Plastic shrinkage cracking in concrete slabs. Part II: numerical experiment and prediction of occurrence, Mag. Concr. Res. 58 (2006) 517–532.

[48] R. Combrinck, W.P. Boshoff, Fundamentals of plastic settlement cracking in concrete, in: Constr. Mater. Struct. Proc. First Int. Conf. Constr. Mater. Struct., IOS Press, 2014: p. 354.

[49] C. Qi, J. Weiss, J. Olek, Assessing the settlement of fresh concrete using a non-contact laser profiling approach, in: Int. Conf. Constr. Mater. ConMat05, 2005.

[50] C. Qi, J. Weiss, J. Olek, Characterization of plastic shrinkage cracking in fiber reinforced concrete using image analysis and a modified Weibull function, Mater. Struct. 36 (2003) 386–395.

[51] A.K. Schindler, Prediction of concrete setting, in: Proc. RILEM Int. Symp. Adv. Concr. Sci. Eng. Ed. By, Citeseer, 2004.

[52] D.P. Bentz, Activation energies of high-volume fly ash ternary blends: hydration and setting, Cem. Concr. Compos. 53 (2014) 214–223.

[53] L. D'Aloia, G. Chanvillard, Determining the "apparent" activation energy of concrete: Ea—numerical simulations of the heat of hydration of cement, Cem. Concr. Res. 32 (2002) 1277–1289.

[54] ACI 302.1R-04, Guide for Concrete Floor and Slab Construction, Am. Concr. Inst. (2004).

[55] A. Sivakumar, M. Santhanam, A quantitative study on the plastic shrinkage cracking in high strength hybrid fibre reinforced concrete, Cem. Concr. Compos. 29 (2007) 575–581.

[56] A. Lund, M. Skoog, R. Thorstensson, Plastiska krympsprickor i betong, Dept Struct. Mech. Eng. R. Inst. Technol. Stockh. Swed. (1997).

[57] F. Sayahi, Plastic Shrinkage Cracking in Concrete (Doctoral dissertation), Luleå University of Technology, 2016.

[58] I. Löfgren, O. Esping, Early age cracking of self-compacting concrete, in: Int. RILEM Conf. Vol. Chang. Hardening Concr. Test. Mitigation" Lyngby, 2006: pp. 251–260.

[59] P. Lura, A. Leemann, Frühschwinden von Beton. Final report of cemsuisse-Projekt 200901, December 2010, (2010) 42 pp.

[60] C.–. Yang, Effects of Water-Cement Ratio on Plastic Shrinkage Cracking of Concrete, J.-CHONGQING JIANZHU Univ. 25 (2003) 77–81.

[61] F. Sayahi, M. Emborg, H. Hedlund, I. Löfgren, PLASTIC SHRINKAGE CRACKING IN SELF-COMPACTING CONCRETE: A PARAMETRIC STUDY, in: MSSCE2016 RILEM 22082016, Rilem publications, 2016: pp. 609–619.

[62] ACI Committee 234, Guide for the Use of Silica Fume in Concrete (ACI 234R-06), Am. Concr. Inst. (2006) 63.

[63] ACI Committee 233, Slag Cement in Concrete and Mortar (ACI 233R-03) (Reapproved 2011), Am. Concr. Inst. (2006) 19.

[64] ACI Committee 232, Use of Fly Ash in Concrete (ACI 232.2R-03), Am. Concr. Inst. (2003) 41.

[65] M.A. Caldarone, High-strength concrete: a practical guide, CRC Press, 2008.

[66] A.M. Neville, Properties of Concrete (4th and final ed.) Longman, Essex UK. (1995).

[67] İ.B. Topçu, V.B. Elgün, Influence of concrete properties on bleeding and evaporation, Cem. Concr. Res. 34 (2004) 275–281.

[68] N.A. Vemuri, M.D. Newlands, K.A. Paine, R.K. Dhir, Early-age shrinkage behaviour of CEM I and fly ash combinations, in: Concr. Durab. Serv. Life Plan., 2009: pp. 474 – 481.

[69] F.T. Olorunsogo, Particle size distribution of GGBS and bleeding characteristics of slag cement mortars, Cem. Concr. Res. 28 (1998) 907–919.

[70] A.A. Almussalam, M. Maslehuddin, M. Abdul-Waris, F.H. Dakhil, O.S.B. Al-Amoudi, Plastic shrinkage cracking of blended cement concretes in hot environments, Mag. Concr. Res. 51 (1999) 241–246.

[71] V. Slowik, M. Schmidt, R. Fritzsch, Capillary pressure in fresh cement-based materials and identification of the air entry value, Cem. Concr. Compos. 30 (2008) 557–565.

[72] O.S.B. Al-Amoudi, M. Maslehuddin, M. Shameem, M. Ibrahim, Shrinkage of plain and silica fume cement concrete under hot weather, Cem. Concr. Compos. 29 (2007) 690–699.

[73] P. Lura, A. Leemann, C. Di Bella, The influence of concrete mixture composition on the risk of plastic shrinkage cracking, in: Istanbul, Turkey, 2013.

[74] K. Yang, M. Zhong, B. Magee, C. Yang, C. Wang, X. Zhu, Z. Zhang, Investigation of effects of Portland cement fineness and alkali content on concrete plastic shrinkage cracking, Constr. Build. Mater. 144 (2017) 279–290.

[75] A. Kronlöf, M. Leivo, P. Sipari, Experimental study on the basic phenomena of shrinkage and cracking of fresh mortar, Cem. Concr. Res. 25 (1995) 1747–1754.

[76] A.M. Alhozaimy, A.I. Al-Negheimish, Plastic Shrinkage in Hot and Arid Environments, Concr. Int. 31 (2009) 26–32.

[77] A. Leemann, P. Nygaard, P. Lura, Impact of admixtures on the plastic shrinkage cracking of self-compacting concrete, Cem. Concr. Compos. 46 (2014) 1–7.

[78] J. Mora-Ruacho, R. Gettu, A. Aguado, Influence of shrinkage-reducing admixtures on the reduction of plastic shrinkage cracking in concrete, Cem. Concr. Res. 39 (2009) 141–146.

[79] M. Wyrzykowski, P. Trtik, B. Münch, J. Weiss, P. Vontobel, P. Lura, Plastic shrinkage of mortars with shrinkage reducing admixture and lightweight aggregates studied by neutron tomography, Cem. Concr. Res. 73 (2015) 238–245.

[80] J. Saliba, E. Rozière, F. Grondin, A. Loukili, Influence of shrinkage-reducing admixtures on plastic and long-term shrinkage, Cem. Concr. Compos. 33 (2011) 209–217.

[81] S.-T. Lin, R. Huang, Effect of viscosity modifying agent on plastic shrinkage cracking of cementitious composites, Mater. Struct. 43 (2010) 651–664.

[82] R. Henkensiefken, P. Briatka, D. Bentz, T. Nantung, J. Weiss, Plastic shrinkage cracking in internally cured mixtures made with pre-wetted lightweight aggregate, Concr. Int. 32 (2010) 49–54.

[83] Y. Ma, M. Tan, K. Wu, Effect of different geometric polypropylene fibers on plastic shrinkage cracking of cement mortars, Mater. Struct. 35 (2002) 165–169.

[84] J. Kaufmann, F. Winnefeld, D. Hesselbarth, Effect of the addition of ultrafine cement and short fiber reinforcement on shrinkage, rheological and mechanical properties of Portland cement pastes, Cem. Concr. Compos. 26 (2004) 541–549.

[85] T. Rahmani, B. Kiani, M. Bakhshi, M. Shekarchizadeh, Application of different fibers to reduce plastic shrinkage cracking of concrete, in: 7th RILEM Int. Conf. Crack. Pavements, Springer, 2012: pp. 635–642.

[86] P. Soroushian, F. Mirza, A. Alhozajiny, Plastic shrinkage cracking of polypropylene fiber reinforced concrete, Mater. J. 92 (1993) 553–560.

[87] P. Soroushian, S. Ravanbakhsh, Control of plastic shrinkage cracking with specialty cellulose fibers, Mater. J. 95 (1998) 429–435.

[88] H.R. Shen, Y.X. She, P.W. Gao, The influence of polypropylene fiber on the performance of concrete pavement, in: Appl. Mech. Mater., Trans Tech Publ, 2012: pp. 1099–1103.

[89] Y. Shao, A. Mirmiran, Control of plastic shrinkage cracking of concrete with carbon fiber-reinforced polymer grids, J. Mater. Civ. Eng. 19 (2007) 441–444.

[90] M. Nemoz-Gaillard, D. Nectoux, E. Dallies, D. Muller, E. des Mines d'Ales, Influence of AR glass fibers on the cracking of concrete: Analysis at the very early age by digital image correlation, in: 23 Int. RILEM Conf. Early Age Crack. Cem. Syst.-EAC01, RILEM Publications, 2002: p. 237.

[91] A. Messan, P. Ienny, D. Nectoux, Free and restrained early-age shrinkage of mortar: Influence of glass fiber, cellulose ether and EVA (ethylene-vinyl acetate), Cem. Concr. Compos. 33 (2011) 402–410.

[92] M. Norfleet, A model to quantify the influence of fiber reinforcement on plastic shrinkage cracking, Purdue University, 2008.

[93] N.S. Berke, M.P. Dallaire, Effect of low addition rates of polypropylene fibers on plastic shrinkage cracking and mechanical properties of concrete, Spec. Publ. 142 (1994) 19–42.

[94] P.N. Balaguru, S.P. Shah, Fiber-reinforced cement composites, 1992.

[95] N. Banthia, R. Gupta, TEST METHOD FOR EVALUATION OF PLASTIC SHRINKAGE CRACKING IN FIBER-REINFORCED CEMENTITIOUS MATERIALS, Exp. Tech. 31 (2007) 44–48.

[96] R. Malathy, K. Subramanian, M. Rameshkumar, Effect of glass fibers on restrained plastic shrinkage cracking of HPC with silica fume, (2007).

[97] A. Hosoda, PLASTIC SHRINKAGE CRACK CONTROLLING MECHANISM OF SYNTHETIC SHORT FIBER, in: 30th Conference on Our World in Concrete and Structures (OWICs), Singapore, 2005. http://cipremier.com/100030033.

[98] J. Branch, A. Rawling, D.J. Hannant, M. Mulheron, The effects of fibres on the plastic shrinkage cracking of high strength concrete, Mater. Struct. 35 (2002) 189–194.

[99] P.S. Mangat, M.M. Azari, Plastic shrinkage of steel fibre reinforced concrete, Mater. Struct. 23 (1990) 186–195.

[100] D. Ravina, Early longitudinal dimensional changes of fresh fly ash mortar exposed to drying conditions, Cem. Concr. Res. 16 (1986) 902–910.

[101] R.E. Cromarty, J.G. Bryden, An apparatus for measuring dimensional changes in fresh cement paste, Mag. Concr. Res. 19 (1967) 239–242.

[102] D.M.F. Orr, G.F. Haigh, An apparatus for measuring the shrinkage characteristics of plastic mortars, Mag. Concr. Res. 23 (1971) 43–48.

[103] H. Gowda, Effects of Retarding Admixtures on Plastic Shrinkage of Portland Cement Paste: Interim Report, Jt. Highw. Res. Proj. Indiana Dep. Transp. Purdue Univ. West Lafayette Indiana. (1973). doi:10.5703/1288284313859.

[104] C.F. Scholer, The Influence of Retarding Admixtures on Volume Changes of Concrete, Jt. Highw. Res. Proj. Indiana Dep. Transp. Purdue Univ. West Lafayette Indiana. (1975). doi:10.5703/1288284313905.

[105] J. Jasiczak, P. Szymański, The influence of melamine based superplasticizer on early concrete shrinkage, Found. Civ. Environ. Eng. 15 (2004) 5–14.

[106] L. Brüll, K. Komlos, B. Majzlan, Early shrinkage of cement pastes, mortars, and concretes, Matér. Constr. 13 (1980) 41–45.

[107] L. Brüll, K. Komlos, Early volume changes of cement pastes and cement mortars, in: Int. Conf. Concr. Early Ages RILEM Paris, 1982: pp. 29–34.

[108] K. Kovler, Testing system for determining the mechanical behaviour of early age concrete under restrained and free uniaxial shrinkage, Mater. Struct. 27 (1994) 324–330.

[109] J. Branch, D.J. Hannant, M. Mulheron, Factors affecting the plastic shrinkage cracking of high-strength concrete, Mag. Concr. Res. 54 (2002) 347–354.

[110] M.D. Newlands, K.A. Paine, N.A. Vemuri, R.K. Dhir, A linear test method for determining early-age shrinkage of concrete, Mag. Concr. Res. 60 (2008) 747–757.

[111] M.A. Sanjuán, A. Moragues, A testing method for measuring plastic shrinkage in polypropylene fibre reinforced mortars, Mater. Lett. 21 (1994) 239–246.

[112] M.A. Sanjuan, B. Bacle, A. Moragues, C. Andrade, Plastic shrinkage and permeability in polypropylene reinforced mortar, ACI Spec. Publ. 124 (1990).

[113] M.A. Sanjuan, A. Moragues, Polypropylene-fibre-reinforced mortar mixes: Optimization to control plastic shrinkage, Compos. Sci. Technol. 57 (1997) 655–660.

[114] R.D. Tolêdo Filho, M.A. Sanjuán, Effect of low modulus sisal and polypropylene fibre on the free and restrained shrinkage of mortars at early age, Cem. Concr. Res. 29 (1999) 1597–1604.

[115] R.D. Toledo Filho, K. Ghavami, M.A. Sanjuán, G.L. England, Free, restrained and drying shrinkage of cement mortar composites reinforced with vegetable fibres, Cem. Concr. Compos. 27 (2005) 537–546.

[116] V. Slowik, E. Schlattner, T. Klink, Experimental investigation into early age shrinkage of cement paste by using fibre Bragg gratings, Cem. Concr. Compos. 26 (2004) 473–479.

[117] A.C. Wong, P.A. Childs, R. Berndt, T. Macken, G.-D. Peng, N. Gowripalan, Simultaneous measurement of shrinkage and temperature of reactive powder concrete at early-age using fibre Bragg grating sensors, Cem. Concr. Compos. 29 (2007) 490–497.

[118] S. Hanehara, H. Hirao, H. Uchikawa, Relationships between autogenous shrinkage, the microstructure and humidity changes at inner part of hardened cement paste at early age, Autogenous Shrinkage Concr. FN Spon Lond. 1999. (1999) 93–104.

[119] Y. Baba, K. Maleesee, T. Kasai, Effects of self-desiccation on shrinkage properties of cement paste at very early ages, in: Thailand, 2005: pp. 194–198.

[120] M. Morioka, A. Hori, H. Hagiwara, E. Sakai, M. Daimon, Measurements of autogenous length changes by laser sensors equipped with digital computer system, in: E. Tazawa (Ed.), E & FN Spon, London, n.d.: pp. 203–210.

[121] E. Bühler, R. Zurbriggen, Mechanisms of early shrinkage and expansion of fast setting flooring compounds, Expans. Agents Expans. Concr. 2 (2007) 005.

[122] E.E. Holt, D.J. Janssen, Influence of early age volume changes on long-term concrete shrinkage, Transp. Res. Rec. J. Transp. Res. Board. 1610 (1998) 28–32.

[123] E. Holt, O. Schodet, Self-compacting concrete: early age shrinkage, Tech. Res. Cent. Finl. VTT Build. Transp. Intern. Rep. (2002).

[124] T.A. Hammer, K.T. Fosså, Influence of entrained air voids on pore water pressure and volume change of concrete before and during setting, Mater. Struct. 39 (2006) 801–808.

[125] T.A. Hammer, Deformations, strain capacity and cracking of concrete in plastic and early hardening phases, NTNU, 2007.

[126] P. Ghoddousi, A.A.S. Javid, Plastic Shrinkage Evaluation of Self-Consolidating Concrete as Repair Materials Based on Restrained and Free Strain Measurements, in: Des. Prod. Place. Self-Consol. Concr., Springer, 2010: pp. 295–306.

[127] P. Turcry, A. Loukili, A study of plastic shrinkage of self-compacting concrete, in: Proc. 3rd Int. RILEM Symp. Self-Compact. Concr. Reyk. RILEM Publ. SARL, 2003: pp. 576–585.

[128] J. Liu, Q. Tian, C. Miao, Investigation on the plastic shrinkage of cementitious materials under drying conditions: mechanism and theoretical model, Mag. Concr. Res. 64 (2012) 551–561.

[129] P. Fontana, S. Pirskawetz, P. Lura, Plastic Shrinkage Cracking Risk of Concrete–Evaluation of Test Methods, in: 7th RILEM Int. Conf. Crack. Pavements, Springer, 2012: pp. 591–600.

[130] D. Lecompte, A. Smits, S. Bossuyt, H. Sol, J. Vantomme, D. Van Hemelrijck, A.M. Habraken, Quality assessment of speckle patterns for digital image correlation, Opt. Lasers Eng. 44 (2006) 1132–1145.

[131] T. Le-Bihan, J.-F. Georgin, M. Michel, J. Ambroise, F. Morestin, Measurements and modeling of cement base materials deformation at early age: The case of sulfo-aluminous cement, Cem. Concr. Res. 42 (2012) 1055–1065.

[132] ASTM C1579-13, Standard Test Method for Evaluating Plastic Shrinkage Cracking of Restrained Fiber Reinforced Concrete (Using a Steel Form Insert), ASTM International, West Conshohocken, PA, 2013, www.astm.org, (n.d.).

[133] A. Sivakumar, Studies on influence of water-cement ratio on the early age shrinkage cracking of concrete systems, J. Civ. Eng. Constr. Technol. 4 (2013).

[134] S. Ranjbar, Effect of pre-wetted perlite and fibers on autogenous and plastic shrinkage of high strength concrete, University of British Columbia, n.d.

[135] R. Combrinck, W.P. Boshoff, Typical plastic shrinkage cracking behaviour of concrete, Mag. Concr. Res. 65 (2013) 486–493.

[136] A. Hossain, S. Shrestha, J. Summers, Properties of concrete incorporating ultrafine fly ash and silica fume, Transp. Res. Rec. J. Transp. Res. Board. (2009) 41–46.

[137] A. Sivakumar, M. Santhanam, Experimental methodology to study plastic shrinkage cracks in high strength concrete, Meas. Monit. Model. Concr. Prop. (2006) 291–296.

[138] W.P. Boshoff, R. Combrinck, Modelling the severity of plastic shrinkage cracking in concrete, Cem. Concr. Res. 48 (2013) 34–39.

[139] S.-T. Lin, R. Huang, T.-L. Weng, Effect of Water Soluble Polymer and Fiber on the Early-Age Shrinkage Cracking of Cementitious Composites, J. Mar. Sci. Technol. 20 (2012) 295–303.

[140] S.-T. Lin, R. Huang, T.-L. Weng, Effect of mineral admixtures and viscosity modifying admixtures on plastic shrinkage cracking of cementitious composites, J. Chin. Inst. Eng. 34 (2011) 287–297.

[141] L. Ruiz-Ripoll, B.E. Barragán, S. Moro, J. Turmo, Digital imaging methodology for measuring early shrinkage cracking in concrete, Strain. 49 (2013) 267–275.

[142] NORDTEST NT BUILD 433, Concrete: Cracking Tendency – Exposure to Drying During the First 24 Hours, (1995).

[143] C.L. Hwang, C.T. Chen, L.A.T. Bui, F.R. Kurniawan, The Study on the Early Age Cracking due to the Addition of Silica Fume into Concrete and the Trouble-Shooting Strategy, in: Adv. Mater. Res., Trans Tech Publ, 2011: pp. 824–829.

[144] O. Esping, Effect of limestone filler BET (H 2 O)-area on the fresh and hardened properties of self-compacting concrete, Cem. Concr. Res. 38 (2008) 938–944.

[145] R.D. Toledo Filho, M.A. Sanjuan, Effect of low modulus sisal and polypropylene fibre on the free and restrained shrinkage of mortars at early age, Cem. Concr. Res. 29 (1999) 1597–1604.

[146] GB/T 50082-2009: Standard for test methods of long-term performance and durability of ordinary concrete, China building industry press, 2009.

[147] S.J. Li, H.P. Qian, Crack Resistance and Permeability of Hybrid Fiber Reinforced Concrete Application in Understructure Work, in: Appl. Mech. Mater., Trans Tech Publ, 2013: pp. 257–261.

[148] N. Banthia, C. Yan, S. Mindess, Restrained shrinkage cracking in fiber reinforced concrete: a novel test technique, Cem. Concr. Res. 26 (1996) 9–14.

[149] N. Banthia, R. Gupta, Plastic shrinkage cracking in cementitious repairs and overlays, Mater. Struct. 42 (2009) 567–579.

[150] S.R.R. Senthilkumar, S.C. Natesan, Prediction of restrained plastic shrinkage cracking in plain cement concrete, Mag. Concr. Res. 57 (2005) 579–587.

[151] B. Nabil, A. Aissa, B.I. Aguida, Effectiveness of Different Solutions to Reduce Plastic Shrinkage in Hot Climate Concreting, in: Vol. Two Three Second Int. Conf. Sustain. Constr. Mater. Technol. June, 2010.

[152] Y. Liu, The Influence of Fly Ash on the Crack Performance of Airport Pavement Concrete by Dumbbell Test Method, in: Adv. Mater. Res., Trans Tech Publ, 2013: pp. 1719–1722.

[153] T.S. Tan, T.H. Wee, S.A. Tan, C.T. Tam, S.L. Lee, A consolidation model for bleeding of cement paste, Adv. Cem. Res. 1 (1987) 18–26.

[154] L. Josserand, O. Coussy, F. de Larrard, Bleeding of concrete as an ageing consolidation process, Cem. Concr. Res. 36 (2006) 1603–1608.

[155] P.H. Morris, P.F. Dux, Analytical solutions for bleeding of concrete due to consolidation, Cem. Concr. Res. 40 (2010) 1531–1540.

[156] A. Radocea, A study on the mechanism of plastic shrinkage of cement-based materials, Chalmers University of Technology, 1992.

[157] P. Morris, P. Dux, Cracking of plastic concrete, Aust. J. Civ. Eng. 1 (2003) 17–21.

[158] V. Slowik, T. Hübner, M. Schmidt, B. Villmann, Simulation of capillary shrinkage cracking in cement-like materials, Cem. Concr. Compos. 31 (2009) 461–469.

[159] V. Slowik, J.W. Ju, Discrete modeling of plastic cement paste subjected to drying, Cem. Concr. Compos. 33 (2011) 925–935.

[160] L.A. RICHARDS, Diagnosis and improvement of saline and alkali soils., Soil Sci. 78 (1954) 154.

[161] A.E. Scheidegger, Physics of flow through porous media, in: Phys. Flow Porous Media, University of Toronto, 1963.

[162] D. Hillel, Environmental soil physics: Fundamentals, applications, and environmental considerations, Academic press, 1998.

[163] R. Lal, M.K. Shukla, Principles of soil physics, CRC Press, 2004.

[164] D.G. Fredlund, H. Rahardjo, Soil mechanics for unsaturated soils, John Wiley & Sons, 1993.

[165] V. Picandet, D. Rangeard, A. Perrot, T. Lecompte, Permeability measurement of fresh cement paste, Cem. Concr. Res. 41 (2011) 330–338.

[166] J.J. Assaad, J. Harb, Use of the falling-head method to assess permeability of freshly mixed cementitious-based materials, J. Mater. Civ. Eng. 25 (2012) 580–588.

[167] L. Reddi, H.I. Inyang, Geoenvironmental engineering: principles and applications, CRC Press, 2000.

[168] H. Wang, Theory of linear poroelasticity with applications to geomechanics and hydrogeology, Princeton University Press, 2000.

[169] M.A. Biot, General theory of three-dimensional consolidation, J. Appl. Phys. 12 (1941) 155–164.

[170] D. Rangeard, A. Perrot, V. Picandet, Y. Mélinge, P. Estellé, Determination of the consolidation coefficient of low compressibility materials: application to fresh cement-based materials, Mater. Struct. 48 (2015) 1475–1483.

[171] S. Ghourchian, M. Wyrzykowski, P. Lura, M. Shekarchi, B. Ahmadi, An investigation on the use of zeolite aggregates for internal curing of concrete, Constr. Build. Mater. 40 (2013) 135–144.

[172] M. Wyrzykowski, P. Lura, F. Pesavento, D. Gawin, Modeling of internal curing in maturing mortar, Cem. Concr. Res. 41 (2011) 1349–1356.

[173] D. Gawin, F. Pesavento, B.A. Schrefler, Hygro-thermo-chemo-mechanical modelling of concrete at early ages and beyond. Part I: hydration and hygro-thermal phenomena, Int. J. Numer. Methods Eng. 67 (2006) 299–331.

[174] M. Wyrzykowski, P. Lura, F. Pesavento, D. Gawin, Modeling of water migration during internal curing with superabsorbent polymers, J. Mater. Civ. Eng. (2011).

[175] D.P. Bentz, W.J. Weiss, Internal curing: a 2010 state-of-the-art review, US Department of Commerce, National Institute of Standards and Technology, 2011.

[176] T.L. Anderson, T.L. Anderson, Fracture mechanics: fundamentals and applications, CRC press, 2005.

[177] G. Ye, P. Lura, van K. van Breugel, Modelling of water permeability in cementitious materials, Mater. Struct. 39 (2006) 877–885.

[178] D.N. Winslow, M.D. Cohen, D.P. Bentz, K.A. Snyder, E.J. Garboczi, Percolation and pore structure in mortars and concrete, Cem. Concr. Res. 24 (1994) 25–37.

[179] A. Perrot, D. Rangeard, V. Picandet, Y. Mélinge, Hydro-mechanical properties of fresh cement pastes containing polycarboxylate superplasticizer, Cem. Concr. Res. 53 (2013) 221–228.

[180] G. Ye, P. Lura, K. Van Breugel, A.L.A. Fraaij, Study on the development of the microstructure in cement-based materials by means of numerical simulation and ultrasonic pulse velocity measurement, Cem. Concr. Compos. 26 (2004) 491–497.

[181] T. Voigt, C.U. Grosse, Z. Sun, S.P. Shah, H.-W. Reinhardt, Comparison of ultrasonic wave transmission and reflection measurements with P-and S-waves on early age mortar and concrete, Mater. Struct. 38 (2005) 729–738.

[182] T.-S. Tan, C.-K. Loh, K.-Y. Yong, T.-H. Wee, Modelling of bleeding of cement paste and mortar, Adv. Cem. Res. 9 (1997) 75–91.

[183] E. Tazawa, Autogenous shrinkage of concrete, CRC Press, 1999.

[184] K. Terzaghi, Soil mechanics in engineering practice, John Wiley & Sons, 1996.

[185] W. Powrie, Soil mechanics: concepts and applications, CRC Press, 2013.

[186] A. Perrot, A. Pierre, S. Vitaloni, V. Picandet, Prediction of lateral form pressure exerted by concrete at low casting rates, Mater. Struct. 48 (2015) 2315–2322.

[187] G. Sant, M. Dehadrai, D. Bentz, P. Lura, C.F. Ferraris, J.W. Bullard, J. Weiss, Detecting the fluid-to-solid transition in cement pastes, Concr. Int. 31 (2009) 53–58.

[188] G. Sant, D. Bentz, J. Weiss, Capillary porosity depercolation in cement-based materials: measurement techniques and factors which influence their interpretation, Cem. Concr. Res. 41 (2011) 854–864.

[189] L. Josserand, F. De Larrard, A method for concrete bleeding measurement, Mater. Struct. 37 (2004) 666–670.

[190] Z. Tian, J. Guo, C. Gu, Study on Permeability Coefficient and Volumetric Deformation Modulus of Fresh Concrete for Different Mix Designs, in: Earth Space 2010 SEngineering Sci. Constr. Oper. Challenging Environ., ASCE, 2010: pp. 751–757.

[191] R.W. Vervoort, S.R. Cattle, Linking hydraulic conductivity and tortuosity parameters to pore space geometry and pore-size distribution, J. Hydrol. 272 (2003) 36–49.

[192] P.C. Carman, Flow of gases through porous media, Academic press, 1956.

[193] B. Ghanbarian, A.G. Hunt, R.P. Ewing, M. Sahimi, Tortuosity in porous media: a critical review, Soil Sci. Soc. Am. J. 77 (2013) 1461–1477.

[194] D. Cornell, D.L. Katz, Flow of gases through consolidated porous media, Ind. Eng. Chem. 45 (1953) 2145–2152.

[195] X. Wei, L. Xiao, Influence of the aggregate volume on the electrical resistivity and properties of portland cement concretes, J. Wuhan Univ. Technol.-Mater Sci Ed. 26 (2011) 965–971.

[196] L. Zong-jin, W. Xiao-sheng, The electrical resistivity of cement paste incorporated with retarder, J. Wuhan Univ. Technol.-Mater Sci Ed. 18 (2003) 76–78.

[197] L. Xiao, Z. Li, Early-age hydration of fresh concrete monitored by non-contact electrical resistivity measurement, Cem. Concr. Res. 38 (2008) 312–319.

[198] M.C.G. Juenger, F. Winnefeld, J.L. Provis, J.H. Ideker, Advances in alternative cementitious binders, Cem. Concr. Res. 41 (2011) 1232–1243.

[199] O.S.B. Al-Amoudi, M. Maslehuddin, T.O. Abiola, Effect of type and dosage of silica fume on plastic shrinkage in concrete exposed to hot weather, Constr. Build. Mater. 18 (2004) 737–743.

[200] N.U. Kockal, F. Turker, Effect of environmental conditions on the properties of concretes with different cement types, Constr. Build. Mater. 21 (2007) 634–645.

[201] ASTM C827 / C827M-10, Standard Test Method for Change in Height at Early Ages of Cylindrical Specimens of Cementitious Mixtures, (2010).

[202] B. En, 197-1 (2000) Cement: composition, specifications and conformity criteria for common cements, Br. Stand. Inst. Lond. (2000).

[203] B. EN, 12350-5 (2000). Testing fresh concrete-Part-5: Flow table test, Br. Stand. (2000).

[204] B. EN, 12350-2, Testing fresh concrete: slump test, Lond. Br. Stand. Inst. (2000).

[205] BS EN 480-4:2005, Admixtures for concrete, mortar and grout. Test methods. Determination of bleeding of concrete, BSI. (2005).

[206] P. Lura, C. Di Bella, Trindler, Walter, Münch, Beat, Leemann, Andreas, An advanced experimental setup to study plastic shrinkage cracking of concrete., in: Dubai, United Arab Emirates, 2011.

[207] R.R. Hocking, Methods and applications of linear models: regression and the analysis of variance, John Wiley & Sons, 2013.

[208] H.F. Taylor, Cement chemistry, Thomas Telford, 1997.

[209] M. Wyrzykowski, S. Ghourchian, A. Assmann, P. Lura, Limiting plastic shrinkage cracking in cement grout with C-S-H seeding, Mater. Struct. (2017) in preparation.

[210] E. Buckingham, Studies on the movement of soil moisture, (1907).

[211] V.T. Dao, P.F. Dux, P.H. Morris, Tensile properties of early-age concrete, ACI Mater. J. 106 (2009).

[212] D.H. Nguyen, V.T. Dao, P. Lura, Tensile properties of concrete at very early ages, Constr. Build. Mater. (2016) under review.

[213] R.R. Hocking, Collinearity in Multiple Linear Regression, Methods Appl. Linear Models Regres. Anal. Var. (2005) 151–192.

[214] F. Ghasemzadeh, M. Pour-Ghaz, Effect of damage on moisture transport in concrete, J. Mater. Civ. Eng. 27 (2014) 04014242.

[215] P. Lura, J. Couch, O.M. Jensen, J. Weiss, Early-age acoustic emission measurements in hydrating cement paste: evidence for cavitation during solidification due to self-desiccation, Cem. Concr. Res. 39 (2009) 861–867.

[216] N. Banthia, R. Gupta, Influence of polypropylene fiber geometry on plastic shrinkage cracking in concrete, Cem. Concr. Res. 36 (2006) 1263–1267.

[217] J. Bear, Hydraulics of Groundwater, McGraw-Hill, 1979.

[218] Introduction to the Subsurface Flow Module, Comsol AB, Stockholm, 2013.

[219] E.E. Alonso, A. Gens, A. Josa, Constitutive model for partially saturated soils, Géotechnique. 40 (1990) 405–430.

[220] D.G. Fredlund, H. Rahardjo, M.D. Fredlund, Unsaturated soil mechanics in engineering practice, John Wiley & Sons, 2012.

[221] A. Perrot, D. Rangeard, Effects of mix design parameters on consolidation behaviour of fresh cement-based materials, Mater. Struct. 50 (2017) 117.

[222] G. Suazo, A. Fourie, J. Doherty, Experimental Study of the Evolution of the Soil Water Retention Curve for Granular Material Undergoing Cement Hydration, J. Geotech. Geoenvironmental Eng. (2016) 04016022.

[223] T.C. Powers, T.L. Brownyard, Studies of the physical properties of hardened Portland cement paste (nine parts), in: Journal of American Concrete Institute. Bulletin 22, Research Laboratories of the Portland Cement Association, 1946.

[224] T.C. Hansen, Physical structure of hardened cement paste. A classical approach, Mater. Struct. 19 (1986) 423–436.

[225] A. Szymkiewicz, Mathematical Models of Flow in Porous Media, in: Model. Water Flow Unsaturated Porous Media, Springer, 2013: pp. 9–47.

[226] R.H. Brooks, A.T. Corey, Properties of porous media affecting fluid flow, J. Irrig. Drain. Div. 92 (1966) 61–90.

[227] E. Shahraeeni, P. Lehmann, D. Or, Coupling of evaporative fluxes from drying porous surfaces with air boundary layer: Characteristics of evaporation from discrete pores, Water Resour. Res. 48 (2012).

[228] G.W. Scherer, Drying, Shrinkage, and Cracking of Cementitious Materials, Transp. Porous Media. (2015) 1–21.

[229] M.T. Van Genuchten, A closed-form equation for predicting the hydraulic conductivity of unsaturated soils, Soil Sci. Soc. Am. J. 44 (1980) 892–898.

[230] W.J. Rawls, D. Gimenez, R. Grossman, Use of soil texture, bulk density, and slope of the water retention curve to predict saturated hydraulic conductivity, Trans. ASAE. 41 (1998) 983–988.

[231] V. Baroghel-Bouny, M. Mainguy, T. Lassabatere, O. Coussy, Characterization and identification of equilibrium and transfer moisture properties for ordinary and high-performance cementitious materials, Cem. Concr. Res. 29 (1999) 1225–1238.

[232] M.A. Biot, D.G. Willis, The elastic coefficients of the theory of consolidation, J Appl Mech. 24 (1957) 594–601.

[233] H. Chen, Autogenous and Thermal Deformations and their Interaction in Early Age Cementitous Materials, EPFL Lausanne. (2013).

[234] COMSOL Multiphysics, The Finite Element Method (FEM), Multiphysics Cyclopedia. (2017). https://www.comsol.com/multiphysics/finite-element-method.

[235] H.F. Taylor, Modification of the Bogue calculation, Adv. Cem. Res. 2 (1989) 73–77.

[236] EN 12350-7, Testing fresh concrete. Air content. Pressure methods, (2009).

[237] J. Zelić, D. Rušić, D. Veza, R. Krstulović, The role of silica fume in the kinetics and mechanisms during the early stage of cement hydration, Cem. Concr. Res. 30 (2000) 1655–1662.

[238] EN 1015-3: Methods of test for mortar for masonry. Determination of consistence of fresh mortar (by flow table), (n.d.).

[239] ASTM C807-13,Standard Test Method for Time of Setting of Hydraulic Cement Mortar by Modified Vicat Needle, (2013).

[240] T.A. Hammer, Effect of silica fume on the plastic shrinkage and pore water pressure of high-strength concretes, Mater. Struct. 34 (2001) 273–278.

[241] J.J. Assaad, J. Harb, Surface settlement of cementitious-based materials determined by oedometer testing, Mater. Struct. 44 (2011) 845–856.

[242] W.J. Weiss, W. Yang, S.P. Shah, Factors influencing durability and early-age cracking in high-strength concrete structures, Spec. Publ. 189 (2000) 387–410.

[243] W.-F. Chen, Plasticity in reinforced concrete, J. Ross Publishing, 2007.

[244] P. Beverly, Fib Model Code for Concrete Structures 2010, Ernst & Sohn, 2013.

[245] S. Mohammadi, Extended finite element method: for fracture analysis of structures, John Wiley & Sons, 2008.

[246] A. Akhavan, F. Rajabipour, Evaluating ion diffusivity of cracked cement paste using electrical impedance spectroscopy, Mater. Struct. (2013) 1–12.

[247] M. Pour-Ghaz, F. Rajabipour, J. Couch, J. Weiss, Modeling fluid transport in cementitious systems with crack-like (notch) geometries, in: Proc. 2nd Int. RILEM Workshop Concr. Durab. Serv. Life Plan. Haifa Isr., 2009.

[248] V. Picandet, A. Khelidj, H. Bellegou, Crack effects on gas and water permeability of concretes, Cem. Concr. Res. 39 (2009) 537–547.

[249] D.H. Nguyen, V.T. Dao, P. Lura, Tensile properties of concrete at very early ages, Constr. Build. Mater. 134 (2017) 563–573.

[250] L. Laloui, C. Cekerevac, Thermo-plasticity of clays: an isotropic yield mechanism, Comput. Geotech. 30 (2003) 649–660.

[251] A. Casagrande, The determination of the pre-consolidation load and its practical significance, in: Proc. Int. Conf. Soil Mech. Found. Eng., Harvard University Cambridge, 1936: pp. 60–64.

[252] A.B. Comsol, Geomechanics module user's guide, Comsol AB, Stockholm, 2012.

[253] B. Bresler, K.S. Pister, Strength of concrete under combined stresses, in: J. Proc., 1958: pp. 321–345.

[254] K. Raoufi, J. Schlitter, D. Bentz, J. Weiss, Parametric assessment of stress development and cracking in internally cured restrained mortars experiencing autogenous deformations and thermal loading, Adv. Civ. Eng. 2011 (2011).

[255] K.J. Bathe, M. Kojic, Inelastic analysis of solids and structures, Springer, 2005.

[256] D.C. Drucker, W. Prager, Soil mechanics and plastic analysis or limit design, Q. Appl. Math. 10 (1952) 157–165.

[257] P. Fontana, S. Pirskawetz, P. Lura, Plastic shrinkage cracking risk of concrete–Evaluation of test methods, in: 7th RILEM Int. Conf. Crack. Pavements, Springer, 2012: pp. 591–600.

[258] A. Hossain, S. Shirazi, J. Persun, N. Neithalath, Properties of concrete containing vitreous calcium aluminosilicate pozzolan, Transp. Res. Rec. J. Transp. Res. Board. (2008) 32–38.

[259] GB/T 50082-2009 (National Standard of the People's Republic of China):The Test Method of Long-term and Durability on Ordinary Concrete, China Architecture and Building Press, 2009.

[260] P.P. Kraai, A proposed test to determine the cracking potential due to drying shrinkage of concrete, Concr. Constr. 30 (1985) 775–778.

[261] C.A. Shaeles, K.C. Hover, Influence of mix proportions and construction operations on plastic shrinkage cracking in thin slabs, Mater. J. 85 (1988) 495–504.

[262] Ö. Eren, K. Marar, Effect of steel fibers on plastic shrinkage cracking of normal and high strength concretes, Mater. Res. 13 (2010) 135–141.

[263] V. Ramakrishnan, R. Zellers, A.K. Patnaik, Plastic shrinkage reduction potential of a new high tenacity monofilament polypropylene fiber, Spec. Publ. 243 (2007) 49–62.

[264] K. Gunasekaran, R. Annadurai, P.S. Kumar, Plastic shrinkage and deflection characteristics of coconut shell concrete slab, Constr. Build. Mater. 43 (2013) 203–207.

[265] F. Pelisser, A.B. da S.S. Neto, H.L. La Rovere, R.C. de Andrade Pinto, Effect of the addition of synthetic fibers to concrete thin slabs on plastic shrinkage cracking, Constr. Build. Mater. 24 (2010) 2171–2176.

[266] N.F. Medina, G. Barluenga, F. Hernández-Olivares, Enhancement of durability of concrete composites containing natural pozzolans blended cement through the use of Polypropylene fibers, Compos. Part B Eng. 61 (2014) 214–221.

[267] M. Umar, A. Sadrekarimi, Accuracy of determining pre-consolidation pressure from laboratory tests, Can. Geotech. J. (2016).

[268] Y. Fung, Foundations of solid mechanics, Prentice Hall, 1965.

[269] J.A. De Wet, Three-Dimensional Consolidation, Highw. Res. Board Bull. (1962).

[270] L.E. Bowles, Foundation analysis and design, McGraw-hill, 1996.

[271] M. Wyrzykowski, P. Lura, Moisture dependence of thermal expansion in cement-based materials at early ages, Cem. Concr. Res. 53 (2013) 25–35.

[272] W.-F. Chen, E. Mizuno, Nonlinear analysis in soil mechanics, Elsevier Amsterdam, 1990.

[273] G. Lu, K. Wang, Theoretical and experimental study on shear behavior of fresh mortar, Cem. Concr. Compos. 33 (2011) 319–327.

[274] E. Bauer, E. Fonseca da Silva, J.G. Gomes De Sousa, M.C. de Freitas Salomão, Friction influence between particles in the behavior of flow of lime-rendering mortars, J. Mater. Civ. Eng. 27 (2014) 04014136.

[275] A. Alexandridis, N.J. Gardner, Mechanical behaviour of fresh concrete, Cem. Concr. Res. 11 (1981) 323–339.

[276] J.A. Collins, Failure of materials in mechanical design: analysis, prediction, prevention, John Wiley & Sons, 1993.

[277] F. d'Onza, A. d'Onofrio, C. Mancuso, Effects of Unsaturated Soil State on the Local Seismic Response of Soil Deposits, in: Proc. 1st Eur. Conf. Unsaturated Soils, Durham, 2008: pp. 531–536.

[278] S.H. Ebrahimi, S. Mohammadi, A. Asadpoure, An extended finite element (XFEM) approach for crack analysis in composite media, Int J Civ Eng. 6 (2008) 198–207.

[279] T. Cajuhi, L. Sanavia, L. De Lorenzis, Phase-field modeling of fracture in variably saturated porous media, Comput. Mech. (2017) 1–20.

[280] F.M. Capaldi, Continuum mechanics: constitutive modeling of structural and biological materials, Cambridge University Press, 2012.

[281] V. Slowik, M. Schmidt, Early age cracking and capillary pressure controlled concrete curing, Adv. Cem.-Based Mater. (2010).

[282] J. Plank, E. Sakai, C.W. Miao, C. Yu, J.X. Hong, Chemical admixtures—Chemistry, applications and their impact on concrete microstructure and durability, Cem. Concr. Res. 78 (2015) 81–99.

[283] J.P. Liu, L. Li, C.W. Miao, Q. Tian, Q.P. Ran, Y.J. Wang, Reduction of water evaporation and cracks on plastic concrete surface by monolayers, Colloids Surf. Physicochem. Eng. Asp. 384 (2011) 496–500.

[284] J.J. Thomas, H.M. Jennings, J.J. Chen, Influence of nucleation seeding on the hydration mechanisms of tricalcium silicate and cement, J. Phys. Chem. C. 113 (2009) 4327–4334.

[285] M. Duriez, R. Lézy, Possibilités nouvelles dans le durcissement rapide des ciments, mortiers et bétons, Ann. L'Institut Tech. BâTim. Des. 98 (1956) 482–483.

[286] L. Nicoleau, The acceleration of cement hydration by seeding: influence of the cement mineralogy, ZKG Int. 1 (2013) 40–49.

[287] BS EN 12350-2:2009,Testing fresh concrete. Slump-test, (n.d.).

[288] EN 12350-5:2009.Testing fresh concrete. Flow table test, (2009).

[289] BS EN 480-4:2005, Admixtures for concrete, mortar and grout. Test methods. Determination of bleeding of concrete, (2005).

[290] A. Karagunduz, K.D. Pennell, M.H. Young, Influence of a nonionic surfactant on the water retention properties of unsaturated soils, Soil Sci. Soc. Am. J. 65 (2001) 1392–1399.

[291] K. Owens, M.I. Russell, G. Donnelly, A. Kirk, P.A.M. Basheer, Use of nanocrystal seeding chemical admixture in improving Portland cement strength development: application for precast concrete industry, Adv. Appl. Ceram. 113 (2014) 478–484.

[292] M. Bräu, L. Ma-Hock, C. Hesse, L. Nicoleau, V. Strauss, S. Treumann, K. Wiench, R. Landsiedel, W. Wohlleben, Nanostructured calcium silicate hydrate seeds accelerate concrete hardening: a combined assessment of benefits and risks, Arch. Toxicol. 86 (2012) 1077–1087.

[293] ASTM C232 / C232M-14, Standard Test Method for Bleeding of Concrete, ASTM International, West Conshohocken, PA. (2014).

[294] Institute of Standards and Industrial Research of Iran, ISIRI 3820.STANDARD TEST METHODS FOR BLEEDING OF CONCRETE., (1996).

[295] AS 1012.6-1999. Methods of testing concrete, Method 6: Method for the determination of bleeding of concrete., (1999).

[296] Japan Concrete Institute, JIS A 1123:2012.Method of test for bleeding of concrete., (2012).

[297] Bureau of Indian Standards, IS 9103:1999.Concrete Admixtures-Specification: Annex D: METHOD OF TEST FOR BLEEDING OF CONCRETE, (1999).

[298] RILEM TC, RILEM CPC 16: Bleeding of concrete, (1994).

[299] A.S. Khan, S. Huang, Continuum theory of plasticity, John Wiley & Sons, 1995.

[300] Z.P. Bažant, Y. Xiang, Size effect in compression fracture: splitting crack band propagation, J. Eng. Mech. 123 (1997) 162–172.

[301] R.M. Jones, Deformation theory of plasticity, Bull Ridge Corporation, 2009.

[302] J.F. Georgin, J.M. Reynouard, Modeling of structures subjected to impact: concrete behaviour under high strain rate, Cem. Concr. Compos. 25 (2003) 131–143.

[303] R. Ulusay, Ö. Aydan, H. Gerçek, M.A. Hindistan, E. Tuncay, Rock Mechanics and Rock Engineering: From the Past to the Future, Taylor & Francis Group, 2016.

[304] D. Sfer, I. Carol, R. Gettu, G. Etse, Study of the behavior of concrete under triaxial compression, J. Eng. Mech. 128 (2002) 156–163.

[305] I.S. Sandler, F.L. Dimaggio, G.Y. Baladi, Generalized cap model for geological materials, J. Geotech. Geoenvironmental Eng. 102 (1976).

[306] W.F. Brace, An extension of the Griffith theory of fracture to rocks, J. Geophys. Res. 65 (1960) 3477–3480.

PLASTIC SHRINKAGE CRACKING IN CONCRETE: FROM MECHANISMS TO MITIGATION STRATEGIES

Sadegh Ghourchian-2018

The problem of global warming is so serious and significant that recently worldwide nations signed the Paris Agreement to take necessary actions to limit the global warming below 2 °C compared to the pre-industrial levels. Many efforts have been made in the field of civil engineering to minimize the contribution of Portland cement production to the man-made CO_2 emissions, by developing green cements and furthermore, producing concretes with improved durability and mechanical performance. The latter is not possible, unless thorough knowledge about volume changes and cracking of concrete at early ages is gained. The aim of this study is to provide fundamental knowledge about the behavior of fresh cementitious materials, which are at high risk of cracking while still fresh (so-called *plastic shrinkage cracking*). Indeed, plastic shrinkage, according to some sources, may be the cause of roughly 80% of early-age cracking in concrete structures.

The front figure is a time sequence of plastic shrinkage cracking, obtained with X-ray radiography. The sample above is the reference plain mortar and below is the mortar containing silica fume. Please refer to Chapter 6 for details.